Dispersion Relations in Scattering and Antenna Problems

Sohl, Christian

2008

Dispersion Relations in Scattering and Antenna Problems

Christian Sohl

Doctoral Dissertation
Electromagnetic Theory

Lund University
Lund, Sweden
2008

Doctoral dissertation which, by due permission of the Faculty of Engineering at Lund University, will be publicly defended on Tuesday 23 September, 2008, at 10.15 a.m. in lecture hall E:1406, Department of Electrical and Information Technology, Ole Römers väg 3, Lund, for the degree of Doctor of Philosophy in Engineering.

Department of Electrical and Information Technology
Electromagnetic Theory
Lund University
P.O. Box 118, S-221 00 Lund, Sweden

Series of licentiate and doctoral theses
ISSN 1654-790X; No. 6
ISBN 978-91-628-7514-5

Typeset in Computer Modern 8 pt using LaTeX 2ε and BibTeX.
Printed in Sweden by Tryckeriet i E-huset, Lund University, Lund.
August 2008

The drawing on p. i is a facsimile of the original illustration by Sir John Tenniel in the classical children's book "Through the Looking Glass" by Lewis Carroll.

. . . "There's the King's Messenger. He's in prison now, being punished: and the trial doesn't even begin till next Wednesday: and of course the crime comes last of all."

"Suppose he never commits the crime?" said Alice.

Lewis Carroll

"Through the Looking Glass", Chapter V

Abstract

This dissertation deals with physical bounds on scattering and absorption of acoustic and electromagnetic waves. A general dispersion relation or sum rule for the extinction cross section of such waves is derived from the holomorphic properties of the scattering amplitude in the forward direction. The derivation is based on the forward scattering theorem via certain Herglotz functions and their asymptotic expansions in the low-frequency and high-frequency regimes. The result states that, for a given interacting target, there is only a limited amount of scattering and absorption available in the entire frequency range. The forward dispersion relation is shown to be valuable for a broad range of frequency domain problems involving acoustic and electromagnetic interaction with matter on a macroscopic scale. In the modeling of a metamaterial, *i.e.*, an engineered composite material that gains its properties by its structure rather than its composition, it is demonstrated that for a narrow frequency band, such a material may possess extraordinary characteristics, but that tradeoffs are necessary to increase its usefulness over a larger bandwidth.

The dispersion relation for electromagnetic waves is also applied to a large class of causal and reciprocal antennas to establish a priori estimates on the input impedance, partial realized gain, and bandwidth of electrically small and wideband antennas. The results are compared to the classical antenna bounds based on eigenfunction expansions, and it is demonstrated that the estimates presented in this dissertation offer sharper inequalities, and, more importantly, a new understanding of antenna dynamics in terms of low-frequency considerations.

The dissertation consists of 11 scientific papers of which several have been published in peer-reviewed international journals. Both experimental results and numerical illustrations are included. The General Introduction addresses closely related subjects in theoretical physics and classical dispersion theory, *e.g.*, the origin of the Kramers-Kronig relations, the mathematical foundations of Herglotz functions, the extinction paradox for scattering of waves and particles, and non-forward dispersion relations with application to the prediction of bistatic radar cross sections.

Sammanfattning (in Swedish)

Avhandlingen behandlar fysikaliska begränsningar på spridning och absorption av akustiska och elektromagnetiska vågor. En allmän dispersionsrelation eller summeringsregel för utsläckningstvärsnittet för sådana vågor härleds från analytiska egenskaper på spridningsamplituden i framåtriktningen. Härledningen baseras på framåtspridningsteoremet via klassen av Herglotz-funktioner och deras asymptotiska utvecklingar i låg- och högfrekvensgränsen. Slutsatsen är att det för en given växelverkande volym endast finns en begränsad mängd spridning och absorption att tillgå i hela frekvensspektrum. Dispersionsrelationen visar sig vara ett värdefullt verktyg för en bred samling problem i frekvensdomänen som behandlar växelverkan av vågor med materia på en makroskopisk skala. För ett metamaterial, det vill säga ett material vars egenskaper erhålls från dess struktur istället för dess sammansättning, medför teorin att ett sådant material mycket väl kan uppvisa en överdådig karakteristik i ett smalt frekvensintervall, men att kompromisser är nödvändiga för att öka dess användbarhet över en större bandbredd.

Dispersionsrelationen för elektromagnetiska vågor tillämpas också på en stor klass av kausala och reciproka antenner för att fastställa a priori begränsningar på impedans, direktivitet och bandbredd för såväl elektriskt små som bredbandiga antenner. Resultaten i avhandlingen jämförs med de klassiska antennbegränsningarna baserade på egenfunktionsutvecklingar och slutsatsen är att de nya begränsningarna ger upphov till såväl skarpare olikheter som en ny fundamental förståelse för en antenns dynamiska egenskaper uttryckt i dess lågfrekvensuppförande.

Avhandlingen består av 11 vetenskapliga artiklar av vilka flera är publicerade i internationella tidskrifter med expertutlåtande. Såväl experimentella resultat som ett flertal numeriska exempel är inkluderade i avhandlingen. Den övergripande introduktionen behandlar närliggande ämnen i teoretisk fysik och klassisk dispersionsteori såsom Kramers-Kronigs relationer, den matematiska grundvalen för Herglotz-funktioner, utsläckningsparadoxen för spridning av vågor och partiklar, samt dispersionsrelationer i godtyckliga riktningar med tillämpning mot prediktion av bistatiska radartvärsnitt.

List of included papers

This dissertation consists of a General Introduction and the following scientific papers which are referred to in the text by their roman numerals:[1]

I. C. Sohl, M. Gustafsson, and G. Kristensson. Physical limitations on broadband scattering by heterogeneous obstacles. *Journal of Physics A: Mathematical and Theoretical*, vol. 40, no. 36, pp. 11165–11182, September 2007.

II. C. Sohl, M. Gustafsson, and G. Kristensson. Physical limitations on metamaterials: Restrictions on scattering and absorption over a frequency interval. *Journal of Physics D: Applied Physics*, vol. 40, no. 22, pp. 7146–7151, November 2007.

III. C. Sohl, C. Larsson, M. Gustafsson, and G. Kristensson. A scattering and absorption identity for metamaterials: Experimental results and comparison with theory. *Journal of Applied Physics*, vol. 103, no. 5, paper 054906, March 2008.

IV. G. Kristensson, C. Larsson, C. Sohl, and M. Gustafsson. Bounds on metamaterials: Theoretical and experimental results. Book chapter to appear in 2008.

V. C. Sohl, M. Gustafsson, and A. Bernland. Some paradoxes associated with a recent summation rule in scattering theory. *Proceedings of the URSI General Assembly*, Chicago, U.S., August 7–16, 2008.[2]

VI. C. Sohl, M. Gustafsson, G. Kristensson, and S. Nordebo. A general approach for deriving bounds in electromagnetic theory. *Proceedings of the URSI General Assembly*, Chicago, U.S., August 7–16, 2008.[3]

VII. M. Gustafsson, C. Sohl, A. Karlsson, and G. Kristensson. A time-domain approach to the extinction paradox for scattering of electromagnetic waves. *Proceedings of the URSI General Assembly*, Chicago, U.S., August 7–16, 2008.

VIII. C. Sohl, M. Gustafsson, and G. Kristensson. The integrated extinction for broadband scattering of acoustic waves. *Journal of the Acoustical Society of America*, vol. 122, no. 6, pp. 3206–3210, December 2007.

IX. M. Gustafsson, C. Sohl, and G. Kristensson. Physical limitations on antennas of arbitrary shape. *Proceedings of the Royal Society A: Mathematical, Physical & Engineering Sciences*, vol. 463, no. 2086, pp. 2589–2607, October 2007.

[1] The order of the authors names indicates their relative contributions to the publications.

[2] Appointed Commission B's Best Student Paper Prize at the URSI General Assembly, Chicago, U.S., August 7–16, 2008.

[3] Honored with a Young Scientist Award at the URSI General Assembly, Chicago, U.S., August 7–16, 2008.

X. C. Sohl and M. Gustafsson. A priori estimates on the partial realized gain of ultra-wideband (UWB) antennas. *Quarterly Journal of Mechanics & Applied Mathematics*, vol. 61, no. 3, pp. 415–430, August 2008.

XI. M. Gustafsson and C. Sohl. Summation rules for the antenna input impedance. *Proceedings of the IEEE International Symposium on Antennas and Propagation*, San Diego, U.S., July 5–12, 2008.

The scientific contribution to this dissertation is derived from the above publications.

Other publications by the author

The author of this dissertation is also the author or co-author of the following scientific publications which are related to but not considered part of the dissertation:

XII. C. Sohl. *Dispersion Relations for Extinction of Acoustic and Electromagnetic Waves*. Licentiate thesis, No. 69, ISSN 1402-8662. Department of Electrical and Information Technology, Lund University, P.O. Box 118, S-221 00 Lund, Sweden, 2007.

XIII. M. Gustafsson, C. Sohl, and G. Kristensson. A forward scattering approach to new bounds in antenna theory: Applications to finite cylindrical regions. Book chapter to appear in L. Joffre and M. Martinez-Vasquez, editors, *Handbook of Small Antennas*, 2009.

XIV. A. Derneryd, M. Gustafsson, G. Kristensson, and C. Sohl. Application of gain-bandwidth bounds on loaded dipole antennas. Journal paper submitted for publication in 2008.

XV. G. Kristensson, C. Sohl, and M. Gustafsson. Physical bounds on scattering by metamaterials. *Proceedings of the URSI General Assembly*, Chicago, U.S., August 7–16, 2008.

XVI. S. Nordebo, M. Gustafsson, C. Sohl, and G. Kristensson. On the optimal limitations for scattering of spherical modes. *Proceedings of the URSI General Assembly*, Chicago, U.S., August 7–16, 2008.

XVII. C. Sohl and M. Gustafsson. A priori estimates on the partial realized gain of UWB-antennas. *Proceedings of the URSI General Assembly*, Chicago, U.S., August 7–16, 2008.

XVIII. M. Gustafsson and C. Sohl. Physical bounds and sum rules in antenna theory. *Proceedings of the URSI General Assembly*, Chicago, U.S., August 7–16, 2008.

XIX. C. Larsson, C. Sohl, G. Kristensson, and M. Gustafsson. Bounds on metamaterials: Experimental results. *Proceedings of the NATO Advanced Research Workshop: Metamaterials for Secure Information and Communication Technologies*, Marrakesh, Morocco, May 7–10, 2008.

XX. G. Kristensson, C. Sohl, C. Larsson, and M. Gustafsson. Bounds on metamaterials: Theoretical results. *Proceedings of the NATO Advanced Research Workshop: Metamaterials for Secure Information and Communication Technologies*, Marrakesh, Morocco, May 7–10, 2008.

XXI. C. Sohl and M. Gustafsson. Theoretical bounds on the directivity and bandwidth of electrically small and wideband antennas. *Proceedings of the IEEE International Symposium on Antennas and Propagation*, San Diego, U.S., July 5–12, 2008.

XXII. M. Gustafsson, C. Sohl, and S. Nordebo. Physical bounds on the antenna scattering matrix. *Proceedings of the IEEE International Symposium on Antennas and Propagation*, San Diego, U.S., July 5–12, 2008.

XXIII. C. Larsson, C. Sohl, M. Gustafsson, and G. Kristensson. Wideband extinction measurements for thin and planar samples. *Proceedings of the IEEE International Symposium on Antennas and Propagation*, San Diego, U.S., July 5–12, 2008.

XXIV. C. Sohl, M. Gustafsson, and G. Kristensson. Bounds on the direct scattering problem of acoustic and electromagnetic waves. *Proceedings of the International Conference on Mathematical Modeling of Wave Phenomena*, Växjö, Sweden, June 9–13, 2008.

XXV. C. Larsson, C. Sohl, M. Gustafsson, and G. Kristensson. Extinction cross section measurements. *Proceedings of the Nordic Conference on Radio Science and Communications*, Växjö, Sweden, June 9–11, 2008.

XXVI. C. Sohl and M. Gustafsson. A priori bounds on the onset frequency of wideband antennas. *Proceedings of the Nordic Conference on Radio Science and Communications*, Växjö, Sweden, June 9–11, 2008.

XXVII. C. Sohl, M. Gustafsson, and G. Kristensson. Bounds on metamaterials in scattering and antenna problems. *Proceedings of the European Conference on Antennas and Propagation*, Edinburgh, U.K., November 11–16, 2007.

XXVIII. M. Gustafsson, C. Sohl, and G. Kristensson. Physical limitations on scattering and absorption of antennas. *Proceedings of the European Conference on Antennas and Propagation*, Edinburgh, U.K., November 11–16, 2007.[4]

XXIX. C. Sohl, M. Gustafsson, and G. Kristensson. Physical limitations on antennas: Isoperimetric inequalities and the effect of metamaterials. *Proceedings of the International Conference on Applied Electromagnetics and Communications*, Dubrovnik, Croatia, September 24–26, 2007.

XXX. C. Sohl, M. Gustafsson, and G. Kristensson. Physical limitations on broadband scattering. *Proceedings of the URSI International Symposium on Electromagnetic Theory*, Ottawa, Canada, July 26–28, 2007.[5]

XXXI. C. Sohl, M. Gustafsson, and G. Kristensson. Physical limitations on G and B for antennas. *Proceedings of the URSI International Symposium on Electromagnetic Theory*, Ottawa, Canada, July 26–28, 2007.

[4]Appointed Best Antennas Poster Prize at the European Conference on Antennas and Propagation, Edinburgh, U.K., November 11–16, 2007.

[5]Honored with a Young Scientist Award at the URSI International Symposium on Electromagnetic Theory, Ottawa, Canada, July 26–28, 2007.

XXXII. M. Gustafsson, C. Sohl, and G. Kristensson. Physical limitations on D/Q for antennas. *Proceedings of the URSI International Symposium on Electromagnetic Theory*, Ottawa, Canada, July 26–28, 2007.

XXXIII. G. Kristensson, C. Sohl, and M. Gustafsson. New physical limitations in scattering and antenna problems. *Proceedings of the URSI International Symposium on Electromagnetic Theory*, Ottawa, Canada, July 26–28, 2007.

The above publications supplement Papers I–XI. Furthermore, bounds on the antenna scattering matrix and optimal limitations for scattering of partial waves are addressed in the spirit of Herglotz functions.

Summary of included papers

The main thread of this dissertation is a forward dispersion relation for the extinction cross section of acoustic and electromagnetic waves. The included papers focus on various aspects and generalizations of this sum rule applied to scattering and antenna problems. A brief summary of each of the appended papers is presented below.

Paper I

This paper deals with physical limitations on scattering and absorption of electromagnetic waves over a frequency interval. The direct scattering problem addressed is plane-wave scattering by a bounded target of arbitrary shape. The scatterer is modeled by a general set of linear and passive constitutive relations which includes heterogeneous and anisotropic material models. A forward dispersion relation for the extinction cross section is derived in terms of the static polarizability dyadics. Various bounds are presented for scattering and absorption over a finite frequency interval, and the theoretical results are exemplified by several numerical simulations.

The author of this dissertation has carried out most of the analysis and the numerical simulations.

Paper II

This paper is an application of the physical limitations on scattering and absorption introduced in Paper I. The paper focuses on temporally dispersive material models which attain negative values of the real part of the permittivity and/or the permeability, *i.e.*, metamaterials. It is concluded that for a single frequency, metamaterials may possess extraordinary characteristics, but with respect to a frequency interval, such materials are no different from other naturally formed substances as long as causality is obeyed. As a consequence, if metamaterials are used to lower the resonance frequency, this is done at the expense of an increasing Q-value at the resonance. The theory is illustrated by numerical simulations of a stratified sphere and a prolate spheroid using the classical Lorentz and Drude dispersion models.

The author of this dissertation has carried out most of the analysis and is responsible for the numerical simulations.

Paper III

This paper presents measurement results on the combined effect of scattering and absorption of electromagnetic waves by a fabricated sample of metamaterial. The engineered composite material, designed as a single-layer planar array of capacitive resonators, is commonly referred to in the literature as a negative permittivity metamaterial. The bounds on the extinction cross section discussed in Paper II are reviewed and compared with the outcome of the measurements. It is concluded that

the experimental results are in good agreement with the theory.

The author of this dissertation has carried out a major part of the analysis including some experimental work.

Paper IV

This paper is an extension of the analysis in Papers II and III. The paper contains several numerical examples with two temporally dispersive spheres modeled by the classical Drude and Lorentz models. Furthermore, the paper contains an attempt to experimentally verify the sum rule by measuring the monostatic radar cross section of a fabricated sample of metamaterial. It is concluded that both numerical simulations and experimental results in the microwave region are in agreement with the theoretical findings.

The author of this dissertation has contributed to the theoretical work and is responsible for the numerical simulations of the polarizability properties.

Paper V

This paper reports on some peculiarities associated with the above-mentioned sum rule. In particular, the paradoxical character of the conductivity model and the perfectly electric conducting boundary condition in the low-frequency limit are investigated. The paradoxical character of the forward dispersion relation lies in the fact that the extinction cross section integrated over all frequencies is independent of the conductivity as long as it is non-zero. This puzzling result can be explained partially by rejecting the conductivity model at low frequencies as suggested by numerical simulations of a homogeneous and isotropic sphere. In addition, the low-frequency behavior of diamagnetic materials is discussed on the basis of Herglotz functions and certain arguments from the theory of special relativity.

The author of this dissertation has carried out most of the analysis and is responsible for the numerical illustration.

Paper VI

This paper reports on a systematic procedure for deriving bounds in electromagnetic theory. The approach is based on the holomorphic properties of certain Herglotz functions and their asymptotic expansions in the low- and high-frequency regimes. A family of integral identities or sum rules is obtained with values governed by the coefficients in the low- and high-frequency expansions. In particular, sum rules for plane-wave scattering by a homogeneous and isotropic sphere are derived and numerically verified by computing the extinction cross section and the bistatic radar cross section in the forward direction. It is concluded that the obtained sum rules

show great potential for deriving new physical bounds in, *e.g.*, scattering and antenna problems.

The author of this dissertation has carried out most of the analysis and is responsible for the numerical illustration.

Paper VII

The extinction paradox states that a perfectly electric conducting target that is large compared to the wavelength removes from the incident radiation exactly twice the amount of power it can intercept by its geometrical cross section area. In this paper, the extinction paradox is generalized to include temporally dispersive material parameters with finite values of the permittivity and the permeability. Using a time-domain approach, it is shown that the high-frequency limit of the extinction cross section depends on the material parameters of the target and that a limiting value not necessarily exists. The theoretical findings are exemplified by numerical illustrations with different values of the extinction cross section in the high-frequency limit.

The author of this dissertation has contributed to the theoretical work and is responsible for one of the numerical simulations.

Paper VIII

This paper focuses on the corresponding sum rule for the extinction cross section of acoustic waves. The derivation is similar to the electromagnetic case in Papers I and II, but certain theoretical challenges are introduced when the ideas are applied to acoustic waves. The effect of both permeable and impermeable boundary conditions are discussed, and it is concluded that the forward dispersion relation is applicable to both the Neumann problem and the transmission problem, whereas the analysis fails for the Dirichlet and Robin boundary conditions. The theory is exemplified by permeable and impermeable scatterers with homogeneous and isotropic material parameters.

The author of this dissertation is responsible for a major part of the analysis.

Paper IX

This paper addresses physical limitations on bandwidth, realized gain, Q-value, and directivity for antennas of arbitrary shape. Based on the forward dispersion relation in Paper I, the product of bandwidth and realizable gain is shown to be bounded from above by the eigenvalues of the high-contrast polarizability dyadic in the long-wavelength limit. These dyadics are proportional to the antenna volume and they are easily determined for geometries of arbitrary shape. Ellipsoidal antenna volumes are analyzed in detail and numerical results for some generic antennas are

presented. The theory is verified against the classical Chu limitations, and shown to yield sharper bounds for the ratio of the directivity and the Q-value for non-spherical geometries.

The author of this dissertation has contributed to both the analysis and the numerical examples.

Paper X

This paper discusses physical bounds on ultra-wideband (UWB) antennas. A sum rule valid for a large class of linear and reciprocal antennas is presented in terms of the electric and magnetic polarizability dyadics. The identity is based on the holomorphic properties of the forward scattering dyadic and includes arbitrarily shaped antennas modeled by linear and time-translational invariant constitutive relations. In particular, a priori estimates on the partial realized gain are introduced, and lower bounds on the onset frequency are derived for two important archetypes of UWB antennas: those with a constant partial realized gain and those with a constant effective antenna aperture. The theoretical findings are illustrated by an equiangular spiral antenna, and comparison with numerical simulations show great potential for future applications in antenna design.

The author of this dissertation has carried out most of the analysis and is responsible for the numerical simulation.

Paper XI

This paper deals with sum rules for the input impedance, admittance, and reflection coefficient of a large class of linear and reciprocal antennas. The derivation is based on Herglotz functions and the systematic approach introduced in Paper VI. The derived sum rules are shown to be governed by the capacitance and the inductance properties of the antenna in the low- and high-frequency regimes. In particular, the results are applied to a first dominant resonance and it is shown to yield a useful estimate of the Q-value in terms of the radiation resistance of the antenna and its capacitance and inductance at low frequencies. The theoretical findings are compared with numerical simulations of different dipole antennas.

The author of this dissertation has contributed to both the theoretical work and the numerical examples.

Preface

This dissertation for the degree of Doctor of Philosophy in Engineering summarizes three and a half years of research I have carried out at the Department of Electrical and Information Technology, formerly the Department of Electroscience, Lund University, Lund, Sweden. Although I started the doctoral studies in February 2005, most of the results presented here were obtained during the fall 2006 and the spring 2007. The dissertation is based on the thesis work in Paper XII for the degree of Licentiate in Engineering, publicly defended at Lund University, September 3, 2007.

The scientific questions addressed in this dissertation concern the implications of causality and passivity on a large class of scattering and antenna problems. This particular research field in the borderland between classical electrodynamics and modern wave mechanics is motivated by its fundamental character and intrinsic beauty, and it has turned out to be a true grain of gold offering several unexplored and stimulating research problems. Some open questions that will be addressed in the future are pointed out in the General Introduction and in the appended papers.

Sölvesborg, August 2008 Christian Sohl

Acknowledgments

I have received help and support from many people without whom this dissertation would not have been possible. I am grateful to all of you, but there are some who deserve special thanks.

First and foremost, I would like to express my deepest gratitude to my supervisors Prof. Gerhard Kristensson and Dr. Mats Gustafsson for their constant encouragement, never-ceasing enthusiasm, and exemplary academic guidance. I am particularly thankful for our pleasant collaboration and their good taste in choosing stimulating research problems. Mats has been a true source of inspiration and I sincerely admire his great intuition in our many discussions on physical problems. Despite the many duties, Gerhard has always offered me time, and his vast theoretical skills have been the major reason for me to leave modern physics and initiate doctoral studies under his guidance. Gerhard and Mats: I will truly remember these years with joy!

Secondly, I thank Prof. Christer Larsson for sharing his expertise on measurement techniques and radar cross section fundamentals, and, in particular, for a fruitful collaboration on the measurement campaigns at Saab Bofors Dynamics, Linköping, April 19, 2007, and February 14, 2008, respectively. I am also grateful to Prof. Klas Malmqvist for his trust in me and his efforts to solve the pitiable financial problems I encountered during the employment freeze at Lund University in February 2005.

Many thanks to Prof. Anders Karlsson for constructive criticism on aspects related to the null-field method, Prof. Anders Melin for sharing his overwhelming knowledge in mathematics, Dr. Daniel Sjöberg for assistance with LaTeX 2_ε and valuable hints on how the academia works, and Prof. Anders Derneryd for his positive attitude in our many stimulating discussions on antennas. Furthermore, I thank secretary Elsbieta Szybicka for taking care of administrative issues, Dr. Lars Olsson for checking the English language, Dr. Richard Lundin for sharing his excellence in undergraduate teaching, and the technical staff Lars Hedenstjerna and Leif Karlsson for their help with many practical problems. I am also grateful to the doctoral students in the Electromagnetic Theory Group for providing a stimulating and relaxed atmosphere, and the former fellow postgraduate Dr. Christian Engström for sharing the author's interest in mathematics.

This work is funded by the Swedish Research Council for Engineering Sciences (contract no. 621-2002-4284) and their financial support is gratefully acknowledged. Travel grants from Sigfrid and Walborg Nordkvist's foundation, Per Westling's foundation, The Royal Physiographic Society, and Ericsson AB are also acknowledged.

Last, but not least, I would like to thank family and friends for their endless love and patience, especially my parents Lena and Per, for distracting me from doing too much research and making these years a truly good time. This dissertation is dedicated to my love Andrea with whom I am ready to begin a new journey.

Contents

General Introduction

Christian Sohl

1 Background

Since the introduction of the Kramers-Kronig relations in Refs. 21 and 54 concerning the propagation of electromagnetic radiation in optical media, dispersion relation techniques have been applied successfully in theoretical physics to study particle collisions and wave interaction with matter.[1] During the last five decades, such relations have shown to be valuable tools in quantum field theory to model strongly interacting particles. Instead of specifying the interaction between the elementary particles in terms of a Lagrangian density, a minimum number of postulates are adapted from which it is hoped that the equations of motions can be derived. For an introduction to dispersion relations in elementary particle physics, see Refs. 31, 39, and 41. The foundation of the Lagrangian approach in classical mechanics and classical electrodynamics is discussed in Refs. 32 and 45.

The underlying idea of dispersion relations is that certain physical amplitudes are the boundary values of holomorphic functions of one or more complex variables. The holomorphic properties of these amplitudes are closely connected with the fundamental principles of passivity and causality via the class of Herglotz functions. In fact, there are at least two remarkable features of dispersion relations in theoretical physics: (i) they provide a consistency check of calculated quantities when the underlying mathematical model a priori is known to satisfy causality, and (ii) they may be used to verify whether a given mathematical model or an experimental outcome behaves causally or not. In addition, dispersion relations can also be used to establish far-reaching connections between quantities and concepts of different physical meanings.

The objective of this General Introduction is to briefly discuss the implications of passivity and causality on the propagation and scattering of acoustic and electromagnetic waves. In other words, the purpose of this General Introduction is not to repeat the foundations of linear acoustics and classical electrodynamics. This has been done in an excellent manner in several classical textbooks, *e.g.*, Refs. 15, 45, 46, 61, 62, 67, 70, 77, and 82. The analysis of fields and waves in the low-frequency limit is found in Refs. 8, 20, and 51 and references therein. Several applications to material modeling and scattering problems are presented in this General Introduction. Linear systems with passivity and causality conditions are also important in certain disciplines of electrical engineering, *e.g.*, network analysis and broadband circuit design, see Refs. 17 and 26. Other classical references on linear systems are Refs. 9, 35, and 36. Dispersion relations based on a somewhat different causality condition, often referred to as microcausality through local commutativity of field operators, play a fundamental role in quantum field theory, see Refs. 65, 72, and 73. The non-causal properties of gauge transformations and the advanced Green function for the wave equation lay outside the scope of this General Introduction. The curious reader may find a comprehensive exposition on these matters in Ref. 45. Many

[1] Dispersion relations should not be confused with the connection between energy and momentum, *i.e.*, wave motion in time and space, which bears the same name in wave mechanics. Neither should the term be confused with dispersion models which are used in material modeling to describe temporally dispersive matter, *e.g.*, the Lorentz model discussed in Sec. 2.10.

of the topics discussed in this General Introduction reflect the author's interest in the subject.

Forward scattering, *i.e.*, scattering at 180° bistatic angle, plays a key role in this dissertation. However, the implications of bistatic scattering with transmitting and receiving sources located at different positions in space are less known compared to the monostatic scattering scenario, see Ref. 52. The reason for this is that the majority of radar applications employ co-located transmitters and receivers. Although it seems difficult to extend the analysis of the non-forward dispersion relations in Sec. 3 to obtain useful information on the monostatic radar cross section, it remains an important subject which will be analyzed in detail in a series of forthcoming papers.

2 Causality and holomorphic properties

This section introduces some elementary properties of linear time-translational invariant systems obeying causality (se definition below). In particular, the damped harmonic oscillator in classical mechanics is discussed, and the Kramers-Kronig relations for the propagation of electromagnetic radiation in isotropic and homogeneous media are derived. The analysis of linear systems is summarized in Refs. 9, 18, 35, 36, 68, and 90. The exposition on the damped harmonic oscillator follows the outline in Ref. 66 and Problem 3.39 in Ref. 72, whereas Refs. 44 and 45 have been valuable for preparing the section on the Kramers-Kronig relations. Other important results in classical dispersion theory are summarized in Refs. 39, 41, 56, 57, 64, 81, and 89.

2.1 Elementary considerations

Consider an arbitrary physical system subject to an external time-dependent action or input $f(t)$, to which the system responds by producing an effect or output $x(t)$. For simplicity, let $f(t)$ and $x(t)$ only be functions of the time variable t. The internal properties of the system are unspecified except for the following general assumptions:

(i) the output $x(t)$ is a linear functional of the input $f(t)$, *i.e.*,

$$x(t) = \int_{-\infty}^{\infty} g(t,t')f(t')\ \mathrm{d}t',$$

where $g(t,t')$ is the impulse response at time t when the system is subject to an input at time t';

(ii) the internal properties of the system do not depend on time, *i.e.*, $g(t,t') = g(t-t')$, or equivalently, if the input $f(t)$ is advanced or delayed by some time interval, the same time shift occurs for the output $x(t)$;

(iii) the system is subject to time-ordered events in the sense that the output $x(t)$ cannot precede the input $f(t)$, *i.e.*, $g(\tau) = 0$ for $\tau = t - t' < 0$.

The three conditions above refer to linearity or superposition, time-translational invariance, and primitive causality (often referred to as one of the most sacred tenets in natural science), respectively. Under these assumptions, the most general form of the output $x(t)$ is[2]

$$x(t) = \int_{-\infty}^{t} g(t-t')f(t') \, \mathrm{d}t'. \tag{2.1}$$

The analysis of (2.1) forms the foundation of the linear system theory in Refs. 9, 18, 35, 36, 68, and 90.

In contrast to primitive causality, there is also a relativistic causality condition known as macroscopic causality which states that no signal, or at least no information, can propagate with a velocity greater than the speed of light in vacuum. However, macroscopic causality is less general than primitive causality since the previous condition depends on the existence of a limiting velocity. For this reason, only primitive causality is addressed in this General Introduction. Furthermore, non-linear equations of motion are excluded from the exposition due to the difficulty of finding general functionals to model such systems. Non-linear equations of motion may also show complications such as self-excitation, sensitivity to initial conditions, and onset of chaos, *cf.*, the discussion in Ref. 39.

In the same manner as the macroscopic causality condition is postulated in special relativity, primitive causality can be regarded as a general principle in natural science, see Refs. 14 and 88. Linear time-translational invariant systems obeying primitive causality are commonly used to model the behavior of the nature. For example, when an external force is acting on a bar that supports small elastic deformations, primitive causality states that no extension of the bar takes place until the applied force is put into action. Another example of time-ordered events in natural sciences is the voltage and current relation in an electrical network. On the other hand, it is not hard to come up with a non-causal system. For example, consider the linear system defined by the negative time delay $t_0 < 0$, *i.e.*, the input $f(t)$ is related to the output via $x(t) = f(t-t_0)$ with the impulse response $g(\tau) = \delta(\tau - t_0)$, where $\delta(\tau)$ denotes the Dirac delta distribution. Such a non-causal system (recall that $g(\tau) = \delta(\tau - t_0)$ has a non-vanishing support for $\tau < 0$) can be thought of as a crystal ball with the ability to predict the future. Many ideal filters in network theory are non-causal in the sense that they have impulse responses that satisfy $g(\tau) \neq 0$ for $\tau < 0$, *cf.*, the discussions in Refs. 17 and 68.

Although many physical models obey a causality condition, there are some frequently used equations of motions in mathematical physics that support non-causal solutions. An example is the heat equation (or more generally any parabolic partial differential equation) which models the variation in temperature over time and space. The heat equation supports information that propagates at infinite speed in direct contradiction with the macroscopic causality condition. However, hyperbolic systems of equations, such as the equations governing linear acoustics or the

[2]Observe that no distinction in notation is made between the one and two variable functions $g(t,t')$ and $g(\tau)$, where $\tau = t - t'$.

Maxwell equations, have solutions that propagate with finite velocities in agreement with macroscopic causality.

The three assumptions (i), (ii), and (iii) stated above have far-reaching consequences on the frequency response associated with $g(\tau)$, *i.e.*, the Fourier integral

$$G(\omega) = \int_0^\infty g(\tau) \mathrm{e}^{\mathrm{i}\omega\tau} \, \mathrm{d}\tau, \tag{2.2}$$

where ω denotes the angular frequency. Here, primitive causality has been used to express (2.2) as an integral over positive τ only rather than the entire real axis. The convergence of (2.2) is guaranteed if, *e.g.*, $g(\tau)$ is absolutely integrable, *i.e.*,

$$\|g\|_1 = \int_0^\infty |g(\tau)| \, \mathrm{d}\tau < \infty. \tag{2.3}$$

Under the assumption of (2.3), it follows from a majorant theorem for generalized integrals that $G(\omega)$ is continuous for real-valued ω. Furthermore, $G(\omega)$ is bounded by $\|g\|_1$, and from the Riemann-Lebesgue lemma it is clear that $G(\omega) \to 0$ as $\omega \to \infty$, see Refs. 11, 68, and 80. The assumption that $g(\tau)$ is absolutely integrable can be further relaxed by introducing the class of temperate distributions, see Refs. 41, 43, and 66.

To this end, it is sufficient to assume that $g(\tau)$ satisfies (2.3). Then it follows from the analysis of the Fourier integral in Refs. 68 and 80 that $G(\omega)$ can be extended to a holomorphic function in the upper half part of the complex ω-plane. This is made plausible by observing that the exponential function in (2.2) significantly improves the convergence of the Fourier integral when its domain of definition is extended to include complex-valued $\omega = \omega' + \mathrm{i}\omega''$ with $\omega'' > 0$. The regular properties of $G(\omega)$, or equivalently, the presence of no singularities in the upper half plane, is thus a direct consequence of primitive causality.

In the lower half part of the complex ω-plane, (2.2) diverges everywhere unless $g(\tau)$ decays faster than exponential on the real τ-axis. In general, $G(\omega)$ has singularities in the lower half plane and may be defined there only as the holomorphic continuation of (2.2) from the upper half plane. Another type of continuation is based on the Schwarz reflection principle in Refs. 1 and 33. Schwarz reflection principle states that if $G(\omega)$ is holomorphic in some region Ω of the complex ω-plane, then $G^*(\omega^*)$ is holomorphic as a function of ω in Ω^* obtained by a reflection of Ω in the real axis, *i.e.*, $\omega \in \Omega^*$ if and only if $\omega^* \in \Omega$.

By complex conjugating (2.2) and invoking that $g(\tau)$ is real-valued, *i.e.*, the output $x(t)$ is a real-valued function for any real-valued input $f(t)$, implies

$$G(-\omega^*) = G^*(\omega), \qquad \operatorname{Im}\omega \geqslant 0. \tag{2.4}$$

The cross symmetry (2.4) implies that the real part of $G(\omega)$ is even and the imaginary part of $G(\omega)$ is odd with respect to the imaginary axis. As a consequence, $G(\omega)$ takes only real values on the imaginary axis.

As an example of (2.4), consider the purely monochromatic input given by the real-valued expression

$$f(t) = \operatorname{Re}(f_0 \mathrm{e}^{-\mathrm{i}\omega t}) = \frac{1}{2}(f_0 \mathrm{e}^{-\mathrm{i}\omega t} + f_0^* \mathrm{e}^{\mathrm{i}\omega t}), \tag{2.5}$$

where $\omega = \omega' + \mathrm{i}0$ is real-valued, and f_0 is a complex-valued constant.[3] Insertion of (2.5) into (2.1) using the change of variables $\tau = t - t'$ yields

$$x(t) = \frac{1}{2} f_0 \mathrm{e}^{-\mathrm{i}\omega t} \int_0^\infty g(\tau) \mathrm{e}^{\mathrm{i}\omega\tau} \, \mathrm{d}\tau + \frac{1}{2} f_0^* \mathrm{e}^{\mathrm{i}\omega t} \int_0^\infty g(\tau) \mathrm{e}^{-\mathrm{i}\omega\tau} \, \mathrm{d}\tau$$
$$= \frac{1}{2} \left(f_0 \mathrm{e}^{-\mathrm{i}\omega t} G(\omega) + f_0^* \mathrm{e}^{\mathrm{i}\omega t} G(-\omega) \right). \quad (2.6)$$

The appropriate condition for (2.6) to be real-valued is just $G(-\omega) = G^*(\omega)$ in agreement with (2.4). Relation (2.6) then implies that $x(t) = \mathrm{Re}(f_0 \mathrm{e}^{-\mathrm{i}\omega t} G(\omega))$, *i.e.*, $f(t)$ generates a monochromatic output $x(t)$ with the same angular frequency ω as the input. The associated impulse response is $g(\tau) = \delta(\tau)$ and (2.2) implies that for real-valued $\omega = \omega' + \mathrm{i}0$,

$$G(\omega) = \int_0^\infty \delta(\tau) \mathrm{e}^{\mathrm{i}\omega\tau} \, \mathrm{d}t' = 1, \quad (2.7)$$

as expected from the definition of a linear system.

2.2 Herglotz functions

Many physical systems are passive in the sense that they consume energy rather than produce energy. Conditions on passivity can be formulated both in the time domain and in the frequency domain, see Ref. 37. In the frequency domain, passivity often takes the form of a restriction on a complex-valued function H that characterizes the physical system. A general condition for a physical system to be passive in the frequency domain is expressed as[4]

$$\mathrm{Im}\, H(G(\omega)) \geqslant 0, \qquad \mathrm{Im}\, \omega \geqslant 0. \quad (2.8)$$

An example of (2.8) is the radiation resistance $R(\omega) = \mathrm{Re}\, Z(\omega) = \mathrm{Im}(\mathrm{i}Z(\omega))$ of a general antenna which is non-negative due to passivity, see Paper XI.

Now consider the class of physical systems for which H is a holomorphic function of $\omega = \omega' + \mathrm{i}\omega''$ in the upper half plane. Since the composition of two holomorphic functions is a new holomorphic function, it follows that $H(G(\omega))$ is holomorphic in the upper half part of the complex ω-plane whenever $H(\omega)$ and $G(\omega)$ are holomorphic in that region. A function with this property that also satisfies (2.8) is called a Herglotz function.[5] The Herglotz property is illustrated schematically in Fig. 1. However, bear in mind that (2.8) must be consistent with (2.4) in the sense that physical quantities are real-valued in the time domain.

[3] The notation $\omega = \omega' + \mathrm{i}0$ should be interpreted as $\omega = \lim_{\omega'' \to 0+} \omega' + \mathrm{i}\omega''$, where ω' and ω'' are real-valued.

[4] Alternatively, one may use the real part convention and define passivity as $\mathrm{Re}\, H(G(\omega)) \geqslant 0$ for $\mathrm{Im}\, \omega \geqslant 0$ by applying (2.8) to $\mathrm{i}H(G(\omega))$ for $\mathrm{Im}\, \omega \geqslant 0$.

[5] The corresponding class of functions defined on the basis of the Laplace transform are termed positive real functions, see Ref. 68. In addition, one requires that positive real functions are real-valued on the real axis. Furthermore, Herglotz functions are closely related to the class of Nevanlinna functions which are holomorphic in the upper half plane with a non-positive imaginary part, see Ref. 3.

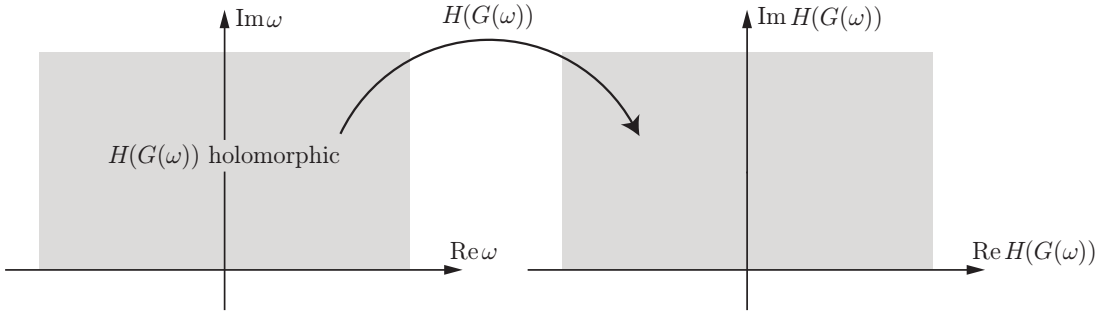

Figure 1: The Herglotz function $H(G(\omega))$ as a mapping from the upper half part of the complex ω-plane into itself.

A general representation of Herglotz functions in terms of a Riemann-Stieltjes integral[6] is discussed in Ref. 74 in connection with the Hamburger moment problem. The theorem states that necessary and sufficient conditions for $H(G(\omega))$ to be a Herglotz function is that a bounded and non-decreasing real-valued function $\mu(t)$ exists such that

$$H(G(\omega)) = A\omega + B + \int_{-\infty}^{\infty} \frac{1+t\omega}{t-\omega}\, \mathrm{d}\mu(t), \qquad \mathrm{Im}\,\omega \geqslant 0, \tag{2.9}$$

where $A \geqslant 0$ and B are real-valued constants (A governed by the asymptotic behavior $H(G(\omega)) = A\omega + \mathcal{O}(1)$ as $|\omega| \to \infty$.).[7] Here, the equality sign in $\mathrm{Im}\,\omega \geqslant 0$ should be interpreted as the limit from the upper half plane when the imaginary part of ω approaches zero. The interpretation of (2.9) is that any Herglotz function can be represented by such a Riemann-Stieltjes integral. The converse statement is also true: any function $\mu(t)$ and pair of constants A and B that satisfy the assumptions above generate a Herglotz function. Recall that (2.9) reduces to the classical Riemann integral with $\mathrm{d}\mu(t) = \mu'(t)\,\mathrm{d}t$ at all points where $\mu(t)$ is differentiable (a prime denotes differentiation with respect to the argument and should not be confused with the primes in ω' and ω'' which refer to the real and imaginary parts of ω, respectively).

It is not hard to show that (2.9) satisfies (2.8). For this purpose, decompose ω as $\omega = \omega' + \mathrm{i}\omega''$, where ω' and ω'' are real-valued. A straightforward calculation then yields

$$\mathrm{Im}\left(\frac{1+t\omega}{t-\omega}\right) = \mathrm{Im}\left(\frac{1+t(\omega'+\mathrm{i}\omega'')}{t-(\omega'+\mathrm{i}\omega'')}\right) = \frac{\omega''(1+t^2)}{(t-\omega')^2+\omega''^2}, \tag{2.10}$$

and since $A \geqslant 0$ and $\mu(t)$ is non-decreasing, it is concluded that for $\omega'' \geqslant 0$,

$$\mathrm{Im}\, H(G(\omega'+\mathrm{i}\omega'')) = \omega''\left(A + \int_{-\infty}^{\infty} \frac{1+t^2}{(t-\omega')^2+\omega''^2}\, \mathrm{d}\mu(t)\right) \geqslant 0. \tag{2.11}$$

[6] For an introduction to the theory of the Riemann-Stieltjes integral, see Refs. 6 and 86.

[7] Here, the parameter t should not be confused with the time variable in Sec. 2.1 which is denoted by the same letter. Furthermore, note that no restriction apply to the constant B in (2.9), *i.e.*, it can take both positive and negative values.

Let us now consider the properties of (2.9) as $\omega = \omega' + \mathrm{i}0$. For this purpose, introduce the following standard result in distribution theory which involves the Dirac distribution on the real ω'-axis, see Refs. 28 and 43:[8]

$$\frac{1}{\omega' \pm \mathrm{i}0} = \mathcal{P}\left(\frac{1}{\omega'}\right) \mp \mathrm{i}\pi\delta(\omega'). \tag{2.12}$$

Under the assumption that $\mu(t)$ is sufficiently regular, (2.12) inserted into (2.9) implies

$$\begin{aligned}\operatorname{Im} H(G(\omega' + \mathrm{i}0)) &= \operatorname{Im} \int_{-\infty}^{\infty} \left\{ \mathcal{P}\left(\frac{1}{t-\omega'}\right) + \mathrm{i}\pi\delta(t-\omega') \right\} (1+t\omega')\mu'(t)\, \mathrm{d}t \\ &= \pi \int_{-\infty}^{\infty} \delta(t-\omega')(1+t\omega')\mu'(t)\, \mathrm{d}t = \pi(1+\omega'^2)\mu'(\omega'). \end{aligned} \tag{2.13}$$

Here, it has been assumed that $\mu(t)$ is a differentiable function of t, *i.e.*, it obeys $\mathrm{d}\mu(t) = \mu'(t)\,\mathrm{d}t$. Note that the assumption that $\mu(t)$ is non-decreasing implies that (2.13) is consistent with (2.8). Inserting (2.13) into (2.9) finally yields

$$H(G(\omega)) = A\omega + B + \frac{1}{\pi} \int_{-\infty}^{\infty} \frac{1+t\omega}{t-\omega} \frac{\operatorname{Im} H(G(t+\mathrm{i}0))}{1+t^2}\, \mathrm{d}t, \qquad \operatorname{Im}\omega \geqslant 0. \tag{2.14}$$

Relation (2.14) defines the Herglotz function $H(G(\omega))$ uniquely whenever the imaginary part of $H(G(\omega))$ is known along the real ω'-axis. Of course, the real-valued constants A and B in (2.14) must be specified. It is also possible to derive a closed-form expression for $\mu(t)$ by integrating (2.13) from $\omega' = t_0$ to $\omega' = t$, *viz.*,

$$\mu(t) = \mu(t_0) + \frac{1}{\pi} \int_{t_0}^{t} \frac{\operatorname{Im} H(G(\omega' + \mathrm{i}0))}{1+\omega'^2}\, \mathrm{d}\omega'. \tag{2.15}$$

The general case when $\mu(t)$ is not differentiable is discussed in Ref. 66 and references therein. The idea is to decompose $\mu(t)$ into a sum of a continuous and non-decreasing function $\mu_{\mathrm{cont}}(t)$ and a denumerable set of finite discontinuities $\mu_n = \mu(t_n + 0) - \mu(t_n - 0)$ (recall that $\mu_n > 0$ since $\mu(t)$ is non-decreasing) at the points $t = t_n$, *i.e.*,

$$\mu(t) = \mu_{\mathrm{cont}}(t) + \sum_n \mu_n \Theta(t - t_n), \tag{2.16}$$

where $\Theta(t)$ denotes the Heaviside step function. Differentiation in distributional sense yields the differential

$$\mathrm{d}\mu(t) = \mathrm{d}\mu_{\mathrm{cont}}(t) + \sum_n \mu_n \delta(t - t_n)\, \mathrm{d}t. \tag{2.17}$$

[8]Here, the principal value $\mathcal{P}(1/\omega)$ is defined by the action (ϕ is a test function which belongs to the class of infinitely differentiable functions of compact support)

$$\begin{aligned}\langle \mathcal{P}(1/\omega), \phi(\omega) \rangle &= \int_{-\infty}^{\infty} \mathcal{P}\left(\frac{1}{\omega}\right) \phi(\omega)\, \mathrm{d}\omega = \mathcal{P} \int_{-\infty}^{\infty} \frac{\phi(\omega)}{\omega}\, \mathrm{d}\omega \\ &= \lim_{\varepsilon \to 0+} \left(\int_{-\infty}^{-\varepsilon} \frac{\phi(\omega)}{\omega}\, \mathrm{d}\omega + \int_{\varepsilon}^{\infty} \frac{\phi(\omega)}{\omega}\, \mathrm{d}\omega \right). \end{aligned}$$

By inserting (2.17) into (2.9) it is concluded that a more general representation of $H(G(\omega))$ reads

$$H(G(\omega)) = A\omega + B + \sum_n \mu_n \frac{1 + t_n\omega}{t_n - \omega} + \int_{-\infty}^{\infty} \frac{1 + t\omega}{t - \omega}\, \mathrm{d}\mu_{\mathrm{cont}}(t), \tag{2.18}$$

where $\operatorname{Im}\omega \geqslant 0$. For further details on (2.9), see Refs. 2, 3, and 86.

2.3 Meĭman's theorem

The Meĭman theorem discussed in Refs. 56 and 75 establishes some important properties of $G(\omega)$. Assume that $\operatorname{Im} G(\omega' + \mathrm{i}0) > 0$ for $\omega' > 0$ and that $G(\omega)$ has no essential singularity at infinity. Then, the Meĭman theorem states that $G(\omega)$ is nonzero in the upper half part of the complex ω-plane, and does not take real values at any finite point in that region except on the imaginary axis, where it decreases monotonically from a positive value to zero at $\omega = \mathrm{i}\infty$.[9]

The assumption of no essential singularity in $G(\omega)$ at infinity is related to the Phragmén-Lindelöf theorem in Ref. 19 which states that if a function is bounded in magnitude on the real axis and holomorphic in the upper half plane, it is either bounded in magnitude also in the upper half plane or it has an essential singularity at infinity, *i.e.*, it contains a phase factor $\mathrm{e}^{-\mathrm{i}\delta\omega}$ for $\delta > 0$ which increases exponentially for complex-valued $\omega = \omega' + \mathrm{i}\omega''$ with $\omega'' > 0$. For details on the proof of the Meĭman theorem and some of its applications, see Refs. 56 and 75.

2.4 Vector-valued generalizations

Only systems with a single input and a single output have been addressed so far. For multiple-input multiple-output systems, the terminal functions $f(t)$ and $x(t)$ must be replaced by their vector-valued analogues $\boldsymbol{f}(t)$ and $\boldsymbol{x}(t)$, respectively. In the same manner, the impulse response $g(\tau)$ is replaced by the matrix-valued kernel $\mathbf{g}(\tau)$. In Paper VIII, a single-input single-output system is considered for scattering of acoustic waves, whereas the appropriate formulation for electromagnetic waves in Papers I–III is based on the multiple-input multiple-output characterization. For the sake of simplicity, both acoustic and electromagnetic waves are treated in this General Introduction with a scalar notation. Once the scalar case has been mastered, the introduction of vector-valued quantities causes no further problems.

2.5 The damped harmonic oscillator

The damped harmonic oscillator (one-dimensional pendulum with viscous damping) is a passive system which satisfies the three conditions on p. 4. It provides a simple,

[9] The Meĭman theorem can be extended to also include the case when $\operatorname{Im} G(\omega' + \mathrm{i}0) = 0$. But since all physical systems are accompanied by some energy dissipation, it is not a severe restriction to omit the equality sign in the condition $\operatorname{Im} G(\omega' + \mathrm{i}0) \geqslant 0$. The theorem resembles Levinson's theorem in Refs. 64 and 79 concerning the bound states of the Schrödinger equation as the roots of the Jost function.

yet accurate, model that is employed in many branches of physics involving wave phenomena, *cf.*, the Lorentz model in Papers I, II, and III for the interaction of electromagnetic waves with temporally dispersive matter. The equation of motion for the oscillator when subject to an external driving force $f(t)$ per unit mass reads

$$\ddot{x}(t) + 2\gamma\dot{x}(t) + \omega_0^2 x(t) = f(t), \tag{2.19}$$

where $x(t)$ measures the displacement from the equilibrium as a function of time t, and the dots are time derivatives.[10] Furthermore, $\gamma \geqslant 0$ and $\omega_0 > 0$ are the damping constant ($1/\gamma$ measures the lifetime or characteristic time scale over which the damping takes place) and the natural frequency of the oscillator, respectively. The condition $\gamma \geqslant 0$ follows from the fact that the frictional force is directed opposite to the velocity of the oscillator.

The energy balance for the oscillator is obtained by multiplying (2.19) with $\dot{x}(t)$ and integrating from $t' = -\infty$ to $t' = t$, *viz.*,

$$E(t) + 2\gamma \int_{-\infty}^{t} \dot{x}^2(t') \, \mathrm{d}t' = \int_{-\infty}^{t} f(t')\dot{x}(t') \, \mathrm{d}t', \tag{2.20}$$

where $E(t) = \dot{x}^2(t)/2 + \omega_0^2 x^2(t)/2$ defines the energy of the oscillator at time t. Observe that (2.20) assumes the oscillator to be at rest at $t = -\infty$. Since the left-hand side of (2.20) is non-negative, it is concluded that

$$\int_{-\infty}^{t} f(t')\dot{x}(t') \, \mathrm{d}t' \geqslant 0 \tag{2.21}$$

for all driving forces $f(t)$. Relation (2.21) is a consequence of the passivity condition $\gamma \geqslant 0$ for the oscillator, see Refs. 53 and 60.

The solution of (2.19) in the force-free case with $f(t) = 0$ is straightforward ($\gamma \neq \omega_0$):

$$x_0(t) = \mathrm{e}^{-\gamma t}\big(a_1 \mathrm{e}^{-\mathrm{i}(\omega_0^2 - \gamma^2)^{1/2} t} + a_2 \mathrm{e}^{\mathrm{i}(\omega_0^2 - \gamma^2)^{1/2} t}\big), \tag{2.22}$$

where the constants a_1 and a_2 are determined from the initial conditions. Although a_1 and a_2 in general are complex-valued they will always produce a real-valued solution $x_0(t)$. For an overcritical damping, $\gamma > \omega_0$, the two terms inside the parenthesis decrease exponentially, whereas the solution with $\gamma < \omega_0$ describes a damped harmonic oscillation. For the critical damping $\gamma = \omega_0$, (2.22) should be replaced by

$$x_0(t) = \mathrm{e}^{-\gamma t}(a_1 t + a_2). \tag{2.23}$$

In this case, the oscillator passes the equilibrium at most one time (set (2.23) equal to zero and solve for t) and has at most one extreme value depending on the initial conditions (use that $\dot{x}_0(t) = \mathrm{e}^{-\gamma t}(-\gamma a_1 t + a_1 - \gamma a_2)$ and solve $\dot{x}_0(t) = 0$ for t).

[10] For example, when a single particle of charge q is subject to a time-harmonic electric field $E(\omega)\mathrm{e}^{-\mathrm{i}\omega t}$ (angular frequency ω) directed along the x-axis, Lorentz force law implies that the external driving force is $f(t) = qE(\omega)\mathrm{e}^{-\mathrm{i}\omega t}$ per unit mass. The polarization of a homogeneous matter composed of such particles is $P(t) = Nqx(t)$, where N measures the number of charge carriers per unit volume.

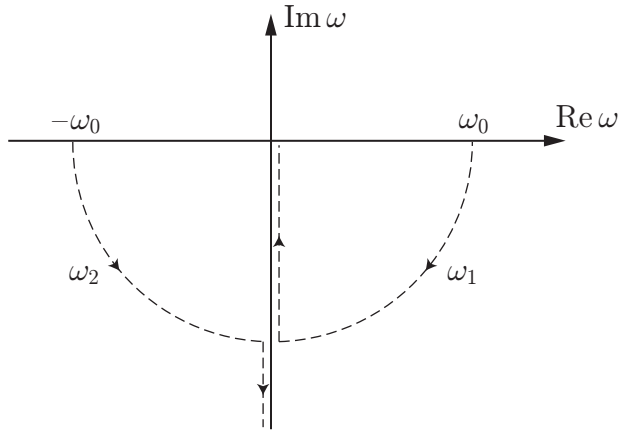

Figure 2: Trajectories for the singularities $\omega_{1,2}$ as function of increasing γ.

From (2.22) it is clear that $\gamma \geqslant 0$ (no production of energy) is crucial to prevent a displacement that increases exponentially with the time.

According to the principle of superposition for ordinary differential equations, a general solution of (2.19) is the sum of the homogeneous solution (2.22) and a corresponding inhomogeneous solution when the external driving force is present on the right-hand side of (2.19). In order to determine this inhomogeneous solution, assume that $f(t)$ can be represented by, *e.g.*, the Fourier integral (also the Laplace transform is applicable by identifying $s = -\mathrm{i}\omega$)

$$f(t) = \frac{1}{2\pi} \int_{-\infty}^{\infty} F(\omega) \mathrm{e}^{-\mathrm{i}\omega t} \, \mathrm{d}\omega. \tag{2.24}$$

Apply the Fourier transform to (2.19) and use the convolution theorem in Ref. 68 (which is valid since $f(t)$ and $g(\tau)$ are absolutely integrable) to obtain

$$x(t) = \frac{1}{2\pi} \int_{-\infty}^{\infty} G(\omega) F(\omega) \mathrm{e}^{-\mathrm{i}\omega t} \, \mathrm{d}\omega = \int_{-\infty}^{\infty} g(t - t') f(t') \, \mathrm{d}t', \tag{2.25}$$

where $G(\omega) = -1/(\omega - \omega_1)(\omega - \omega_2)$ is the frequency response of the oscillator, and $\omega_{1,2} = -\mathrm{i}\gamma \pm (\omega_0^2 - \gamma^2)^{1/2}$ are the roots of the characteristic polynomial $\omega^2 + 2\mathrm{i}\gamma\omega - \omega_0^2 = 0$. If the damping is weak, *i.e.*, $\gamma \ll \omega_0$, the complex-valued roots can be approximated by $\omega_{1,2} \approx -\mathrm{i}\gamma \pm \omega_0$ from which it is clear that the frequency response goes through sharp resonances located at $\omega \approx \pm\omega_0$. The paths described by the singularities $\omega_{1,2}$ in the complex ω-plane as the damping increases from $\gamma = 0$ to $\gamma = \infty$ are illustrated in Fig. 2. Note that the singularities coincide for $\gamma = \omega_0$, and that they separate in such a manner that one of them approaches $\omega = -\mathrm{i}\infty$ as $\gamma = \infty$ while the other singularity tends to $\omega = 0$. From the condition $\gamma \geqslant 0$ it is clear that these singularities always lie in the lower half part of the complex ω-plane.

Since $G(\omega)$ is defined as the Fourier transform of $g(\tau)$, the problem (2.19) is thus reduced to evaluate the Fourier integral

$$g(\tau) = \frac{1}{2\pi} \int_{-\infty}^{\infty} \frac{-1}{(\omega - \omega_1)(\omega - \omega_2)} \mathrm{e}^{-\mathrm{i}\omega\tau} \, \mathrm{d}\omega. \tag{2.26}$$

This is conveniently done by means of residue calculus, see Refs. 1 and 33, for which the criterion $\gamma \geqslant 0$ plays an important role. The integrand in (2.26) is singular at $\omega = \pm\omega_0$ when $\gamma = 0$, and should be interpreted as a Cauchy principal value. In this case, excluding the singularities on the real axis with small semicircles of vanishing radii yields $g(\tau) = \sin(\omega_0\tau)/\omega_0$ irrespectively of the sign of τ.

In the general case when $\gamma > 0$, (2.26) supports a closure in the upper half plane if and only if $\tau < 0$. A closure in the form of an infinite semicircle does not contribute to the integral since $G(\omega)$ vanishes sufficiently rapid as the magnitude of ω tends to infinity. Since $\gamma > 0$ implies that $\operatorname{Im}\omega_{1,2} < 0$, the singularities of $G(\omega)$ are strictly located in the lower half plane, and the Cauchy integral theorem implies that $g(\tau) = 0$ for $\tau < 0$. But this property is merely the primitive causality discussed in Sec. 2.1. It is thus concluded that the damped harmonic oscillator with $\gamma \geqslant 0$ is a linear time-translational invariant system that satisfies passivity and primitive causality. For $\tau > 0$, the appropriate region for closure is the lower half plane. In this case, the method of residues yields

$$\frac{1}{2\pi}\oint \frac{-1}{(\omega-\omega_1)(\omega-\omega_2)}\mathrm{e}^{-\mathrm{i}\omega\tau}\,\mathrm{d}\omega = \mathrm{i}\sum_{i=1,2}\operatorname*{Res}_{\omega=\omega_i}\frac{1}{(\omega-\omega_1)(\omega-\omega_2)}\mathrm{e}^{-\mathrm{i}\omega\tau}. \tag{2.27}$$

The additional minus sign on the right-hand side of (2.27) is due to the negative orientation of the contour integral.

A partial fraction decomposition of $G(\omega) = -1/(\omega-\omega_1)(\omega-\omega_2)$ reads

$$G(\omega) = \frac{-1}{(\omega-\omega_1)(\omega-\omega_2)} = \frac{-1}{\omega_1-\omega_2}\left(\frac{1}{\omega-\omega_1} - \frac{1}{\omega-\omega_2}\right). \tag{2.28}$$

Recall that the residue of (2.28) at $\omega = \omega_i$ is the coefficient in front of $1/(\omega-\omega_i)$ in the Laurent series expansion (bear in mind that the singularities at $\omega = \omega_i$ are simple). Thus, for $\omega_1 \neq \omega_2$ (or equivalently $\gamma \neq \omega_0$), we have

$$\operatorname*{Res}_{\omega=\omega_i}\frac{1}{(\omega-\omega_1)(\omega-\omega_2)}\mathrm{e}^{-\mathrm{i}\omega\tau} = \frac{(-1)^{i+1}}{\omega_1-\omega_2}\mathrm{e}^{-\mathrm{i}\omega_i\tau}, \qquad i = 1, 2. \tag{2.29}$$

For $\omega_1 = \omega_2$ (or equivalently $\gamma = \omega_0$), the residue (2.29) is equal to $-\mathrm{i}\tau\mathrm{e}^{-\gamma\tau}$ (if $f(\omega) = g(\omega)/(\omega-\bar{\omega})^n$ for some integer $n > 0$, where g is holomorphic at $\omega = \bar{\omega}$, then $\operatorname{Res}_{\omega=\bar{\omega}} f(\omega) = g^{(n-1)}(\bar{\omega})/(n-1)!$). Hence, (2.26) and (2.27) imply that the motion of the oscillator due to the Dirac delta excitation $f(t) = \delta(t)$ is

$$g(\tau) = \mathrm{e}^{-\gamma\tau}\frac{\sin((\omega_0^2-\gamma^2)^{1/2}\tau)}{(\omega_0^2-\gamma^2)^{1/2}}\Theta(\tau), \tag{2.30}$$

irrespectively of the sign of τ. This is the Green function of (2.19), see Ref. 76.

The impulse response (2.30) is also valid as $\gamma = \omega_0$ in which case the limiting value of (2.30) yields $g(\tau) = \tau\mathrm{e}^{-\gamma\tau}$ for $\tau > 0$. Observe that this expression coincides with the corresponding expression when the residue $-\mathrm{i}\tau\mathrm{e}^{-\gamma\tau}$ is inserted into (2.27). The frequency $(\omega_0^2-\gamma^2)^{1/2}$ in (2.30) and the characteristic time scale $1/\gamma$ are related

to the real and imaginary parts of $\omega_{1,2}$, respectively, whereas the sum of the moduli of the residua is the amplitude $(\omega_0^2-\gamma^2)^{-1/2}\mathrm{e}^{-\gamma\tau}$ of (2.30).

The inhomogeneous solution of (2.19) is finally obtained by inserting (2.30) into (2.25), *viz.*,

$$x(t)=\frac{1}{(\omega_0^2-\gamma^2)^{1/2}}\int_{-\infty}^{t}\mathrm{e}^{-\gamma(t-t')}\sin((\omega_0^2-\gamma^2)^{1/2}(t-t'))f(t')\,\mathrm{d}t'. \tag{2.31}$$

The full solution to the problem is given by the sum of (2.31) and either (2.22) or (2.23) depending on whether $\gamma\neq\omega_0$ or $\gamma=\omega_0$. The upper limit of integration in (2.31) clearly illustrates the idea that the displacement $x(t)$ only depends on the external driving force $f(t')$ for times $t'<t$, *cf.*, the causal relation (2.1). Recall that $g(\tau)$ can be established using more general techniques for calculating the Green function, see Refs. 76 and 78.

2.6 The Abraham-Lorentz equation of motion

A somewhat more complicated situation occurs when the phenomenological damping term $2\gamma\dot{x}(t)$ in (2.19) is replaced by the radiation reaction of a charged particle, *i.e.*, the recoil effect of the particle on itself due to radiation. The Abraham-Lorentz model[11] discussed in Refs. 45 and 71 is the simplest possible radiation reaction consistent with energy conservation. It yields a term in (2.19) proportional to the third time derivative of $x(t)$, *viz.*,

$$-\alpha\dddot{x}(t)+\ddot{x}(t)+\omega_0^2x(t)=f(t), \tag{2.32}$$

where $\alpha>0$.[12] The interpretation of the radiation reaction is that it quantifies the recoil effect as momentum is carried away from the particle due to emitted radiation.

From the analysis of the damped harmonic oscillator in Sec 2.5, it is clear that the frequency response associated with (2.32) is determined by the roots of the characteristic polynomial $-\mathrm{i}\alpha\omega^3-\omega^2+\omega_0^2=0$. From the fundamental theorem of algebra, it follows that these roots satisfy $\omega_1+\omega_2+\omega_3=\mathrm{i}/\alpha$. This means that at least one of the roots is located in the upper half part of the complex ω-plane (recall that $\alpha>0$). Thus, the frequency response of (2.32) is meromorphic rather than holomorphic in the upper half plane. As a consequence, the solution of (2.32) is either violating primitive causality or passivity. A solution to (2.32) which is passive is necessarily non-causal and admits self-acceleration, *i.e.*, the particle starts to accelerate a time interval of order α before the external driving force is applied. As a comfort, α is a very small number.

Another unpleasant consequence of (2.32) is the runaway solution for $\omega_0=0$ which implies that the free-particle acceleration $\ddot{x}(t)=\ddot{x}(0)\mathrm{e}^{t/\alpha}$, *i.e.*, the solution

[11] Also termed the Abraham-Lorentz-Dirac model since it was generalized by P. A. M. Dirac in Ref. 22 to account for the effects of special relativity.

[12] More explicitly, $\alpha=\mu_0q^2/6\pi mc_0$, where q is the charge and m is rest mass of the particle, and μ_0 and c_0 are the vacuum permeability and velocity of light in free space, respectively. For the electron, $\alpha=6\cdot10^{-24}\,\mathrm{s}$, which is the typical time it takes for light to travel across its spatial extension (the classical electron radius is $2.818\cdot10^{-15}\,\mathrm{m}$).

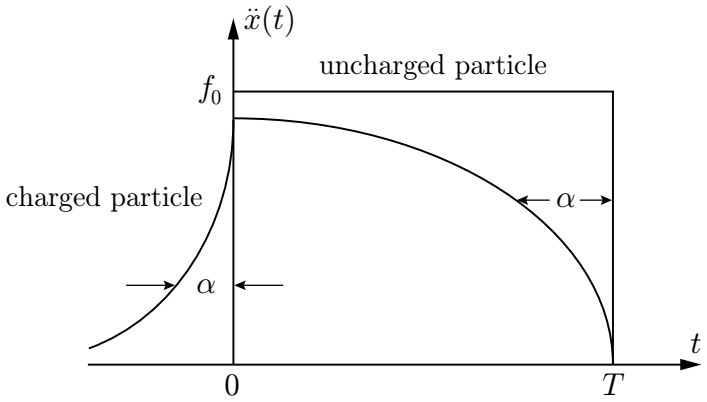

Figure 3: Illustration of self-acceleration and violation of primitive causality for a charged particle in the Abraham-Lorentz model.

of (2.32) with $\omega_0 = 0$ and $f(t) = 0$, increases exponentially with time. Many of these intriguing difficulties also persist in the generalized Abraham-Lorentz-Dirac model consistent with special relativity. For an introduction to the physical origin of the radiation reaction, see also Ref. 34.

To illustrate the phenomenon of self-acceleration, consider a charged particle subject to the following external force per unit mass: $f(t) = f_0$ for $0 < t < T$, and zero otherwise.[13] Then (2.32) with $\omega_0 = 0$ reads

$$-\alpha \dddot{x}(t) + \ddot{x}(t) = f(t). \tag{2.33}$$

In contrast to the uncharged particle with the acceleration $\ddot{x}(t) = f_0$ for $0 < t < T$ and zero otherwise (set $\alpha = 0$ in (2.33) to obtain $\ddot{x}(t) = f(t)$), the solution of (2.33) and its derivatives $\dot{x}(t)$ and $\ddot{x}(t)$ must be continuous in time although $f(t)$ is discontinuous. To prove this, integrate (2.33) from $t' = t - \varepsilon$ to $t' = t + \varepsilon$ for $\varepsilon > 0$. The physical interpretation of the statement is that the radiation reaction suppresses any rapid change in $\ddot{x}(t)$. Imposing the continuity condition of $\ddot{x}(t)$ at $t = 0$ and $t = T$ implies that either the runaway solution for $t > T$ or the self-acceleration for $t < 0$ can be eliminated, but not both of them. By preventing an exponentially increasing acceleration for $t > T$, the solution of (2.33) becomes

$$\ddot{x}(t) = \begin{cases} f_0 \left(1 - \mathrm{e}^{-T/\alpha}\right) \mathrm{e}^{t/\alpha}, & t < 0 \\ f_0 \left(1 - \mathrm{e}^{(t-T)/\alpha}\right), & 0 < t < T \\ 0, & t > T \end{cases} . \tag{2.34}$$

This solution clearly violates primitive causality in the sense that the particle respond a time interval of order α before $f(t)$ is applied, see Fig. 3.

The motion of a charged particle due to a Dirac delta excitation $f(t) = \delta(t)$ may also be analyzed. For this purpose, let $\varepsilon > 0$ and integrate (2.32) from $t = -\varepsilon$ to

[13] The following discussion is merely the solution of Problems 11.19 and 11.28 in Ref. 34.

$t = \varepsilon$ to obtain

$$-\alpha(\ddot{x}(\varepsilon) - \ddot{x}(-\varepsilon)) + \dot{x}(\varepsilon) - \dot{x}(-\varepsilon) = \int_{-\varepsilon}^{\varepsilon} \delta(t)\ \mathrm{d}t = 1. \tag{2.35}$$

If $\dot{x}(t)$ is continuous at the origin then (2.35) implies that $\ddot{x}(t)$ is discontinuous with the jump condition $\ddot{x}(0+) - \ddot{x}(0-) = -1/\alpha$. From this discontinuity it is straightforward to determine the solution of (2.32):

$$\ddot{x}(t) = \begin{cases} A\mathrm{e}^{t/\alpha}, & t < 0 \\ (A - 1/\alpha)\mathrm{e}^{t/\alpha}, & t > 0 \end{cases}. \tag{2.36}$$

In order to eliminate the runaway solution for $t > 0$, one must choose $A = 1/\alpha$. On the other hand, to prevent a self-acceleration for $t < 0$ it is required that $A = 0$. Obviously, both of these conditions cannot be satisfied simultaneously. If the runaway solution is eliminated from (2.36) then $\ddot{x}(t) = \mathrm{e}^{t/\alpha}/\alpha$ for $t < 0$ and zero otherwise. Integrating this solution for $t < 0$ yields

$$\dot{x}(t) = \int_{-\infty}^{t} \ddot{x}(t')\ \mathrm{d}t' = \frac{1}{\alpha}\int_{-\infty}^{t} \mathrm{e}^{t/\alpha}\ \mathrm{d}t = \mathrm{e}^{t/\alpha}, \tag{2.37}$$

where it is assumed that the particle is at rest at $t = -\infty$. The corresponding calculation for $t > 0$ reads

$$\dot{x}(t) = \dot{x}(0) + \int_{0}^{t} \ddot{x}(t')\ \mathrm{d}t' = 1. \tag{2.38}$$

It is therefore concluded that the runaway-free solutions of (2.33) are

$$\dot{x}(t) = \begin{cases} \mathrm{e}^{t/\alpha}, & t < 0 \\ 1, & t > 0 \end{cases} \qquad \ddot{x}(t) = \begin{cases} \mathrm{e}^{t/\alpha}/\alpha, & t < 0 \\ 0, & t > 0 \end{cases} \tag{2.39}$$

These results should be be compared with the corresponding expressions for an uncharged particle ($\alpha = 0$ in (2.33)): $\ddot{x}(t) = \delta(t)$ and $\dot{x}(t) = \Theta(t)$, where $\Theta(t)$ denotes the Heaviside step function.

It is important to check that (2.33) is consistent with the conservation of energy. First, the work done by the external force is calculated:

$$W_{\mathrm{ext}} = \int_{-\infty}^{\infty} f(t)\ \mathrm{d}x = \int_{-\infty}^{\infty} f(t)\dot{x}(t)\ \mathrm{d}t = \int_{-\infty}^{\infty} \delta(t)\dot{x}(t)\ \mathrm{d}t = \dot{x}(0) = 1. \tag{2.40}$$

The total energy radiated per unit mass is[14]

$$W_{\mathrm{rad}} = \int_{-\infty}^{\infty} P_{\mathrm{rad}}(t)\ \mathrm{d}t = \frac{\mu_0 q^2}{6\pi m c_0}\int_{-\infty}^{\infty} (\ddot{x}(t))^2\ \mathrm{d}t = \frac{\mu_0 q^2}{6\pi m c_0}\int_{-\infty}^{0} \mathrm{e}^{2t/\alpha}\ \mathrm{d}t = \frac{1}{2}, \tag{2.41}$$

[14]For a non-relativistic particle of charge q and rest mass m, the total power radiated per unit mass is given by the Larmor formula, see Refs. 45 and 71,

$$P_{\mathrm{rad}}(t) = \frac{\mu_0 q^2}{6\pi m c_0}(\ddot{x}(t))^2.$$

where $\alpha = \mu_0 q^2/6\pi m c_0$ has been used, see Footnote 12 on p. 14. Since the initial kinetic energy is zero (the particle is assumed to be at rest at $t = -\infty$), the final kinetic energy per unit mass is $W_{\text{kin}} = \dot{x}(0)/2 = 1/2$. Thus it is concluded that (2.33) is consistent with energy conservation since $W_{\text{ext}} = W_{\text{kin}} + W_{\text{rad}}$.

Many of the intriguing implications of (2.33) are not entirely understood nearly a century ago after the proposal of the Abraham-Lorentz equation of motion. Similar non-causal effects appear in, *e.g.*, Condon's model of chiral materials in classical electrodynamics, see Ref. 55.

2.7 The origin of dispersion relations

The holomorphic properties of the frequency response $G(\omega)$ are utilized in this section to derive some important relations in classical dispersion theory. For this purpose, consider the following Cauchy integral with $\omega = \omega' + \mathrm{i}\omega''$ (as usual ω' and ω'' are real-valued) located inside the arbitrary closed contour C in the upper half plane:[15]

$$G(\omega) = \frac{1}{2\pi\mathrm{i}} \oint_C \frac{G(\bar{\omega})}{\bar{\omega} - \omega} \, \mathrm{d}\bar{\omega}. \tag{2.42}$$

Let the contour C be defined by the real axis and an infinite semicircle, and assume that $G(\omega' + \mathrm{i}0)$ vanishes sufficiently rapid at infinity along the real ω'-axis. Then, for any $\omega = \omega' + \mathrm{i}\varepsilon$ with $\varepsilon > 0$,

$$G(\omega' + \mathrm{i}0) = \lim_{\varepsilon \to 0+} \frac{1}{2\pi\mathrm{i}} \int_{-\infty}^{\infty} \frac{G(\bar{\omega})}{\bar{\omega} - \omega' - \mathrm{i}\varepsilon} \, \mathrm{d}\bar{\omega}. \tag{2.43}$$

The integral (2.43) can be evaluated using (2.12), *i.e.*,

$$\lim_{\varepsilon \to 0+} \frac{1}{\bar{\omega} - \omega' - \mathrm{i}\varepsilon} = \mathcal{P}\left(\frac{1}{\bar{\omega} - \omega'}\right) + \mathrm{i}\pi\delta(\bar{\omega} - \omega'). \tag{2.44}$$

The origin of the Dirac distribution in (2.44) is the contribution from a small semicircle on the real axis enclosing the singularity at $\bar{\omega} = \omega' + \mathrm{i}0$, see Fig. 4. The contour in Fig. 4 is similar to the integration paths in the appended papers with the singularity located at $\bar{\omega} = 0$.

Under the assumption that $G(\omega' + \mathrm{i}0)$ is sufficiently regular at the real axis to interchange the Cauchy principal value $\mathcal{P}$ and the limit $\varepsilon \to 0+$, (2.44) inserted into (2.43) yields[16]

$$G(\omega' + \mathrm{i}0) = \frac{1}{2\pi\mathrm{i}} \mathcal{P} \int_{-\infty}^{\infty} \frac{G(\bar{\omega})}{\bar{\omega} - \omega'} \, \mathrm{d}\bar{\omega} + \frac{1}{2} G(\omega' + \mathrm{i}0), \tag{2.45}$$

[15] Here, $\bar{\omega}$ should not be confused with the complex conjugate of ω which is denoted by ω^*.

[16] Recall from Footnote 8 on p. 9 that the integral in (2.45) is defined as

$$\mathcal{P} \int_{-\infty}^{\infty} \frac{G(\bar{\omega})}{\bar{\omega} - \omega'} \, \mathrm{d}\bar{\omega} = \lim_{\epsilon \to 0+} \left(\int_{-\infty}^{\omega - \epsilon} + \int_{\omega + \epsilon}^{\infty} \right) \frac{G(\bar{\omega})}{\bar{\omega} - \omega'} \, \mathrm{d}\bar{\omega}.$$

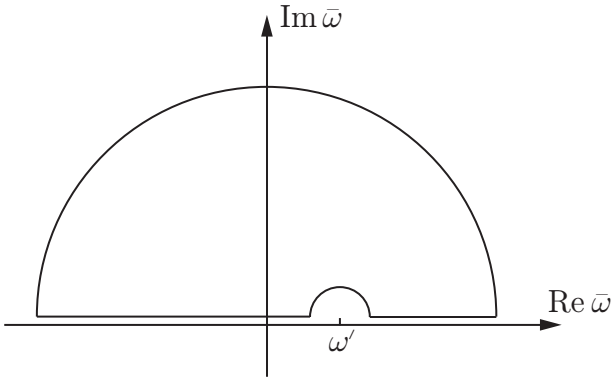

Figure 4: Integration contour in (2.42). The radii of the small and large semicircles approach zero and infinity, respectively.

or equivalently,

$$G(\omega' + \mathrm{i}0) = \frac{1}{\pi \mathrm{i}} \mathcal{P} \int_{-\infty}^{\infty} \frac{G(\bar{\omega})}{\bar{\omega} - \omega'} \, \mathrm{d}\bar{\omega}. \tag{2.46}$$

Relation (2.46) is recognized as the Hilbert transform of $G(\bar{\omega})$ along the real $\bar{\omega}$-axis, see Ref. 80. It can be split into the first and second Plemelj formulae by applying the real and imaginary parts to (2.46). By using the cross symmetry (2.4), *i.e.*, the fact that $\mathrm{Re}\, G(\bar{\omega})$ and $\mathrm{Im}\, G(\bar{\omega})$ are even and odd in $\bar{\omega}$, respectively, one obtains the following transform pair:

$$\mathrm{Re}\, G(\omega' + \mathrm{i}0) = \frac{2}{\pi} \mathcal{P} \int_0^{\infty} \frac{\bar{\omega}\, \mathrm{Im}\, G(\bar{\omega})}{\bar{\omega}^2 - \omega'^2} \, \mathrm{d}\bar{\omega} \tag{2.47}$$

$$\mathrm{Im}\, G(\omega' + \mathrm{i}0) = \frac{-2\omega'}{\pi} \mathcal{P} \int_0^{\infty} \frac{\mathrm{Re}\, G(\bar{\omega})}{\bar{\omega}^2 - \omega'^2} \, \mathrm{d}\bar{\omega} \tag{2.48}$$

Recall that (2.47) and (2.48) are a direct consequence of primitive causality. Furthermore, the structure of (2.47) and (2.48) is similar to (2.14).

The two Plemelj formulae (2.47) and (2.48) imply each other (at least if they are expressed as integrals over the entire real axis rather than the positive semi axis), so it is sufficient to keep only one of them. For our purpose, (2.47) is appropriate for analyzing the extinction cross section of acoustic and electromagnetic waves in the appended papers. In fact, relations (2.47) and (2.48) are the starting point of the classical dispersion theory discussed in, *e.g.*, Refs. 39, 41, 44, and 89. The Plemelj formulae are also the foundations of the forward and non-forward dispersion relations discussed in Sec. 3. Relations (2.47) and (2.48) can also be generalized to include functionals of $G(\omega)$ that satisfy (2.4), since sums, products, and compositions of holomorphic functions likewise are holomorphic, *cf.*, the dispersion relation for $1/G(\omega)$ in Sec. 2.10 (recall that $G(\omega)$ is nowhere zero in the upper half plane due to Meĭman's theorem in Sec. 2.3). However, in order to preserve the upper half plane as the appropriate domain where the composite function is holomorphic, the Herglotz property (2.8) is required.

From a direct integration it is straightforward to show that the frequency response for the damped harmonic oscillator in Sec. 2.5 satisfies (2.46) and thereby also (2.47) and (2.48). To show this, make a partial fraction decomposition of the integrand in (2.46), *i.e.*,

$$\frac{G(\bar{\omega})}{\bar{\omega}-\omega'} = \frac{1}{(\omega'-\omega_1)(\omega_1-\omega_2)}\frac{1}{\bar{\omega}-\omega_1} - \frac{1}{(\omega'-\omega_2)(\omega_1-\omega_2)}\frac{1}{\bar{\omega}-\omega_2} - \frac{1}{(\omega'-\omega_1)(\omega'-\omega_2)}\frac{1}{\bar{\omega}-\omega'}, \quad (2.49)$$

where $G(\bar{\omega}) = -1/(\bar{\omega}-\omega_1)(\bar{\omega}-\omega_2)$ has been used. The last term in (2.49) does not contribute to (2.46) since $\mathcal{P}\int_{-\infty}^{\infty} \mathrm{d}\bar{\omega}/(\bar{\omega}-\omega') = 0$.[17] However, the first two terms contribute according to (decompose the integrand into its real and imaginary parts)

$$\mathcal{P}\int_{-\infty}^{\infty} \frac{\mathrm{d}\bar{\omega}}{\bar{\omega}-\omega_{1,2}} = \int_{-\infty}^{\infty} \frac{\bar{\omega} \mp (\omega_0^2-\gamma^2)^{1/2}}{(\bar{\omega} \mp (\omega_0^2-\gamma^2)^{1/2})^2+\gamma^2}\,\mathrm{d}\bar{\omega} - \mathrm{i}\gamma\int_{-\infty}^{\infty} \frac{\mathrm{d}\bar{\omega}}{(\bar{\omega} \mp (\omega_0^2-\gamma^2)^{1/2})^2+\gamma^2}, \quad (2.50)$$

where the upper and lower signs refer to $\omega_{1,2} = -\mathrm{i}\gamma \pm (\omega_0^2-\gamma^2)^{1/2}$, respectively. The first integral on the right-hand side of (2.50) has the primitive function $\ln((\bar{\omega} \mp (\omega_0^2-\gamma^2)^{1/2})^2+\gamma^2)/2$ which yields

$$\int_{-\infty}^{\infty} \frac{\bar{\omega} \mp (\omega_0^2-\gamma^2)^{1/2}}{(\bar{\omega} \mp (\omega_0^2-\gamma^2)^{1/2})^2+\gamma^2}\,\mathrm{d}\bar{\omega} = \frac{1}{2}\lim_{\bar{\omega}\to\infty} \ln\frac{(\bar{\omega} \mp (\omega_0^2-\gamma^2)^{1/2})^2+\gamma^2}{(\bar{\omega} \pm (\omega_0^2-\gamma^2)^{1/2})^2+\gamma^2} = 0. \quad (2.51)$$

The corresponding primitive function for the second integral on the right-hand side is $\gamma^{-1}\arctan((\bar{\omega} \mp (\omega_0^2-\gamma^2)^{1/2})/\gamma)$. Thus, since $\gamma \geqslant 0$,

$$\mathcal{P}\int_{-\infty}^{\infty} \frac{\mathrm{d}\bar{\omega}}{\bar{\omega}-\omega_{1,2}} = -\mathrm{i}\lim_{\bar{\omega}\to\infty} \arctan\left(\frac{\bar{\omega} \mp (\omega_0^2-\gamma^2)^{1/2}}{\gamma}\right) = -\mathrm{i}\pi. \quad (2.52)$$

By combining (2.49), (2.51), and (2.52) it follows that

$$\frac{1}{\mathrm{i}\pi}\mathcal{P}\int_{-\infty}^{\infty} \frac{G(\bar{\omega})}{\bar{\omega}-\omega'}\,\mathrm{d}\bar{\omega} = \frac{-1}{\omega_1-\omega_2}\left(\frac{1}{\omega'-\omega_1} - \frac{1}{\omega'-\omega_2}\right) = G(\omega'), \quad (2.53)$$

where the last equality is given by (2.28). In other words, the frequency response of the damped harmonic oscillator satisfies (2.46) and consequently also (2.47) and (2.48).

[17] This statement follows from the fact that ω' is real-valued and

$$\mathcal{P}\int_{-\infty}^{\infty} \frac{\mathrm{d}\bar{\omega}}{\bar{\omega}-\omega'} = \lim_{\varepsilon\to 0+}\left(\int_{-\infty}^{\omega'-\varepsilon} + \int_{\omega'+\varepsilon}^{\infty}\right)\frac{\mathrm{d}\bar{\omega}}{\bar{\omega}-\omega'} = \lim_{\varepsilon\to 0+}\ln\left|\frac{\omega'-\varepsilon}{\omega'+\varepsilon}\right| = 0.$$

This result also follows from the fact that the function $h(\bar{\omega}) = 1/(\bar{\omega}-\omega')$ for a fixed ω' satisfies $h(2\omega'-\bar{\omega}) = -h(\bar{\omega})$, *i.e.*, $h(\bar{\omega})$ is odd with respect to $\bar{\omega}$ around the discontinuity point $\bar{\omega} = \omega'$.

Various sum rules can be derived from the asymptotic behavior of the Plemelj formulae. They are often based on the following hand waving arguments. Consider the limiting values of (2.47) and (2.48) as the argument ω' becomes infinitely large.[18] Since $1/(\bar{\omega}^2 - \omega'^2) = -1/\omega'^2 + \mathcal{O}(1/\omega'^4)$ as $\omega' \to \infty$, it follows that

$$\operatorname{Re} G(\omega' + \mathrm{i}0) \sim \frac{-2}{\pi\omega'^2} \int_0^\infty \bar{\omega} \operatorname{Im} G(\bar{\omega}) \, \mathrm{d}\bar{\omega} \tag{2.54}$$

$$\operatorname{Im} G(\omega' + \mathrm{i}0) \sim \frac{2}{\pi\omega'} \int_0^\infty \operatorname{Re} G(\bar{\omega}) \, \mathrm{d}\bar{\omega} \tag{2.55}$$

Relations (2.54) and (2.55) are referred to as superconvergent sum rules, see Refs. 4 and 5. Such sum rules are often established on the basis of the Kramers-Kronig relations, see Sec. 2.10, and additional physical assumptions in the high-frequency regime, *e.g.*, the requirement that the electromagnetic response of the medium under consideration is described by a Lorentz model (*i.e.*, the damped harmonic oscillator in Sec. 2.5) for frequencies far beyond any material resonances. However, (2.54) and (2.55) can also be established using rigorous arguments on the asymptotic behavior of the Hilbert transform, see Ref. 80 and references therein.

Another interesting relation for real-valued $\omega = \omega' + \mathrm{i}0$ is obtained by evaluating the integral of $\bar{\omega}G(\bar{\omega})/(\bar{\omega}^2 + \omega'^2)$ with respect to the contour defined by the real axis and an infinite semicircle in the upper half part of the complex $\bar{\omega}$-plane, *i.e.*, the same contour as in Fig. 4 except for the small semicircle centered at $\omega' = \omega$. Under the assumption that the contribution from the infinite semicircle vanishes, the method of residues yields for $\omega' > 0$ that (recall that if $f(\bar{\omega})$ is holomorphic and has a simple singularity at $\bar{\omega} = \omega$, then $\operatorname{Res}_{\bar{\omega}=\omega} f(\bar{\omega}) = \lim_{\bar{\omega}\to\omega}(\bar{\omega} - \omega) f(\bar{\omega})$)

$$\int_{-\infty}^{\infty} \frac{\bar{\omega}G(\bar{\omega})}{\bar{\omega}^2 + \omega'^2} \, \mathrm{d}\bar{\omega} = 2\pi\mathrm{i} \operatorname*{Res}_{\bar{\omega}=\mathrm{i}\omega'} \frac{\bar{\omega}G(\bar{\omega})}{\bar{\omega}^2 + \omega'^2} = 2\pi\mathrm{i} \lim_{\bar{\omega}\to\mathrm{i}\omega'} \frac{\bar{\omega}G(\bar{\omega})}{\bar{\omega} + \mathrm{i}\omega'} = \mathrm{i}\pi G(\mathrm{i}\omega'). \tag{2.56}$$

The real part of (2.56) vanishes since $\bar{\omega} \operatorname{Re} G(\bar{\omega})/(\bar{\omega}^2 + \omega'^2)$ is an odd function of $\bar{\omega}$ (the cross symmetry (2.4) states that $\operatorname{Re} G(\bar{\omega})$ is even in $\bar{\omega}$). However, since $\bar{\omega} \operatorname{Im} G(\bar{\omega})/(\bar{\omega}^2 + \omega'^2)$ is even and $G(\mathrm{i}\omega')$ is real-valued, the imaginary part of (2.56) yields

$$G(\mathrm{i}\omega') = \frac{2}{\pi} \int_0^\infty \frac{\bar{\omega} \operatorname{Im} G(\bar{\omega})}{\bar{\omega}^2 + \omega'^2} \, \mathrm{d}\bar{\omega}. \tag{2.57}$$

Integrating both sides in (2.57) from $\omega' = 0$ to $\omega' = \infty$ yields the identity

$$\int_0^\infty G(\mathrm{i}\omega') \, \mathrm{d}\omega' = \frac{2}{\pi} \int_0^\infty \operatorname{Im} G(\bar{\omega}) \int_0^\infty \frac{\bar{\omega}}{\bar{\omega}^2 + \omega'^2} \, \mathrm{d}\omega' \, \mathrm{d}\bar{\omega} = \int_0^\infty \operatorname{Im} G(\bar{\omega}) \, \mathrm{d}\bar{\omega}, \tag{2.58}$$

where it has been used that the inner integral is equal to $\lim_{\omega'\to\infty} \arctan(\omega'/\bar{\omega}) = \pi/2$. Note that (2.58) only is valid when $G(\omega)$ is sufficiently regular to interchange the order of integration in ω' and $\bar{\omega}$. The relation (2.58) can also be derived by a direct application of Cauchy's integral theorem to a quarter-circle contour in the first quadrant of the complex $\bar{\omega}$-plane. The interpretation of (2.58) is that it relates the

[18] This is merely Problem 7.3.4 in Ref. 7.

values of $G(\omega)$ on the imaginary axis to those of $\mathrm{Im}\, G(\omega' + \mathrm{i}0)$ on the real axis. Provided that the integral on the left-hand side exists, (2.58) suggests that $\mathrm{Im}\, G(\omega' + \mathrm{i}0)$ is integrable rather than square integrable as required by the Titchmarsh theorem, see Sec. 2.8.

2.8 The Titchmarsh theorem

In some cases, it is more natural to establish conditions on the asymptotic behavior of the frequency response $G(\omega' + \mathrm{i}0)$ for real-valued $\omega = \omega' + \mathrm{i}0$, instead of assuming that $G(\bar{\omega})/(\bar{\omega} - \omega')$ becomes identically zero when integrated over a large semicircle or any other contour in the upper half plane. The ideas in this section are therefore restated in a form appropriate for $G(\omega' + \mathrm{i}0)$ when it is square integrable on the real axis. From the Parseval theorem (also termed the Plancherel theorem in Ref. 25) it follows that

$$\int_{-\infty}^{\infty} |G(\omega' + \mathrm{i}0)|^2 \, \mathrm{d}\omega' = 2\pi \int_0^{\infty} |g(\tau)|^2 \, \mathrm{d}\tau < C, \tag{2.59}$$

where C is a constant. Introduce $\omega = \omega' + \mathrm{i}\omega''$ (as usual ω' and ω'' are real-valued) and recall that $G(\omega' + \mathrm{i}\omega'')$ is the Fourier transform of $\mathrm{e}^{-\omega''\tau} g(\tau)$ evaluated at the point ω'. For $\omega'' > 0$, another application of the Parseval theorem yields

$$\int_{-\infty}^{\infty} |G(\omega' + \mathrm{i}\omega'')|^2 \, \mathrm{d}\omega' = 2\pi \int_0^{\infty} \mathrm{e}^{-2\omega''\tau} |g(\tau)|^2 \, \mathrm{d}\tau < 2\pi \int_0^{\infty} |g(\tau)|^2 \, \mathrm{d}\tau. \tag{2.60}$$

The estimate (2.60) implies that $G(\omega)$ belongs to the Hardy class H^2, see Refs. 24 and 29, *i.e.*,

$$\int_{-\infty}^{\infty} |G(\omega' + \mathrm{i}\omega'')|^2 \, \mathrm{d}\omega' < C \tag{2.61}$$

uniformly for all $\omega'' > 0$. This is an important result illuminated in a set of theorems in Ref. 80 collectively referred to as the Titchmarsh theorem.

The Titchmarsh theorem. *If $G(\omega')$ is square integrable on the real ω'-axis, the following three conditions are equivalent:*

i. the inverse Fourier transform of $G(\omega)$ vanishes for $\tau < 0$, i.e.,

$$g(\tau) = \frac{1}{2\pi} \int_{-\infty}^{\infty} G(\omega') \mathrm{e}^{-\mathrm{i}\omega'\tau} \, \mathrm{d}\omega' = 0, \quad \tau < 0;$$

ii. $G(\omega')$ is, for almost all ω', the limit as $\omega'' \to 0+$ of $G(\omega' + \mathrm{i}\omega'')$; the function $G(\omega' + \mathrm{i}\omega'')$ is holomorphic in the upper half part of the complex ω-plane and there satisfies (2.61)*;*

iii. the real and imaginary parts of $G(\omega)$ obey (2.47) *and* (2.48)*.*

The equivalence in Titchmarsh's theorem holds in the sense that each of the above conditions are both necessary and sufficient for the others to be true. Loosely speaking, the theorem states that for a frequency response that vanishes sufficiently

rapid at infinity, the following statements express one single property in three different ways: (i) having a Fourier transform that vanishes on the negative real axis, (ii) being holomorphic in the upper half part of the complex ω-plane, and (iii) obeying a dispersion relation.

2.9 Dispersion relations with one subtraction

The requirement of square integrability in the Titchmarsh theorem is often violated in physical problems. Physical considerations suggest that for a passive system with a square integrable (or finite energy) input $f(t)$, there exists a constant C such that the output $x(t)$ satisfies

$$\int_{-\infty}^{\infty} |x(t)|^2 \, \mathrm{d}t \leqslant C \int_{-\infty}^{\infty} |f(t)|^2 \, \mathrm{d}t. \tag{2.62}$$

For many physical systems, conservation of energy implies that C is bounded from above by unity. Irrespectively of the value of C, the Parseval theorem states that along the real ω'-axis,

$$\int_{-\infty}^{\infty} |X(\omega')|^2 \, \mathrm{d}\omega' = \int_{-\infty}^{\infty} |G(\omega')|^2 |F(\omega')|^2 \, \mathrm{d}\omega' \leqslant C \int_{-\infty}^{\infty} |F(\omega')|^2 \, \mathrm{d}\omega', \tag{2.63}$$

where $X(\omega')$ denotes the Fourier transform of $x(t)$. The inequality (2.63) is satisfied if $|G(\omega')|^2 \leqslant C$, *i.e.*, $G(\omega')$ is bounded pointwise in ω' (belongs to the function space L^∞) rather than being square integrable. Although the Titchmarsh theorem is not directly applicable to bounded functions, $G(\omega) = G(\omega' + \mathrm{i}\omega'')$ still defines a holomorphic function in the upper half plane.

As pointed out in the previous paragraph, a common situation in physical problems occurs when $G(\omega')$ is bounded rather than square integrable. Then, for an arbitrary point $\tilde{\omega}$ on the real axis, the Titchmarsh theorem can be applied to $(G(\omega) - G(\tilde{\omega}))/(\omega - \tilde{\omega})$ which is square integrable on the real axis if $G(\omega' + \mathrm{i}0)$ is differentiable at $\omega' = \tilde{\omega}$, *i.e.*, $\lim_{\omega' \to \tilde{\omega}} (G(\omega' + \mathrm{i}0) - G(\tilde{\omega}))/(\omega' - \tilde{\omega})$ exists. To see this, decompose the integral according to

$$\int_{-\infty}^{\infty} \left| \frac{G(\omega' + \mathrm{i}0) - G(\tilde{\omega})}{\omega' - \tilde{\omega}} \right|^2 \mathrm{d}\omega' = \left(\int_{-\infty}^{\alpha} + \int_{\alpha}^{\beta} + \int_{\beta}^{\infty} \right) \left| \frac{G(\omega' + \mathrm{i}0) - G(\tilde{\omega})}{\omega' - \tilde{\omega}} \right|^2 \mathrm{d}\omega', \tag{2.64}$$

where $\tilde{\omega}$ belongs to the open interval (α, β). Now use the triangle inequality $|G(\omega' + \mathrm{i}0) - G(\tilde{\omega})| \leqslant |G(\omega' + \mathrm{i}0)| + |G(\tilde{\omega})|$ and $|G(\omega' + \mathrm{i}0)|^2 \leqslant C$ to obtain

$$|G(\omega' + \mathrm{i}0) - G(\tilde{\omega})|^2 \leqslant (\sqrt{C} + \sqrt{C})^2 = 4C. \tag{2.65}$$

The first integral on the right-hand side of (2.64) is bounded since

$$\int_{-\infty}^{\alpha} \left| \frac{G(\omega' + \mathrm{i}0) - G(\tilde{\omega})}{\omega' - \tilde{\omega}} \right|^2 \mathrm{d}\omega' \leqslant 4C \int_{-\infty}^{\alpha} \frac{\mathrm{d}\omega'}{(\omega' - \tilde{\omega})^2} = \frac{4C}{\tilde{\omega} - \alpha} < \infty. \tag{2.66}$$

A similar estimate for the third integral in (2.64) yields $4C/(\beta - \tilde{\omega})$ which is finite (just substitute α with β in (2.66) and compensate with a minus sign). Since the integrand in (2.64) by assumption is differentiable at $\omega' = \tilde{\omega}$ it is also continuous at this point. But since any continuous function is locally integrable it follows that also the second integral on the right-hand side of (2.64) is finite. Thus, (2.64) is square integrable.

The dispersion relation with one subtraction constant is obtained by applying $(G(\omega) - G(\tilde{\omega}))/(\omega - \tilde{\omega})$ to (2.46), *i.e.*,

$$G(\omega' + \mathrm{i}0) = G(\tilde{\omega}) + \frac{\omega' - \tilde{\omega}}{\mathrm{i}\pi} \mathcal{P} \int_{-\infty}^{\infty} \frac{G(\bar{\omega}) - G(\tilde{\omega})}{\bar{\omega} - \tilde{\omega}} \frac{\mathrm{d}\bar{\omega}}{\bar{\omega} - \omega'}. \tag{2.67}$$

At $\omega' = \tilde{\omega}$ the right-hand side of (2.67) reduces to $G(\tilde{\omega})$ as expected (recall that the integral is bounded). Relation (2.67) is particularly useful when $\tilde{\omega} = 0$, *i.e.*, the subtraction constant is obtained from static considerations, or $\tilde{\omega} = \infty$. Since $(\omega' - \tilde{\omega})/(\bar{\omega} - \tilde{\omega}) = 1 + \mathcal{O}(1/\tilde{\omega})$ as $\tilde{\omega} \to \infty$, the latter case implies

$$G(\omega' + \mathrm{i}0) = G_\infty + \frac{1}{\mathrm{i}\pi} \mathcal{P} \int_{-\infty}^{\infty} \frac{G(\bar{\omega}) - G_\infty}{\bar{\omega} - \omega'} \, \mathrm{d}\bar{\omega} = G_\infty + \frac{1}{\mathrm{i}\pi} \mathcal{P} \int_{-\infty}^{\infty} \frac{G(\bar{\omega})}{\bar{\omega} - \omega'} \, \mathrm{d}\bar{\omega}. \tag{2.68}$$

Here, $G_\infty = \lim_{\tilde{\omega} \to \infty} G(\tilde{\omega})$ and $\mathcal{P} \int_{-\infty}^{\infty} \mathrm{d}\bar{\omega}/(\bar{\omega} - \omega') = 0$ have been used, *cf.*, Footnote 17 on p. 19. A repeated application of (2.67) yields dispersion relations with $n + 1$ subtractions (n is a positive integer) suitable for the asymptotic behavior $G(\omega') = \mathcal{O}(\omega'^n)$ as $\omega' \to \infty$. Dispersion relations with more than one subtraction are analyzed in great detail in Refs. 41 and 66.

2.10 The Kramers-Kronig relations

Also the Kramers-Kronig relations (named after the contemporary discoveries by R. de L. Kronig and H. A. Kramers in Refs. 21 and 54), which model the propagation of electromagnetic waves in homogeneous and isotropic media, originate from (2.47) and (2.48). To illustrate this, introduce the complex-valued permittivity $\epsilon(\omega')$ relative to free space (as usual ω' rather than $\omega = \omega' + \mathrm{i}\omega''$ is the physical frequency). Set $G(\omega) = \epsilon(\omega) - \epsilon_\infty$, where $\epsilon_\infty = \lim_{\omega' \to \infty} \epsilon(\omega')$ denotes the instantaneous response of the medium (the limit is taken along the real ω'-axis whereas ω is the complex frequency confined to the upper half plane).[19] Then $G(\omega)$ satisfies (2.4), and, under the assumption of strict passivity, *i.e.*, $\operatorname{Im} \epsilon(\omega') > 0$ for $\omega' > 0$, it follows from Meĭman's theorem on p. 10 that $\epsilon(\omega)$ is real-valued only on the imaginary axis among all finite points in the upper half part of the complex ω-plane. On the imaginary axis, $\epsilon(\omega) - \epsilon_\infty$ decreases monotonically as $\omega \to \mathrm{i}\infty$.[20]

[19] The present analysis is restricted to isotropic media. However, the formulae presented in this section also hold in the anisotropic case for the Rayleigh quotients or quadratic forms $\boldsymbol{a}^* \cdot \boldsymbol{\epsilon}(\omega) \cdot \boldsymbol{a}$ ($\boldsymbol{a}$ is an arbitrary complex-valued vector with $|\boldsymbol{a}| = 1$) of the permittivity dyadic $\boldsymbol{\epsilon}(\omega)$. It should also be mentioned that $\epsilon(\omega)$ can be replaced by the permeability $\mu(\omega)$ in the subsequent expressions.

[20] This conclusion is merely the first part of Problem 7.24 in Ref. 45.

Physical reasons in Ref. 45 suggest that the frequency response $G(\omega') = \epsilon(\omega') - \epsilon_\infty$ satisfies $\operatorname{Re} G(\omega') = \mathcal{O}(\omega'^{-2})$ and $\operatorname{Im} G(\omega') = \mathcal{O}(\omega'^{-3})$ as $\omega' \to \infty$. However, the conductivity model and the Debye model[21] vanish slower at infinity, but still sufficiently fast to be square integrable. For the conductivity model, one has $\operatorname{Re} G(\omega') = 0$ and $\operatorname{Im} G(\omega') = \mathcal{O}(\omega'^{-1})$ as $\omega' \to \infty$, while the Debye model satisfies $\operatorname{Re} G(\omega') = \mathcal{O}(\omega'^{-2})$ and $\operatorname{Im} G(\omega') = \mathcal{O}(\omega'^{-1})$ as $\omega' \to \infty$. Thus, (2.47) and (2.48) imply, in the absence of a conductivity term, the following constraints on the permittivity known as the Kramers-Kronig relations:[22]

$$\operatorname{Re} \epsilon(\omega' + \mathrm{i}0) = \epsilon_\infty + \frac{2}{\pi} \mathcal{P} \int_0^\infty \frac{\bar{\omega} \operatorname{Im} \epsilon(\bar{\omega})}{\bar{\omega}^2 - \omega'^2} \, \mathrm{d}\bar{\omega} \tag{2.69}$$

$$\operatorname{Im} \epsilon(\omega' + \mathrm{i}0) = \frac{-2\omega'}{\pi} \mathcal{P} \int_0^\infty \frac{\operatorname{Re} \epsilon(\bar{\omega})}{\bar{\omega}^2 - \omega'^2} \, \mathrm{d}\bar{\omega} \tag{2.70}$$

Since the instantaneous response is non-unique from a modeling point of view, see Ref. 38, (2.69) and (2.70) are often phrased with $\epsilon_\infty = 1$. The Kramers-Kronig relations can also be formulated in the refractive index $n(\omega) = (\epsilon(\omega)\mu(\omega))^{1/2}$ by applying (2.47) and (2.48) to $G(\omega) = n(\omega) - n_\infty$ with $n_\infty = \lim_{\omega' \to \infty} n(\omega')$, see Refs. 44 and 66.

When a static conductivity $\varsigma > 0$ is present in $\epsilon(\omega')$, (2.69) still remains valid whereas the right-hand side of (2.70) must be modified with the additional term $\varsigma/\omega'\epsilon_0$, see Ref. 57 and the discussion in Paper II, *i.e.*,

$$\operatorname{Im} \epsilon(\omega' + \mathrm{i}0) = \frac{\varsigma}{\omega'\epsilon_0} - \frac{2\omega'}{\pi} \mathcal{P} \int_0^\infty \frac{\operatorname{Re} \epsilon(\bar{\omega})}{\bar{\omega}^2 - \omega'^2} \, \mathrm{d}\bar{\omega}. \tag{2.71}$$

The term $\varsigma/\omega'\epsilon_0$ refers to the contribution from a small semicircle that encloses the singularity at $\omega' = 0$, *cf.*, the contour in Fig. 4.

A number of important results can be derived from the Kramers-Kronig relations when no conductivity term is present. For this purpose, assume that $\operatorname{Im} \epsilon(\omega')$ is sufficiently well-behaved at the origin to interchange the Cauchy principal value and the limit $\omega' \to 0+$. Under this assumption, the static limit of (2.69) yields the sum rule

$$\epsilon(0) = \epsilon_\infty + \frac{2}{\pi} \mathcal{P} \int_0^\infty \frac{\operatorname{Im} \epsilon(\bar{\omega})}{\bar{\omega}} \, \mathrm{d}\bar{\omega}, \tag{2.72}$$

[21] The conductivity model is defined by the additive term $\mathrm{i}\varsigma/\omega'\epsilon_0$, while the Debye model is $\epsilon(\omega') = \epsilon_\infty + (\epsilon_\mathrm{s} - \epsilon_\infty)/(1 - \mathrm{i}\omega'\tau)$, where $\epsilon_\mathrm{s} = \epsilon(0)$ denotes the static permittivity. Both the conductivity $\varsigma > 0$ and the relaxation time $\tau > 0$ are assumed to be independent of ω'. For an introduction to dispersion models for temporally dispersive matter, see Ref. 13 and references therein.

[22] Note that the instantaneous response ϵ_∞ disappears from the integral in (2.70) since

$$\mathcal{P} \int_0^\infty \frac{\mathrm{d}\bar{\omega}}{\bar{\omega}^2 - \omega'^2} = \lim_{\varepsilon \to 0+} \frac{-1}{2\omega'} \left\{ \ln\left(\frac{\bar{\omega} + \omega'}{\bar{\omega} - \omega'}\right)\Big|_{\bar{\omega} = -\infty}^{\omega' - \varepsilon} + \ln\left(\frac{\bar{\omega} + \omega'}{\bar{\omega} - \omega'}\right)\Big|_{\bar{\omega} = \omega' + \varepsilon}^{\infty} \right\}$$
$$= \lim_{\varepsilon \to 0+} \frac{1}{2\omega'} \ln\left(\frac{\varepsilon + 2\omega'}{\varepsilon - 2\omega'}\right) = 0.$$

This is also clear from a partial fraction decomposition of $1/(\bar{\omega}^2 - \omega'^2)$ and Footnote 17.

where it has been used that (2.70) implies $\operatorname{Im}\epsilon(0) = 0$. From (2.72) and the passivity condition $\operatorname{Im}\epsilon(\bar{\omega}) \geqslant 0$ for $\bar{\omega} > 0$, it is clear that the static permittivity $\epsilon(0)$ is larger than or equal to ϵ_∞. This result is among other things important in the analysis of temporally dispersive matter in Paper II. Finally, note that $G(\omega) = \epsilon(\omega) - \epsilon_\infty$ also satisfies (2.58) provided it vanishes sufficiently fast at infinity, *i.e.*,

$$\int_0^\infty \epsilon(\mathrm{i}\bar{\omega}) - \epsilon_\infty \, \mathrm{d}\bar{\omega} = \int_0^\infty \operatorname{Im}\epsilon(\bar{\omega}) \, \mathrm{d}\bar{\omega}. \tag{2.73}$$

Recall that the right hand side of (2.73) is non-negative. However, (2.73) is not directly applicable to the conductivity model since then both the left and right hand sides of (2.73) diverge.

The Meĭman theorem on p. 10, and the fact that ϵ_∞ is real-valued, implies that $\epsilon(\omega)$ is nowhere zero in the upper half of the ω-plane. Hence, also the reciprocal value of $\epsilon(\omega)$ is holomorphic in that half-plane, and (2.47) and (2.48) hold for $G(\omega) = 1/\epsilon(\omega) - 1/\epsilon_\infty$, *i.e.*,

$$\operatorname{Re}\left\{\frac{1}{\epsilon(\omega' + \mathrm{i}0)}\right\} = \frac{1}{\epsilon_\infty} + \frac{2}{\pi}\mathcal{P}\int_0^\infty \frac{\bar{\omega}}{\bar{\omega}^2 - \omega'^2} \operatorname{Im}\left\{\frac{1}{\epsilon(\bar{\omega})}\right\} \mathrm{d}\bar{\omega} \tag{2.74}$$

$$\operatorname{Im}\left\{\frac{1}{\epsilon(\omega' + \mathrm{i}0)}\right\} = \frac{-2\omega'}{\pi}\mathcal{P}\int_0^\infty \frac{1}{\bar{\omega}^2 - \omega'^2} \operatorname{Re}\left\{\frac{1}{\epsilon(\bar{\omega})}\right\} \mathrm{d}\bar{\omega} \tag{2.75}$$

Note that (2.74) and (2.75) can be rewritten in terms of $\operatorname{Re}\epsilon(\omega')$ and $\operatorname{Im}\epsilon(\omega')$ by observing that

$$\operatorname{Re}\left\{\frac{1}{\epsilon(\omega')}\right\} = \frac{\operatorname{Re}\epsilon(\omega')}{|\epsilon(\omega')|^2}, \qquad \operatorname{Im}\left\{\frac{1}{\epsilon(\omega')}\right\} = \frac{-\operatorname{Im}\epsilon(\omega')}{|\epsilon(\omega')|^2}. \tag{2.76}$$

Both (2.69) and (2.70) as well as (2.74) and (2.75) can be used to derive superconvergent sum rules, see Refs. 5 and 45. However, the reader should be careful to consult Ref. 58 due to its many misprints and lack of physical clarity.

A Gedankenexperiment associated with the Kramers-Kronig relations is presented in Ref. 39. Consider a pair of spectacles with, say, green glasses subject to a flashlight in a dark room. The light as a function of time is modeled as a δ-twinkle, *i.e.*, as the Dirac delta distribution

$$\delta(t) = \frac{1}{2\pi}\int_{-\infty}^\infty \mathrm{e}^{\mathrm{i}\omega t} \, \mathrm{d}\omega. \tag{2.77}$$

The interpretation of (2.77) is that the δ-twinkle contains all frequencies in such a way that the waves interfere destructively at all times except at $t = 0$. Now, consider a pair of ideal green glasses which transmits green light in some region of the spectrum, but absorbs all other waves necessary for the mutual cancelation at times $t \neq 0$. Suppose that there is no connection between the real and imaginary parts of the refractive index, *i.e.*, the refractive and absorptive properties of $n(\omega)$. Why then is it not possible to see in the dark with the green glasses? A simple explanation is given by the Kramers-Kronig relations which state that the refractive

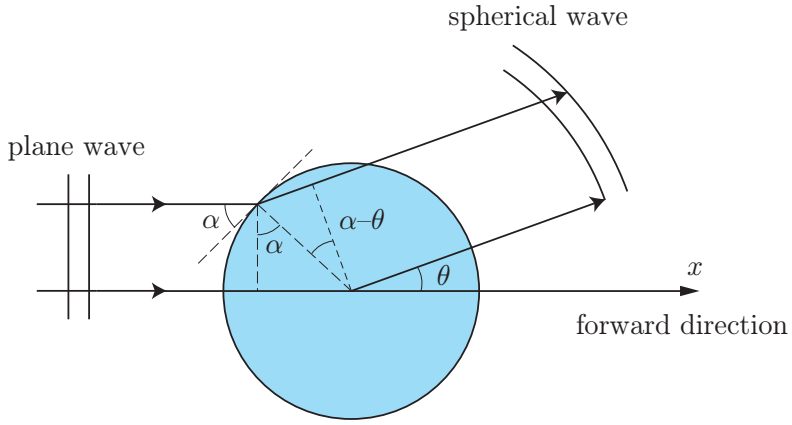

Figure 5: Geometry for non-forward scattering by a spherical symmetric target.

index must depend on ω in such a way that the transmitted waves in the green region of the spectrum obtain the right phase shifts necessary for the destructive interference at times $t \neq 0$. In fact, there is no green or any other colored glasses which simply can absorb a part of the visible spectrum without possessing refraction.

An extension of Kramers-Kronig relations to heterogeneous media is presented in Ref. 87 based on Herglotz functions similar to $\omega(\epsilon(\omega) - \epsilon_\infty)$. Kramers-Kronig relations can also be derived for acoustic waves; the homogeneous case is due to V. L. Ginzberg in Ref. 30.

3 Dispersion relations in scattering theory

Dispersion relations for scattering of acoustic and electromagnetic waves are briefly discussed in this section as an introduction to the appended papers.[23] The ideas in this section follow the expositions in Refs. 64 and 89. However, the dispersion relations in Refs. 41, 64, and 66 for partial waves are excluded from this section since new results on this topic will soon appear in a forthcoming paper. For an introduction to the theory of scattering of acoustic and electromagnetic waves, see Refs. 10, 12, 13, 16, 23, 27, 50, 59, 62, and 83.

3.1 Non-forward dispersion relations

Non-forward dispersion relations deal with physical constraints on scattering of waves by a fixed obstacle. For simplicity, consider the spherical symmetric target of radius a in Fig. 5 subject to the following plane wave excitation of either acoustic or electromagnetic origin:

$$f(\tau) = \frac{1}{2\pi} \int_{-\infty}^{\infty} F(\omega') \mathrm{e}^{-\mathrm{i}\omega'\tau/c} \, \mathrm{d}\omega', \tag{3.1}$$

[23] The results in this section expect to hold also for the larger class of hyperbolic systems including elastic waves, see Refs. 25 and 85.

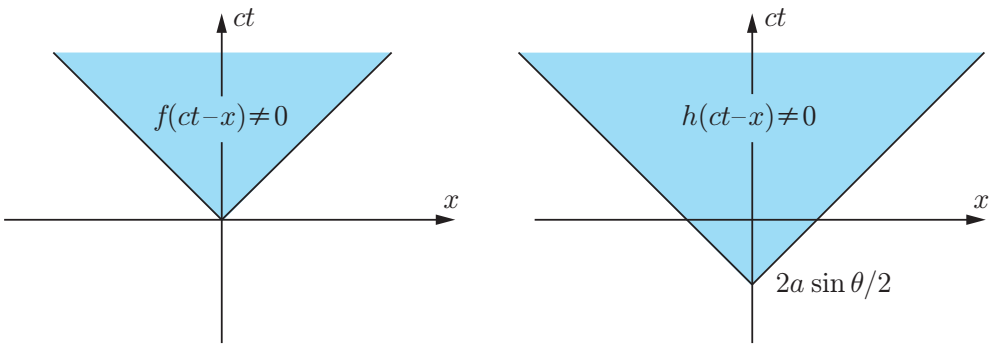

Figure 6: Light cones for the incident and scattered waves, $f(\tau)$ and $h(\tau)$, respectively, where $\tau = ct - x$.

where $\tau = ct - x$. Here, c denotes the phase velocity of the surrounding medium which is assumed to be lossless, isotropic, and homogeneous.[24] For a fixed scattering angle θ, the path difference between a wave deflected at the surface of the scatterer and a reference wave in free space propagating through the origin is, according to Fig. 5,

$$\Delta(\alpha) = a(\sin\alpha - \sin(\alpha - \theta)). \tag{3.2}$$

The maximal path difference (3.2) occurs for $\alpha = \theta/2$ (solve $\mathrm{d}\Delta(\alpha)/\mathrm{d}\alpha = 0$ to get $\alpha - \theta = \pm\alpha + 2\pi k$, where k is an integer, and invoke the constraint $0 < \alpha < \pi/2$) with

$$\max_{0<\alpha<\pi/2} \Delta(\alpha) = 2a\sin\theta/2. \tag{3.3}$$

Thus, the shortest path for the scattered wave to reach any radial distance exterior to the target is $2a\sin\theta/2$ shorter than the path through the origin of the scatterer.

Now assume that $f(\tau) = 0$ for $\tau < 0$ (implying that $F(\omega)$ is holomorphic in the upper half part of the complex ω-plane) in the sense that the incident wave front is governed by the equation $\tau = 0$, or equivalently, $ct - x = 0$. As a consequence, the scattered wave $h(\tau)$ at large distance does not reach the radial point x until $\tau > -2a\sin\theta/2$. The number $-2a\sin\theta/2$ is purely negative for $\theta \neq 0$ and illustrates the non-causal behavior of the scattered field. At any radial point x with a scattering angle $\theta \neq 0$, the scattered field $h(\tau)$ thus precedes the incident field $f(\tau)$. The time difference between the two fields is $2a/c\sin\theta/2$ which vanishes for $\theta = 0$. This observation is illustrated by the two light cone diagrams in Fig. 6.

Introduce $H(\omega)$ as the Fourier transform of $h(\tau)$ analogous to (3.1), *i.e.*,

$$H(\omega) = \int_{-\infty}^{\infty} h(\tau)\mathrm{e}^{\mathrm{i}\omega\tau}\,\mathrm{d}\tau, \tag{3.4}$$

[24]For both acoustic and electromagnetic waves, it is assumed that c exceeds the phase velocity of the scatterer if the latter is permeable; otherwise, the present analysis should be modified with the same technique as discussed for the Dirichlet boundary condition in Paper VIII. An important difference in scattering of acoustic and electromagnetic waves is that in the former case, the phase velocity of the scatterer often exceeds c, *cf.*, a metal obstacle in a fluid such as water or air at normal pressure, while in the latter case, the surrounding medium is often free space and the opposite relation holds.

where $\omega = \omega' + \mathrm{i}\omega''$ is the complex-valued generalization of the angular frequency ω'. Let $S(\omega, \theta) = x\mathrm{e}^{-\mathrm{i}\omega x/c}H(\omega)/F(\omega)$ denote the associated scattering amplitude. Since $F(\omega)$ is arbitrary and holomorphic in the upper half part of the ω-plane, it follows that also $\mathrm{e}^{2\mathrm{i}\omega a/c\sin\theta/2}S(\omega, \theta)$ is holomorphic in that region.[25] However, the function $\mathrm{e}^{2\mathrm{i}\omega a/c\sin\theta/2}S(\omega, \theta)$ does not vanish as the magnitude of ω becomes infinitely large, since many boundary conditions in wave mechanics satisfy $S(\omega', \theta) = \mathcal{O}(\omega')$ as $\omega' \to \infty$ along the real axis, see Ref. 16. Thus, $S(\omega, \theta)/\omega^2$ rather than $S(\omega, \theta)$ vanishes sufficiently rapid at infinity, and $G(\omega) = \mathrm{e}^{2\mathrm{i}\omega a/c\sin\theta/2}S(\omega, \theta)/\omega^2$ inserted into (2.47) yields[26]

$$\mathrm{Re}\left\{\mathrm{e}^{2\mathrm{i}\omega' a/c\sin\theta/2}\frac{S(\omega', \theta)}{\omega'^2}\right\} = \frac{2}{\pi}\mathcal{P}\int_0^\infty \frac{\bar{\omega}}{\bar{\omega}^2 - \omega'^2}\,\mathrm{Im}\left\{\mathrm{e}^{2\mathrm{i}\bar{\omega} a/c\sin\theta/2}\frac{S(\bar{\omega}, \theta)}{\bar{\omega}^2}\right\}\mathrm{d}\bar{\omega}. \tag{3.5}$$

The exponential factor $\mathrm{e}^{2\mathrm{i}\omega' a/c\sin\theta/2}$ corresponds to a time delay of the light cone on the right-hand side of Fig. 6. Equivalently, it corresponds to an essential singularity in the scattering amplitude $S(\omega, \theta)$ at infinite frequency. In particular, the exponential factor reduces to $\mathrm{e}^{2\mathrm{i}\omega' a/c}$ for scattering in the backward direction (*i.e.*, monostatic scattering) $\theta = \pi$. Note that (3.5) can be formulated also as a dispersion relation with two subtractions, *cf.*, the discussion in Sec. 2.9.

A drawback of (3.5) for $\theta \neq 0$ is that it depends on the choice of origin in Fig. 5, and that the real and imaginary parts of $S(\omega', \theta)$ are mixed on both sides of (3.5) due to the exponential factor

$$\mathrm{e}^{2\mathrm{i}\omega' a/c\sin\theta/2} = \cos(2\omega' a/c\sin\theta/2) + \mathrm{i}\sin(2\omega' a/c\sin\theta/2). \tag{3.6}$$

The signs of the real and imaginary parts of (3.6) are indefinite, *i.e.*, both terms in (3.6) take both positive and negative values as ω' changes. There have been attempts, however yet unsuccessful, to regard $\mathrm{e}^{2\mathrm{i}\omega a/c\sin\theta/2}S(\omega, \theta)/\omega^2$ as a function of the two variables ω and $\zeta = 2\omega\sin\theta/2$ for a fixed scattering angle $\theta \neq 0$. The exponential factor becomes constant for a fixed momentum transfer ζ, and one seeks a holomorphic continuation of this new function. The difficulties involved in such an extension are briefly discussed in Refs. 39, 64, and 89. For an overview of the theory of complex-valued functions in several variables, see Ref. 42.

Jung's theorem in Ref. 49 can be used to extend (3.5) to include scatterers of arbitrary shape instead of just spherical symmetric targets. The theorem states that the radius of the smallest sphere circumscribing a scatterer of diameter D is less than or equal to $\sqrt{6}D/4$. Equality holds if and only if the scatterer contains the vertices of a tetrahedron of edge lengths equal to D. Thus, (3.5) can be extended

[25] Note that the argument of the exponential factor $\mathrm{e}^{2\mathrm{i}\omega a/c\sin\theta/2}$ is $2\mathrm{i}\frac{\omega a}{c}\sin\frac{\theta}{2}$. This expression corresponds to the phase shift obtained when the scattered field is time delayed $2\frac{a}{c}\sin\frac{\theta}{2}$ relative to the incident field. By invoking this time delay the scattering problem becomes causal since the scattered field no longer precedes the incident field in the direction characterized by the scattering angle θ.

[26] The asymptotic behavior $S(\omega', \theta) = \mathcal{O}(\omega')$ as $\omega' \to \infty$ is motivated by the forward direction $\theta = 0$. For non-forward scattering, (3.5) can also be formulated with other weight functions than $1/\omega^2$ which vanish slower at infinity.

to include scatterers of arbitrary shape if the radius a is replaced by a_0 satisfying[27]

$$a_0 \geqslant \frac{\sqrt{6}}{4} D. \tag{3.7}$$

In particular, (3.5) subject to the static limit $\omega' \to 0+$ yields (recall that $S(0,\theta) = \lim_{\omega\to 0+} S(\omega,\theta)$ is real-valued)

$$\lim_{\omega'\to 0+} \frac{S(\omega',\theta)}{\omega'^2} = \frac{2}{\pi}\int_0^\infty \frac{1}{\bar{\omega}^3} \operatorname{Im}\left\{ \mathrm{e}^{2\mathrm{i}\bar{\omega}a_0/c\sin\theta/2} S(\bar{\omega},\theta)\right\} \mathrm{d}\bar{\omega}, \tag{3.8}$$

where it has been assumed that $S(\omega',\theta) = \mathcal{O}(\omega'^2)$ as $\omega' \to 0+$, and that $S(\omega',\theta)$ is sufficiently regular to interchange Cauchy's principal value and the static limit.[28] Thus, passivity and primitive causality implies that (3.8) holds for any a_0 that satisfies (3.7) although the left-hand side of (3.8) is independent of a_0.

3.2 Forward dispersion relations

The dispersion relation (3.5) becomes particularly useful when it is applied to the forward direction $\theta = 0$. In this case, the exponential factor $\mathrm{e}^{2\mathrm{i}\omega a/c\sin\theta/2}$ becomes unity, and (3.5) reduces to

$$\frac{S(\omega',0)}{\omega'^2} = \frac{2}{\pi}\mathcal{P}\int_0^\infty \frac{\bar{\omega}}{\bar{\omega}^2-\omega'^2}\,\frac{\operatorname{Im} S(\bar{\omega},0)}{\bar{\omega}^2}\,\mathrm{d}\bar{\omega}. \tag{3.9}$$

The forward dispersion relation (3.9) is independent of the size of the target and the choice of origin in Fig. 5. The relation is given experimental significance by invoking the optical theorem

$$\sigma_{\mathrm{ext}}(\omega) = \frac{4\pi c}{\omega}\operatorname{Im} S(\omega,0). \tag{3.10}$$

The optical theorem states that the scattering amplitude in the forward direction determines the extinction cross section $\sigma_{\mathrm{ext}}(\omega)$, *i.e.*, the combined effect of absorption and scattering in all directions. The extinction cross section is defined as the sum of the scattered and absorbed power divided by the incident power flux. The optical theorem is common to many disparate scattering phenomena such as acoustic waves, electromagnetic waves, and elementary particles, see Refs. 64 and 66. A historical survey of the optical theorem from a century ago to modern applications is given in Ref. 63.

[27] Of course, a priori knowledge of the shape of the scatterer improves the bound on a_0. For example, for a sphere it is sufficient that a_0 is greater than or equal to $D/2$, in contrast to (3.7) which gives the lower bound $0.61D$.

[28] For a non-spherical target, the appearance of $\sin\theta/2$ in the exponential factor $\mathrm{e}^{2\mathrm{i}\omega' a/c\sin\theta/2}$ should be replaced by $\sqrt{(1-\hat{\boldsymbol{k}}\cdot\hat{\boldsymbol{x}})/2}$, where $\hat{\boldsymbol{k}}$ denotes the direction of incidence and $\hat{\boldsymbol{x}}$ denotes the direction of observation. The exponential factor then takes the more general form

$$\exp\left\{2\mathrm{i}\frac{\omega' a_0}{c}\sqrt{\frac{1-\hat{\boldsymbol{k}}\cdot\hat{\boldsymbol{x}}}{2}}\right\}.$$

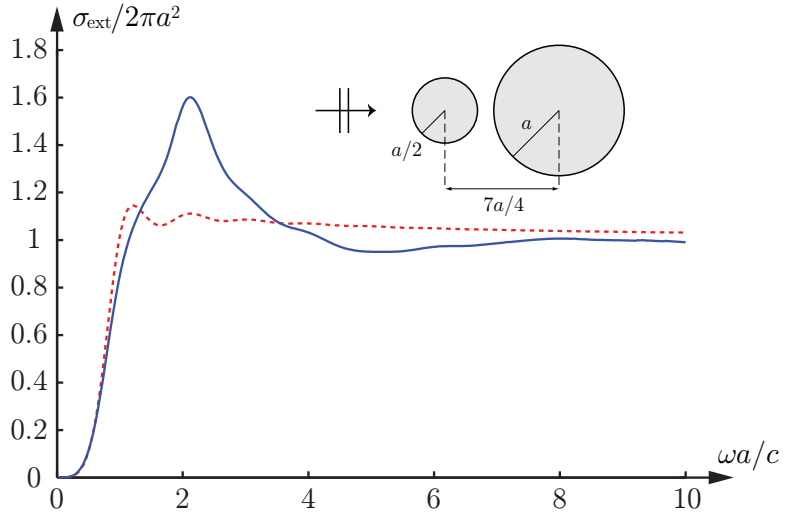

Figure 7: The extinction cross section in units of $2\pi a^2$ for scattering of electromagnetic waves by two spheres (solid curve) and a single sphere (dashed curve) in the perfectly electric conducting limit.

Two numerical examples of the extinction cross section for scattering of electromagnetic waves in free space are presented below.[29] The first geometry consists of two spheres with radii $a/2$ and a separated by a distance of $7a/4$. The extinction cross section for this geometry as a function of the scaled frequency variable $\omega a/c$ is depicted in Fig. 7. The background medium is assumed to be free space and the spheres are modeled by perfectly electric conducting material parameters. The external excitation is a plane wave impinging along the symmetry axis of the spheres and the curves in Fig. 7 are depicted in units of $2\pi a^2$, *i.e.*, twice the projected cross section area in the forward direction. The solid curve is the extinction cross section for the two spheres while the dotted curve represents a single sphere of radius a. The second geometry consists of two parallel circular disks with radii $a/2$ and a separated by a distance of $a/2$. The circular disks are modeled by perfectly electric conducting material parameters and subject to a plane wave incident along the symmetry axis of the disks. The solid curve depicts the extinction cross section for the two disks, while the dotted curve measures the corresponding quantity for a single disk of radius a. From Figs. 7 and 8 it is plausible that the extinction cross section approaches twice the projected cross section area in the forward direction, as suggested by the extinction paradox, see the discussion below.

For many boundary conditions in wave mechanics, including the transmission problems of acoustic and electromagnetic waves, $S(\omega', 0) = \mathcal{O}(\omega'^2)$ as $\omega' \to 0+$.

[29]The examples in Figs. 7 and 8 are calculated using the method of moments as described in Ref. 40.

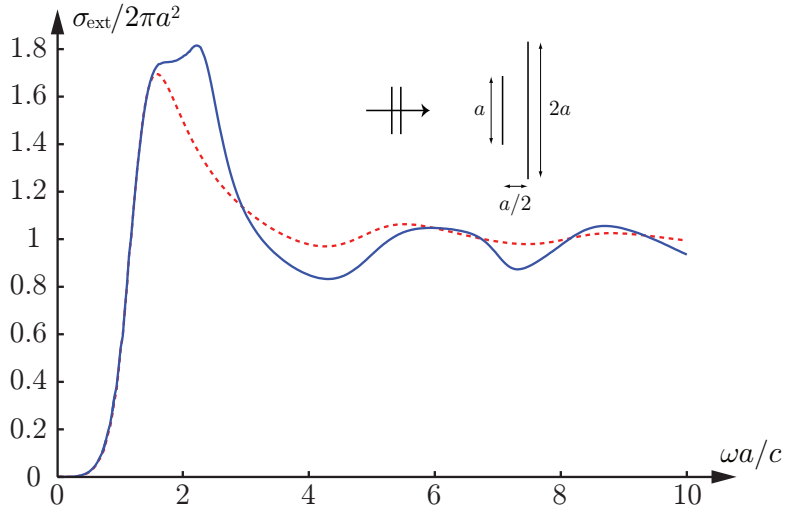

Figure 8: The extinction cross section in units of $2\pi a^2$ for scattering of electromagnetic waves by two parallel circular disks (solid curve) and a single circular disk (dashed curve) in the perfectly electric conducting limit.

Under this assumption, (3.9) implies[30]

$$\lim_{\omega' \to 0+} \frac{S(\omega', 0)}{\omega'^2} = \frac{1}{2\pi^2 c} \int_0^\infty \frac{\sigma_{\text{ext}}(\bar{\omega})}{\bar{\omega}^2} \, \mathrm{d}\bar{\omega}. \tag{3.11}$$

The forward dispersion relation (3.11) is particularly useful since the sign of the integrand is definite (recall that the extinction cross section is non-negative since it is defined as the sum of the scattered and absorbed power divided by the incident power flux). In addition, both the integrand and the left-hand side of (3.11) have experimental significance, and the important variational results of D. S. Jones in Refs. 47 and 48 can be applied to (3.11). Recall that (3.11) holds for arbitrary targets since it does not contain reference to either the shape or the composition of the scatterer. Applications of this relation to various problems in theoretical physics, involving wave interaction with matter, are presented in the appended papers. In particular, (3.11) is the starting point for the physical bounds on antennas discussed in Papers IX and X.

Scattering of acoustic (Dirichlet & Neumann) and electromagnetic (PEC) waves by an impermeable sphere of radius a is illustrated in Fig. 9. In the figure, the extinction cross section is depicted for both the perfectly electric conducting boundary condition, and the Neumann and Dirichlet problems for acoustic waves. In addition, statistics on the acoustic and electromagnetic partial wave decompositions of the integral in (3.11) are included on the right-hand side of the figure.[31] From the

[30]The extension to other weight functions than $1/\omega'^2$ for a given static limit of $S(\omega', 0)$ is addressed in Paper VI.

[31]For an introduction to partial waves in scattering by impermeable spheres, see Ref. 84. Additional results on the interpretation of (3.11) in terms of partial waves, including a set of peculiar integral relations for the spherical Bessel and Hankel functions, will be presented in a forthcom-

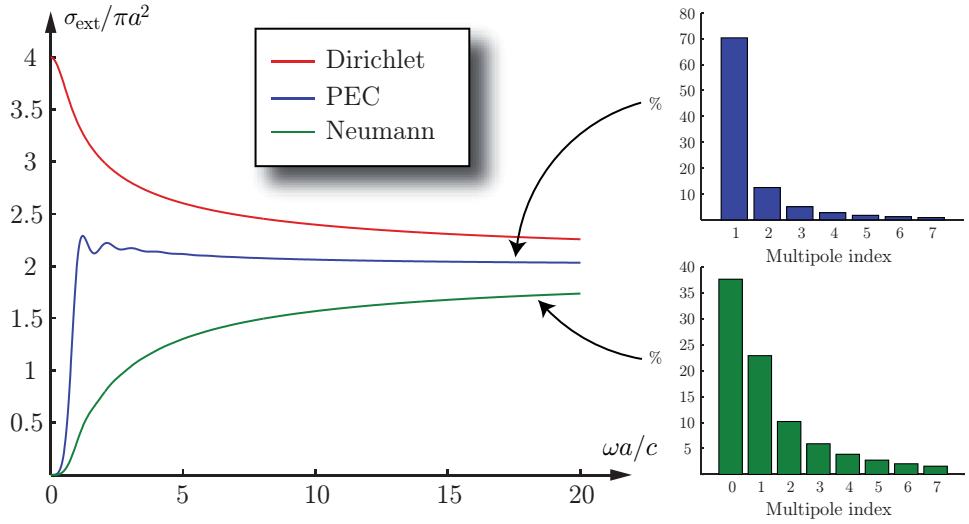

Figure 9: Partial wave decomposition of (3.11) for scattering of acoustic and electromagnetic waves by an impermeable sphere of radius a.

statistics, it is seen that the integral in (3.11) is dominated by the lowest order multipole term for both the PEC and Neumann boundary conditions. Note, however, the absence of a monopole term, *i.e.*, zeroth order rotationally symmetric multipole term, in the electromagnetic case due to a result by Brouwer in algebraic topology, that a continuous tangential vector field on the unit sphere must vanish somewhere. Popularly speaking, the theorem suggests that it is impossible to smoothly comb a hedgehog without leaving a bald spot or making a parting.

The static limit of the Dirichlet condition is the major reason why the upper curve in Fig. 9 does not satisfy (3.11), see the discussion in Paper VIII. Furthermore, integration by parts in (3.11) becomes useful when the curves in Fig. 9 a priori are known to be monotonically increasing. Then a similar identity to (3.11) with a definite sign in the integrand can be established for the derivative $\mathrm{d}\sigma_{\text{ext}}(\omega')/\,\mathrm{d}\omega'$. This technique is feasible for the Neumann problem, but obviously not for the PEC boundary condition due to its oscillatory behavior.

The fact that the extinction cross sections in Figs. 7, 8, and 9 approach twice the projected cross section area in the forward direction is known as the extinction paradox. From geometrical optics, one naively expects, that at short wavelengths a particle will remove as much energy as is incident upon it. However, in this limit, geometrical optics is not applicable, since the particle always will have edges in the

ing paper. For example, any passive and causal function $\epsilon = \epsilon(\kappa)$ satisfying the Kramers-Kronig relations (2.69) and (2.70) also obeys the integral identity

$$\mathrm{Re}\int_0^\infty \sum_{l=1}^\infty (2l+1)\frac{\mathrm{j}_l(\kappa)(\kappa\epsilon^{1/2}\mathrm{j}_l(\kappa\epsilon^{1/2}))' - \epsilon(\kappa\mathrm{j}_l(\kappa))'\mathrm{j}_l(\kappa\epsilon^{1/2})}{\mathrm{h}_l(\kappa)(\kappa\epsilon^{1/2}\mathrm{j}_l(\kappa\epsilon^{1/2}))' - \epsilon(\kappa\mathrm{h}_l(\kappa))'\mathrm{j}_l(\kappa\epsilon^{1/2})}\frac{\mathrm{d}\kappa}{\kappa^4} = \pi\lim_{\kappa\to 0+}\frac{\epsilon-1}{\epsilon+2}, \tag{3.12}$$

where j_l and h_l denote the spherical Bessel and Hankel functions of the first kind, respectively. Here, $(\kappa\mathrm{f}_l(\kappa))' = \kappa\mathrm{f}_l'(\kappa) + \mathrm{f}_l(\kappa)$ for complex-valued κ with $\mathrm{f}_l'(\kappa) = l\mathrm{f}_l(\kappa)/\kappa - \mathrm{f}_{l+1}(\kappa)$, where f_l denotes any of j_l and h_l. Similar integral identities can be derived for scattering of acoustic waves.

neighborhood of where geometrical optics fails to be valid. The paradoxical character of the short wavelength limit is, *e.g.*, relieved by recalling that the observation is made at great distance far beyond where a shadow can be distinguished. For a discussion of the extinction paradox in terms of physical optics, see Refs. 13 and 83. A more general discussion using the partial wave expansion is given in Ref. 69. The corresponding paradox in the scattering theory of the Schrödinger equation is discussed in Ref. 91. Finally, a time-domain approach to the extinction paradox for scattering of electromagnetic waves is presented in Paper VII.

References

[1] L. V. Ahlfors. *Complex Analysis*. McGraw-Hill, New York, second edition, 1966.

[2] N. I. Akhiezer. *The Classical Moment Problem and Some Related Questions in Analysis*. Oliver and Boyd, Edinburgh, 1965.

[3] N. I. Akhiezer and M. Krein. *Some Questions in the Theory of Moments*. John Wiley & Sons, New York, 1959.

[4] M. Altarelli, D. L. Dexter, and H. M. Nussenzveig. Superconvergence and sum rules for the optical constants. *Phys. Rev. B*, **6**(12), 4502–4509, 1972.

[5] M. Altarelli and D. Y. Smith. Superconvergence and sum rules for the optical constants: Physical meaning, comparison with experiment, and generalization. *Phys. Rev. B*, **9**(4), 1290–1298, 1974.

[6] T. M. Apostol. *Mathematical Analysis: A Modern Approach to Advanced Calculus*. Addison-Wesley, Reading, 1960.

[7] G. B. Arfken and H. J. Weber. *Mathematical Methods for Physicists*. Academic Press, New York, fifth edition, 2001.

[8] J. Avelin. *Polarizability Analysis of Canonical Dielectric and Bi-anisotropic Scatterers*. Doctoral thesis, Helsinki University of Technology, Department of Electrical and Communications Engineering, P.O. Box 3000, FI-02015 TKK, Finland, 2003.

[9] N. Balabanian and T. A. Bickart. *Electrical Network Theory*. John Wiley & Sons, New York, 1969.

[10] P. W. Barber and S. C. Hill. *Light Scattering by Particles: Computational Methods*. World Scientific Publisher, Singapore, 1990.

[11] C. M. Bender and S. A. Orszag. *Advanced Mathematical Methods for Scientists and Engineers*. McGraw-Hill, New York, 1978.

[12] B. J. Berne and R. Pecora. *Dynamic Light Scattering: With Applications to Chemistry, Biology, and Physics*. John Wiley & Sons, New York, 1976.

[13] C. F. Bohren and D. R. Huffman. *Absorption and Scattering of Light by Small Particles*. John Wiley & Sons, New York, 1983.

[14] M. Born. *Natural Philosophy of Cause and Chance*. Dover Publications, New York, 1965.

[15] M. Born and E. Wolf. *Principles of Optics*. Cambridge University Press, Cambridge, U.K., seventh edition, 1999.

[16] J. J. Bowman, T. B. A. Senior, and P. L. E. Uslenghi. *Electromagnetic and Acoustic Scattering by Simple Shapes*. North-Holland, Amsterdam, 1969.

[17] H. J. Carlin and P. P. Civalleri. *Wideband Circuit Design*. CRC Press, Boca Raton, 1998.

[18] D. K. Cheng. *Analysis of Linear Systems*. Addison-Wesley, Reading, 1959.

[19] J. B. Conway. *Functions of One Complex Variable*. Springer-Verlag, New York, 1973.

[20] G. Dassios and R. Kleinman. *Low Frequency Scattering*. Oxford University Press, Oxford, 2000.

[21] R. de L. Kronig. On the theory of dispersion of X-rays. *J. Opt. Soc. Am.*, **12**(6), 547–557, 1926.

[22] P. A. M. Dirac. Classical theory of radiating electrons. *Proc. R. Soc. A*, **167**, 148–169, 1938.

[23] A. Doicu, T. Wriedt, and Y. A. Eremin. *Light Scattering by Systems of Particles. Null-field Method with Discrete Sources: Theory and Programs*. Springer-Verlag, Berlin, 2006.

[24] P. L. Duren. *Theory of H^p Spaces*. Dover Publications, New York, 2000.

[25] L. C. Evans. *Partial Differential Equations*. American Mathematical Society, Providence, Rhode Island, 1998.

[26] R. M. Fano. Theoretical limitations on the broadband matching of arbitrary impedances. *Journal of the Franklin Institute*, **249**(1,2), 57–83 and 139–154, 1950.

[27] L. B. Felsen and N. Marcuvitz. *Radiation and Scattering of Waves*. IEEE Press, Piscataway, 1994.

[28] F. G. Friedlander and M. Joshi. *Introduction to the Theory of Distributions*. Cambridge University Press, Cambridge, second edition, 1998.

[29] J. B. Garnett. *Bounded Analytic Functions*. Springer-Verlag, New York, revised first edition, 2007.

[30] V. L. Ginzberg. Concerning the general relationship between absorption and dispersion of sound waves. *Sov. Phys. Acoust.*, **1**, 32–41, 1955.

[31] M. L. Goldberger and K. M. Watson. *Collision Theory*. Dover Publications, New York, 2004.

[32] H. Goldstein, C. Poole, and J. Safko. *Classical Mechanics*. Addison-Wesley, Reading, third edition, 2002.

[33] R. E. Greene and S. G. Krantz. *Function Theory of One Complex Variable*. American Mathematical Society, Providence, Rhode Island, third edition, 2006.

[34] D. J. Griffiths. *Introduction to Electrodynamics*. Prentice-Hall, Inc., Englewood Cliffs, New Jersey, third edition, 1999.

[35] E. A. Guillemin. *The Mathematics of Circuit Analysis*. John Wiley & Sons, New York, 1959.

[36] E. A. Guillemin. *Theory of Linear Physical Systems*. John Wiley & Sons, New York, 1963.

[37] M. Gustafsson. *Wave Splitting in Direct and Inverse Scattering Problems*. Doctoral thesis, Lund University, Department of Electrical and Information Technology, P.O. Box 118, S-221 00 Lund, Sweden, 2000.

[38] M. Gustafsson. On the non-uniqueness of the electromagnetic instantaneous response. *J. Phys. A: Math. Gen.*, **36**, 1743–1758, 2003.

[39] R. Hagedorn. *Introduction to Field Theory and Dispersion Relations*. Pergamon Press, Oxford, 1964.

[40] R. F. Harrington. *Field Computation by Moment Methods*. Macmillan, New York, 1968.

[41] J. Hilgevoord. *Dispersion Relations and Causal Description: An Introduction to Dispersion Relations in Field Theory*. North-Holland, Amsterdam, 1960.

[42] L. Hörmander. *An Introduction to Complex Analysis in Several Variables*. North-Holland, Amsterdam, 1973.

[43] L. Hörmander. *The Analysis of Linear Partial Differential Operators I*. Grundlehren der mathematischen Wissenschaften 256. Springer-Verlag, Berlin, second edition, 1990.

[44] J. D. Jackson. Introduction to dispersion relation techniques. In G. R. Screaton, editor, *Dispersion Relations*, chapter 1, pages 1–63. Interscience Publishers, New York, 1960.

[45] J. D. Jackson. *Classical Electrodynamics*. John Wiley & Sons, New York, third edition, 1999.

[46] D. S. Jones. *The Theory of Electromagnetism*. Pergamon, New York, 1964.

[47] D. S. Jones. Low frequency electromagnetic radiation. *J. Inst. Maths. Applics.*, **23**(4), 421–447, 1979.

[48] D. S. Jones. Scattering by inhomogeneous dielectric particles. *Quart. J. Mech. Appl. Math.*, **38**, 135–155, 1985.

[49] H. W. E. Jung. Über die kleinste Kugel, die eine räumliche Figur einschliesst. *Journal für die reine und angewandte Mathematik*, **123**, 241–257, 1901.

[50] M. Kerker. *The Scattering of Light and Other Electromagnetic Radiation*. Academic Press, New York, 1969.

[51] R. E. Kleinman and T. B. A. Senior. Rayleigh scattering. In V. V. Varadan and V. K. Varadan, editors, *Low and High Frequency Asymptotics*, volume 2 of *Handbook on Acoustic, Electromagnetic and Elastic Wave Scattering*, chapter 1, pages 1–70. Elsevier Science Publishers, Amsterdam, 1986.

[52] E. F. Knott, J. F. Shaeffer, and M. T. Tuley. *Radar Cross Section*. SciTech Publishing Inc., 5601 N. Hawthorne Way, Raleigh, NC 27613, 2004.

[53] H. König and J. Meixner. Lineare Systeme und lineare Transformationen. *Math. Nachr.*, **19**, 265–322, 1958.

[54] M. H. A. Kramers. La diffusion de la lumière par les atomes. *Atti. Congr. Int. Fis. Como*, **2**, 545–557, 1927.

[55] G. Kristensson. Condon's model on optical rotatory power and causality — a scientific trifle. Technical Report LUTEDX/(TEAT-7080)/1–23/(1999), Lund University, Department of Electrical and Information Technology, P.O. Box 118, S-221 00 Lund, Sweden, 1999.

[56] L. D. Landau and E. M. Lifshitz. *Statistical Physics, Part 1*. Butterworth-Heinemann, Linacre House, Jordan Hill, Oxford, third edition, 1980.

[57] L. D. Landau, E. M. Lifshitz, and L. P. Pitaevskiĭ. *Electrodynamics of Continuous Media*. Pergamon Press, Oxford, second edition, 1984.

[58] V. Lucarini, J. J. Saarinen, K.-E. Peiponen, and E. M. Vartiainen. *Kramers-Kronig Relations in Optical Materials Research*. Springer-Verlag, Berlin, 2005.

[59] P. A. Martin. *Multiple Scattering: Interaction of Time-Harmonic Waves with N Obstacles*, volume 107 of *Encyclopedia of Mathematics and its Applications*. Cambridge University Press, Cambridge, U.K., 2006.

[60] J. Meixner. Thermodynamische Erweiterung der Nachwirkungstheorie. *Zeitschrift für Physik A: Hadrons and Nuclei*, **139**(1), 30–43, 1954.

[61] P. M. Morse and H. Feshbach. *Methods of Theoretical Physics*, volume 1 and 2. McGraw-Hill, New York, 1953.

[62] P. M. Morse and K. U. Ingard. *Theoretical Acoustics*. McGraw-Hill, New York, 1968.

[63] R. G. Newton. Optical theorem and beyond. *Am. J. Phys*, **44**, 639–642, 1976.

[64] R. G. Newton. *Scattering Theory of Waves and Particles*. Dover Publications, New York, second edition, 2002.

[65] K. Nishijima. *Fields and Particles: Field Theory and Dispersion Relations*. W. A. Benjamin, Inc., New York, 1969.

[66] H. M. Nussenzveig. *Causality and Dispersion Relations*. Academic Press, London, 1972.

[67] W. K. H. Panofsky and M. Phillips. *Classical Electricity and Magnetism*. Addison-Wesley, Reading, second edition, 1962.

[68] A. Papoulis. *The Fourier Integral and its Applications*. McGraw-Hill, New York, 1962.

[69] R. Peierls. *Surprises in Theoretical Physics*. Princeton University Press, Princeton, 1979.

[70] J. W. S. Rayleigh. *The Theory of Sound*, volume 1 and 2. Dover Publications, New York, second edition, 1945.

[71] F. Rohrlich. *Classical Charged Particles: Foundations of Their Theory*. Addison-Wesley, Reading, 1965.

[72] P. Roman. *Advanced Quantum Theory: An Outline of the Fundamental Ideas*. Addison-Wesley, Reading, 1965.

[73] J. J. Sakurai. *Advanced Quantum Mechanics*. Addison-Wesley, Reading, 1967.

[74] J. A. Shohat and J. D. Tamarkin. *The Problem of Moments*. American Mathematical Society, New York, 1943.

[75] C. Sohl. *Dispersion Relations for Extinction of Acoustic and Electromagnetic Waves*. Licentiate thesis, Lund University, Department of Electrical and Information Technology, P.O. Box 118, S-221 00 Lund, Sweden, 2007.

[76] I. Stakgold. *Green's Functions and Boundary Value Problems*. John Wiley & Sons, New York, 1979.

[77] J. A. Stratton. *Electromagnetic Theory*. McGraw-Hill, New York, 1941.

[78] C.-T. Tai. *Dyadic Green's Functions in Electromagnetic Theory*. Intext Educational Publishers, Scranton, 1971.

[79] J. R. Taylor. *Scattering Theory: The Quantum Theory of Nonrelativistic Collisions*. Robert E. Krieger Publishing Company, Malabar, 1983.

[80] E. C. Titchmarsh. *Introduction to the Theory of Fourier Integrals*. Oxford University Press, Oxford, second edition, 1948.

[81] J. S. Toll. Causality and the dispersion relation: Logical foundations. *Phys. Rev.*, **104**(6), 1760–1770, 1956.

[82] J. G. van Bladel. *Electromagnetic Fields*. IEEE Press, New York, 2007.

[83] H. van de Hulst. *Light Scattering by Small Particles*. John Wiley & Sons, Inc., New York, 1957.

[84] V. V. Varadan, Y. Ma, V. K. Varadan, and A. Lakhtakia. Scattering of waves by spheres and cylinders. In V. V. Varadan, A. Lakhtakia, and V. K. Varadan, editors, *Field Representations and Introduction to Scattering*, volume 1 of *Handbook on Acoustic, Electromagnetic and Elastic Wave Scattering*, chapter 4, pages 211–324. Elsevier Science Publishers, Amsterdam, 1991.

[85] V. V. Varadan and V. K. Varadan. Acoustic, electromagnetic and elastodynamics fields. In V. V. Varadan, A. Lakhtakia, and V. K. Varadan, editors, *Field Representations and Introduction to Scattering*, Acoustic, Electromagnetic and Elastic Wave Scattering, chapter 1, pages 1–35. Elsevier Science Publishers, Amsterdam, 1991.

[86] H. S. Wall. *Analytic Theory of Continued Fractions*. D. Van Nostrand Company, New York, 1948.

[87] R. L. Weaver and Y.-H. Pao. Dispersion relations for linear wave propagation in homogeneous and inhomogeneous media. *J. Math. Phys.*, **22**(9), 1909–1918, 1981.

[88] H. Weyl. *Philosophy of Mathematics and Natural Science*. Princeton University Press, Princeton, 1949.

[89] D. Y. Wong. Dispersion relations and applications. In E. P. Wigner, editor, *Dispersion Relations and their Connection with Causality*, chapter 4, pages 68–96. Academic Press, New York, 1964. Proceedings of the International School of Physics "Enrico Fermi", Course XXIX, held at Verenna on Lake Como, Villa Monastero, July 15–August 3, 1963.

[90] L. A. Zadeh and C. A. Desoer. *Linear System Theory: The State Space Approach*. McGraw-Hill, New York, 1963.

[91] W. Żakowicz. On the extinction paradox. *Acta Physica Polonica A*, **101**(3), 369–385, 2002.

Physical limitations on broadband scattering by heterogeneous obstacles

Paper I

Christian Sohl, Mats Gustafsson, and Gerhard Kristensson

Based on: Physical limitations on broadband scattering by heterogeneous obstacles. *Journal of Physics A: Mathematical and Theoretical*, vol. 40, no. 36, pp. 11165–11182, September 2007.

Abstract

In this paper, new physical limitations on the extinction cross section and broadband scattering are investigated. A measure of broadband scattering in terms of the integrated extinction is derived for a large class of scatterers based on the holomorphic properties of the forward scattering dyadic. Closed-form expressions of the integrated extinction are given for the homogeneous ellipsoids and theoretical bounds are discussed for arbitrary heterogeneous scatterers. Finally, the theoretical results are illustrated by numerical computations for a series of generic scatterers.

1 Introduction

The relation between the extinction cross section and the forward scattering dyadic, nowadays known as the optical theorem, dates back to the work of Rayleigh more than a century ago [28]. Since then, the concept has fruitfully been extended to high-energy physics where it today plays an essential role in analyzing particle collisions [20]. This is one striking example of how results, with minor modifications, can be used in both electromagnetic and quantum mechanic scattering theory. Another example of such an analogy is presented in this paper, and it is believed that more analogies of this kind exist, see *e.g.*, the excellent books by Taylor [29] and Nussenzveig [22].

As far as the authors know, a broadband measure for scattering of electromagnetic waves was first introduced by Purcell [24] in 1969 concerning absorption and emission of radiation by interstellar dust. Purcell derived the integrated extinction for a very narrow class of scatterers via the Kramers-Kronig relations [17, pp. 279–283]. A slightly different derivation of the same result was done by Bohren and Huffman [4, pp. 116–117]. In both references it was noticed that the integrated extinction is proportional to the volume of the scatterer, with proportionality factor depending only on the shape and the long wavelength limit response of the scatterer. Based upon this observation, Bohren and Huffman conjecture [4, p. 117]:

> *Regardless of the shape of the particle, however, it is plausible on physical grounds that integrated extinction should be proportional to the volume of an arbitrary particle, where the proportionality factor depends on its shape and static dielectric function.*

Curiosity whether this supposition is true and the generalization of the results to a wider class of scatterers have been the main driving forces of the present study.

Physical limitations on scattering of electromagnetic waves play an important role in the understanding of wave interaction with matter. Specifically, numerous papers addressing physical limitations in antenna theory are found in the literature. Unfortunately, they are almost all restricted to the spherical geometry, deviating only slightly from the pioneering work of Chu [5] in 1948. In contrast to antenna theory, there are, however, few papers addressing physical limitations in scattering by electromagnetic waves. An invaluable exception is given by the fundamental work

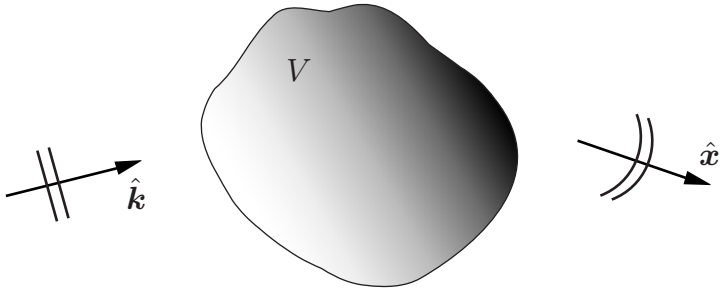

Figure 1: Illustration of the scattering problem. The scatterer V is subject to a plane wave incident in the $\hat{\boldsymbol{k}}$-direction.

of Nussenzveig [21] in which both scattering by waves and particles are analyzed in terms of causality. Other exceptions of importance for the present paper are the Rayleigh scattering bounds derived by Jones [10, 11].

The results of Purcell mentioned above are generalized in several ways in this paper. The integrated extinction is proved to be valid for anisotropic heterogeneous scatterers of arbitrary shape. Specifically, this quantity is analyzed in detail for the ellipsoidal geometry. Several kinds of upper and lower bounds on broadband scattering for isotropic material models are presented. These limitations give a means of determining if an extinction cross section is realizable or not.

The paper is organized as follows: in Sec. 2, the integrated extinction is derived for a large class of scatterers based on the holomorphic properties of the forward scattering dyadic. Next, in Sec. 3, bounds on broadband scattering are discussed for arbitrary isotropic heterogeneous scatterers. In the following section, Sec. 4, some closed-form expressions of the integrated extinction are given. Moreover, in Sec. 5, numerical results on the extinction cross section are presented and compared with the theoretical bounds. Finally, some future work and possible applications are discussed in Sec. 6.

Throughout this paper, vectors are denoted in italic bold face, and dyadics in roman bold face. A hat (ˆ) on a vector denotes that the vector is of unit length.

2 Broadband scattering

The scattering problem considered in this paper is Fourier-synthesized plane wave scattering by a bounded heterogeneous obstacle of arbitrary shape, see Fig. 1. The scatterer is modeled by anisotropic constitutive relations [17, Ch. XI] and assumed to be surrounded by free space. The analysis presented in this paper includes the perfectly electric conducting material model, as well as general temporal dispersion with or without a conductivity term.

2.1 The forward scattering dyadic

The scattering properties of V are described by the far field amplitude, $\boldsymbol{F}$, defined in terms of the scattered field, $\boldsymbol{E}_\mathrm{s}$, as [15, Sec. 2]

$$\boldsymbol{E}_\mathrm{s}(t,\boldsymbol{x}) = \frac{\boldsymbol{F}(\mathrm{c}_0 t - x, \hat{\boldsymbol{x}})}{x} + \mathcal{O}(x^{-2}) \quad \text{as } x \to\to \infty, \tag{2.1}$$

where c_0 is the speed of light in vacuum, and $\hat{\boldsymbol{x}} = \boldsymbol{x}/x$ with $x = |\boldsymbol{x}|$. The far field amplitude is related to the incident field, $\boldsymbol{E}_\mathrm{i}(\mathrm{c}_0 t - \hat{\boldsymbol{k}} \cdot \boldsymbol{x})$, which is impinging in the $\hat{\boldsymbol{k}}$-direction, via the linear and time-translational invariant convolution

$$\boldsymbol{F}(\tau, \hat{\boldsymbol{x}}) = \int_{-\infty}^{\infty} \mathbf{S}_\mathrm{t}(\tau - \tau', \hat{\boldsymbol{k}}, \hat{\boldsymbol{x}}) \cdot \boldsymbol{E}_\mathrm{i}(\tau') \, \mathrm{d}\tau'. \tag{2.2}$$

The dimensionless temporal scattering dyadic $\mathbf{S}_\mathrm{t}$ is assumed to be causal in the forward direction, $\hat{\boldsymbol{k}}$, in the sense that the scattered field cannot precede the incident field [21, pp. 15–16], *i.e.*,

$$\mathbf{S}_\mathrm{t}(\tau, \hat{\boldsymbol{k}}, \hat{\boldsymbol{k}}) = \mathbf{0} \quad \text{for } \tau < 0. \tag{2.3}$$

The Fourier transform of (2.1) evaluated in the forward direction is

$$\boldsymbol{E}_\mathrm{s}(k, x\hat{\boldsymbol{k}}) = \frac{\mathrm{e}^{\mathrm{i}kx}}{x} \mathbf{S}(k, \hat{\boldsymbol{k}}) \cdot \boldsymbol{E}_0 + \mathcal{O}(x^{-2}) \quad \text{as } x \to \infty, \tag{2.4}$$

where k is a complex variable in the upper half plane with $\operatorname{Re} k = \omega/\mathrm{c}_0$. Here, the amplitude of the incident field is $\boldsymbol{E}_0$, and the forward scattering dyadic, $\mathbf{S}$, is given by the Fourier representation

$$\mathbf{S}(k, \hat{\boldsymbol{k}}) = \int_{0^-}^{\infty} \mathbf{S}_\mathrm{t}(\tau, \hat{\boldsymbol{k}}, \hat{\boldsymbol{k}}) \mathrm{e}^{\mathrm{i}k\tau} \, \mathrm{d}\tau. \tag{2.5}$$

The imaginary part of k improves the convergence of (2.5) and extends the elements of $\mathbf{S}$ to holomorphic functions in the upper half plane for a large class of dyadics $\mathbf{S}_\mathrm{t}$. Recall that $\mathbf{S}(\mathrm{i}k, \hat{\boldsymbol{k}})$ is real-valued for real-valued k and $\mathbf{S}(\mathrm{i}k, \hat{\boldsymbol{k}}) = \mathbf{S}^*(-\mathrm{i}k^*, \hat{\boldsymbol{k}})$ [21, Sec. 1.3–1.4].

The scattering cross section σ_s and absorption cross section σ_a are defined as the ratio of the scattered and absorbed power, respectively, to the incident power flow density in the forward direction. The sum of the scattering and absorption cross sections is the extinction cross section,

$$\sigma_\mathrm{ext} = \sigma_\mathrm{s} + \sigma_\mathrm{a}. \tag{2.6}$$

The three cross sections are by definition real-valued and non-negative. The extinction cross section is related to the forward scattering dyadic, $\mathbf{S}$, via the optical theorem [20, pp. 18–20]

$$\sigma_\mathrm{ext}(k) = \frac{4\pi}{k} \operatorname{Im}\left\{ \hat{\boldsymbol{p}}_\mathrm{e}^* \cdot \mathbf{S}(k, \hat{\boldsymbol{k}}) \cdot \hat{\boldsymbol{p}}_\mathrm{e} \right\}. \tag{2.7}$$

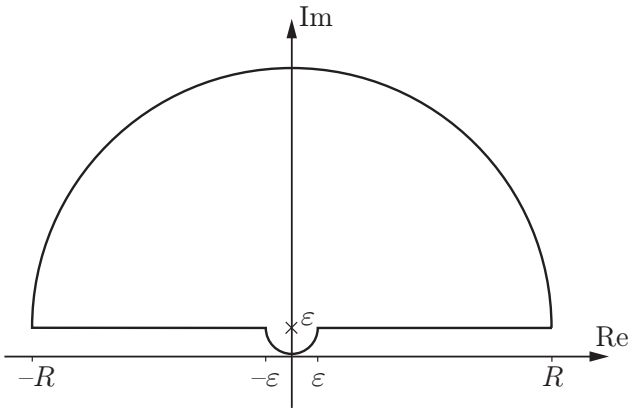

Figure 2: Integration contour used in the Cauchy integral theorem in (2.8).

Here, k is real-valued, and $\hat{\boldsymbol{p}}_{\mathrm{e}} = \boldsymbol{E}_0/|\boldsymbol{E}_0|$ is a complex-valued vector, independent of k, that represents the electric polarization, and, moreover, satisfies $\hat{\boldsymbol{p}}_{\mathrm{e}} \cdot \hat{\boldsymbol{k}} = 0$.

The holomorphic properties of $\mathbf{S}$ can be used to determine an integral identity for the extinction cross section. To simplify the notation, let $\varrho(k) = \hat{\boldsymbol{p}}_{\mathrm{e}}^* \cdot \mathbf{S}(k, \hat{\boldsymbol{k}}) \cdot \hat{\boldsymbol{p}}_{\mathrm{e}}/k^2$. The Cauchy integral theorem with respect to the contour in Fig. 2 then yields

$$\varrho(\mathrm{i}\varepsilon) = \int_0^\pi \frac{\varrho(\mathrm{i}\varepsilon - \varepsilon \mathrm{e}^{\mathrm{i}\phi})}{2\pi}\, \mathrm{d}\phi + \int_0^\pi \frac{\varrho(\mathrm{i}\varepsilon + R\mathrm{e}^{\mathrm{i}\phi})}{2\pi}\, \mathrm{d}\phi + \int_{\varepsilon<|k|<R} \frac{\varrho(k+\mathrm{i}\varepsilon)}{2\pi \mathrm{i} k}\, \mathrm{d}k, \quad (2.8)$$

where k in the last integral on the right hand side is real-valued.

The left hand side of (2.8) and the integrand in the first integral on the right hand side are well-defined in the limit $\varepsilon \to 0$ and given by the long wavelength limit [15, p. 18]

$$\varrho(\mathrm{i}\varepsilon) = \frac{1}{4\pi} (\hat{\boldsymbol{p}}_{\mathrm{e}}^* \cdot \boldsymbol{\gamma}_{\mathrm{e}} \cdot \hat{\boldsymbol{p}}_{\mathrm{e}} + \hat{\boldsymbol{p}}_{\mathrm{m}}^* \cdot \boldsymbol{\gamma}_{\mathrm{m}} \cdot \hat{\boldsymbol{p}}_{\mathrm{m}}) + \mathcal{O}(\varepsilon) \quad \text{as } \varepsilon \to\!\to 0. \quad (2.9)$$

Here, $\hat{\boldsymbol{p}}_{\mathrm{m}} = \hat{\boldsymbol{k}} \times \hat{\boldsymbol{p}}_{\mathrm{e}}$ denotes the magnetic polarization and $\boldsymbol{\gamma}_{\mathrm{e}}$ and $\boldsymbol{\gamma}_{\mathrm{m}}$ are the electric and magnetic polarizability dyadics, respectively, see App. A for their explicit definitions. These dyadics are real-valued and symmetric. This result also includes the effect of a conductivity term [15, pp. 49–51].

The second term on the right hand side of (2.8) is assumed to approach zero and does not contribute in the limit $R \to \infty$. This is physically reasonable since the short wavelength response of a material is non-unique from a modeling point of view [8]. The assumption is also motivated by the extinction paradox [31, pp. 107–113], *i.e.*,

$$\varrho(k) = -\frac{A(\hat{\boldsymbol{k}})}{2\pi \mathrm{i} k} \left(1 + \mathcal{O}(|k|^{-1})\right) \quad \text{as } |k| \to \infty, \qquad \operatorname{Im} k \geqslant 0, \quad (2.10)$$

where A denotes the projected area in the forward direction.

In the last term on the right hand side of (2.8) it is assumed that ϱ is sufficiently regular to extend the contour to the real axis. Under this assumption, the real part

of (2.8) yields

$$\varrho(0) = \frac{1}{\pi}\int_{-\infty}^{\infty} \frac{\operatorname{Im}\varrho(k)}{k}\,\mathrm{d}k = \frac{1}{4\pi^2}\int_{-\infty}^{\infty} \frac{\sigma_{\mathrm{ext}}(k)}{k^2}\,\mathrm{d}k = \frac{1}{4\pi^3}\int_0^{\infty} \sigma_{\mathrm{ext}}(\lambda)\,\mathrm{d}\lambda, \qquad (2.11)$$

where we have used the optical theorem, (2.7). In this expression $\lambda = 2\pi/k$ is the vacuum wavelength.

In fact, the assumptions on ϱ can be relaxed, and the analysis can be generalized to certain classes of distributions [21, pp. 33–43]. However, the integral in (2.11) is classically well-defined for the examples considered in this paper. The relation (2.11) can also be derived using the Hilbert transform [30, Ch. V].

2.2 The integrated extinction

We are now ready to utilize the main result in the previous section. Moreover, the properties of the polarizability dyadics are exploited and different material models are discussed.

Insertion of the long wavelength limit (2.9) into (2.11) yields the integrated extinction

$$\int_0^{\infty} \sigma_{\mathrm{ext}}(\lambda)\,\mathrm{d}\lambda = \pi^2\left(\hat{\boldsymbol{p}}_{\mathrm{e}}^{*}\cdot\boldsymbol{\gamma}_{\mathrm{e}}\cdot\hat{\boldsymbol{p}}_{\mathrm{e}} + \hat{\boldsymbol{p}}_{\mathrm{m}}^{*}\cdot\boldsymbol{\gamma}_{\mathrm{m}}\cdot\hat{\boldsymbol{p}}_{\mathrm{m}}\right). \qquad (2.12)$$

Note that (2.12) is independent of any temporal dispersion, depending only on the long wavelength limit response of the scatterer in terms of $\boldsymbol{\gamma}_{\mathrm{e}}$ and $\boldsymbol{\gamma}_{\mathrm{m}}$. Closed-form expressions of $\boldsymbol{\gamma}_{\mathrm{e}}$ and $\boldsymbol{\gamma}_{\mathrm{m}}$ exist for the homogeneous ellipsoids, see Sec. 4. The polarizability dyadics for more general obstacles are summarized in Kleinman & Senior [15, p. 31].

For pure electric ($\boldsymbol{\gamma}_{\mathrm{m}} = \mathbf{0}$) and pure magnetic ($\boldsymbol{\gamma}_{\mathrm{e}} = \mathbf{0}$) scatterers, the integrated extinction depends only on $\hat{\boldsymbol{p}}_{\mathrm{e}}$ and $\hat{\boldsymbol{p}}_{\mathrm{m}}$, respectively, and hence not on $\hat{\boldsymbol{k}} = \hat{\boldsymbol{p}}_{\mathrm{e}} \times \hat{\boldsymbol{p}}_{\mathrm{m}}$. Moreover, the integrated extinction for a scatterer with isotropic polarizability dyadics, *i.e.*, $\boldsymbol{\gamma}_{\mathrm{e}} = \gamma_{\mathrm{e}}\mathbf{I}$ and $\boldsymbol{\gamma}_{\mathrm{m}} = \gamma_{\mathrm{m}}\mathbf{I}$, is independent of $\hat{\boldsymbol{p}}_{\mathrm{e}}$ and $\hat{\boldsymbol{p}}_{\mathrm{m}}$ as well as $\hat{\boldsymbol{k}}$.

An important model in many applications is the perfectly conducting case (PEC), which is formally obtained in the long wavelength limit by the limits [15, pp. 39–40]

$$\chi_{\mathrm{e}}(\boldsymbol{x}) \to \infty \quad \text{and} \quad \chi_{\mathrm{m}}(\boldsymbol{x}) \searrow -1. \qquad (2.13)$$

Since the long wavelength limit lacks a natural length scale it follows that the integrated extinction for any heterogeneous scatterer is proportional to the volume $|V| = \int_V \mathrm{d}v$, where $\mathrm{d}v$ is the volume measure with respect to $\boldsymbol{x}$ — a result conjectured by Bohren and Huffman [4, p. 117] for spherical scatterers. A brief derivation of this statement for anisotropic, heterogeneous material parameters is presented in App. A.

Randomly oriented scatterers are valuable in many applications [24]. The broadband scattering properties of an ensemble of randomly oriented scatterers is quantified by the averaged integrated extinction,

$$\int_0^{\infty} \bar{\sigma}_{\mathrm{ext}}(\lambda)\,\mathrm{d}\lambda = \frac{\pi^2}{3}\operatorname{tr}(\boldsymbol{\gamma}_{\mathrm{e}} + \boldsymbol{\gamma}_{\mathrm{m}}). \qquad (2.14)$$

An interesting variational result based on (2.14) states that among all isotropic, homogeneous scatterers of equal volume and susceptibilities, the spherical scatterer minimizes the averaged integrated extinction [10, Thm. 3].

3 Bounds on broadband scattering

The main result of Sec. 2.2 is now exploited. Firstly, upper and lower bounds on the integrated extinction utilizing the eigenvalue properties of the polarizability dyadics are established. These estimates are followed by two additional upper and lower bounds based on the results of Jones [10, 11].

3.1 Bandwidth estimates

Since the extinction cross section is non-negative, it is clear that for any wavelength interval $\Lambda \subset [0, \infty)$,

$$|\Lambda| \min_{\lambda \in \Lambda} \sigma(\lambda) \leqslant \int_{\Lambda} \sigma(\lambda) \, \mathrm{d}\lambda \leqslant \int_0^{\infty} \sigma_{\mathrm{ext}}(\lambda) \, \mathrm{d}\lambda, \tag{3.1}$$

where $|\Lambda|$ is the absolute bandwidth and σ denotes any of the extinction, scattering and absorption cross sections σ_{ext}, σ_{s}, and σ_{a}, respectively. This seemingly trivial estimate gives a fundamental limitation on the product between the bandwidth and the amplitude of the cross sections, see Fig. 7.

3.2 Increasing material parameters

An important variational result can be established for isotropic material parameters with the long wavelength limit response given by the electric and magnetic susceptibilities, $\chi_{\mathrm{e}}(\boldsymbol{x})$ and $\chi_{\mathrm{m}}(\boldsymbol{x})$, respectively. The result states that the integrated extinction increase monotonically with increasing $\chi_{\mathrm{e}}(\boldsymbol{x})$ and $\chi_{\mathrm{m}}(\boldsymbol{x})$ for each $\boldsymbol{x} \in \mathbb{R}^3$ [11, Thm. 1], *i.e.*,

$$\chi_{i1}(\boldsymbol{x}) \leqslant \chi_{i2}(\boldsymbol{x}), \quad \boldsymbol{x} \in \mathbb{R}^3 \quad \Longrightarrow \quad \int_0^{\infty} \sigma_{\mathrm{ext}1}(\lambda) \, \mathrm{d}\lambda \leqslant \int_0^{\infty} \sigma_{\mathrm{ext}2}(\lambda) \, \mathrm{d}\lambda, \tag{3.2}$$

where $i = \mathrm{e}, \mathrm{m}$. Recall that Kramers-Kronig relations [17, pp. 279–281] implies that $\chi_{\mathrm{e}}(\boldsymbol{x})$ and $\chi_{\mathrm{m}}(\boldsymbol{x})$ pointwise are non-negative, provided the conductivity is zero. If the conductivity of the scatterer is non-zero, the electric polarizability dyadic, $\boldsymbol{\gamma}_{\mathrm{e}}$, can be determined by letting the electric susceptibility becoming infinitely large [15, pp. 49–50]. As a consequence of (3.2), no heterogeneous scatterer has a larger integrated extinction than the corresponding homogeneous one with maximal susceptibility.

3.3 Eigenvalue estimates

The static polarizability dyadics $\boldsymbol{\gamma}_{\mathrm{e}}$ and $\boldsymbol{\gamma}_{\mathrm{m}}$ are real-valued and symmetric, and hence diagonalizable with real-valued eigenvalues $\gamma_{\mathrm{e}j}$ and $\gamma_{\mathrm{m}j}$ with $j = 1, 2, 3$, respectively, ordered as $\gamma_{\mathrm{e}1} \geqslant \gamma_{\mathrm{e}2} \geqslant \gamma_{\mathrm{e}3}$ and $\gamma_{\mathrm{m}1} \geqslant \gamma_{\mathrm{m}2} \geqslant \gamma_{\mathrm{m}3}$. Since the right hand

side of (2.12) is the Rayleigh quotients of $\boldsymbol{\gamma}_\mathrm{e}$ and $\boldsymbol{\gamma}_\mathrm{m}$, their largest and smallest eigenvalues bound (2.12) according to standard matrix theory,[1] *viz.*,

$$\pi^2(\gamma_{\mathrm{e}3}+\gamma_{\mathrm{m}3}) \leqslant \int_0^\infty \sigma_{\mathrm{ext}}(\lambda)\ \mathrm{d}\lambda \leqslant \pi^2(\gamma_{\mathrm{e}1}+\gamma_{\mathrm{m}1}), \tag{3.3}$$

Equality on the left (right) hand side of (3.3) holds when $\hat{\boldsymbol{p}}_\mathrm{e}$ is a unit eigenvector of $\boldsymbol{\gamma}_\mathrm{e}$ with eigenvalue $\gamma_{\mathrm{e}3}$ ($\gamma_{\mathrm{e}1}$) and $\hat{\boldsymbol{p}}_\mathrm{m}$ simultaneously is a unit eigenvector of $\boldsymbol{\gamma}_\mathrm{m}$ with eigenvalue $\gamma_{\mathrm{m}3}$ ($\gamma_{\mathrm{m}1}$).

3.4 Scatterers of arbitrary shape

Broadband scattering in the sense of the integrated extinction is according to (3.3) directly related to the eigenvalues of the static polarizability dyadics. Lemma 2 in Jones [11] applied to (3.3) yields

$$\pi^2 \int_V \frac{\chi_\mathrm{e}(\boldsymbol{x})}{\chi_\mathrm{e}(\boldsymbol{x})+1}+\frac{\chi_\mathrm{m}(\boldsymbol{x})}{\chi_\mathrm{m}(\boldsymbol{x})+1}\ \mathrm{d}v \leqslant \int_0^\infty \sigma_{\mathrm{ext}}(\lambda)\ \mathrm{d}\lambda \leqslant \pi^2 \int_V \chi_\mathrm{e}(\boldsymbol{x})+\chi_\mathrm{m}(\boldsymbol{x})\ \mathrm{d}v. \tag{3.4}$$

The bounds in (3.4) are sharp in the sense that equality can be obtained as a limiting process for certain homogeneous ellipsoids, see Sec. 4.

The right hand side of (3.4) is bounded from above by $|V|\|\chi_\mathrm{e}+\chi_\mathrm{m}\|_\infty$, where $\|f\|_\infty = \sup_{\boldsymbol{x}\in V}|f(\boldsymbol{x})|$ denotes the supremum norm. As a consequence, the upper bound on the integrated extinction for any heterogeneous scatterer is less than or equal to the integrated extinction for the corresponding homogeneous scatterer with susceptibilities $\|\chi_\mathrm{e}\|_\infty$ and $\|\chi_\mathrm{m}\|_\infty$. This observation leads to the conclusion that there is no fundamental difference on the integrated extinction between scattering by heterogeneous and homogeneous obstacles.

For weak scatterers in the sense of the Born-approximation, $\|\chi_\mathrm{e}+\chi_\mathrm{m}\|_\infty \ll 1$, and (3.4) implies

$$\int_0^\infty \sigma_{\mathrm{ext}}(\lambda)\ \mathrm{d}\lambda = \pi^2 \int_V \chi_\mathrm{e}(\boldsymbol{x})+\chi_\mathrm{m}(\boldsymbol{x})\ \mathrm{d}v + \mathcal{O}(\|\chi_\mathrm{e}+\chi_\mathrm{m}\|_\infty^2), \tag{3.5}$$

where the Taylor series expansion $1/(1+x) = 1+\mathcal{O}(x)$ for $|x|<1$ have been used. Note that (3.5) reduces to a particularly simple form for homogeneous scatterers.

3.5 Star-shaped scatterers

Due to (3.2), it is possible to derive upper bounds on the integrated extinction by applying the bounds to the corresponding homogeneous scatterer with susceptibilities $\|\chi_\mathrm{e}\|_\infty$ and $\|\chi_\mathrm{m}\|_\infty$. To this end, assume V is star-shaped in the sense that $K_V \neq \emptyset$, where K_V is the set of $\boldsymbol{x} \in V$ such that for all $\boldsymbol{y} \in V$ and $0 \leqslant s \leqslant 1$ the straight line $\boldsymbol{x}+(1-s)\boldsymbol{y}$ is contained in V, *i.e.*, if it has an interior point from which its entire boundary can be seen. For a convex scatterer, $K_V = V$.

[1] If the eigenvectors corresponding to the largest eigenvalues are the same for the electric and the magnetic cases, the bounds in (3.3) can be sharpened.

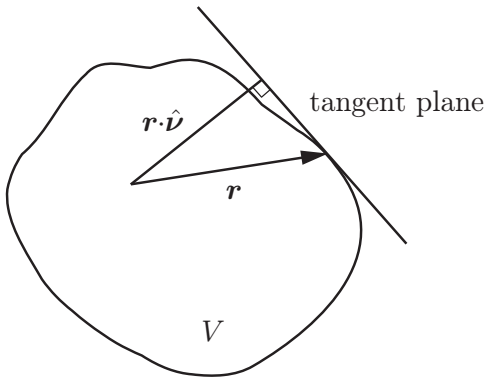

Figure 3: Geometry for the star-shape parametrization.

A refined upper bound on $\gamma_{\mathrm{e}1}$ and $\gamma_{\mathrm{m}1}$ [10, Thm. 5] applied to (3.3), also taking into account the shape of V, yields the inequality

$$\int_0^\infty \sigma_{\mathrm{ext}}(\lambda)\ \mathrm{d}\lambda \leqslant \pi^2|V|\psi\left(\frac{\|\chi_{\mathrm{e}}\|_\infty}{\psi+\|\chi_{\mathrm{e}}\|_\infty}+\frac{\|\chi_{\mathrm{m}}\|_\infty}{\psi+\|\chi_{\mathrm{m}}\|_\infty}\right), \tag{3.6}$$

where the geometrical factor ψ is defined by

$$\psi=\frac{3}{|V|}\max_j\int_S\frac{(\hat{\boldsymbol{e}}_j\cdot\boldsymbol{r})^2}{\boldsymbol{r}\cdot\hat{\boldsymbol{\nu}}}\ \mathrm{d}S\leqslant\frac{9}{|V|}\int_S\frac{r^2}{\boldsymbol{r}\cdot\hat{\boldsymbol{\nu}}}\ \mathrm{d}S. \tag{3.7}$$

Here, $\hat{\boldsymbol{e}}_j$ denote mutually orthonormal vectors and $\mathrm{d}S$ is the surface measure of S with respect to $\boldsymbol{r}$ (S is the bounding surface of V). The denominator in (3.7) is the distance from the tangent plane to the origin, see Fig. 3. The upper bound in (3.7) is independent of the coordinate system orientation but depends on the location of the origin.

Furthermore, the right hand side of (3.6) is bounded from above by either $\|\chi_{\mathrm{e}}\|_\infty$ and $\|\chi_{\mathrm{m}}\|_\infty$ or ψ. The first case yields (3.4) for a homogeneous scatterer (material parameters $\|\chi_{\mathrm{e}}\|_\infty$ and $\|\chi_{\mathrm{m}}\|_\infty$), while the latter implies

$$\int_0^\infty \sigma_{\mathrm{ext}}(\lambda)\ \mathrm{d}\lambda \leqslant 2\pi^2|V|\psi, \tag{3.8}$$

irrespectively of the material parameters of V. By comparing (3.4) with (3.8), it is clear that (3.8) provides the sharpest bound when $2\psi < \|\chi_{\mathrm{e}}+\chi_{\mathrm{m}}\|_\infty$. Note that (3.2) implies that it is possible to evaluate (3.7) for any surface circumscribing the scatterer V.

The geometrical factor for the oblate spheroid is $\psi=3(4+\xi^{-2})/5$ and for the prolate spheroid $\psi=3(3+2\xi^{-2})/5$ (the origin at the center of the spheroid), where $\xi\in[0,1]$ is the ratio of the minor to the major semi-axis. In particular, $\psi=3$ for the sphere. The bound in (3.6) is isoperimetric since equality holds for the homogeneous sphere, see Sec. 4. The geometrical factor ψ for the circular cylinder of radius b and length ℓ is[2] $\psi=\max\{3+3b^2/\ell^2, 3+\ell^2/2b^2\}$.

[2]This expression deviates from the result of Jones [10].

3.6 Jung's theorem

Jung's theorem [13] gives an optimal upper bound on the radius of a bounded subset $V \subset \mathbb{R}^3$ in terms of its diameter, $\operatorname{diam} V$. The theorem states that V is contained in the unique sphere of radius $R_V \leqslant \sqrt{6}/4 \operatorname{diam} V$, with equality if and only if the closure of V contains the vertices of a tetrahedron of edge lengths equal to $\operatorname{diam} V$. Since $\psi = 3$ for the sphere and $|V|$ is bounded from above by the volume of the sphere of radius R_V, (3.6) yields

$$\int_0^\infty \sigma_{\mathrm{ext}}(\lambda)\, \mathrm{d}\lambda \leqslant \frac{\pi^3 3\sqrt{6}}{8} (\operatorname{diam} V)^3 \left(\frac{\|\chi_{\mathrm{e}}\|_\infty}{3 + \|\chi_{\mathrm{e}}\|_\infty} + \frac{\|\chi_{\mathrm{m}}\|_\infty}{3 + \|\chi_{\mathrm{m}}\|_\infty} \right). \tag{3.9}$$

The right hand side of (3.9) can be estimated from above independently of the material parameters. We get

$$\int_0^\infty \sigma_{\mathrm{ext}}(\lambda)\, \mathrm{d}\lambda \leqslant \frac{\pi^3 3\sqrt{6}}{4} (\operatorname{diam} V)^3, \tag{3.10}$$

which is useful in cases where the right hand side of (3.8) diverges.

In this section, we have applied Jung's theorem to a sphere circumscribing the scatterer. There are, however, other choices of circumscribing surfaces that can be utilized [9].

4 Homogeneous ellipsoidal scatterers

For homogeneous, anisotropic ellipsoidal scatterers with susceptibility dyadics $\boldsymbol{\chi}_{\mathrm{e}}$ and $\boldsymbol{\chi}_{\mathrm{m}}$, closed-form expressions of $\boldsymbol{\gamma}_{\mathrm{e}}$ and $\boldsymbol{\gamma}_{\mathrm{m}}$ exist [12], *viz.*,

$$\boldsymbol{\gamma}_i = |V| \boldsymbol{\chi}_i \cdot (\mathbf{I} + \mathbf{L} \cdot \boldsymbol{\chi}_i)^{-1}, \quad i = \mathrm{e}, \mathrm{m} \tag{4.1}$$

where $\mathbf{L}$ and $\mathbf{I}$ are the depolarizing and unit dyadics in $\mathbb{R}^3$, respectively. In terms of the semi-axes a_j in the $\hat{\boldsymbol{e}}_j$-direction, the volume $|V| = 4\pi a_1 a_2 a_3/3$. The depolarizing dyadic has unit trace, and is real-valued and symmetric [32], and, hence, diagonalizable with real-valued eigenvalues. Its eigenvalues are the depolarizing factors L_j [6, 23]

$$L_j = \frac{a_1 a_2 a_3}{2} \int_0^\infty \frac{\mathrm{d}s}{(s + a_j^2)\sqrt{(s + a_1^2)(s + a_2^2)(s + a_3^2)}}, \quad j = 1, 2, 3. \tag{4.2}$$

The depolarizing factors satisfy $0 \leqslant L_j \leqslant 1$ and $\sum_j L_j = 1$.

Closed-form expressions of (4.2) exist in the special case of the ellipsoids of revolution, *i.e.*, the prolate and oblate spheroids. In terms of the eccentricity $e = \sqrt{1 - \xi^2}$, where $\xi \in [0, 1]$ is the ratio of the minor to the major semi-axis, the depolarizing factors are (symmetry axis along the $\hat{\boldsymbol{e}}_3$-direction)

$$L_1 = L_2 = \frac{1}{4e^3} \left(2e - (1 - e^2) \ln \frac{1 + e}{1 - e} \right), \qquad L_3 = \frac{1 - e^2}{2e^3} \left(\ln \frac{1 + e}{1 - e} - 2e \right), \tag{4.3}$$

and

$$L_1 = L_2 = \frac{1-e^2}{2e^2}\left(-1 + \frac{\arcsin e}{e\sqrt{1-e^2}}\right), \qquad L_3 = \frac{1}{e^2}\left(1 - \frac{\sqrt{1-e^2}}{e}\arcsin e\right), \quad (4.4)$$

for the prolate and oblate spheroids, respectively. In particular, $L_j = 1/3$ for the sphere.

The integrated extinction for anisotropic homogeneous ellipsoidal scatterers is given by (4.1) inserted into (2.12). The result is

$$\int_0^\infty \sigma_{\text{ext}}(\lambda)\ \mathrm{d}\lambda = \pi^2|V| \sum_{i=\text{e,m}} \hat{\boldsymbol{p}}_i^* \cdot \boldsymbol{\chi}_i \cdot (\mathbf{I} + \mathbf{L}\cdot\boldsymbol{\chi}_i)^{-1} \cdot \hat{\boldsymbol{p}}_i. \quad (4.5)$$

For isotropic material parameters, $\boldsymbol{\chi}_\text{e} = \chi_\text{e}\mathbf{I}$ and $\boldsymbol{\chi}_\text{m} = \chi_\text{m}\mathbf{I}$, (4.5) reduces to

$$\int_0^\infty \sigma_{\text{ext}}(\lambda)\ \mathrm{d}\lambda = \pi^2|V| \sum_{j=1}^{3} \left(\frac{\kappa_{\text{e}j}\chi_\text{e}}{1+\chi_\text{e}L_j} + \frac{\kappa_{\text{m}j}\chi_\text{m}}{1+\chi_\text{m}L_j}\right), \quad (4.6)$$

where $\kappa_{\text{e}j} = |\hat{\boldsymbol{p}}_\text{e}\cdot\hat{\boldsymbol{e}}_j|^2$ and $\kappa_{\text{m}j} = |\hat{\boldsymbol{p}}_\text{m}\cdot\hat{\boldsymbol{e}}_j|^2$ are the polarization vectors projected onto the mutually orthonormal vectors $\hat{\boldsymbol{e}}_j$. Note that $\sum_j \kappa_{\text{e}j} = \sum_j \kappa_{\text{m}j} = 1$, and that the averaged integrated extinction is characterized by $\kappa_{\text{e}j} = \kappa_{\text{m}j} = 1/3$. For prolate and oblate spheroids, which are axially symmetric with respect to the $\hat{\boldsymbol{e}}_3$-axis, a plane wave incident at an angle θ to this axis, yields

$$\begin{cases} \kappa_{\text{e}1} + \kappa_{\text{e}2} = 1 \\ \kappa_{\text{e}3} = 0 \\ \kappa_{\text{m}1} + \kappa_{\text{m}2} = \cos^2\theta \\ \kappa_{\text{m}3} = \sin^2\theta \end{cases} \quad \text{(TE)} \qquad \begin{cases} \kappa_{\text{m}1} + \kappa_{\text{m}2} = 1 \\ \kappa_{\text{m}3} = 0 \\ \kappa_{\text{e}1} + \kappa_{\text{e}2} = \cos^2\theta \\ \kappa_{\text{e}3} = \sin^2\theta \end{cases} \quad \text{(TM)} \quad (4.7)$$

In the limit as the volume goes to zero, the integrated extinction vanishes for a scatterer with finite susceptibilities. To obtain a non-zero integrated extinction, the scatterer has either to be conducting or evaluated in the high-contrast limit, see *e.g.*, the PEC disk below. In the long wavelength PEC limit, see (2.13), the integrated extinction becomes

$$\int_0^\infty \sigma_{\text{ext}}(\lambda)\ \mathrm{d}\lambda = \pi^2|V| \sum_{j=1}^{3} \left(\frac{\kappa_{\text{e}j}}{L_j} - \frac{\kappa_{\text{m}j}}{1-L_j}\right). \quad (4.8)$$

The right hand side of (4.6) is bounded from above by χ_i and from below by $\chi_i/(1+\chi_i)$. The bounds in (3.4) are sharp in the sense that χ_i and $\chi_i/(1+\chi_i)$ are obtained at arbitrary precision for the infinite needle and disk of constant volume $|V|$, respectively. In fact, the upper bound holds for an infinite needle oriented along the $\hat{\boldsymbol{e}}_3$-direction ($L_1 + L_2 = 1$) with parallel polarization ($\kappa_{i3} = 1$). The corresponding equality for the lower bound holds for the infinite disk with unit normal vector $\hat{\boldsymbol{e}}_3$ ($L_3 = 1$) and parallel polarization ($\kappa_{i3} = 1$).

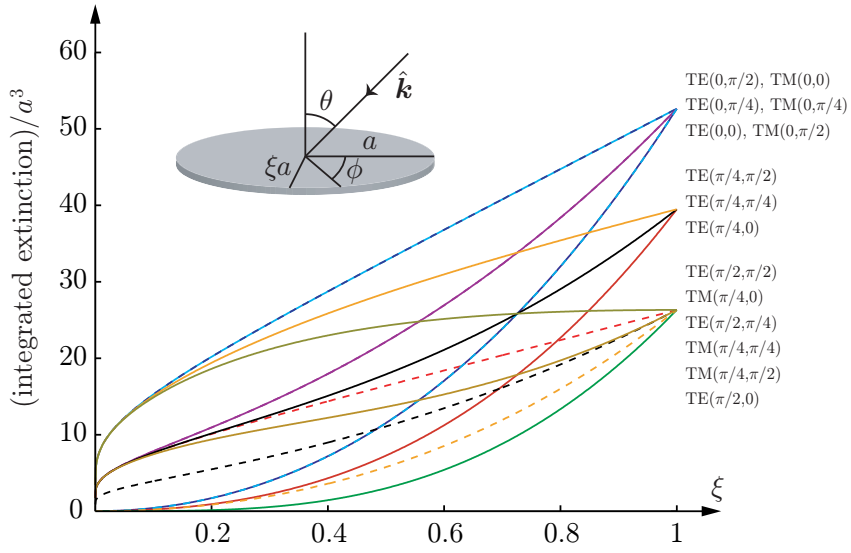

Figure 4: The integrated extinction (4.10) in units of a^3 as function of the semi-axis ratio ξ for the PEC elliptic disk. The notations $\mathrm{TE}(\theta,\phi)$ and $\mathrm{TM}(\theta,\phi)$ refer to the TE- and TM-polarizations for $\theta,\phi \in \{0,\pi/4,\pi/2\}$.

A simple example of (4.6) is given by the homogeneous sphere for which the integrated extinction is equal to $3\pi^2|V|\sum_i \chi_i/(\chi_i+3)$ independent of $\kappa_{\mathrm{e}j}$ and $\kappa_{\mathrm{m}j}$, which also is the result of Bohren and Huffman for the non-magnetic case [4, p. 117]. In particular, the PEC limit (2.13) implies that the integrated extinction for the sphere is equal to $3\pi^2|V|/2$. Similar results for stratified dielectric spheres are obtained using recursive compositions of Möbius transformations. For the case of two layers, see Sec. 5.5.

The integrated extinction for the PEC elliptic disk is given by (4.8), and the integrals in (4.2), as the semi-axis a_3 approaches zero, are available in the literature [6, p. 507], [23]. The result is

$$\begin{cases} L_1/|V| = \dfrac{3}{4\pi a^3 e^2}\,(\mathrm{K}-\mathrm{E}) \\ L_2/|V| = \dfrac{3}{4\pi a^3 e^2}\,\big(\mathrm{E}/(1-e^2)-\mathrm{K}\big) \\ (L_3-1)/|V| = -\dfrac{3\mathrm{E}}{4\pi a^3(1-e^2)} \end{cases} \tag{4.9}$$

where a is the major semi-axis, and $\mathrm{E}=\mathrm{E}(e^2)$ and $\mathrm{K}=\mathrm{K}(e^2)$ are the complete elliptic integrals of first and second kind, respectively [1, p. 590]. We obtain

$$\int_0^\infty \sigma_{\mathrm{ext}}(\lambda)\,\mathrm{d}\lambda = \frac{4\pi^3 a^3}{3}\begin{cases} B\cos^2\phi + C\sin^2\phi - A\sin^2\theta & (\mathrm{TE}) \\ \big(B\sin^2\phi + C\cos^2\phi\big)\cos^2\theta & (\mathrm{TM}) \end{cases} \tag{4.10}$$

where θ and ϕ are the spherical angles of the incident direction, $\hat{\boldsymbol{k}}$. The factors A,

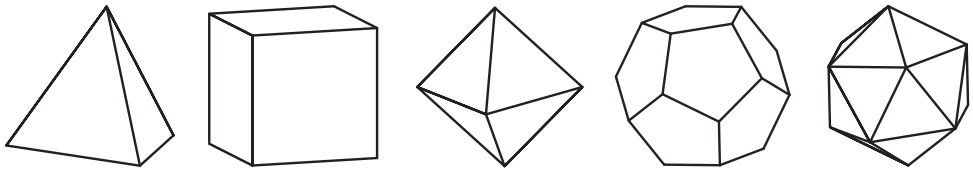

49.6$|V|$ 35.9$|V|$ 35.0$|V|$ 31.4$|V|$ 30.9$|V|$

Figure 5: The integrated extinctions for the Platonic solids based on MoM-calculations [25]. The Platonic solids are from left to right the tetrahedron, hexahedron, octahedron, dodecahedron and icosahedron, with 4, 6, 8, 12 and 20 faces, respectively.

B, and C are defined as

$$A = \frac{1-e^2}{\mathrm{E}}, \quad B = \frac{e^2(1-e^2)}{\mathrm{E}-(1-e^2)\mathrm{K}}, \quad C = \frac{e^2}{\mathrm{K}-\mathrm{E}}. \tag{4.11}$$

Note that the TM-polarization vanishes for $\theta = \pi/2$ independently of $\phi \in [0, 2\pi)$. The integrated extinction (4.10) can also be derived from the long wavelength limit of the T-matrix approach [3].

The integrated extinction in the right hand side of (4.10) as function of ξ is depicted in Fig. 4. Note the degeneracy of the integrated extinction at the end points $\xi = 0$ and $\xi = 1$, corresponding to the PEC needle of length $2a$ and the PEC circular disk of radius a, respectively.

5 Numerical results

In this section, we illustrate the theoretical results obtained above by several numerical examples. Specifically, we calculate the extinction cross sections and the eigenvalues of the polarizability dyadics for a set of scatterers with isotropic material parameters. These results are then compared to the theoretical results presented in Secs. 2, 3, and 4.

5.1 Platonic solids

Since the homogeneous Platonic solids are invariant under a set of appropriate point groups, their polarizability dyadics are isotropic. By (2.12) this implies that the integrated extinctions are independent of both polarization and incident direction. The five Platonic solids are depicted in Fig. 5, see also Tab. 1, together with the integrated extinctions in the non-magnetic, high-contrast limit, *i.e.*, $\chi_{\mathrm{e}} \to \infty$.

A common lower bound on the integrated extinctions in Fig. 5 is obtained by (4.6) for the volume-equivalent sphere. This lower bound is motivated by Jones' result [10, Thm. 3], and the fact that the polarizability dyadics are isotropic. The result is $14.80|V|$.

Platonic solids	$\gamma_e/\lvert V\rvert$	γ_e/a^3	**Int. ext.**	$\lvert V\rvert/a^3$
Tetrahedron	5.03	0.593	$49.6\lvert V\rvert$	$\sqrt{2}/12$
Hexahedron	3.64	3.64	$35.9\lvert V\rvert$	1
Octahedron	3.55	1.67	$35.0\lvert V\rvert$	$\sqrt{2}/3$
Dodecahedron	3.18	24.4	$31.4\lvert V\rvert$	$(15+7\sqrt{5})/4$
Icosahedron	3.13	6.83	$30.9\lvert V\rvert$	$5(3+\sqrt{5})/12$

Table 1: The eigenvalues γ_e and the integrated extinction for the Platonic solids in units of $|V|$ in the high-contrast limit $\chi_e \to \infty$. The last column gives the volume of the Platonic solids expressed in the edge length a.

Upper bounds on the integrated extinctions are given by the smallest circumscribing high-contrast spheres, which based on solid geometry are found to be $241.60|V|$, $80.54|V|$, $61.98|V|$, $44.62|V|$ and $48.96|V|$ for the tetrahedron, hexahedron, octahedron, dodecahedron and icosahedron, respectively, see (3.2). The upper and lower bounds are seen to be quite close to the numerical values presented in Fig. 5, at least for the dodecahedron and icosahedron, which do not deviate much from the volume-equivalent sphere. Since the Platonic solids are star-shaped with respect to all interior points, a somewhat different set of upper bounds can be derived from (3.6).

5.2 Dielectric spheroids

The averaged extinction cross section, $\bar{\sigma}_{\text{ext}}$, as function of the radius ka for a prolate and oblate spheroid is illustrated in Fig. 6. The solid curve depicts the averaged extinction cross section (equal to the extinction cross section) for the volume-equivalent sphere of radius a, and the dashed and dotted curves correspond to the prolate and oblate spheroids, respectively, of semi-axis ratio $\xi = 1/2$. The scatterers are non-magnetic with electric susceptibility $\chi_e = 1$. Note that the largest variation of the curves in Fig. 6 occurs for the sphere due to the fact that its extinction cross section is independent of the polarization and the direction of incidence, which implies that no resonances are averaged out in contrast to the case for the prolate and oblate spheroids.

The numerically integrated averaged extinction cross sections for $ka \in [0, 20]$ agree within relative errors of 1.2% with the theoretical values $7.46|V|$ and $7.48|V|$ based on (4.6) for the prolate and oblate spheroids, respectively. The corresponding values for the sphere are 0.7% and $7.40|V|$. The calculations are based on the T-matrix approach [19].

According to Sec. 2, a lower bound on the averaged integrated extinctions for the spheroids is $7.40|V|$ corresponding to the volume-equivalent sphere. Based on (3.4), lower and upper bounds common to the three curves in Fig. 6 are $4.93|V|$ and $9.87|V|$, respectively. Using the star-shaped bound (3.6), these upper bounds are improved to $8.57|V|$ and $8.17|V|$ for the prolate and the oblate spheroids, respectively. Both the lower and upper bounds are reasonable close to the theoretical

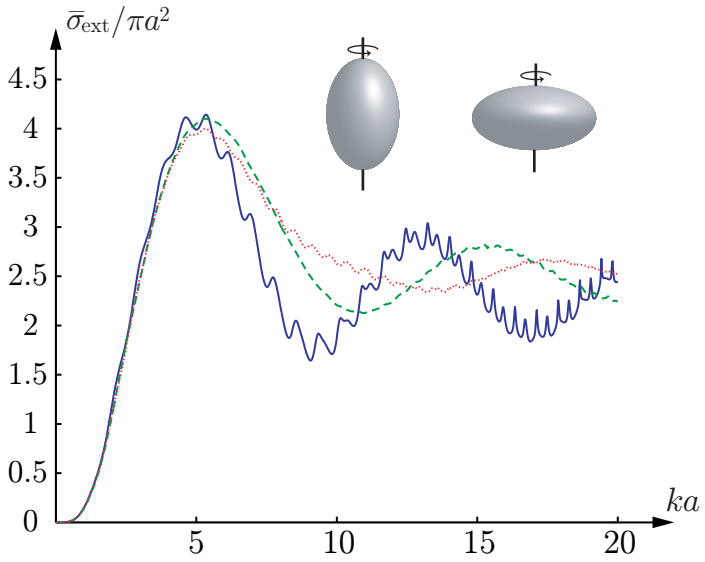

Figure 6: The averaged extinction cross section, $\bar{\sigma}_{\text{ext}}$, in units of πa^2 as function of ka for a prolate (dashed) and oblate (dotted) non-magnetic spheroid with electric susceptibility $\chi_{\text{e}} = 1$ and semi-axis ratio $\xi = 1/2$. The extinction cross section for the volume-equivalent sphere of radius a (solid) is included.

values.

5.3 Lorentz dispersive circular cylinder

The averaged extinction cross section, $\bar{\sigma}_{\text{ext}}$, as function of the frequency for a Lorentz dispersive circular cylinder is depicted in Fig. 7. The ratio of the cylinder length ℓ to its radius b is $\ell/b = 2$. The cylinder is non-magnetic with electric susceptibility given by the Lorentz model [4, Sec. 9.1]

$$\chi_{\text{e}}(\omega) = \frac{\omega_{\text{p}}^2}{\omega_0^2 - \omega^2 - \text{i}\omega\nu}, \tag{5.1}$$

where ω_{p} is the plasma frequency, ν the collision frequency and ω_0 the resonance frequency. Explicit values of ω_{p}, ω_0 and ν are $\omega_{\text{p}} = \omega_0 = 4\pi \cdot 10^9\,\text{rad/s}$, $\nu = 0.7 \cdot 10^9\,\text{rad/s}$, and $\omega_{\text{p}} = \omega_0 = 20\pi \cdot 10^9\,\text{rad/s}$, $\nu = 10^{10}\,\text{rad/s}$, respectively. The Lorentz parameters are chosen such that all three curves in the left figure have the same long wavelength susceptibility $\chi_{\text{e}} = \chi_{\text{e}}(0) = 1$. The first two curves with peaks at 2 GHz and 10 GHz depict the dispersive case, while the third for comparison illustrates the results for the non-dispersive case. The three curves in the left figure have the same integrated extinctions, since their long wavelength susceptibilities coincide. The calculation is based on the T-matrix approach [19].

A numerical calculation of the eigenvalues of the polarizability dyadic for the dielectric cylinder is performed by adopting the finite element method (FEM). The results are $0.773|V|$, $0.749|V|$, and $0.749|V|$. This result implies that the numerically

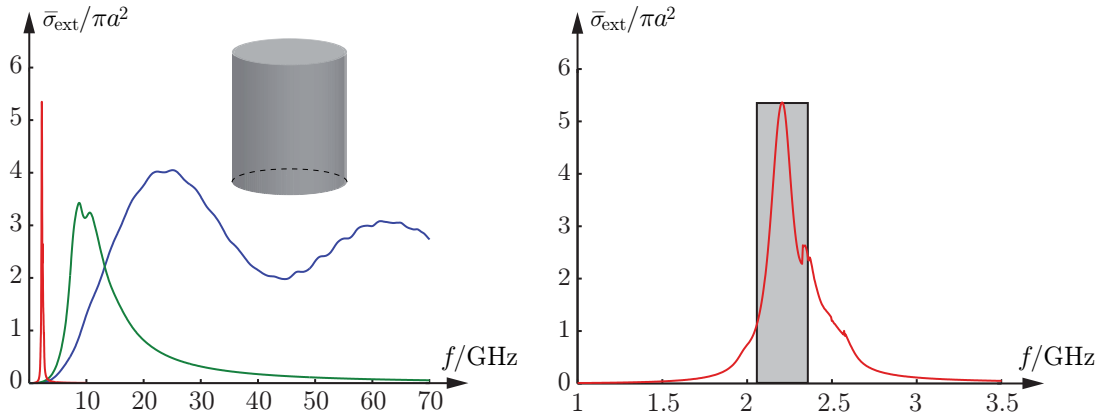

Figure 7: The averaged extinction cross section, $\bar{\sigma}_{\text{ext}}$, in units of πa^2 as function of the frequency in GHz for a non-magnetic Lorentz dispersive circular cylinder with volume-equivalent sphere of radius $a = 1\,\text{cm}$. The three curves in the left figure have the same long wavelength response $\chi_{\text{e}} = 1$. The first two curves with peaks at 2 GHz and 10 GHz are Lorentz dispersive, while the third curve is non-dispersive. The right figure is a close-up of the 2 GHz peak in the left figure.

computed averaged extinction cross section, $\bar{\sigma}_{\text{ext}}$, in (2.14) is $7.47|V|$. The numerically calculated integrated extinction in the interval $f \in [0, 70]\,\text{GHz}$ is $7.43|V|$ for the first, and $7.44|V|$ for the second curve in Fig. 7.

Common lower and upper bounds on the integrated extinctions based on (3.4) are $4.94|V|$ and $9.87|V|$, respectively. A sharper lower bound is $7.40|V|$ corresponding to the volume-equivalent sphere. An upper bound can for comparison be obtained from (3.6). For $\ell/b = 2$ this implies $\psi = 5$ and the upper bound $8.23|V|$, which is sharper than the bound based on (3.4).

The figure on the right hand side of Fig. 7 is a close-up of the 2 GHz peak. The boundary curve of the box corresponds to an artificial scatterer with averaged extinction cross section supported at the peak, *i.e.*, for an averaged extinction cross section that vanishes everywhere outside the box. The integrated extinction for the boundary curve of the box and the three curves in the left hand side of Fig. 7 coincide.

5.4 Debye dispersive non-spherical raindrop

The averaged extinction cross section, $\bar{\sigma}_{\text{ext}}$, as function of the frequency for a falling raindrop is depicted in Fig. 8. The axially symmetric drop is parameterized by the polar angle θ and the radial distance

$$r(\theta) = r_0 \left(1 + \sum_{k=0}^{10} c_k \cos k\theta \right), \tag{5.2}$$

where r_0 is determined from the condition of the volume-equivalence with the sphere of radius a, *i.e.*, $|V| = \frac{2\pi}{3} \int_0^\pi r^3(\theta) \sin\theta \, \mathrm{d}\theta$ with $|V| = 4\pi a^3/3$. The radius of the

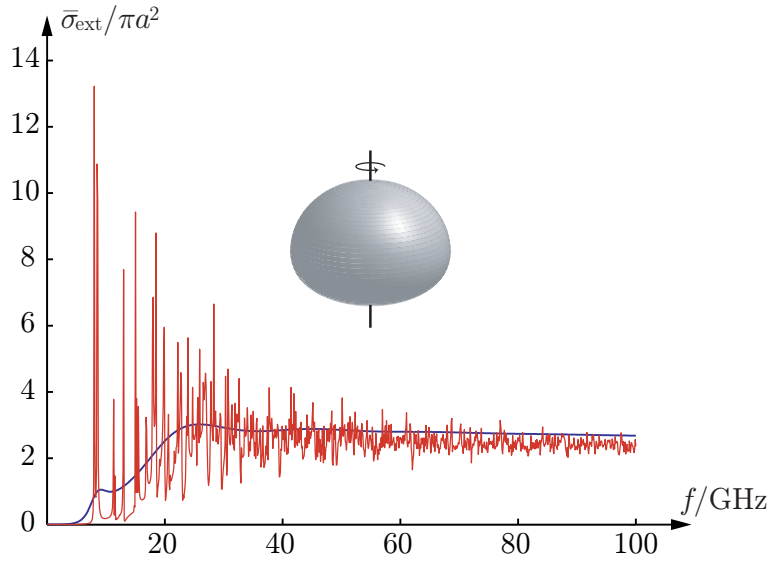

Figure 8: The averaged extinction cross section, $\bar{\sigma}_{\text{ext}}$, in units of πa^2 as function of the frequency in GHz for a raindrop of volume-equivalent radius $a = 2\,\text{mm}$. The smooth curve is for the Debye-model (5.3), while the oscillatory curve is for the non-dispersive case. The two curves have the same long wavelength response and therefore also the same integrated extinctions.

volume-equivalent sphere used in Fig. 8 is $a = 2\,\text{mm}$ with associated shape coefficients $c_0 = -0.0458$, $c_1 = 0.0335$, $c_2 = -0.1211$, $c_3 = 0.0227$, $c_4 = 0.0083$, $c_5 = -0.0089$, $c_6 = 0.0012$, $c_7 = 0.0021$, $c_8 = -0.0013$, $c_9 = -0.0001$ and $c_{10} = 0.0008$ [2]. The calculation is based on the T-matrix approach [19].

The smooth curve in Fig. 8 is for the non-magnetic Debye model [4, Sec. 9.5]

$$\chi_{\text{e}}(\omega) = \chi_\infty + \frac{\chi_{\text{s}} - \chi_\infty}{1 - \text{i}\omega\tau}, \tag{5.3}$$

where τ is the relaxation time and χ_∞ and χ_{s} are the short and long wavelength susceptibilities, respectively. Pure water at 20°C is considered with $\chi_{\text{s}} = 79.2$, $\chi_\infty = 4.6$ and $\tau = 9.36\,\text{ps}$ [14, p. 43]. The curve with largest variation is for the non-dispersive case with an susceptibility identical to the long wavelength limit, χ_{s}, of (5.3).

Since the long wavelength susceptibilities coincide for the two curves in Fig. 8, their integrated extinctions are equal according to (2.14). The eigenvalues of the polarizability dyadics for the raindrop can be obtained by numerical computations. A finite element method (FEM) computation gives the three eigenvalues: $2.43|V|$, $3.21|V|$, and $3.21|V|$, respectively. This result implies that the numerically computed averaged extinction cross section, $\bar{\sigma}_{\text{ext}}$, in (2.14) is $29.1|V|$. If we numerically integrate the average extinction cross section in Fig. 8 over $f \in [0, 100]\,\text{GHz}$, we get $26.4|V|$ for the dispersive and $25.6|V|$ for the non-dispersive curve, respectively. The reason why the numerically integrated extinctions are about 10% below the FEM values is due to the finite integration interval.

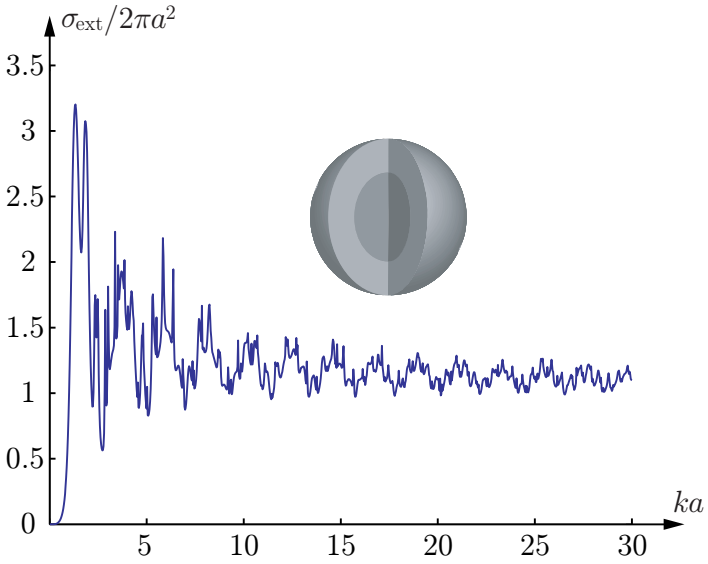

Figure 9: The extinction cross section, σ_{ext}, in units of $2\pi a^2$ as function of the radius ka for a dielectric stratified sphere with two layers of equal volume. The electric and magnetic susceptibilities are $\chi_{\text{e}1} = 2$ and $\chi_{\text{m}1} = 1$ for the core and $\chi_{\text{e}2} = 1$ and $\chi_{\text{m}2} = 2$ for the outer layer.

Lower and upper bounds on the integrated extinctions, given by (3.4), are $9.75|V|$ and $782|V|$, respectively, which are rather crude. A more accurate lower bound is given by the non-magnetic, volume-equivalent sphere with static susceptibilities $\chi_{\text{e}} = \chi_{\text{s}}$, for which (4.6) yields $28.5|V|$. The star-shaped bound in Sec. 3.5 is also applicable. The result for the raindrop is $32.15|V|$. We observe that both the lower and upper bounds approximate the true value very well.

5.5 Dielectric stratified sphere

Due to spherical symmetry, the polarizability dyadics of a stratified sphere are isotropic and easily computed by recursive applications of Möbius transformations. In particular, the integrated extinction for two layers with electric and magnetic susceptibilities $\chi_{\text{e}1}$ and $\chi_{\text{m}1}$ in the core, and $\chi_{\text{e}2}$ and $\chi_{\text{m}2}$ in the outer layer, respectively, is

$$\int_0^\infty \sigma_{\text{ext}}(\lambda)\, \mathrm{d}\lambda = 3\pi^2|V| \sum_{i=\text{e,m}} \frac{\chi_{i2}(\chi_{i1} + 2\chi_{i2} + 3) + \varsigma^3(2\chi_{i2} + 3)(\chi_{i1} - \chi_{i2})}{(\chi_{i2} + 3)(\chi_{i1} + 2\chi_{i2} + 3) + 2\varsigma^3\chi_{i2}(\chi_{i1} - \chi_{i2})}, \quad (5.4)$$

where ς is the ratio of the inner to the outer radius. The special cases $\varsigma = 0$ and $\varsigma = 1$ correspond to homogeneous spheres with susceptibilities χ_{i2} and χ_{i1}, respectively, see Sec. 4. Moreover, both $\chi_{i1} = \chi_{i2}$ and $\chi_{i2} = 0$ yield the homogeneous sphere of susceptibility χ_{i1}, with the volume of the sphere being a fraction ς^3 of the volume $|V|$ in the latter case.

The extinction cross section, σ_{ext}, as function of the radius ka for the stratified sphere with two layers of equal volume, $\varsigma = 1/\sqrt[3]{2}$, is depicted in Fig. 9. The used

susceptibilities are $\chi_{\mathrm{e}1} = 2$ and $\chi_{\mathrm{m}1} = 1$ in the core, and $\chi_{\mathrm{e}2} = 1$ and $\chi_{\mathrm{m}2} = 2$ in the outer layer. The calculations are based on the Mie-series approach [18]. Note that the curve in Fig. 9 approaches twice the geometrical cross section area in the short wavelength limit. Compare this observation with the extinction paradox [31, pp. 107–108].

The numerically integrated extinction is $19.1|V|$ for $ka \in [0, 30]$ and $19.3|V|$ for $ka \in [0, 100]$, with relative errors of 1.7% and 0.5%, respectively, compared to the theoretical value $19.4|V|$ given by (5.4).

Lower and upper bounds on the integrated extinction based on the inequality in (3.2) are $14.8|V|$ and $23.7|V|$, respectively, corresponding to the volume-equivalent homogeneous sphere with minimal and maximal susceptibilities, $\inf_{\boldsymbol{x}\in V} \chi_i$ and $\sup_{\boldsymbol{x}\in V} \chi_i$, respectively. Note that this upper bound coincides with the one obtained from (3.6), but that both the lower and upper bounds based on (3.2) are sharper than the ones given by (3.4).

5.6 PEC circular disk

The integrated extinction for the PEC circular disk of radius a is given by (4.10) in the limit $\xi \to 1$. The result is

$$\int_0^\infty \sigma_{\mathrm{ext}}(\lambda)\ \mathrm{d}\lambda = \frac{8\pi^2 a^3}{3} \begin{cases} 1 + \cos^2\theta & (\mathrm{TE}) \\ 2\cos^2\theta & (\mathrm{TM}) \end{cases} \tag{5.5}$$

The right hand side of (5.5) can also be derived from the long wavelength limit of the T-matrix approach [16].

The extinction cross section, σ_{ext}, as function of the radius ka for the PEC circular disk is depicted in Fig. 10. The notations TE(θ) and TM(θ) refer to the TE- and TM-polarizations, respectively, and the stars denote the short wavelength limit $\cos\theta$ given by the extinction paradox [31, pp. 107–108]. Note the degeneracy of both polarizations for normal incidence, and that the extinction cross section vanishes identically for TM($\pi/2$). The calculation is based on the T-matrix approach [16].

To find the numerically integrated extinctions, the integration interval $ka \in [0, 15]$ does not suffice to get reasonable accuracy. However, by extending the integrand above $ka = 15$ by the expected short wavelength limit, we obtain relative errors of 0.5% compared to the exact results of (5.5).

The bounds discussed in Sec. 3 are not directly applicable to the PEC circular disk since the disk has zero volume. However, a crude upper bound is obtained by the circumscribing PEC sphere. The result is $1.5\pi^2$, in units of the volume of the circumscribing sphere. Compare this with the exact results of (5.5) in terms of the volume of the circumscribing sphere — the factor 1.5 for the circumscribing sphere is to be compared with $4/\pi \approx 1.27$ at $\theta = 0$ incidence.

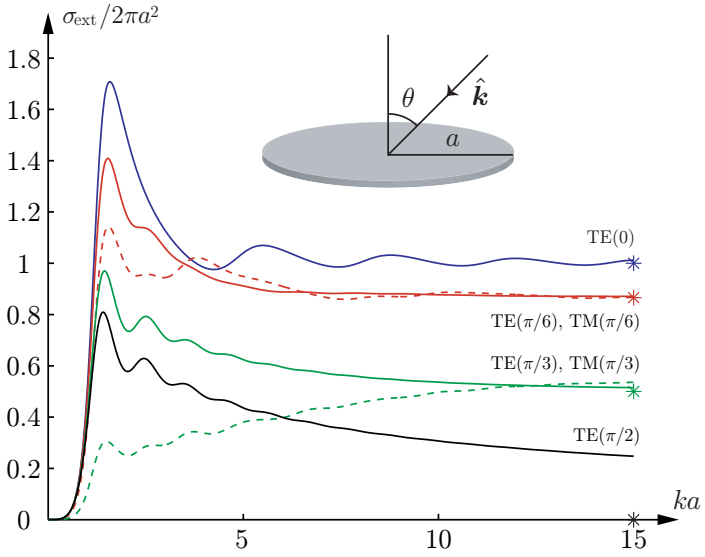

Figure 10: The extinction cross section, σ_{ext}, in units of $2\pi a^2$ as function of the radius ka for the PEC circular disk. The solid and dashed lines are for the TE- and TM-polarizations, respectively, and the stars denote the short wavelength limits $\cos\theta$.

5.7 PEC needle

The integrated extinction for the PEC needle of length $2a$ oriented along the $\hat{\boldsymbol{e}}_3$-direction is given by (4.3) and (4.8) in the limit $\xi \to 0$. The result is

$$\int_0^\infty \sigma_{\text{ext}}(\lambda)\, \mathrm{d}\lambda = \frac{4\pi^3 a^3}{3} \begin{cases} \mathcal{O}(\xi^2) & \text{(TE)} \\ \dfrac{\sin^2\theta}{\ln 2/\xi - 1} + \mathcal{O}(\xi^2) & \text{(TM)} \end{cases} \tag{5.6}$$

The right hand side of (5.6) can also be derived from the long wavelength limit of the T-matrix [3].

The integrated extinction (5.6) is seen to vanish for both polarizations in the limit $\xi \to 0$. Since the extinction cross section is non-negative, this implies that it vanishes almost everywhere except on a set of measure zero consisting of the denumerable resonances for which an integer multiple of $\lambda/2$ coincides with the length of the needle. This result is illustrated numerically in Fig. 11, which shows the extinction cross section, σ_{ext}, for the PEC needle for the TM-polarization at normal incidence. Note that, due to symmetry, only resonances corresponding to ka equal to an odd multiple of $\pi/2$ are excited at normal incidence. The numerically integrated extinctions in Fig. 11 agree well with (5.6). The relative errors are less than 0.5% with an integration interval $ka \in [0, 12]$ for the three curves.

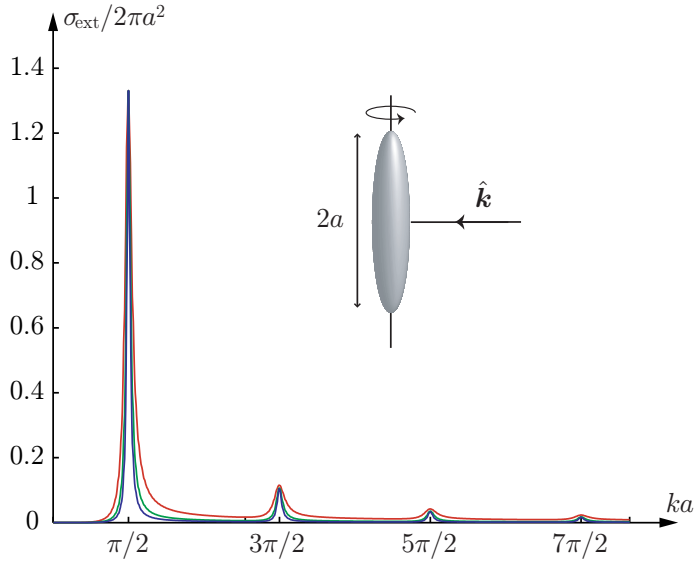

Figure 11: The extinction cross section, σ_{ext}, in units of $2\pi a^2$ as function of ka for the PEC needle of length $2a$. The needle is approximated by a prolate spheroid with semi-axis ratio 10^{-3} for the outermost, 10^{-5} for the intervening, and 10^{-7} for the innermost curve. The calculation is based on the T-matrix approach [3].

6 Concluding remarks

The integrated extinction is an example of what is referred to in modern physics as a dispersion relation [21]. The basic idea for the dispersion relations is that certain linear and causal physical quantities with known high-frequency (short wavelength) asymptotic are boundary values of holomorphic functions of one or more complex variables.

The major results of this paper are the proof and illustrations of the integrated extinction for linear, passive, and anisotropic scatterers. It is shown that the integrated extinction is monotonically increasing in the material properties. Moreover, the electric and magnetic material properties contribute equally to the integrated extinction. It is also shown that the integrated extinction is useful in deriving physical limitations on broadband scattering.

The integrated extinction is particularly important from an antenna point of view, since it generalizes the physical limitations on the antenna performance derived by Chu [5] for the smallest circumscribing sphere. These new limitations, which can be shown to relate bandwidth and directivity of any antenna in terms of volume and shape, are reported in [7]. The integrated extinction is also of great interest in applications to broadband scattering by artificial material models such as metamaterials. In this application, it provides physical limitations on scattering by general material models [27]. Moreover, the bounds presented in Sec. 3 may be of use to bound material parameters in inverse scattering problems. All these applications to material modeling and inverse scattering problems are currently under investigation, and will be reported in forthcoming papers.

Additional theoretical work on the integrated extinction also includes bi-anisotropy and diamagnetics, which will be reported elsewhere. Finally, it should be noted that the concept of the integrated extinction with minor changes also holds in linear acoustics [26].

Acknowledgments

The financial support by the Swedish Research Council is gratefully acknowledged.

Appendix A The polarizability dyadics

For an anisotropic scatterer modeled by the material dyadic $\boldsymbol{\tau}$ (electric susceptibility dyadic $\boldsymbol{\chi}_{\mathrm{e}}$ without a conductivity term, or magnetic susceptibility dyadic $\boldsymbol{\chi}_{\mathrm{m}}$), the total electric field $\boldsymbol{E}$ (similarly for the magnetic field $\boldsymbol{H}$) satisfies

$$\begin{cases} \nabla \times \boldsymbol{E}(\boldsymbol{x}) = \boldsymbol{0} \\ \nabla \cdot ((\boldsymbol{\tau}(\boldsymbol{x}) + \mathbf{I}) \cdot \boldsymbol{E}(\boldsymbol{x})) = 0 \end{cases} \quad \boldsymbol{x} \in \mathbb{R}^3 \tag{A.1}$$

Here, $\boldsymbol{\tau}$ is assumed to be a symmetric dyadic at all points $\boldsymbol{x}$ and sufficiently regular to justify the operations below.

Decompose the total field $\boldsymbol{E}$ as $\boldsymbol{E}_j = E_0\hat{\boldsymbol{e}}_j + \boldsymbol{E}_{\mathrm{s}j}$, where $j = 1, 2, 3$. The pertinent partial differential equation for the scattered field $\boldsymbol{E}_{\mathrm{s}j}$ is then

$$\begin{cases} \nabla \times \boldsymbol{E}_{\mathrm{s}j}(\boldsymbol{x}) = \boldsymbol{0} \\ \nabla \cdot ((\boldsymbol{\tau}(\boldsymbol{x}) + \mathbf{I}) \cdot \boldsymbol{E}_{\mathrm{s}j}(\boldsymbol{x})) = -E_0 \nabla \cdot (\boldsymbol{\tau}(\boldsymbol{x}) \cdot \hat{\boldsymbol{e}}_j) \end{cases} \quad \boldsymbol{x} \in \mathbb{R}^3 \tag{A.2}$$

together with the asymptotic condition $\boldsymbol{E}_{\mathrm{s}j}(\boldsymbol{x}) \to \mathcal{O}(|\boldsymbol{x}|^{-3})$ as $|\boldsymbol{x}| \to \infty$.

The first condition in (A.2) implies that there exists a potential Φ_j related to the scattered field as $\boldsymbol{E}_{\mathrm{s}j} = -\nabla\Phi_j$ satisfying

$$\begin{cases} \nabla \cdot ((\boldsymbol{\tau}(\boldsymbol{x}) + \mathbf{I}) \cdot \nabla\Phi_j(\boldsymbol{x})) = E_0 \nabla \cdot (\boldsymbol{\tau}(\boldsymbol{x}) \cdot \hat{\boldsymbol{e}}_j) \\ \Phi_j(\boldsymbol{x}) \to \mathcal{O}(|\boldsymbol{x}|^{-2}) \text{ as } |\boldsymbol{x}| \to \infty \end{cases} \quad \boldsymbol{x} \in \mathbb{R}^3 \tag{A.3}$$

This problem has a unique solution. The entries of the polarizability dyadic $\boldsymbol{\gamma}$ ($\boldsymbol{\gamma}_{\mathrm{e}}$ or $\boldsymbol{\gamma}_{\mathrm{m}}$ depending on whether the problem is electric or magnetic) is then ($i, j = 1, 2, 3$)

$$\hat{\boldsymbol{e}}_i \cdot \boldsymbol{\gamma} \cdot \hat{\boldsymbol{e}}_j = \frac{1}{E_0} \hat{\boldsymbol{e}}_i \cdot \int_{\mathbb{R}^3} \boldsymbol{\tau}(\boldsymbol{x}) \cdot \boldsymbol{E}_j(\boldsymbol{x}) \, \mathrm{d}v. \tag{A.4}$$

Scale this solution by a factor α, *i.e.*, let $\boldsymbol{x} \longrightarrow \boldsymbol{x}' = \alpha\boldsymbol{x}$, with material dyadic $\boldsymbol{\tau}'(\boldsymbol{x}') = \boldsymbol{\tau}(\boldsymbol{x})$, and denote the solution to the new problem by $\Phi'_j(\boldsymbol{x}')$. The new problem then satisfies

$$\begin{cases} \nabla' \cdot \big((\boldsymbol{\tau}'(\boldsymbol{x}') + \mathbf{I}) \cdot \nabla'\Phi'_j(\boldsymbol{x}')\big) = E_0 \nabla' \cdot (\boldsymbol{\tau}'(\boldsymbol{x}') \cdot \hat{\boldsymbol{e}}_j) \\ \Phi'_j(\boldsymbol{x}') \to 0 \text{ as } |\boldsymbol{x}'| \to \infty \end{cases} \quad \boldsymbol{x}' \in \mathbb{R}^3 \tag{A.5}$$

or in the unscaled coordinates

$$\begin{cases} \alpha^{-2}\nabla\cdot\big((\boldsymbol{\tau}(\boldsymbol{x})+\mathbf{I})\cdot\nabla\Phi_j'(\alpha\boldsymbol{x})\big) = E_0\alpha^{-1}\nabla\cdot(\boldsymbol{\tau}(\boldsymbol{x})\cdot\hat{\boldsymbol{e}}_j) \\ \Phi_j'(\alpha\boldsymbol{x})\to 0 \text{ as } |\boldsymbol{x}|\to\infty \end{cases} \quad \boldsymbol{x}\in\mathbb{R}^3 \tag{A.6}$$

Due to the unique solubility of the boundary value problem (A.3), $\Phi_j'(\boldsymbol{x}') = \alpha\Phi_j(\boldsymbol{x})$, and consequently $\boldsymbol{E}_j'(\boldsymbol{x}') = \boldsymbol{E}_j(\boldsymbol{x}) = \boldsymbol{E}_j(\boldsymbol{x}'/\alpha)$. The polarizability dyadic for the scaled problem then becomes

$$\hat{\boldsymbol{e}}_i\cdot\boldsymbol{\gamma}'\cdot\hat{\boldsymbol{e}}_j = \hat{\boldsymbol{e}}_i\cdot\int_{\mathbb{R}^3}\boldsymbol{\tau}'(\boldsymbol{x}')\cdot\boldsymbol{E}_j'(\boldsymbol{x}')\,\mathrm{d}v = \alpha^3\hat{\boldsymbol{e}}_i\cdot\int_{\mathbb{R}^3}\boldsymbol{\tau}(\boldsymbol{x})\cdot\boldsymbol{E}_j(\boldsymbol{x})\,\mathrm{d}v, \tag{A.7}$$

and we see that $\boldsymbol{\gamma}$ scales with the volume $|V|\sim\alpha^3$.

A.1 Symmetry

The polarizability dyadic $\boldsymbol{\gamma}$ is symmetric, since $\boldsymbol{\tau}$ is assumed symmetric at all points $\boldsymbol{x}$. In fact, from (A.4),

$$\hat{\boldsymbol{e}}_i\cdot\boldsymbol{\gamma}\cdot\hat{\boldsymbol{e}}_j = \hat{\boldsymbol{e}}_i\cdot\int_{\mathbb{R}^3}\boldsymbol{\tau}(\boldsymbol{x})\cdot\hat{\boldsymbol{e}}_j\,\mathrm{d}v - \frac{1}{E_0}\hat{\boldsymbol{e}}_i\cdot\int_{\mathbb{R}^3}\boldsymbol{\tau}(\boldsymbol{x})\cdot\nabla\Phi_j(\boldsymbol{x})\,\mathrm{d}v. \tag{A.8}$$

The last integral in (A.8) is rewritten as

$$\begin{aligned} &\hat{\boldsymbol{e}}_i\cdot\int_{\mathbb{R}^3}\boldsymbol{\tau}(\boldsymbol{x})\cdot\nabla\Phi_j(\boldsymbol{x})\,\mathrm{d}v \\ &= \int_{\mathbb{R}^3}\nabla\cdot(\hat{\boldsymbol{e}}_i\cdot\boldsymbol{\tau}(\boldsymbol{x})\Phi_j(\boldsymbol{x}))\,\mathrm{d}v - \int_{\mathbb{R}^3}\nabla\cdot(\hat{\boldsymbol{e}}_i\cdot\boldsymbol{\tau}(\boldsymbol{x}))\,\Phi_j(\boldsymbol{x})\,\mathrm{d}v \\ &= -\int_{\mathbb{R}^3}\nabla\cdot(\boldsymbol{\tau}(\boldsymbol{x})\cdot\hat{\boldsymbol{e}}_i)\,\Phi_j(\boldsymbol{x})\,\mathrm{d}v \\ &= -\frac{1}{E_0}\int_{\mathbb{R}^3}\nabla\cdot((\boldsymbol{\tau}(\boldsymbol{x})+\mathbf{I})\cdot\nabla\Phi_i(\boldsymbol{x}))\,\Phi_j(\boldsymbol{x})\,\mathrm{d}v, \end{aligned} \tag{A.9}$$

due to (A.3) provided $\boldsymbol{\tau}$ is symmetric at all points $\boldsymbol{x}$. Furthermore,

$$\begin{aligned} &\hat{\boldsymbol{e}}_i\cdot\int_{\mathbb{R}^3}\boldsymbol{\tau}(\boldsymbol{x})\cdot\nabla\Phi_j(\boldsymbol{x})\,\mathrm{d}v \\ &= -\frac{1}{E_0}\int_{\mathbb{R}^3}\nabla\cdot\{((\boldsymbol{\tau}(\boldsymbol{x})+\mathbf{I})\cdot\nabla\Phi_i(\boldsymbol{x}))\,\Phi_j(\boldsymbol{x})\}\,\mathrm{d}v \\ &+ \frac{1}{E_0}\int_{\mathbb{R}^3}\nabla\Phi_j(\boldsymbol{x})\cdot((\boldsymbol{\tau}(\boldsymbol{x})+\mathbf{I})\cdot\nabla\Phi_i(\boldsymbol{x}))\,\mathrm{d}v \\ &= \frac{1}{E_0}\int_{\mathbb{R}^3}\nabla\Phi_j(\boldsymbol{x})\cdot((\boldsymbol{\tau}(\boldsymbol{x})+\mathbf{I})\cdot\nabla\Phi_i(\boldsymbol{x}))\,\mathrm{d}v. \end{aligned} \tag{A.10}$$

The polarizability dyadic (A.8) therefore becomes

$$\hat{\boldsymbol{e}}_i\cdot\boldsymbol{\gamma}\cdot\hat{\boldsymbol{e}}_j = \hat{\boldsymbol{e}}_i\cdot\int_{\mathbb{R}^3}\boldsymbol{\tau}(\boldsymbol{x})\cdot\hat{\boldsymbol{e}}_j\,\mathrm{d}v - \frac{1}{E_0^2}\int_{\mathbb{R}^3}\nabla\Phi_j(\boldsymbol{x})\cdot((\boldsymbol{\tau}(\boldsymbol{x})+\mathbf{I})\cdot\nabla\Phi_i(\boldsymbol{x}))\,\mathrm{d}v, \tag{A.11}$$

which clearly is symmetric in the indices i and j if $\boldsymbol{\tau}$ is symmetric at all points $\boldsymbol{x}$.

A.2 High-contrast limit

In the high-contrast limit, when the entries of the material dyadic become infinitely large independent of $\boldsymbol{x}$, the appropriate surface integral representation of the polarizability dyadic is [15, p. 22]

$$\hat{\boldsymbol{e}}_i \cdot \boldsymbol{\gamma} \cdot \hat{\boldsymbol{e}}_j = \frac{1}{E_0} \hat{\boldsymbol{e}}_i \cdot \sum_{n=1}^{N} \int_{S_n} (\hat{\boldsymbol{\nu}}(\boldsymbol{x}) \Phi_j(\boldsymbol{x}) - \boldsymbol{x} \hat{\boldsymbol{\nu}}(\boldsymbol{x}) \cdot \nabla \Phi_j(\boldsymbol{x})) \, \mathrm{d}S, \tag{A.12}$$

where S_n, $n = 1, 2, \ldots, N$ denote the bounding surfaces (outward-directed unit normal $\hat{\boldsymbol{\nu}}$) of the domain outside the material (we assume that $\boldsymbol{\tau}$ is compactly supported). Moreover, $\Psi_j(\boldsymbol{x}) = \Phi_j(\boldsymbol{x}) - E_0 x_j$, is the solution to ($n = 1, 2, \ldots, N$)

$$\begin{cases} \nabla^2 \Psi_j(\boldsymbol{x}) = 0, \quad \boldsymbol{x} \text{ outside } S_n \\ \displaystyle\int_{S_n} \hat{\boldsymbol{\nu}}(\boldsymbol{x}) \cdot \nabla \, \Psi_j(\boldsymbol{x})|_+ \, \mathrm{d}S = 0 \\ \Psi_j(\boldsymbol{x}) \to -E_0 x_j + \mathcal{O}(|\boldsymbol{x}|^{-2}) \text{ as } |\boldsymbol{x}| \to \infty \end{cases} \tag{A.13}$$

With similar arguments as above, we find that the eigenvalues of the high-contrast polarizability dyadic also scale with the volume. For the relation with the capacitance concept, we refer to [15].

References

[1] M. Abramowitz and I. A. Stegun, editors. *Handbook of Mathematical Functions*. Applied Mathematics Series No. 55. National Bureau of Standards, Washington D.C., 1970.

[2] K. V. Beard and C. C. Chuang. A new model for the equilibrium shape of raindrops. *J. Atmos. Sci.*, **44**(11), 1509–1524, 1986.

[3] J. Björkberg and G. Kristensson. Electromagnetic scattering by a perfectly conducting elliptic disk. *Canad. J. Phys.*, **65**(7), 723–734, 1987.

[4] C. F. Bohren and D. R. Huffman. *Absorption and Scattering of Light by Small Particles*. John Wiley & Sons, New York, 1983.

[5] L. J. Chu. Physical limitations of omni-directional antennas. *Appl. Phys.*, **19**, 1163–1175, 1948.

[6] R. E. Collin. *Field Theory of Guided Waves*. IEEE Press, New York, second edition, 1991.

[7] M. Gustafsson, C. Sohl, and G. Kristensson. Physical limitations on antennas of arbitrary shape. *Proc. R. Soc. A*, **463**(2086), 2589–2607, 2007.

[8] M. Gustafsson. On the non-uniqueness of the electromagnetic instantaneous response. *J. Phys. A: Math. Gen.*, **36**, 1743–1758, 2003.

[9] F. John. Extremum problems with inequalities as subsidiary conditions. In O. E. Friedrichs, K. O. Neugebauer and J. J. Stoker, editors, *Studies and Essays: Courant Anniversary Volume*, pages 187–204. Wiley-Interscience, New York, 1948.

[10] D. S. Jones. Low frequency electromagnetic radiation. *J. Inst. Maths. Applics.*, **23**(4), 421–447, 1979.

[11] D. S. Jones. Scattering by inhomogeneous dielectric particles. *Quart. J. Mech. Appl. Math.*, **38**, 135–155, 1985.

[12] R. C. Jones. A generalization of the dielectric ellipsoid problem. *Phys. Rev.*, **68**(3–4), 93–96, 1945.

[13] H. W. E. Jung. Über die kleinste Kugel, die eine räumliche Figur einschliesst. *Journal für die reine und angewandte Mathematik*, **123**, 241–257, 1901.

[14] U. Kaatze. Microwave dielectric properties of water. In A. Kraszewski, editor, *Microwave Aquametry*, chapter 2, pages 37–53. IEEE Press, New York, 1996.

[15] R. E. Kleinman and T. B. A. Senior. Rayleigh scattering. In V. V. Varadan and V. K. Varadan, editors, *Low and High Frequency Asymptotics*, volume 2 of *Handbook on Acoustic, Electromagnetic and Elastic Wave Scattering*, chapter 1, pages 1–70. Elsevier Science Publishers, Amsterdam, 1986.

[16] G. Kristensson and P. C. Waterman. The T-matrix for acoustic and electromagnetic scattering by circular disks. *J. Acoust. Soc. Am.*, **72**(5), 1612–1625, 1982.

[17] L. D. Landau, E. M. Lifshitz, and L. P. Pitaevskiĭ. *Electrodynamics of Continuous Media*. Pergamon Press, Oxford, second edition, 1984.

[18] G. Mie. Beiträge zur Optik trüber Medien, speziell kolloidaler Metallösungen. *Ann. Phys. Leipzig*, **25**, 377–445, 1908.

[19] M. I. Mishchenko and L. D. Travis. Capabilities and limitations of a current FORTRAN implementation of the T-matrix method for randomly oriented, rotationally symmetric scatterers. *J. Quant. Spectrosc. Radiat. Transfer*, **60**(3), 309–324, 1998.

[20] R. G. Newton. *Scattering Theory of Waves and Particles*. Dover Publications, New York, second edition, 2002.

[21] H. M. Nussenzveig. *Causality and Dispersion Relations*. Academic Press, London, 1972.

[22] H. M. Nussenzveig. *Diffraction Effects in Semiclassical Scattering*. Cambridge University Press, Cambridge, U.K., 1992.

[23] J. A. Osborn. Demagnetizing factors of the general ellipsoid. *Phys. Rev.*, **67**, 351–357, 1945.

[24] E. M. Purcell. On the absorption and emission of light by interstellar grains. *J. Astrophys.*, **158**, 433–440, 1969.

[25] A. Sihvola, P. Ylä-Oijala, S. Järvenpää, and J. Avelin. Polarizabilities of Platonic solids. *IEEE Trans. Antennas Propagat.*, **52**(9), 2226–2233, 2004.

[26] C. Sohl, M. Gustafsson, and G. Kristensson. The integrated extinction for broadband scattering of acoustic waves. Technical Report LUTEDX/(TEAT-7156)/1–10/(2007), Lund University, Department of Electrical and Information Technology, P.O. Box 118, S-221 00 Lund, Sweden, 2007. http://www.eit.lth.se.

[27] C. Sohl, M. Gustafsson, and G. Kristensson. Physical limitations on metamaterials: Restrictions on scattering and absorption over a frequency interval. Technical Report LUTEDX/(TEAT-7154)/1–11/(2007), Lund University, Department of Electrical and Information Technology, P.O. Box 118, S-221 00 Lund, Sweden, 2007. http://www.eit.lth.se.

[28] J. W. Strutt. On the light from the sky, its polarization and colour. *Phil. Mag.*, **41**, 107–120 and 274–279, April 1871. Also published in Lord Rayleigh, Scientific Papers, volume I, Cambridge University Press, Cambridge, 1899.

[29] J. R. Taylor. *Scattering Theory: The Quantum Theory of Nonrelativistic Collisions*. Robert E. Krieger Publishing Company, Malabar, 1983.

[30] E. C. Titchmarsh. *Introduction to the Theory of Fourier Integrals*. Oxford University Press, Oxford, second edition, 1948.

[31] H. van de Hulst. *Light Scattering by Small Particles*. John Wiley & Sons, Inc., New York, 1957.

[32] A. D. Yaghjian. Electric dyadic Green's functions in the source region. *Proc. IEEE*, **68**(2), 248–263, 1980.

Physical limitations on metamaterials: Restrictions on scattering and absorption over a frequency interval

Paper II

Christian Sohl, Mats Gustafsson, and Gerhard Kristensson

Based on: C. Sohl, M. Gustafsson, and G. Kristensson. Physical limitations on metamaterials: Restrictions on scattering and absorption over a frequency interval. *Journal of Physics D: Applied Physics*, vol. 40, no. 22, pp. 7146–7151, November 2007.

Abstract

A limitation on the extinction cross section, valid for all scatterers satisfying some basic physical assumptions, is investigated. The physical bound is obtained from the holomorphic properties of the forward scattering dyadic. The analysis focuses on the consequences for engineered composite materials with negative permittivity and permeability, *i.e.*, metamaterials. From a broadband point of view, the limitations imply that there is no fundamental difference between metamaterials and ordinary materials with respect to scattering and absorption. The analysis is illustrated by three numerical examples of metamaterials modeled by temporal dispersion.

1 Introduction

Since the investigation of negative refractive index materials by V. G. Veselago in Ref. 14, there has been an enormous theoretical and experimental interest in the possibilities of such materials. These materials are often referred to as metamaterials, even though a metamaterial in general is a much broader concept of a structured material, and not necessarily composed of materials with negative permittivity and permeability values. Negative refractive index materials seem not to occur naturally, and if they can be manufactured, they are often claimed to possess extraordinary properties promising for various physical applications, see Refs. 9 and 11, and references therein.

The scattering properties of obstacles consisting of metamaterials have been of considerable scientific interest during the last decade. Mostly canonical geometries, such as concentric spheres and cylinders, see *e.g.*, Ref. 10, have been employed, and designs of scatterers that both increase and decrease the scattering properties have been reported in the literature.

The analysis presented in this paper shows that, from a broadband point of view, the scattering and absorption properties of any material (not just metamaterials) that satisfies certain basic physical assumptions, are limited by the static electric and magnetic behavior of the composed materials. In particular, it is shown that, when these bounds are applied to low-frequency resonances of metamaterials, large scattering effects have to be traded for bandwidth. Specifically, the lower the resonance frequency, the higher its Q-value. For a single frequency, metamaterials may possess exceptional characteristics, but, since bandwidth is essential in many applications, it is important to study metamaterials over a frequency interval, and with physically realistic dispersion models.

The results presented in this paper are independent of how the material that constitutes the scatterer is constructed or produced. This broad range of material models is a consequence of the fact that the analysis is solely based on the principles of causality and power conservation applied to a set of linear, passive, and time-translational invariant constitutive relations.

This paper is a direct application of the theory for broadband scattering introduced in Ref. 12. In addition to material modeling, the theory has also been applied

successfully to physical bounds on arbitrary antennas in Refs. 1 and 3. The underlying mathematical description for broadband scattering is motivated by the study of causality and dispersion relations in the scattering theory of waves and particles in Refs. 7 and 8.

2 Derivation of the integrated extinction

Consider a localized and bounded scatterer with support $V \subset \mathbb{R}^3$ of arbitrary shape. The electromagnetic field in V is modeled by the Maxwell equations with general heterogeneous and anisotropic constitutive relations. The constitutive relations are expressed in terms of the electric and magnetic susceptibility dyadics, $\boldsymbol{\chi}_{\mathrm{e}}$ and $\boldsymbol{\chi}_{\mathrm{m}}$, respectively. Due to the heterogeneous character of $\boldsymbol{\chi}_{\mathrm{e}}$ and $\boldsymbol{\chi}_{\mathrm{m}}$, V can be interpreted both as a single scatterer and as a set of multiple scatterers. The present analysis includes the perfectly electric conducting material model as well as general temporal dispersion with or without a conductivity term. The analysis can also be extended with minor changes to bi-anisotropic materials with the same conclusions drawn.

The direct scattering problem addressed in this paper is Fourier-synthesized plane wave scattering by V (time dependence $\mathrm{e}^{-\mathrm{i}\omega t}$, where $\omega \in [0, \infty)$ denotes the angular frequency). The incident wave is assumed to impinge in the $\hat{\boldsymbol{k}}$-direction with an electric field $\boldsymbol{E}_{\mathrm{i}}$ depending only on the difference $\tau = \mathrm{c}_0 t - \hat{\boldsymbol{k}} \cdot \boldsymbol{x}$, where $\boldsymbol{x}$ denotes the position vector in space. Introduce the far-field amplitude $\boldsymbol{F}$ via $\boldsymbol{E}_{\mathrm{s}} = \boldsymbol{F}(\mathrm{c}_0 t - x; \hat{\boldsymbol{x}})/x + \mathcal{O}(x^{-2})$ as $x \to \infty$, where $\boldsymbol{E}_{\mathrm{s}}$ represents the scattered electric field. Under the assumption that the constitutive relations of V are linear and time-translational invariant, $\boldsymbol{F}$ is given by the convolution

$$\boldsymbol{F}(\tau; \hat{\boldsymbol{x}}) = \int_{-\infty}^{\infty} \mathbf{S}_{\mathrm{t}}(\tau - \tau'; \hat{\boldsymbol{k}}, \hat{\boldsymbol{x}}) \cdot \boldsymbol{E}_{\mathrm{i}}(\tau') \, \mathrm{d}\tau'. \tag{2.1}$$

Here, $\mathbf{S}_{\mathrm{t}}$ is assumed to be primitive causal in the forward direction, *i.e.*, $\mathbf{S}_{\mathrm{t}}(\tau, \hat{\boldsymbol{k}}, \hat{\boldsymbol{k}}) = \mathbf{0}$ for $\tau < 0$, see Ref. 8. Furthermore, introduce the forward scattering dyadic $\mathbf{S}$ as the Fourier transform of $\mathbf{S}_{\mathrm{t}}$ evaluated in the forward direction, *i.e.*,

$$\mathbf{S}(k; \hat{\boldsymbol{k}}) = \int_{0^-}^{\infty} \mathbf{S}_{\mathrm{t}}(\tau; \hat{\boldsymbol{k}}, \hat{\boldsymbol{k}}) \mathrm{e}^{\mathrm{i}k\tau} \, \mathrm{d}\tau, \tag{2.2}$$

where $k = \omega/\mathrm{c}_0$ is the wave number in free space. The Fourier transform (2.2) corresponds to an ensemble of plane waves with time dependence $\mathrm{e}^{-\mathrm{i}\omega t}$. The extension of (2.2) to complex-valued k with $\operatorname{Im} k \geqslant 0$ improves the convergence of the integral and implies that $\mathbf{S}$ is holomorphic in the upper half part of the complex k-plane. Recall that the cross symmetry $\mathbf{S}(k; \hat{\boldsymbol{k}}) = \mathbf{S}^*(-k^*; \hat{\boldsymbol{k}})$ for $\operatorname{Im} k \geqslant 0$ is a direct consequence of such an extension.

Introduce $\boldsymbol{E}_0$ as the Fourier amplitude of the incident wave, and let $\hat{\boldsymbol{e}} = \boldsymbol{E}_0/|\boldsymbol{E}_0|$ denote the associated electric polarization. Recall that $\boldsymbol{E}_0$ is subject to the constraint of transverse wave propagation, *i.e.*, $\boldsymbol{E}_0 \cdot \hat{\boldsymbol{k}} = 0$. Under the assumption that $\hat{\boldsymbol{e}}$ and $\hat{\boldsymbol{k}}$ are independent of k, it follows from the analysis above that also

$\varrho(k) = \hat{\boldsymbol{e}}^* \cdot \mathbf{S}(k; \hat{\boldsymbol{k}}) \cdot \hat{\boldsymbol{e}}/k^2$ is holomorphic for $\operatorname{Im} k > 0$. Cauchy's integral theorem applied to ϱ then yields, see Ref. 12,

$$\varrho(\mathrm{i}\varepsilon) = \int_0^\pi \frac{\varrho(\mathrm{i}\varepsilon - \varepsilon \mathrm{e}^{\mathrm{i}\phi})}{2\pi} \,\mathrm{d}\phi + \int_0^\pi \frac{\varrho(\mathrm{i}\varepsilon + R\mathrm{e}^{\mathrm{i}\phi})}{2\pi} \,\mathrm{d}\phi + \int_{\varepsilon<|k|<R} \frac{\varrho(k+\mathrm{i}\varepsilon)}{2\pi \mathrm{i} k} \,\mathrm{d}k. \quad (2.3)$$

Here, it is assumed that ϱ is sufficiently regular to extend the integration contour to the real axis in the last integral on the right-hand side of (2.3). Relation (2.3) is subject to the limits $\varepsilon \to 0+$ and $R \to \infty$.

The long-wavelength limit of ϱ on the left-hand side of (2.3) and the integrand in the first integral on the right-hand side can be derived from a power series expansion of the Maxwell equations. The result is, see Ref. 4,

$$\varrho(\varepsilon) = \frac{1}{4\pi} \Big(\hat{\boldsymbol{e}}^* \cdot \boldsymbol{\gamma}_\mathrm{e} \cdot \hat{\boldsymbol{e}} + (\hat{\boldsymbol{k}} \times \hat{\boldsymbol{e}}^*) \cdot \boldsymbol{\gamma}_\mathrm{m} \cdot (\hat{\boldsymbol{k}} \times \hat{\boldsymbol{e}}) \Big) + \mathcal{O}(\varepsilon) \quad \text{as } \varepsilon \to 0+, \quad (2.4)$$

where $\boldsymbol{\gamma}_\mathrm{e}$ and $\boldsymbol{\gamma}_\mathrm{m}$ denote the electric and magnetic polarizability dyadics, respectively. For the appropriate definitions of $\boldsymbol{\gamma}_\mathrm{e}$ and $\boldsymbol{\gamma}_\mathrm{m}$, and some of their physical properties, see Ref. 12 and references therein.

The second integral on the right-hand side of (2.3) vanishes in the limit as $R \to \infty$ according to the extinction paradox in Ref. 13. In terms of ϱ, a generalization of the extinction paradox states that $\varrho(k) = -A/(2\pi \mathrm{i} k) + \mathcal{O}(|k|^{-2})$ as $|k| \to \infty$. The constant A is real-valued since $\mathbf{S}(\mathrm{i}k; \hat{\boldsymbol{k}})$ is real-valued for real-valued k. For a large class of scatterers, A coincides with the geometrical cross section area in the forward direction. The disappearance of the second integral on the right-hand side of (2.3) is also supported by the fact that the high-frequency response of a material is non-unique from a modeling point of view, see Ref. 2.

From the above details, it is clear that the real part of (2.3) when subject to the limits $\varepsilon \to 0+$ and $R \to \infty$, yields

$$\varrho(0) = \frac{1}{2}\varrho(0) + \frac{1}{8\pi^2} \int_{-\infty}^{\infty} \frac{\sigma_\mathrm{ext}(k)}{k^2} \,\mathrm{d}k, \quad (2.5)$$

where the optical theorem $\sigma_\mathrm{ext}(k) = 4\pi k \operatorname{Im} \varrho(k)$ has been utilized, see Ref. 12. Here, the extinction cross section σ_ext is defined as the sum of the scattered and absorbed power divided by the power flux of the incident wave. Recall that the optical theorem is a direct consequence of power conservation, see Ref. 7. Relation (2.4) inserted into (2.5) using the wavelength variable $\lambda = 2\pi/k$ finally yields

$$\int_0^\infty \sigma_\mathrm{ext}(\lambda) \,\mathrm{d}\lambda = \pi^2 \Big(\hat{\boldsymbol{e}}^* \cdot \boldsymbol{\gamma}_\mathrm{e} \cdot \hat{\boldsymbol{e}} + (\hat{\boldsymbol{k}} \times \hat{\boldsymbol{e}}^*) \cdot \boldsymbol{\gamma}_\mathrm{m} \cdot (\hat{\boldsymbol{k}} \times \hat{\boldsymbol{e}}) \Big). \quad (2.6)$$

The left-hand side of (2.6) is referred to as the integrated extinction. For additional details on the derivation of (2.6), see Ref. 12.

Relation (2.6) is slightly modified when an isotropic conductivity term $\mathrm{i}\varsigma/\omega\epsilon_0$ is introduced in $\boldsymbol{\chi}_\mathrm{e}$ for some region of V, see Ref. 12. The scalar conductivity ς is non-negative and assumed independent of ω. In the presence of a conductivity term, the analysis in Ref. 4 shows that the right-hand side of (2.6) should be evaluated

in the limit as the eigenvalues of $\boldsymbol{\chi}_{\mathrm{e}}$ approach infinity independently of $\boldsymbol{\chi}_{\mathrm{m}}$. The perfectly electric conducting case is obtained as the eigenvalues of $\boldsymbol{\chi}_{\mathrm{m}}$ in addition approach -1.

Electric and magnetic material properties are seen to be treated on equal footing in (2.6), both in terms of polarization and material description. Furthermore, the right-hand side of (2.6) depends solely on the long-wavelength limit or static response of V, while the left-hand side is a dynamic quantity which unites the scattering and absorption properties of V. Recall that $\boldsymbol{\gamma}_{\mathrm{e}}$ and $\boldsymbol{\gamma}_{\mathrm{m}}$ only are functions of the geometry of V and the long-wavelength susceptibilities $\boldsymbol{\chi}_{\mathrm{e}}(0) = \lim_{\omega\to 0} \boldsymbol{\chi}_{\mathrm{e}}(\omega)$ and $\boldsymbol{\chi}_{\mathrm{m}}(0) = \lim_{\omega\to 0} \boldsymbol{\chi}_{\mathrm{m}}(\omega)$. Here, $\boldsymbol{\chi}_{\mathrm{e}}(0)$ and $\boldsymbol{\chi}_{\mathrm{m}}(0)$ are real-valued in the case of vanishing conductivity. For heterogeneous structures, the long-wavelength susceptibilities $\boldsymbol{\chi}_{\mathrm{e}}(0)$ and $\boldsymbol{\chi}_{\mathrm{m}}(0)$ also depend on the position vector $\boldsymbol{x}$.

In many applications, the scatterer is randomly oriented with respect to an ensemble of incident waves. For this purpose, the averaged extinction cross section $\bar{\sigma}_{\mathrm{ext}}$ is conveniently introduced by averaging (2.6) over the unit sphere in $\mathbb{R}^3$, *i.e.*,

$$\int_0^\infty \bar{\sigma}_{\mathrm{ext}}(\lambda)\, \mathrm{d}\lambda = \frac{\pi^2}{3} \operatorname{trace}(\boldsymbol{\gamma}_{\mathrm{e}} + \boldsymbol{\gamma}_{\mathrm{m}}). \tag{2.7}$$

For non-spherical particles, (2.7) provides a neat verification of (2.6) without specifying the orientation of V with respect to the incident wave, see Sec. 4.1.

3 Bounds on scattering and absorption

For applications to exotic material models such as metamaterials, it is beneficial to introduce the high-contrast polarizability dyadic $\boldsymbol{\gamma}_\infty$ as the limit of either $\boldsymbol{\gamma}_{\mathrm{e}}$ or $\boldsymbol{\gamma}_{\mathrm{m}}$ when the eigenvalues of $\boldsymbol{\chi}_{\mathrm{e}}(0)$ or $\boldsymbol{\chi}_{\mathrm{m}}(0)$ simultaneously become infinitely large. From the variational results of $\boldsymbol{\gamma}_{\mathrm{e}}$ and $\boldsymbol{\gamma}_{\mathrm{m}}$ discussed in Ref. 12 and references therein, it follows that both $\boldsymbol{\gamma}_{\mathrm{e}}$ and $\boldsymbol{\gamma}_{\mathrm{m}}$ are bounded from above by $\boldsymbol{\gamma}_\infty$, *i.e.*,

$$\int_0^\infty \sigma_{\mathrm{ext}}(\lambda)\, \mathrm{d}\lambda \leqslant \pi^2 \left(\hat{\boldsymbol{e}}^* \cdot \boldsymbol{\gamma}_\infty \cdot \hat{\boldsymbol{e}} + (\hat{\boldsymbol{k}} \times \hat{\boldsymbol{e}}^*) \cdot \boldsymbol{\gamma}_\infty \cdot (\hat{\boldsymbol{k}} \times \hat{\boldsymbol{e}}) \right). \tag{3.1}$$

The right-hand side of (3.1) is independent of any material parameters, depending only on the geometry and the orientation of V with respect to the incident wave. The right-hand side can, independent of $\hat{\boldsymbol{e}}$ and $\hat{\boldsymbol{k}}$, further be estimated from above by the eigenvalues of $\boldsymbol{\gamma}_\infty$, see Ref. 12.

The integrated extinction can be used to derive various bounds and variational results for broadband scattering. Since the extinction cross section σ_{ext} by definition is non-negative, the left-hand side of (2.6) can be estimated as

$$|\Lambda| \inf_{\lambda\in\Lambda} \sigma(\lambda) \leqslant \int_\Lambda \sigma(\lambda)\, \mathrm{d}\lambda \leqslant \int_0^\infty \sigma_{\mathrm{ext}}(\lambda)\, \mathrm{d}\lambda, \tag{3.2}$$

where $\Lambda \subset [0,\infty)$ denotes an arbitrary wavelength interval with absolute bandwidth $|\Lambda|$. Here, σ represents any of the scattering, absorption and extinction cross

sections, see Ref. 12 for their appropriate definitions. The quantity $|\Lambda| \inf_{\lambda\in\Lambda} \sigma(\lambda)$ in (3.2) is particularly useful for box-shaped bounds, *viz.*,

$$|\Lambda| \inf_{\lambda\in\Lambda} \sigma(\lambda) \leqslant \pi^2 \left(\hat{\boldsymbol{e}}^* \cdot \boldsymbol{\gamma}_\mathrm{e} \cdot \hat{\boldsymbol{e}} + (\hat{\boldsymbol{k}} \times \hat{\boldsymbol{e}}^*) \cdot \boldsymbol{\gamma}_\mathrm{m} \cdot (\hat{\boldsymbol{k}} \times \hat{\boldsymbol{e}}) \right). \tag{3.3}$$

From (3.2) and (3.3) it is clear that the long-wavelength limit response of V also provides upper bounds on scattering and absorption within any finite wavelength interval Λ. Analogous to (3.1), the right-hand side of (3.3) can also be estimated from above by $\boldsymbol{\gamma}_\infty$ and its associated eigenvalues. An important consequence of the fact that (2.6) and (3.3) only depend on the long-wavelength limit response of V is that they are independent of any temporal dispersion.

The fact that (2.6) and (3.3) are independent of any temporal dispersion implies that there is no fundamental difference in scattering and absorption (in a broadband sense) between metamaterials and ordinary materials, as long as the static properties of the materials are identical. In fact, it is well known that passive materials must be temporally dispersive since the Kramers-Kronig relations imply that $\boldsymbol{\chi}_\mathrm{e}(0)$ and $\boldsymbol{\chi}_\mathrm{m}(0)$ elementwise are non-negative in the absence of a conductivity term, see Ref. 5. Recall that the Kramers-Kronig relations are a direct consequence of causality and passivity, see Ref. 8.

When an isotropic conductivity term $\mathrm{i}\varsigma/\omega\epsilon_0$ is present in $\boldsymbol{\chi}_\mathrm{e}$, the Kramers-Kronig relations must be modified due to the singular behavior of $\boldsymbol{\chi}_\mathrm{e}$. As mentioned above, the analysis in Ref. 4 shows that the introduction of such a term in $\boldsymbol{\chi}_\mathrm{e}$ implies that $\boldsymbol{\gamma}_\mathrm{e}$ should be substituted for $\boldsymbol{\gamma}_\infty$ on the right-hand side of (2.6) and (3.3).

Two popular models for temporal dispersion for metamaterials are the Drude and Lorentz models, see (4.3) and Ref. 8, respectively. The Drude model is often preferred over the Lorentz model since it provides a wider bandwidth over which the eigenvalues of $\boldsymbol{\chi}_\mathrm{e}$ and $\boldsymbol{\chi}_\mathrm{m}$ attain values with a real part less than -1. However, based on the above arguments, it is uninteresting from the point of view of (2.6) and (3.3) which dispersion model is used to characterize metamaterials as long as the model is passive and it satisfies causality.

In summary, the physical bounds on scattering and absorption discussed in Ref. 12 also hold for any passive and causal metamaterial. For a single frequency, metamaterials may possess extraordinary physical properties, but over a frequency interval they are with respect to scattering and absorption not different from materials with non-negative real parts of the eigenvalues of $\boldsymbol{\chi}_\mathrm{e}$ and $\boldsymbol{\chi}_\mathrm{m}$.

4 Numerical synthesis of metamaterials

In the following, numerical results for three temporally dispersive scatterers are discussed in terms of the physical bounds in Sec. 3. The examples provide a numerical synthesis of three different fictitious metamaterials. For convenience, the examples are restricted to isotropic material parameters, *i.e.*, $\boldsymbol{\chi}_\mathrm{e} = \chi_\mathrm{e}\mathbf{I}_3$ and $\boldsymbol{\chi}_\mathrm{m} = \chi_\mathrm{m}\mathbf{I}_3$, where $\mathbf{I}_3$ denotes the unit dyadic in $\mathbb{R}^3$. A similar example for a Lorentz dispersive finite cylinder is given in Ref. 12.

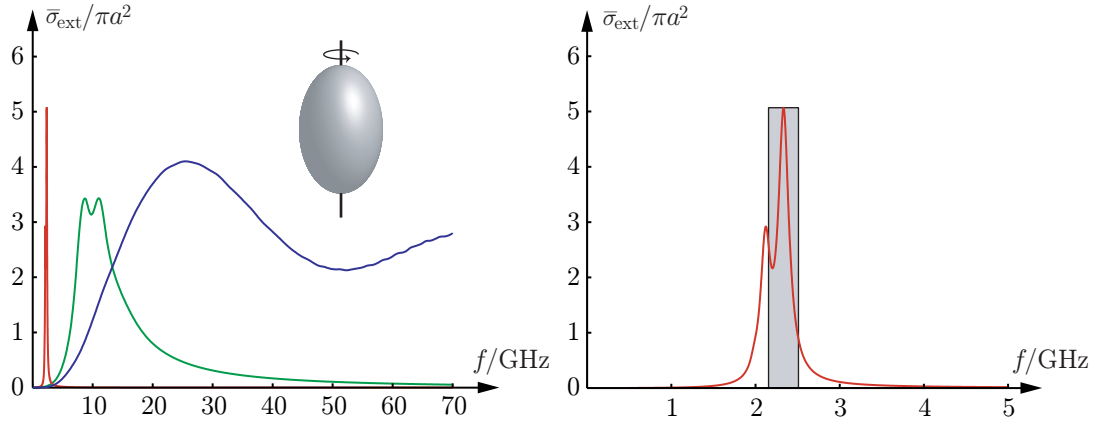

Figure 1: The averaged extinction cross section $\bar{\sigma}_{\text{ext}}$ as a function of the frequency in GHz for a prolate spheroid with semi-axis ratio $\xi = 1/2$. Note the normalization with πa^2, where $a = 1\,\text{cm}$ denotes the radius of the volume-equivalent sphere. The right figure is an expansion of the left figure for low frequencies.

4.1 The Lorentz dispersive prolate spheroid

The averaged extinction cross section $\bar{\sigma}_{\text{ext}}$ for a homogeneous and non-magnetic ($\chi_{\text{m}} = 0$) prolate spheroid with semi-axis ratio $\xi = 1/2$ is depicted in Fig. 1. The prolate spheroid is temporally dispersive with electric susceptibility given by the Lorentz model, see Ref. 8,

$$\chi_{\text{e}}(\omega) = \frac{\omega_{\text{p}}^2}{\omega_0^2 - \omega^2 - \text{i}\omega\nu}, \tag{4.1}$$

where $(\omega - \omega_0)\,\text{Re}\,\chi_{\text{e}}(\omega) \leqslant 0$ and $\text{Im}\,\chi_{\text{e}}(\omega) \geqslant 0$ for $\omega \in [0, \infty)$. Explicit values of ω_{p}, ω_0, and ν for the two curves with peaks at 2 GHz and 10 GHz are $\omega_{\text{p}} = \omega_0 = 4\pi \cdot 10^9\,\text{rad/s}$, $\nu = 7 \cdot 10^8\,\text{rad/s}$, and $\omega_{\text{p}} = \omega_0 = 20\pi \cdot 10^9\,\text{rad/s}$, $\nu = 10^{10}\,\text{rad/s}$, respectively. The third curve in the left figure represents the non-dispersive case with $\chi_{\text{e}} = 1$, independent of ω. Since the three curves in the left figure have the same values of χ_{e} in the long-wavelength limit, *i.e.*, $\chi_{\text{e}}(0) = 1$, it follows from (2.6) that their integrated extinctions are identical.

Closed-form expressions of the averaged integrated extinction (2.7) exist for the prolate and oblate spheroids, see Ref. 12. For a non-magnetic spheroid with semi-axis ratio ξ,

$$\int_0^\infty \bar{\sigma}_{\text{ext}}(\lambda)\,\text{d}\lambda = \frac{4\pi^3 a^3}{9} \sum_{j=1}^{3} \frac{1}{1 + L_j(\xi)}, \tag{4.2}$$

where $L_j(\xi)$ denote the associated depolarizing factors, and a is the radius of the volume-equivalent sphere. For a prolate spheroid with semi-axis ratio $\xi = 1/2$, the depolarizing factors are approximately given by $L_1(1/2) = L_2(1/2) = 0.4132$ and $L_3(1/2) = 0.1736$, see Ref. 12. For the prolate spheroid in Fig. 1, $a = 1\,\text{cm}$, and the right-hand side of (4.2) is equal to $31.24\,\text{cm}^3$. The integrated extinction $31.24\,\text{cm}^3$ is numerically confirmed with arbitrary precision for the three curves in Fig. 1.

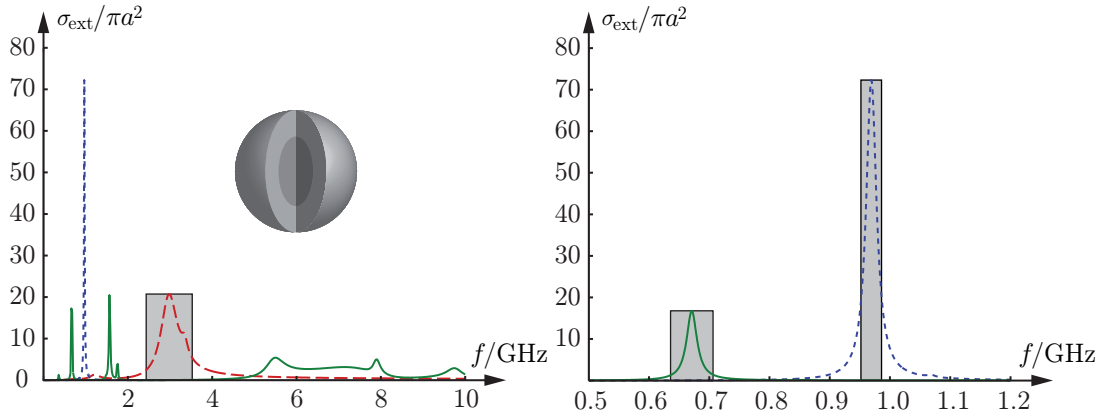

Figure 2: The extinction cross section σ_{ext} as a function of the frequency in GHz for a stratified sphere which attains simultaneously negative values of the permittivity and the permeability. Note the normalization with the geometrical cross section area πa^2, where $a = 1\,\text{cm}$ denotes the outer radius of the sphere. The right figure is an expansion of the left figure for low frequencies.

The right figure in Fig. 1 is a close-up of the 2 GHz peak in the left figure. The shaded box represents an artificial scatterer with the averaged integrated extinction $31.24\,\text{cm}^3$ centered around the peak. The integrated extinction for the boundary curve of the box and the three curves in the left figure are identical. Note that the width of the box is approximately equal to the bandwidth of the peak when evaluated at half amplitude. The calculation in Fig. 1 is based on the null-field method in Ref. 6. For a similar example given by the Lorentz dispersive cylinder, see Ref. 12.

4.2 The Drude dispersive stratified sphere

The extinction cross section σ_{ext} for a stratified sphere with two layers of equal volume is depicted in Fig. 2. The stratified sphere is temporally dispersive with identical electric ($\ell = \text{e}$) and magnetic ($\ell = \text{m}$) material parameters given by the Drude model

$$\chi_\ell(\omega) = \frac{\text{i}\varsigma}{\epsilon_0\omega(1 - \text{i}\omega\tau)}, \qquad \ell = \text{e}, \text{m}, \tag{4.3}$$

where $\varsigma > 0$ and $\tau > 0$. The real and imaginary parts of (4.3) read

$$\chi_\ell(\omega) = \frac{-\varsigma\tau}{\epsilon_0(1 + \omega^2\tau^2)} + \text{i}\frac{\varsigma}{\epsilon_0\omega(1 + \omega^2\tau^2)}, \qquad \ell = \text{e}, \text{m}. \tag{4.4}$$

Since $\text{Re}\,\chi_\ell(\omega) < -1$ for low frequencies, the stratified sphere in Fig. 2 attains simultaneously negative values of the permittivity and the permeability at these frequencies. The calculation in Fig. 2 is based on a Möbius transformation applied to the classical Mie series expansion in Refs. 7 and 8.

The two curves in the left figure with peaks at 0.97 GHz (dotted line) and 3.0 GHz (dashed line) correspond to a homogeneous sphere with identical material properties

in the inner and outer layers. These two curves are characterized by the relaxation times $\tau = 10^{-8}\,\mathrm{s}$ and $\tau = 10^{-9}\,\mathrm{s}$, respectively, and with conductivity $\varsigma = 10\,\mathrm{S/m}$ in both cases. For the third curve (solid line) with peaks at 0.67 GHz and 1.6 GHz, the material parameters of the outer layer are $\tau = 8 \cdot 10^{-9}\,\mathrm{s}$ and $\varsigma = 10\,\mathrm{S/m}$, while the inner layer is non-dispersive with $\chi_{\mathrm{e}1} = 10$ and $\chi_{\mathrm{m}1} = 0$ independent of $\omega \in [0, \infty)$. The right figure provides a close-up of the peaks at 0.67 GHz and 0.97 GHz.

Closed-form expressions of the electric and the magnetic polarizability dyadics exist for the stratified sphere, see Ref. 12. For a stratified sphere of two layers, the integrated extinction can be expressed as

$$\int_0^\infty \sigma_{\mathrm{ext}}(\lambda)\,\mathrm{d}\lambda = 4\pi^3 a^3 \sum_{\ell=\mathrm{e,m}} \frac{\chi_{\ell 2}(\chi_{\ell 1} + 2\chi_{\ell 2} + 3) + \zeta^3(2\chi_{\ell 2} + 3)(\chi_{\ell 1} - \chi_{\ell 2})}{(\chi_{\ell 2} + 3)(\chi_{\ell 1} + 2\chi_{\ell 2} + 3) + 2\zeta^3\chi_{\ell 2}(\chi_{\ell 1} - \chi_{\ell 2})}, \quad (4.5)$$

where a denotes the outer radius, and $\chi_{\ell 1}$ and $\chi_{\ell 2}$ represent the long-wavelength susceptibilities of the inner and the outer layers, respectively. Furthermore, $\zeta \in [0, 1]$ denotes the quotient between the inner and the outer radii.

Since (4.3) is characterized by a conductivity term which is singular at $\omega = 0$, the above discussion implies that the right-hand side of (4.5) is subject to the limits $\chi_{\mathrm{e}2} \to \infty$ and $\chi_{\mathrm{m}2} \to \infty$. Based on this observation, it is concluded that the integrated extinction for the three curves in Fig. 2 are identical and equal to $8\pi^3 a^3$ or $248.0\,\mathrm{cm}^3$, where $a = 1\,\mathrm{cm}$ has been used. In contrast to the limits $\chi_{\mathrm{e}1} \to \infty$ and $\chi_{\mathrm{m}1} \to \infty$, this result is independent of ζ as well as $\chi_{\mathrm{e}1}$ and $\chi_{\mathrm{m}1}$. Note that (2.4) and (2.6) yield that the integrated extinction $8\pi^3 a^3$ is equivalent to the long-wavelength limit $\varrho(0) = 2a^3$. The integrated extinction $248.0\,\mathrm{cm}^3$ is numerically confirmed with arbitrary precision for the three curves in Fig. 2.

The physical bound (3.3) is depicted by the shaded boxes in Fig. 2 (close-up at low frequencies on the right-hand side of Fig. 2). These boxes correspond to artificial scatterers with extinction cross sections supported at the peaks 0.67 GHz, 0.97 GHz, and 3.0 GHz. The integrated extinction of each box is equal to $248.0\,\mathrm{cm}^3$ and coincides with the integrated extinction for any other curve in the figure. From Fig. 2 it is seen how the width of the boxes increase as the peaks are suppressed in magnitude and shifted towards higher frequencies. Note that the tiny peaks at 0.36 GHz (solid line) and 1.2 GHz (dashed line) constitute a large part of the integrated extinction, thus implying that the peaks at 0.67 GHz and 3.0 GHz do not fit the boxes that well in comparison with the box centered at 0.97 GHz. Recall that the area of the boxes in Fig. 2 only depends on the properties of V in the long-wavelength limit, and is hence independent of any temporal dispersion for positive frequencies.

The extinction cross section for a non-magnetic stratified sphere with two layers of equal volume is depicted in Fig. 3. The stratified sphere is temporally dispersive with electric susceptibility χ_{e} given by the Drude model (4.3). The two curves in the left figure with peaks at 0.96 GHz (dotted line) and 2.7 GHz (dashed line) correspond to the homogeneous case with identical material parameters in both layers: $\tau = 10^{-8}\,\mathrm{s}$ and $\tau = 10^{-9}\,\mathrm{s}$, respectively, with $\varsigma = 10\,\mathrm{S/m}$ in both cases. For the third curve with a peak at 1.4 GHz (solid line), the material parameters of the

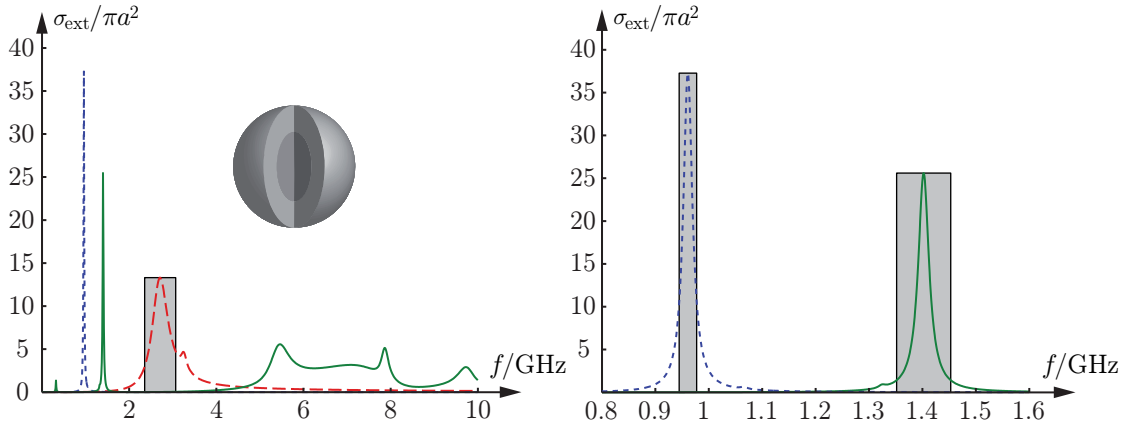

Figure 3: The extinction cross section σ_{ext} as function of the frequency in GHz for a non-magnetic stratified sphere which attain negative values of the permittivity. Note the normalization with the geometrical cross section πa^2, where $a = 1\,\text{cm}$ denotes the outer radius of the sphere.

outer layer is $\varsigma = 10\,\text{S/m}$ and $\tau = 10^{-8}\,\text{s}$, while the inner layer is non-dispersive with $\chi_{\text{e1}} = 10$ independent of $\omega \in [0, \infty)$. The left figure in Fig. 3 is a close-up of the peaks at 0.96 GHz and 1.4 GHz with the associated box-shaped bounds marked in the figure.

Since the stratified sphere in Fig. 3 has the same electric long-wavelength response as the scatterer in Fig. 2, but in addition is non-magnetic, it follows from (4.5) that the integrated extinction of the scatterer in Fig. 3 is half the integrated extinction of the scatterer in Fig. 2, *i.e.*, $4\pi^3 a^3$ or $124.0\,\text{cm}^3$. This observation is a direct consequence of the symmetry in (4.5) with respect to electric ($\ell = \text{e}$) and magnetic ($\ell = \text{m}$) material parameters. The result is also supported by the fact that the amplitude of, say, the peak at 0.97 GHz in Fig. 2 is approximately twice as large as the corresponding peak at 0.96 GHz in Fig. 3.

5 Conclusions

The conclusions of this paper are clear: independent of how the materials in the scatterer are defined and modeled by temporal dispersion (*i.e.*, irrespective of the sign of the real parts of the permittivity and permeability for positive frequencies), the holomorphic properties of the forward scattering dyadic imply that, from a broadband point of view, there is no fundamental difference in scattering and absorption between metamaterials and ordinary materials. For a single frequency, metamaterials may possess extraordinary properties, but with respect to any bandwidth, such materials are not different from any other naturally formed substances as long as causality and passivity are obeyed. As a consequence, if metamaterials are used to lower the resonance frequency, this is done at the cost of an increasing Q-value of the resonance. The present analysis includes materials modeled by anisotropy and heterogeneity, and can be extended to general bi-anisotropic materials as well.

For example, the introduction of chirality does not contribute to the integrated extinction since all chiral effects vanish in the long-wavelength limit.

It is believed that there are more physical quantities that apply to the theory of broadband scattering in Ref. 12. Thus far, the theoretical findings have been applied successfully to arbitrary antennas in Refs. 1 and 3 to yield physical bounds on antenna performance and information capacity. Similar broadband bounds on cloaking and invisibility using metamaterials and other exotic material models are currently under investigation.

Acknowledgments

The financial support by the Swedish Research Council is gratefully acknowledged. The authors are also grateful for fruitful discussions with Prof. Anders Karlsson at the Department of Electrical and Information Technology, Lund University, Sweden.

References

[1] M. Gustafsson, C. Sohl, and G. Kristensson. Physical limitations on antennas of arbitrary shape. *Proc. R. Soc. A*, **463**(2086), 2589–2607, 2007.

[2] M. Gustafsson. On the non-uniqueness of the electromagnetic instantaneous response. *J. Phys. A: Math. Gen.*, **36**, 1743–1758, 2003.

[3] M. Gustafsson, C. Sohl, and G. Kristensson. Physical limitations on antennas of arbitrary shape. Technical Report LUTEDX/(TEAT-7153)/1–37/(2007), Lund University, Department of Electrical and Information Technology, P.O. Box 118, S-221 00 Lund, Sweden, 2007. http://www.eit.lth.se.

[4] R. E. Kleinman and T. B. A. Senior. Rayleigh scattering. In V. V. Varadan and V. K. Varadan, editors, *Low and High Frequency Asymptotics*, volume 2 of *Handbook on Acoustic, Electromagnetic and Elastic Wave Scattering*, chapter 1, pages 1–70. Elsevier Science Publishers, Amsterdam, 1986.

[5] L. D. Landau, E. M. Lifshitz, and L. P. Pitaevskiĭ. *Electrodynamics of Continuous Media*. Pergamon Press, Oxford, second edition, 1984.

[6] M. I. Mishchenko and L. D. Travis. Capabilities and limitations of a current FORTRAN implementation of the T-matrix method for randomly oriented, rotationally symmetric scatterers. *J. Quant. Spectrosc. Radiat. Transfer*, **60**(3), 309–324, 1998.

[7] R. G. Newton. *Scattering Theory of Waves and Particles*. Springer-Verlag, New York, 1982.

[8] H. M. Nussenzveig. *Causality and Dispersion Relations*. Academic Press, London, 1972.

[9] S. A. Ramakrishna. Physics of negative refractive index materials. *Reports on Progress in Physics*, **68**(2), 449–521, 2005.

[10] R. Ruppin. Extinction properties of a sphere with negative permittivity and permeability. *Solid State Commun.*, **116**, 411–415, 2000.

[11] D. R. Smith, J. B. Pendry, and M. C. K. Wiltshire. Metamaterials and negative refractive index. *Science*, **305**(5685), 788–792, 2004.

[12] C. Sohl, M. Gustafsson, and G. Kristensson. Physical limitations on broadband scattering by heterogeneous obstacles. *J. Phys. A: Math. Theor.*, **40**(36), 11165–11182, 2007.

[13] H. van de Hulst. *Light Scattering by Small Particles*. John Wiley & Sons, Inc., New York, 1957.

[14] V. G. Veselago. The electrodynamics of substances with simultaneously negative values of ϵ and μ. *Sov. Phys. Usp.*, **10**(4), 509–514, 1968.

A scattering and absorption identity for metamaterials: Experimental results and comparison with theory

Paper III

Christian Sohl, Christer Larsson, Mats Gustafsson, and Gerhard Kristensson

Based on: C. Sohl, C. Larsson, M. Gustafsson, and G. Kristensson. A scattering and absorption identity for metamaterials: Experimental results and comparison with theory. *Journal of Applied Physics*, vol. 103, no. 5, paper 054906, March 2008.

Abstract

A dispersion relation for the combined effect of scattering and absorption of electromagnetic waves is presented for a large class of linear and passive material models. By invoking the optical theorem, the result states that the extinction cross section integrated over all frequencies is equal to the static limit of the extinction volume. The present paper focuses on an attempt to experimentally verify this sum rule by measuring the monostatic radar cross section of a fabricated sample of metamaterial. In particular, the paper utilizes the idea that, for a specific class of targets, the scattered fields in the forward and backward directions are identical. It is concluded that the theoretical findings are in good agreement with measurements performed in the frequency range $[3.2, 19.5]$ GHz.

1 Introduction

Since the contemporary discoveries of the Kramers-Kronig relations [3, 6] in 1926–1927, dispersion relation techniques have been applied successfully to disparate wave phenomena to model the structural properties of wave interaction with matter. There are at least two main advantages of dispersion relations for the analysis of electromagnetic waves: (i) they provide a consistency check of calculated quantities when the underlying mathematical model is known to satisfy causality, and (ii) they may be used to verify whether a given mathematical model or an experimental outcome behaves causally or not. In addition, based on the field theory in Ref. 9, dispersion relations can also be used to establish far-reaching connections between concepts of different physical meanings. A comprehensive review of dispersion relations in material modeling and scattering theory is presented in Ref. 16.

The optical theorem or forward scattering theorem relates the extinction cross section, or the combined effective area of absorption and scattering, to the forward scattering dyadic [8]. As a consequence, the magnitude and phase of the scattered field in a single direction solely determine the total power extinguished from an applied external field. In a series of papers, see Refs. 13, 14 and 15, the use of a forward dispersion relation for the combined effect of scattering and absorption is exploited by invoking the optical theorem. In particular, it is established that the extinction cross section integrated over all frequencies is related to the static or long-wavelength polarizability dyadics. This result is rather intriguing, and one of its many consequences shows great potential for future applications in antenna theory [4, 12].

Although, the theory of broadband extinction of acoustic and electromagnetic waves is by now well established [13, 14], and numerical simulations show excellent agreement with the theory, its experimental verification is of scientific importance. Thus, the purpose of the present paper is to verify a certain aspect of these theoretical findings by measuring the monostatic radar cross section of a fabricated sample of metamaterial. The choice of considering a metamaterial is due to the fact that such materials do not occur naturally, and if they can be manufactured, they are often claimed to possess extraordinary properties that are promising for various

engineering applications. In addition, experimental challenges associated with the extinction measurements are discussed in the paper. For example, to circumvent the weak signal strength of the forward scattered field in comparison with the incident field, the present paper utilizes the idea that, for a specific class of targets, the scattered fields in the forward and backward directions are identical.

The main theoretical results used in this paper are summarized in Sec. 2, and the experimental results are developed and explained in Sec. 3. Finally, the paper is ended with some conclusions.

2 A scattering and absorption identity

Consider the direct scattering problem of a plane electromagnetic wave $\mathrm{e}^{\mathrm{i}k\hat{\boldsymbol{k}}\cdot\boldsymbol{x}}\hat{\boldsymbol{e}}$ (time dependence $\mathrm{e}^{-\mathrm{i}2\pi ft}$) of unit amplitude impinging in the $\hat{\boldsymbol{k}}$-direction on a target embedded in free space with phase velocity c_0. The material of the scatterer is modeled by a set of linear and passive constitutive relations that are assumed to be time invariant [16]. Let $\hat{\boldsymbol{k}}$ and $\hat{\boldsymbol{e}}$ be independent of the wave number $k = 2\pi f/\mathrm{c}_0 \in [0, \infty)$, and introduce the differential cross section [5, 10]

$$\frac{\mathrm{d}\sigma}{\mathrm{d}\Omega}(k; \hat{\boldsymbol{k}} \curvearrowright \hat{\boldsymbol{x}}, \hat{\boldsymbol{e}}) = |\mathbf{S}(k; \hat{\boldsymbol{k}} \curvearrowright \hat{\boldsymbol{x}}) \cdot \hat{\boldsymbol{e}}|^2 \tag{2.1}$$

as a measure of the disturbance of the applied field due to the presence of the target. Here, the notation $\hat{\boldsymbol{k}} \curvearrowright \hat{\boldsymbol{x}}$ refers to the scattering of a plane wave evaluated at the origin into an outgoing spherical wave in the $\hat{\boldsymbol{x}}$-direction. The scattering dyadic $\mathbf{S}$ is independent of $\hat{\boldsymbol{e}}$, and it is defined in terms of the scattered electric field $\boldsymbol{E}_\mathrm{s}$ as [9]

$$\mathbf{S}(k; \hat{\boldsymbol{k}} \curvearrowright \hat{\boldsymbol{x}}) \cdot \hat{\boldsymbol{e}} = \lim_{x\to\infty} x\mathrm{e}^{-\mathrm{i}kx}\boldsymbol{E}_\mathrm{s}(k; \boldsymbol{x}), \tag{2.2}$$

where $x = |\boldsymbol{x}|$ denotes the magnitude of the position vector, and $\hat{\boldsymbol{x}} = \boldsymbol{x}/x$. In particular, 4π times the differential cross section in the backward direction, $\hat{\boldsymbol{x}} = -\hat{\boldsymbol{k}}$, yields the monostatic radar cross section [5, 10]

$$\sigma_\mathrm{RCS}(k; \hat{\boldsymbol{k}}, \hat{\boldsymbol{e}}) = 4\pi|\mathbf{S}(k; \hat{\boldsymbol{k}} \curvearrowright -\hat{\boldsymbol{k}}) \cdot \hat{\boldsymbol{e}}|^2. \tag{2.3}$$

A target's overall scattering properties are commonly quantified by the scattering cross section σ_s, defined as the total power scattered in all directions divided by the incident power flux. It is obtained by integrating (2.1) over the unit sphere with respect to the $\hat{\boldsymbol{x}}$-direction, *i.e.*,

$$\sigma_\mathrm{s}(k; \hat{\boldsymbol{k}}, \hat{\boldsymbol{e}}) = \int_\Omega \frac{\mathrm{d}\sigma}{\mathrm{d}\Omega}(k; \hat{\boldsymbol{k}} \curvearrowright \hat{\boldsymbol{x}}, \hat{\boldsymbol{e}})\ \mathrm{d}S, \tag{2.4}$$

where the surface measure $\mathrm{d}S = \sin\theta\,\mathrm{d}\theta\,\mathrm{d}\phi$ depends on the zenith and azimuthal variables $\theta \in [0, \pi]$ and $\phi \in [0, 2\pi)$, respectively. Based on (2.4), the extinction cross section $\sigma_\mathrm{ext} = \sigma_\mathrm{s} + \sigma_\mathrm{a}$ is defined as the sum of the scattering and absorption cross sections, where the latter is a measure of the absorbed power in the target [1].

The extinction cross section is also determined from the knowledge of the scattering dyadic in the forward direction, $\hat{\boldsymbol{x}} = \hat{\boldsymbol{k}}$, *viz.*,

$$\sigma_{\text{ext}}(k; \hat{\boldsymbol{k}}, \hat{\boldsymbol{e}}) = \frac{4\pi}{k} \operatorname{Im} \left\{ \hat{\boldsymbol{e}}^* \cdot \mathbf{S}(k; \hat{\boldsymbol{k}} \curvearrowright \hat{\boldsymbol{k}}) \cdot \hat{\boldsymbol{e}} \right\}, \tag{2.5}$$

where an asterisk denotes the complex conjugate. Relation (2.5) is known as the optical theorem, and it is applicable to many different wave motions such as acoustic waves, electromagnetic waves, and elementary particles [8, 16].

From the integral representations in Ref. 17, or the discussion on p. 11 in Ref. 10, it follows that, for a planar and infinitely thin target, the forward and backward scattering dyadics are equal, *i.e.*,

$$\mathbf{S}(k; \hat{\boldsymbol{k}} \curvearrowright \hat{\boldsymbol{k}}) \cdot \hat{\boldsymbol{e}} = \mathbf{S}(k; \hat{\boldsymbol{k}} \curvearrowright -\hat{\boldsymbol{k}}) \cdot \hat{\boldsymbol{e}}. \tag{2.6}$$

For this specific class of targets, (2.6) enables extinction measurements to be carried out by simply detecting the scattered field in the backward direction. Of course, both the magnitude and phase of the scattered field have to be identified. In particular, (2.6) implies that the differential cross sections in the forward and backward directions are identical, *i.e.*,

$$\frac{\mathrm{d}\sigma}{\mathrm{d}\Omega}(k; \hat{\boldsymbol{k}} \curvearrowright \hat{\boldsymbol{k}}, \hat{\boldsymbol{e}}) = \frac{\mathrm{d}\sigma}{\mathrm{d}\Omega}(k; \hat{\boldsymbol{k}} \curvearrowright -\hat{\boldsymbol{k}}, \hat{\boldsymbol{e}}). \tag{2.7}$$

Note that more general methods must be introduced to experimentally determine the forward scattered field when the above-stated assumptions are violated; see pp. 320–323 in Ref. 1.

A dispersion relation for the combined effect of scattering and absorption of electromagnetic waves is derived in Ref. 14 from the holomorphic properties of the forward scattering dyadic. The result is a sum rule for the extinction cross section valid for a large class of linear and passive targets:

$$\int_0^\infty \frac{\sigma_{\text{ext}}(k; \hat{\boldsymbol{k}}, \hat{\boldsymbol{e}})}{k^2} \, \mathrm{d}k = 2\pi^2 \varrho(0; \hat{\boldsymbol{k}}, \hat{\boldsymbol{e}}), \tag{2.8}$$

where the static limit on the right-hand side of (2.8) is non-negative [14]. Here, the extinction volume $\varrho(k; \hat{\boldsymbol{k}}, \hat{\boldsymbol{e}})$ is defined by the complex-valued quantity

$$\varrho(k; \hat{\boldsymbol{k}}, \hat{\boldsymbol{e}}) = \frac{\hat{\boldsymbol{e}}^* \cdot \mathbf{S}(k; \hat{\boldsymbol{k}} \curvearrowright \hat{\boldsymbol{k}}) \cdot \hat{\boldsymbol{e}}}{k^2}. \tag{2.9}$$

In particular, the extinction cross section is related to the imaginary part of the extinction volume via the optical theorem $\sigma_{\text{ext}}(k; \hat{\boldsymbol{k}}, \hat{\boldsymbol{e}}) = 4\pi k \operatorname{Im} \varrho(k; \hat{\boldsymbol{k}}, \hat{\boldsymbol{e}})$. The extinction volume satisfies the Hilbert transform, *i.e.*, the improper integral [18]

$$\varrho(k; \hat{\boldsymbol{k}}, \hat{\boldsymbol{e}}) = \frac{1}{\mathrm{i}\pi} \mathcal{P} \int_{-\infty}^{\infty} \frac{\varrho(k'; \hat{\boldsymbol{k}}, \hat{\boldsymbol{e}})}{k' - k} \, \mathrm{d}k', \tag{2.10}$$

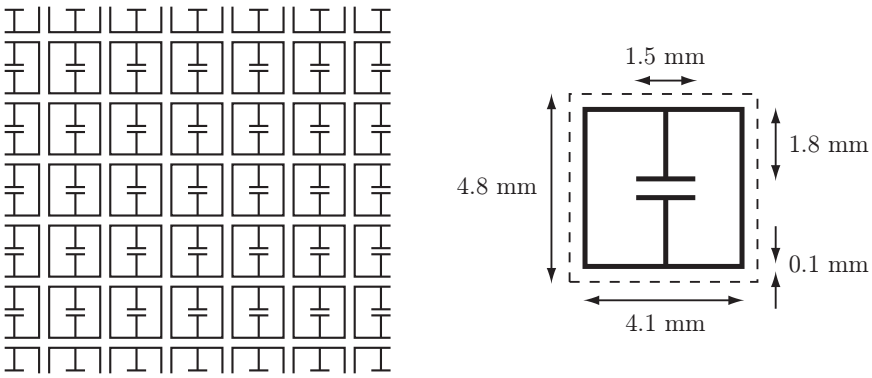

Figure 1: A section of the fabricated sample (left) and a close-up of the square unit cell (right). The linewidth of the printed circuits is 0.1 mm.

where $\mathcal{P}$ denotes the Cauchy principal value. The fact that the extinction cross section is non-negative implies that the left-hand side of (2.8) can be estimated from below by the corresponding integral over the finite interval $[k_1, k_2]$, *viz.*,

$$\int_{k_1}^{k_2} \frac{\sigma(k;\hat{\boldsymbol{k}},\hat{\boldsymbol{e}})}{k^2}\,\mathrm{d}k \leqslant \int_0^{\infty} \frac{\sigma_{\mathrm{ext}}(k;\hat{\boldsymbol{k}},\hat{\boldsymbol{e}})}{k^2}\,\mathrm{d}k = 2\pi^2\varrho(0;\hat{\boldsymbol{k}},\hat{\boldsymbol{e}}), \tag{2.11}$$

where σ denotes any of σ_{ext}, σ_{s}, and σ_{a}. The interpretation of (2.11) is that there is only a limited amount of scattering and absorption available in the range $[k_1, k_2]$, and that this amount is bounded from above by the static limit of the extinction volume [14, 15].

3 Experimental results

In this section, measurements of the extinction cross section are presented for a fabricated sample of metamaterial. The sample design and the experimental setup are described, and the outcome of the measurements is compared with the theoretical results in Sec. 2.

3.1 Sample design and experimental setup

The fabricated sample is designed as a single-layer planar array of capacitive resonators tuned to be resonant at 8.5 GHz. It consists of 29×29 unit cells supported by a square FR4 substrate of edge length $a = 140$ mm and thickness 0.3 mm, see Fig. 1. The relative dielectric constant of the substrate varies between 4.4 and 4.2 in the frequency range $f \in [3.2, 19.5]$ GHz, with an overall loss tangent less than $5 \cdot 10^{-3}$. In the literature, the sample design in Fig. 1 is commonly referred to as a negative permittivity metamaterial [11].

Monostatic radar cross section measurements are performed in the anechoic chamber at Saab Bofors Dynamics, Linköping, Sweden. The sample is mounted on an expanded polystyrene sample holder and placed on a pylon. Dual polarized

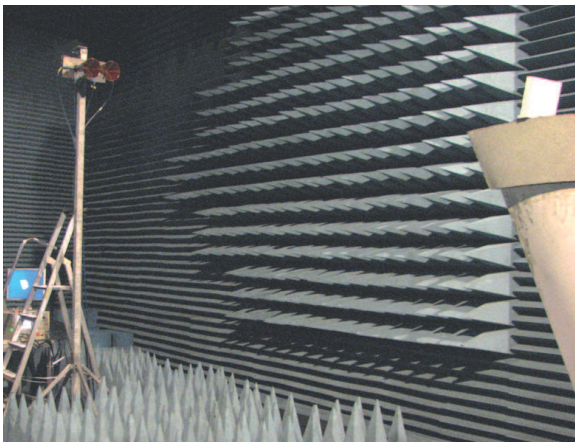

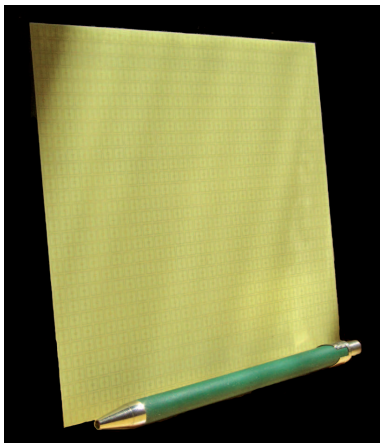

Figure 2: The experimental setup in the anechoic chamber (left) and the fabricated sample with 29×29 unit cells supported by a square FR4 substrate of edge length 140 mm (right).

ridged circular waveguide horns are positioned at a distance of 3.5 m from the sample, see Fig. 2, and an Agilent Performance Network Analyzer (PNA) is used for transmitting a continuous wave without online hardware or software gating. The polarizations of the transmitted and received fields are parallel to the capacitors in the printed circuit, *i.e.*, vertically in Fig. 1. The original frequency range $[2, 20]$ GHz is reduced to $[3.2, 19.5]$ GHz due to a range domain filtering of the data. The latter frequency interval is sampled with 7246 equidistant points corresponding to an unambiguous spatial range of 66.7 m, which is sufficient to avoid influence of room reverberations.

Calibration including both amplitude and phase is performed using a metal plate with the same outer dimensions as the sample in Fig. 2. A physical optics approximation for a perfectly electric conducting plate is adopted as the calibration reference, see p. 523 in Ref. 10. In order to validate the calibration, a method of moments calculation is also performed. It is concluded that the method of moments solution does not deviate significantly from the physical optics approximation. In addition to being a calibration reference, the metal plate is also used to align the experimental setup using the specular reflection of the plate.

The data from the measurements are processed by a coherent subtraction of the background followed by a calibration. The frequency domain data are then transformed to the range domain, where the response from the sample is selected from the range profile using a 1.1 m spatial gate. Finally, the selected data are transformed back to the frequency domain.

3.2 Measurement results and comparison with theory

The monostatic radar cross section of the sample is depicted by the solid line on the left-hand side of Fig. 3. In the figure, the first resonance at $f_0 \approx 8.5$ GHz is observed as well as an increase in the monostatic radar cross section with frequency,

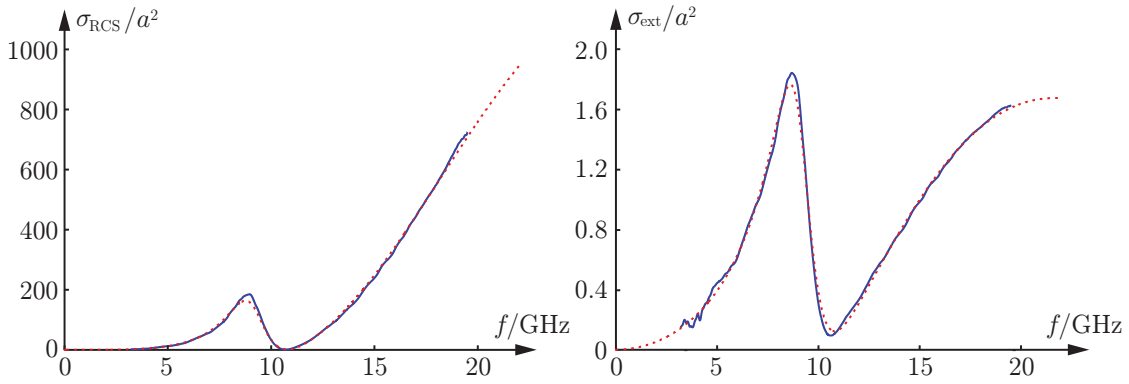

Figure 3: The monostatic radar cross section (left) and the extinction cross section (right) in units of the projected area a^2. The solid lines correspond to measured data whereas the dashed lines are given by (3.1).

consistent with the specular reflection of the sample. As the sample is sufficiently thin compared with the considered wavelengths, the forward scattering dyadic is approximated by the scattering dyadic in the backward direction. In particular, this approximation is used to calculate the extinction cross section via the optical theorem (2.5). The result is depicted on the right-hand side of Fig. 3. From the figure, it is seen that the extinction cross section is non-negative, confirming the validity of (2.6) since phase deviations in the scattering dyadic introduce significant errors in the extinction cross section.

The forward scattering dyadic is also used to determine the extinction volume, and the result is depicted on the left-hand side of Fig. 4. From the figure it is observed that the real part of the extinction volume vanishes at the resonance frequency $f_0 \approx 8.5\,\mathrm{GHz}$, whereas at the same frequency, the corresponding imaginary part attains its maximum value. This observation can be understood by approximating the resonance on the left-hand side of Fig. 4 with a modified Lorentz resonance model, see pp. 228–232 in Ref. 1. Also, note in Fig. 4 that the frequency scaling in (2.9) amplifies the noise in the measurements for low frequencies.

The function $\zeta(k;\hat{\boldsymbol{k}},\hat{\boldsymbol{e}}) = 4\pi\,\mathrm{Im}\,\varrho(k;\hat{\boldsymbol{k}},\hat{\boldsymbol{e}})/k$, corresponding to the integrand in (2.8), is depicted on the right-hand side of Fig. 4. Compared with the left figure, additional noise amplification for low frequencies is observed. The shaded area on the right-hand side is estimated by numerical integration to $7.1\,\mathrm{cm}^3$ and indicated by a dot in the left figure. Since ζ is non-negative, the value $7.1\,\mathrm{cm}^3$ is, according to (2.11), a priori a lower bound on the static limit of the extinction volume. Obviously, this static limit is underestimated by the integral since ζ cannot vanish identically outside the considered frequency range.

The extinction volume is also used to verify that the experimental outcome behaves causally in the sense that the extinction volume satisfies (2.10). In Fig. 5, it is observed that the Hilbert transform resembles the overall frequency dependence of the real and imaginary parts of the extinction volume. However, it is clear from the figure that the finite frequency interval of the measured data limits its usefulness

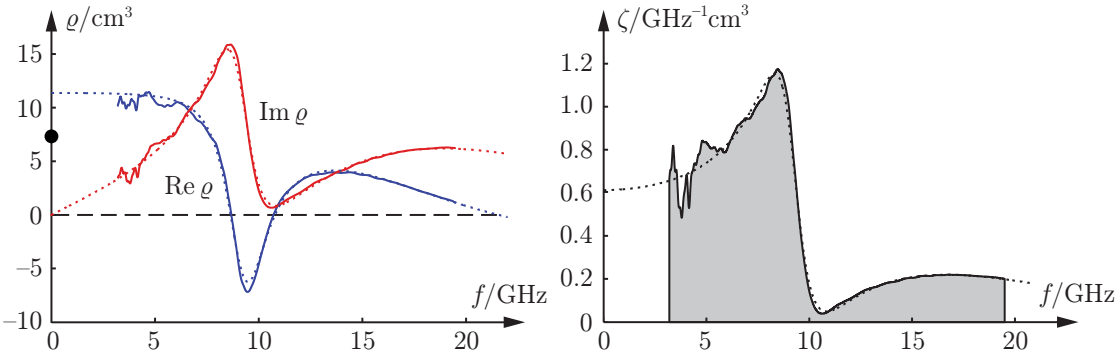

Figure 4: The extinction volume (left) and $\zeta(k;\hat{\boldsymbol{k}},\hat{\boldsymbol{e}}) = 4\pi \operatorname{Im} \varrho(k;\hat{\boldsymbol{k}},\hat{\boldsymbol{e}})/k$ (right). The solid lines correspond to measured data whereas the dashed lines are given by (3.1). The shaded area in the right figure is marked by a dot in the left figure.

as a method of reconstructing an unknown component of a holomorphic function. The offsets in Fig. 5 can be adjusted for since the mean values of the solid curves are non-zero, *cf.*, the properties of the Hilbert transform in Ref. 18.

A feasible technique to approximate the extinction volume is to use meromorphic functions with roots and zeros in the lower half of the complex f-plane. Numerical tests using the algorithm in Ref. 7 indicate that it is sufficient to consider rational functions with numerator and denominator of second and fourth degree, respectively. Such functions can be represented by the sum of two modified Lorentz resonance models via

$$\varrho_{\text{appr}}(f;\hat{\boldsymbol{k}},\hat{\boldsymbol{e}}) = \sum_{n=1}^{2} \varrho_n \frac{f_n^2 - \mathrm{i}f\nu_n}{f_n^2 - 2\mathrm{i}ff_n/Q_n - f^2}. \tag{3.1}$$

The approximation (3.1) is depicted by the dotted line on the left-hand side of Fig. 4. Here, $f_1 = 9.3\,\text{GHz}$, $Q_1 = 7.8$, $\varrho_1 = 1.3\,\text{cm}^3$, and $\nu_1 = -27\,\text{GHz}$ for the first term, and $f_2 = 20\,\text{GHz}$, $Q_2 = 1.6$, $\varrho_2 = 10\,\text{cm}^3$, and $\nu_2 = 3.6\,\text{GHz}$ for the second term. In particular, the static limit of (3.1) is given by $\varrho_1 + \varrho_2 \approx 11\,\text{cm}^3$. The associated meromorphic approximations of the monostatic radar cross section and the extinction cross section follow from (3.1) and the definitions in Sec. 2. These approximations are represented by the dotted lines in Figs. 3 and 4, and it is concluded that the approximations are in good agreement with the experimental results.

The approximation (3.1) is also used to establish a sharper bound on the static limit of the extinction volume. In fact, the shaded area $7.1\,\text{cm}^3$ on the right-hand side of Fig. 4 should be compared with the corresponding area $9.8\,\text{cm}^3$ obtained by integrating the dotted line over the frequency range $[0, 22]\,\text{GHz}$. The lower bound $9.8\,\text{cm}^3$ is quite close to the static limit $11\,\text{cm}^3$, which would be the true value of $\varrho(0;\hat{\boldsymbol{k}},\hat{\boldsymbol{e}})$ if the extinction volume on the left-hand side of Fig. 4 is completely determined by this approximation. The fact that the dotted line on the right-hand side of Fig. 4 is non-zero in the static limit is also supported by the analysis of the lossy transmission problem on pp. 191–192 in Ref. 2.

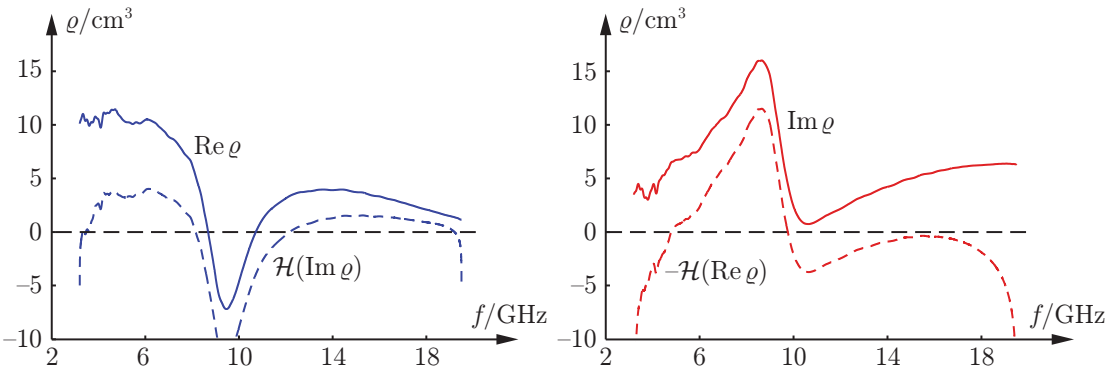

Figure 5: The real and imaginary parts of the extinction volume (solid lines) and the corresponding reconstructed quantities using the Hilbert transform $\mathcal{H}$ (dashed lines).

4 Conclusions

This paper reports on measurements of the extinction cross section and the extinction volume for a fabricated sample of a negative permittivity metamaterial. It is experimentally verified that the extinction cross section integrated over the frequency interval $[3.2, 19.5]$ GHz yields a lower bound on the static limit of the extinction volume. Also, by using the Hilbert transform and the meromorphic approximation (3.1), it is made plausible that the extinction volume indeed is a holomorphic function in the upper half part of the complex k-plane and satisfies the asymptotic behavior discussed in Ref. 14. Among other things, the experimental results in this paper are important for the support of the far-reaching conclusion made in Ref. 15: there is no fundamental difference between metamaterials and naturally formed substances with respect to the absorption and scattering over a frequency interval.

Similar measurements on split ring resonators (SRR) will be presented in a forthcoming paper. Forward scattering measurements on extended targets introduce further experimental challenges that also will be addressed in the future.

Acknowledgments

The financial support by the Swedish Research Council is gratefully acknowledged. The authors also thank Carl-Gustaf Svensson and Mats Andersson at Saab Bofors Dynamics, Linköping, Sweden, for generous hospitality and practical assistance throughout the measurements.

References

[1] C. F. Bohren and D. R. Huffman. *Absorption and Scattering of Light by Small Particles*. John Wiley & Sons, New York, 1983.

[2] G. Dassios and R. Kleinman. *Low Frequency Scattering*. Oxford University Press, Oxford, 2000.

[3] R. de L. Kronig. On the theory of dispersion of X-rays. *J. Opt. Soc. Am.*, **12**(6), 547–557, 1926.

[4] M. Gustafsson, C. Sohl, and G. Kristensson. Physical limitations on antennas of arbitrary shape. *Proc. R. Soc. A*, **463**(2086), 2589–2607, 2007.

[5] E. F. Knott, J. F. Shaeffer, and M. T. Tuley. *Radar Cross Section*. SciTech Publishing Inc., 5601 N. Hawthorne Way, Raleigh, NC 27613, 2004.

[6] M. H. A. Kramers. La diffusion de la lumière par les atomes. *Atti. Congr. Int. Fis. Como*, **2**, 545–557, 1927.

[7] E. C. Levi. Complex-curve fitting. *IRE Trans. on Automatic Control*, **AC-4**, 37–44, 1959.

[8] R. G. Newton. Optical theorem and beyond. *Am. J. Phys*, **44**, 639–642, 1976.

[9] R. G. Newton. *Scattering Theory of Waves and Particles*. Dover Publications, New York, second edition, 2002.

[10] G. T. Ruck, D. E. Barrick, W. D. Stuart, and C. K. Krichbaum. *Radar Cross-Section Handbook*, volume 1 and 2. Plenum Press, New York, 1970.

[11] D. Schurig, J. J. Mock, and D. R. Smith. Electric-field-coupled resonators for negative permittivity metamaterials. *Appl. Phys. Lett.*, **88**, 041109, 2006.

[12] C. Sohl and M. Gustafsson. A priori estimates on the partial realized gain of ultra-wideband (UWB) antennas. *Quart. J. Mech. Appl. Math.*, **61**(3), 415–430, 2008.

[13] C. Sohl, M. Gustafsson, and G. Kristensson. The integrated extinction for broadband scattering of acoustic waves. *J. Acoust. Soc. Am.*, **122**(6), 3206–3210, 2007.

[14] C. Sohl, M. Gustafsson, and G. Kristensson. Physical limitations on broadband scattering by heterogeneous obstacles. *J. Phys. A: Math. Theor.*, **40**(36), 11165–11182, 2007.

[15] C. Sohl, M. Gustafsson, and G. Kristensson. Physical limitations on metamaterials: Restrictions on scattering and absorption over a frequency interval. *J. Phys. D: Applied Phys.*, **40**(22), 7146–7151, 2007.

[16] C. Sohl. *Dispersion Relations for Extinction of Acoustic and Electromagnetic Waves*. Licentiate thesis, Lund University, Department of Electrical and Information Technology, P.O. Box 118, S-221 00 Lund, Sweden, 2007.

[17] S. Ström. Introduction to integral representations and integral equations for time-harmonic acoustic, electromagnetic and elastodynamic wave fields. In V. V. Varadan, A. Lakhtakia, and V. K. Varadan, editors, *Field Representations and Introduction to Scattering*, volume 1 of *Handbook on Acoustic, Electromagnetic and Elastic Wave Scattering*, chapter 2, pages 37–141. Elsevier Science Publishers, Amsterdam, 1991.

[18] E. C. Titchmarsh. *Introduction to the Theory of Fourier Integrals*. Oxford University Press, Oxford, second edition, 1948.

Bounds on metamaterials: Theoretical and experimental results

Gerhard Kristensson, Christer Larsson, Christian Sohl, and Mats Gustafsson

Paper IV

Based on: G. Kristensson, C. Larsson, C. Sohl, and M. Gustafsson. Bounds on metamaterials: Theoretical and experimental results. Book chapter to appear in 2008.

Abstract

A dispersion relation for the combined effect of scattering and absorption of electromagnetic waves is employed. By invoking the optical theorem, the result states that the extinction cross section integrated over all frequencies is related to the static polarizability dyadics. In particular, it is established that the integrated extinction is the same for all materials having identical static properties, irrespectively whether the permittivity or the permeability have negative real parts at non-zero frequencies or not. The theory is illustrated numerically, and, moreover, it is verified experimentally on a sample consisting of a single-layer planar array of capacitive resonators claimed to form a negative permittivity metamaterial. It is concluded that the theory is in good agreement with measurements in the microwave region.

1 Background

In a series of papers [15–17], the holomorphic properties of the forward scattering amplitude have been exploited and experimentally verified. As a result, a sum rule for the extinction cross section is established. This outcome hinges on the physical principles of causality and energy conservations — both well established and tested — and relates the (weighted) integrated extinction to the static material properties of the obstacle. A rather intriguing consequence of this sum rule is that the static properties measure the broadband scattering and absorption strengths of the obstacle. This fact implies a renaissance for polarizability analyzes of obstacles, but also an appreciation of the large efforts made in the past, and that now prove helpful, see *e.g.*, [3, 18]. This attribute has also been used in antenna applications to give new bounds on the product of gain and bandwidth of antennas of arbitrary shape [2, 14].

The direct measurement of the forward radar cross section (RCS) in free space is experimentally difficult since the largest part of the detected field at the receiving antenna consists of a direct illumination by the transmitting antenna. The direct illumination contributes with a dominating background that has to be removed from the detected field, either using coherent background subtraction or other signal processing methods. Monostatic RCS measurements are therefore to be preferred, compared to forward RCS measurements, if they can be used for the purpose at hand. This paper describes a method to determine the extinction cross section for a thin and non-magnetic planar object over a large bandwidth in the microwave region. The method is based on a conventional measurement of the monostatic RCS and the fact that the RCS amplitude in the forward and backward directions are equal if the illuminated object is planar and non-magnetic [12, 17]. The monostatic method is compared to and validated with a more general measurement technique based on the RCS in the forward direction.

2 A sum rule for the extinction cross section

This section sets the notation of the problem and states the main theoretical results used in this paper, but no proofs are given. For proofs we refer to the pertinent published papers [15, 16].

Consider the scattering problem of a plane electromagnetic wave $\boldsymbol{E}\exp\{\mathrm{i}k\hat{\boldsymbol{k}}\cdot\boldsymbol{x}\}$ (time dependence $\exp\{-\mathrm{i}\omega t\}$) impinging in the $\hat{\boldsymbol{k}}$-direction on a target embedded in free space. The wave number in free space is denoted by $k=\omega/\mathrm{c}_0$. The target can be a single scatterer or it may consist of several non-connected parts. The material of the scatterer is modeled by a set of linear and passive constitutive relations which are assumed to be invariant under time translations (*i.e.*, stationary constitutive relations). The scattering dyadic $\mathbf{S}$ is independent of $\boldsymbol{E}$, and it is defined in terms of the scattered electric field $\boldsymbol{E}_\mathrm{s}$ as [1, 7]

$$\mathbf{S}(k;\hat{\boldsymbol{k}}\curvearrowright\hat{\boldsymbol{x}})\cdot\boldsymbol{E}=\lim_{x\to\infty}x\,\mathrm{e}^{-\mathrm{i}kx}\boldsymbol{E}_\mathrm{s}(k;\boldsymbol{x}) \tag{2.1}$$

where $x=|\boldsymbol{x}|$ denotes the magnitude of the position vector, and $\hat{\boldsymbol{x}}=\boldsymbol{x}/x$. A target's overall scattering properties are commonly quantified by the scattering cross section σ_s, defined as the total power scattered in all directions divided by the incident power flux. The extinction cross section $\sigma_\mathrm{ext}=\sigma_\mathrm{s}+\sigma_\mathrm{a}$ is defined as the sum of the scattering and absorption cross sections, where the latter is a measure of the absorbed power in the target [1]. The extinction cross section is also determined from the knowledge of the scattering dyadic in the forward direction, $\hat{\boldsymbol{x}}=\hat{\boldsymbol{k}}$, *viz.*,

$$\sigma_\mathrm{ext}(k;\hat{\boldsymbol{k}},\hat{\boldsymbol{e}})=\frac{4\pi}{k}\,\mathrm{Im}\left\{\hat{\boldsymbol{e}}^*\cdot\mathbf{S}(k;\hat{\boldsymbol{k}}\curvearrowright\hat{\boldsymbol{k}})\cdot\hat{\boldsymbol{e}}\right\} \tag{2.2}$$

An asterisk denotes the complex conjugate, and the electric polarization $\hat{\boldsymbol{e}}=\boldsymbol{E}/|\boldsymbol{E}|$. Relation (2.2) is known as the optical theorem or forward scattering theorem [1, 7].

A dispersion relation for the combined effect of scattering and absorption of electromagnetic waves is derived in Ref. 15 from the holomorphic properties of the forward scattering dyadic. One of the underlying assumptions of the result is that the forward scattering is causal, *i.e.*, the scattered field must not proceed the incident field in the forward direction. The result is a sum rule for the extinction cross section valid for a large class of linear and passive targets:[1]

$$\int_0^\infty\frac{\sigma_\mathrm{ext}(k;\hat{\boldsymbol{k}},\hat{\boldsymbol{e}})}{k^2}\,\mathrm{d}k=\frac{\pi}{2}\left(\hat{\boldsymbol{e}}^*\cdot\boldsymbol{\gamma}_\mathrm{e}\cdot\hat{\boldsymbol{e}}+(\hat{\boldsymbol{k}}\times\hat{\boldsymbol{e}}^*)\cdot\boldsymbol{\gamma}_\mathrm{m}\cdot(\hat{\boldsymbol{k}}\times\hat{\boldsymbol{e}})\right) \tag{2.3}$$

where $\boldsymbol{\gamma}_\mathrm{e}$ and $\boldsymbol{\gamma}_\mathrm{m}$ denote the electric and magnetic polarizability dyadics, respectively [3, 18]. This identity holds for all scatterers satisfying the assumption above, and it constitutes the main theoretical result used in this paper. This rather intriguing result has far-reaching consequences on how much an obstacle scatters and absorbs, and it also quantifies the interaction between parts with different materials.

[1] A similar, but less developed, sum rule has been reported in the literature, see *e.g.*, [9, p. 423]. The first employment of the sum rule in electromagnetics seems to go back to Purcell, who presented the sum rule for dielectric spheroidal scatterers [11].

The electric (or magnetic) polarizability dyadic is accessible as an analytic expression for a limited set of canonical bodies, *e.g.*, a homogenous, isotropic dielectric sphere of radius a with static permittivity $\epsilon(0)$ has the polarizability dyadic $\boldsymbol{\gamma}_{\mathrm{e}}$ [3, 18]

$$\boldsymbol{\gamma}_{\mathrm{e}} = 3\frac{\epsilon(0)-1}{\epsilon(0)+2}\frac{4\pi a^3}{3}\mathbf{I} \tag{2.4}$$

where $\mathbf{I}$ denotes the unit dyadic. Fortunately, for other more complex geometries, the polarizability dyadic is easy to compute using *e.g.*, a finite element (FEM) solver.

The integrand on the left-hand side of (2.3) is non-negative. Therefore, for any finite frequency interval $K = k_0[1 - B/2, 1 + B/2]$ with center frequency k_0 and relative bandwidth B, the identity implies for some $\kappa \in K$

$$\frac{B\sigma(\kappa)}{k_0(1-B^2/4)} = \int_K \frac{\sigma(k)}{k^2}\,\mathrm{d}k \leqslant \frac{\pi}{2}\left(\hat{\boldsymbol{e}}^* \cdot \boldsymbol{\gamma}_{\mathrm{e}} \cdot \hat{\boldsymbol{e}} + (\hat{\boldsymbol{k}} \times \hat{\boldsymbol{e}}^*) \cdot \boldsymbol{\gamma}_{\mathrm{m}} \cdot (\hat{\boldsymbol{k}} \times \hat{\boldsymbol{e}})\right) \tag{2.5}$$

where σ denotes any of the cross sections $\sigma_{\mathrm{ext}}, \sigma_{\mathrm{s}}$, and σ_{a}. For all scatterers with the same static polarizability dyadics, this inequality shows that large scattering in a frequency interval is traded for smaller bandwidth, since the left-hand side of the inequality is bounded from above by the right-hand side.

The extinction cross section σ_{ext} measures the total interaction of the incident plane wave with the obstacle, and the integral on the left-hand side of (2.3) provides a measure of the overall scattering and the absorption properties of the obstacle. As a consequence of (2.3), large scattering or absorption effects, *i.e.*, a large left-hand side of (2.3), call for large electric and/or magnetic polarizability dyadics. In other applications, like cloaking, the extinction effects must be small (at least in a finite frequency interval) and the electric and magnetic polarizability dyadics have to be as small as possible for a given volume. In both cases, the static properties act as a measure of the dynamic effects. We also immediately conclude that all scatterers having the same right-hand side, *i.e.*, polarizability properties, have the same integrated extinction.

The effects of (2.3) are exploited in this paper, and in a few numerical examples, see Sect. 4, we illustrate that two materials with the same static properties have identical integrated extinctions. Several of these examples show metamaterial characteristics, *i.e.*, the material has temporally dispersive material parameters where both the real parts of the permittivity and the permeability are negative in the same frequency interval. In all cases it is the static properties of the obstacle that determine the integrated scattering properties. The experimental verification of the sum rule is presented in Sect. 5.

3 Material modeling

At a single frequency, when causality has no meaning, the material modeling of the scatterer is less critical. However, dealing with the broadband properties of a scatterer, it becomes important to use physically suitable dispersion models. In

particular, the models have to be consistent with the passivity and causality assumptions made above. As a consequence, the material models have to satisfy the Kramers-Kronig relations [1, 5]. This is a consequence of the fact that $f(\omega) = \omega\epsilon(\omega)$ is a Herglotz function [8] in the variable ω. Basically, a Herglotz function is analytic in the upper half complex plane, and it maps the upper complex plane into itself.

In this paper we use the Lorentz model, which models the resonance behavior of many solid materials. The relative permittivity of the Lorentz model is:

$$\epsilon(\omega) = \epsilon_\infty - \frac{\omega_\mathrm{p}^2}{\omega^2 - \omega_0^2 + \mathrm{i}\omega\nu} = \epsilon_\infty - \frac{(\omega_\mathrm{p} a/\mathrm{c}_0)^2}{(ka)^2 - (\omega_0 a/\mathrm{c}_0)^2 + \mathrm{i}ka(\nu a/\mathrm{c}_0)} \tag{3.1}$$

The positive constant ϵ_∞ is the optical response of the permittivity, and the constant ω_p is the plasma frequency that models the strength of the dispersion. The resonance frequency of the model is determined by the angular frequency, ω_0, and the collision frequency $\nu > 0$. With appropriate choice of the material parameters, the real part of the permittivity becomes negative. The explicit value of the permittivity in the static limit ($\omega = 0$) is $\epsilon(0) = \epsilon_\infty + \omega_\mathrm{p}^2/\omega_0^2$. A similar model is also used for the relative permeability μ. The Lorentz model employed in this paper has the parameters $\epsilon_\infty = 1$, $\omega_\mathrm{p} a/\mathrm{c}_0 = 3$, $\omega_0 a/\mathrm{c}_0 = 2$, and $\nu a/\mathrm{c}_0 = 0.6$.

The Drude model is a special case of the Lorentz model for which $\omega_0 = 0$, *i.e.*,

$$\epsilon(\omega) = \frac{((ka)^2 + (\nu a/\mathrm{c}_0)^2)\epsilon_\infty - (\omega_\mathrm{p} a/\mathrm{c}_0)^2}{(ka)^2 + (\nu a/\mathrm{c}_0)^2} + \mathrm{i}\frac{(\omega_\mathrm{p} a/\mathrm{c}_0)^2(\nu a/\mathrm{c}_0)}{ka((ka)^2 + (\nu a/\mathrm{c}_0)^2)} \tag{3.2}$$

This choice implies that the real part of the permittivity is negative over a large frequency interval, *i.e.*, $\omega^2 \leqslant \omega_\mathrm{p}^2/\epsilon_\infty - \nu^2$. This model is used to describe the dispersive behavior of metamaterials, and at low frequencies it shows strong affinity with the conductivity model $\epsilon(\omega) = \epsilon_\infty + \mathrm{i}\varsigma/(\epsilon_0\omega)$. In fact, the conductivity $\varsigma = \epsilon_0\omega_\mathrm{p}^2/\nu$ can be identified from Drude's model.

4 Numerical illustrations — sphere-doublets

In this section, we illustrate the theoretical results presented in Sect. 2 in two numerical examples using the material models described in Sect. 3. The scattering geometry consists of two spheres, radii a and b, respectively, as illustrated in Fig. 1. In all examples, the plane wave impinges along the symmetry axis of the scatterer with an electric polarization $\hat{\boldsymbol{e}}$ in the xy-plane, which can be either a real- or a complex-valued unit vector. All frequencies are measured in the dimensionless parameter $\kappa = ka$, and all cross sections are scaled with $2\pi a^2$. The identity in (2.3), then reads

$$\int_0^\infty \frac{\sigma_\mathrm{ext}(\kappa; \hat{\boldsymbol{k}}, \hat{\boldsymbol{e}})}{\kappa^2}\,\mathrm{d}\kappa = \frac{\pi}{3}\frac{1}{4\pi a^3/3}\left(\hat{\boldsymbol{e}}^* \cdot \boldsymbol{\gamma}_\mathrm{e} \cdot \hat{\boldsymbol{e}} + (\hat{\boldsymbol{k}} \times \hat{\boldsymbol{e}}^*) \cdot \boldsymbol{\gamma}_\mathrm{m} \cdot (\hat{\boldsymbol{k}} \times \hat{\boldsymbol{e}})\right) \tag{4.1}$$

The numerical computations in this paper utilize the null-field approach, which is an efficient method to evaluate scattering by non-connected objects [10].

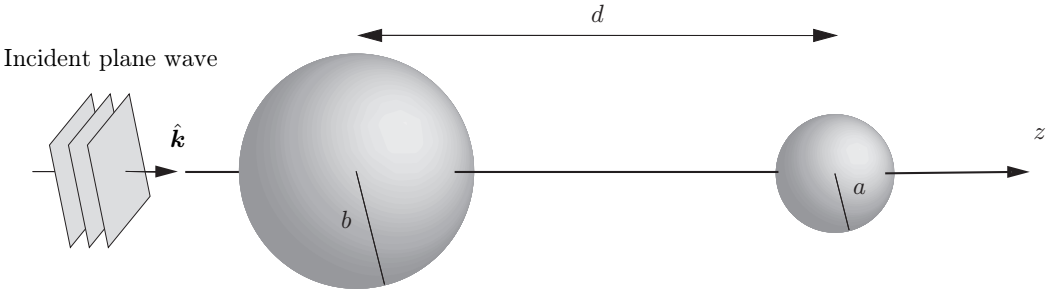

Figure 1: The geometry of the two spheres. The sphere with radius a is located at $d\hat{\boldsymbol{z}}/2$ and the sphere with radius b is located at $-d\hat{\boldsymbol{z}}/2$. The direction of the incident wave in all examples is $\hat{\boldsymbol{k}} = \hat{\boldsymbol{z}}$.

In the first example the extinction cross section of two identical touching Drude spheres (radii $a = b$ and $d = 2a$) is computed for two material settings. In the first setting $\epsilon = \mu$ at all frequencies, *i.e.*, a material that shows metamaterial characteristics at low frequencies, and in the second setting both spheres are non-magnetic, $\mu = 1$. The result is shown to the left in Fig. 2. Explicit values of the permittivities are given in Sect. 3.

The contribution to both the electric and the magnetic polarizability dyadics in the case $\epsilon = \mu$ is [19]

$$\hat{\boldsymbol{e}}^* \cdot \boldsymbol{\gamma}_{\mathrm{e}} \cdot \hat{\boldsymbol{e}} = (\hat{\boldsymbol{k}} \times \hat{\boldsymbol{e}}^*) \cdot \boldsymbol{\gamma}_{\mathrm{m}} \cdot (\hat{\boldsymbol{k}} \times \hat{\boldsymbol{e}}) = \frac{9}{2}\zeta(3)\frac{4\pi a^3}{3} \tag{4.2}$$

where $\zeta(z)$ is the Riemann zeta-function. The non-magnetic spheres have no magnetic contribution, but only an electric contribution. The right-hand side of (4.1) for the two curves in Fig. 2 therefore assumes the values $3\pi\zeta(3) = 11.33$ and $3\pi\zeta(3)/2 = 5.66$, respectively. These figures are retrieved using numerical integration over the frequency interval in Fig. 2 with 3 digits (11.3 and 5.66, respectively). It is intriguing to conclude that these numbers are independent of all the material parameters of the Drude spheres, *i.e.*, independent of ϵ_∞, ω_{p}, and ν.

A further verification of the integrated extinction in (4.1) is presented to the right in Fig. 2. This figure shows the analytically computed polarizability, γ, of two identical Drude spheres [19] as a function of the separating distance d. The values obtained by numerical integration according to (4.1) are shown with circles.

The second example illustrates the computation of the extinction cross sections for two different sets of material parameters with identical static values. Two touching, $d = 3a$, non-magnetic Lorentz spheres, radii a and $b = 2a$, respectively, are used. The result is displayed in Fig. 3. The solid curve shows the extinction cross section when the two spheres have materials as given in Sect. 3. The broken curve shows the extinction cross section for two Lorentz spheres both having parameters $\epsilon_\infty = 1$, $\omega_{\mathrm{p}}a/\mathrm{c}_0 = 4.5$, $\omega_0 a/\mathrm{c}_0 = 3$, and $\nu a/\mathrm{c}_0 = 0.6$. These two sets of materials have a static permittivity $\epsilon(0) = 13/4$, and therefore the same right-hand side of (4.1). The boxes shown in Fig. 3 also have the same integrated extinction, and they indicate the bandwidth of the scattering at the first resonance frequency.

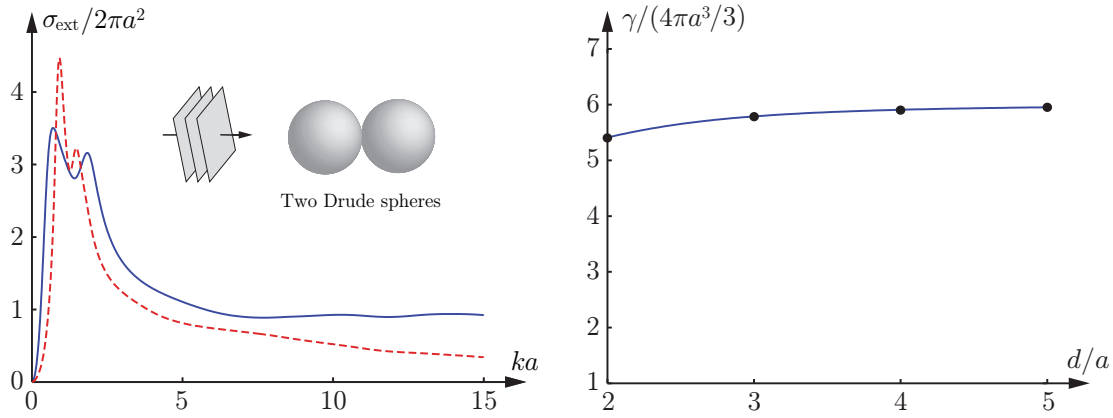

Figure 2: Left figure: The extinction cross section of two equal, touching ($d = 2a$) Drude spheres (radii $a = b$) as a function of ka. The solid curve shows the extinction cross section for $\epsilon = \mu$, and the broken curve when both spheres are non-magnetic, $\mu = 1$. All cross sections are normalized with $2\pi a^2$. Right figure: The electric (or magnetic) polarizability, normalized with $4\pi a^3/3$, for the same geometry as a function of the separation distance d. The circles illustrate the numerical values.

The polarizability dyadic contributions from the two Lorentz spheres are the same, *i.e.*,

$$\hat{\boldsymbol{e}}^* \cdot \boldsymbol{\gamma}_{\rm e} \cdot \hat{\boldsymbol{e}} = 11.29 \frac{4\pi a^3}{3} \tag{4.3}$$

The right-hand side of (4.1) then becomes 11.82 in both cases. The integrated extinction is computed using numerical integration over the frequency interval in Fig. 3. The results are 11.8 and 11.7, respectively, for the two curves.

5 Experimental verification

The bistatic RCS, $\sigma_{\rm RCS}$, is defined as

$$\sigma_{\rm RCS}(k; \hat{\boldsymbol{x}}, \hat{\boldsymbol{e}}_{\rm s}) = |A(k; \hat{\boldsymbol{x}}, \hat{\boldsymbol{e}}_{\rm s})|^2 \tag{5.1}$$

where $A(k; \hat{\boldsymbol{x}}, \hat{\boldsymbol{e}}_{\rm s}) = 2\sqrt{\pi}\hat{\boldsymbol{e}}_{\rm s}^* \cdot \mathbf{S}(k; \hat{\boldsymbol{k}} \curvearrowright \hat{\boldsymbol{x}}) \cdot \hat{\boldsymbol{e}}$, and where $\hat{\boldsymbol{e}}_{\rm s}$ denotes the polarization of the scattered field in the $\hat{\boldsymbol{x}}$ direction. Evaluated in the backward direction, $\hat{\boldsymbol{x}} = -\hat{\boldsymbol{k}}$, produces the familiar expression for the monostatic RCS [4, 12]. Using this notation, the sum rule for the extinction cross section in (2.3) then reads

$$\frac{1}{\pi^{3/2}} \int_0^\infty \frac{\sigma_{\rm ext}(k; \hat{\boldsymbol{k}}, \hat{\boldsymbol{e}})}{k^2} \, {\rm d}k = \lim_{k \to 0} \frac{A(k; \hat{\boldsymbol{k}}, \hat{\boldsymbol{e}})}{k^2} \tag{5.2}$$

From the integral representations of the scattered field or the discussion in Ref. 12, it follows that for a planar and infinitely thin scatterer subject to a wave impinging at normal incidence, the RCS amplitudes in the forward and backward directions, $\hat{\boldsymbol{x}} = \hat{\boldsymbol{k}}$ and $\hat{\boldsymbol{x}} = -\hat{\boldsymbol{k}}$, respectively, are identical, *i.e.*,

$$A(k; \hat{\boldsymbol{k}}, \hat{\boldsymbol{e}}) = A(k; -\hat{\boldsymbol{k}}, \hat{\boldsymbol{e}}) \tag{5.3}$$

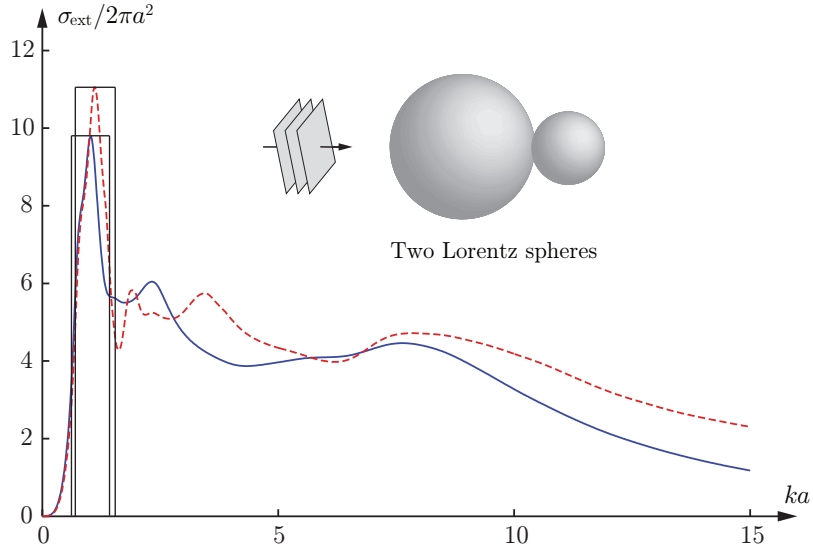

Figure 3: The extinction cross section of two touching Lorentz spheres as a function of ka. Both spheres have identical material parameters and they are non-magnetic, $\mu = 1$, with radii a and $b = 2a$. The data of the scatterers are given in the text. The boxes have the same integrated extinction as both curves. All cross sections are normalized with $2\pi a^2$.

Combining this relation with the optical theorem makes it possible to determine σ_{ext} and verify (5.2) from a conventional measurement of the monostatic RCS amplitude.

The sample design shown in Fig. 4 was used for the experiments. The fabricated single-layer planar array of capacitive resonators is referred to in the literature as a negative permittivity metamaterial [13]. The sample is tuned to be resonant at 8.5 GHz. It consists of 29×29 unit cells supported by a 0.3 mm thick 140 mm $\times$ 140 mm square FR4 substrate, see Fig. 4. The relative dielectric constant of the substrate varies between 4.4 and 4.2 in the frequency range $[2, 20]$ GHz with an overall loss tangent less than $5 \cdot 10^{-3}$.

5.1 Quasi-monostatic and forward RCS measurements

Monostatic RCS measurements are performed in an anechoic chamber with two dual-polarized ridged circular waveguide horns positioned at a distance of 3.5 m from the sample, see the left hand side of Fig. 5. The polarizations of the transmitted and received waves are vertical with respect to the pattern in Fig. 4 — only the co-polarized contribution enters in the optical theorem. The frequency interval $[3.2, 19.5]$ GHz is sampled with 7246 equidistant points corresponding to an unambiguous range of 66.7 m (445 ns). This is sufficient to avoid influence of room reverberations.

Calibration including both amplitude and phase is performed using a metal plate with the same outer dimensions as the sample. The measured data are processed by a coherent subtraction of the background. The frequency domain data is then transformed to the range domain, where the response from the sample is selected from

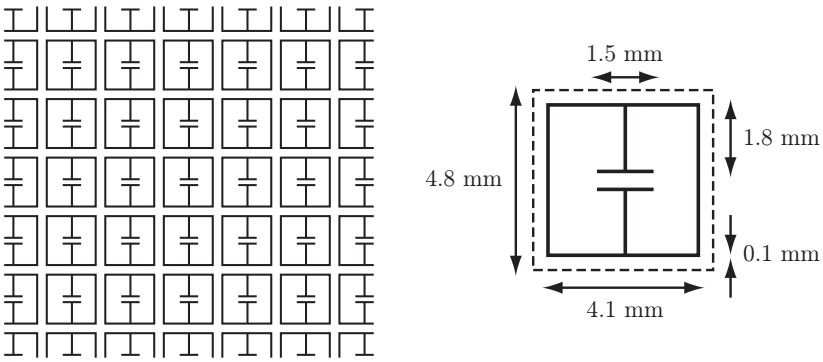

Figure 4: A section of the array of capacitive resonators (left figure) and one unit cell of the array (right figure).

the range profile using a 1.1 m spatial gate. Finally, the selected data is transformed back to the frequency domain.

The background subtraction combined with the time gating gives a background level of better than -50 dBsm for the frequency range above 5 GHz and -40 dBsm to -30 dBsm for the lowest part of the frequency range. The high background level at the lower frequencies is a consequence of the wideband horn illumination of the walls at these frequencies. This background level can be maintained for hours by using a single background measurement.

Forward RCS measurements are performed using a different setup with ridged waveguide horns in an ordinary laboratory area. The antennas are positioned facing each other at a distance of 6.0 m with the sample at the midpoint between the antennas, see the right-hand side of Fig. 5. The frequency interval $[2.5, 16]$ GHz is sampled with 5086 equidistant points corresponding to an unambiguous time range of 378 ns. The unambiguous time range is sufficient to avoid influence of room reverberations such as delayed scattering from the floor and the walls in the laboratory area.

Calibration including both amplitude and phase is performed using a high precision sphere with radius 6.00 cm. The raw data from the calibration is then processed by a coherent subtraction of the background. The fabricated sample is then measured. A new measurement of the background is coherently subtracted from the sample measurement. The repeated background measurements are important in order to increase the efficiency of the background subtraction and to obtain the background levels. We perform the background measurements within less than 2 minutes after each sample (calibration) measurement.

The calibrated frequency domain data is transformed to the time domain, where the response from the sample is selected from the time profile using a 1.7 ns time gate. The size of the gate is chosen to minimize the influence from the background. Finally, the selected data is transformed back to the frequency domain. The background subtraction combined with the time gating gives a background level of less than -40 dBsm.

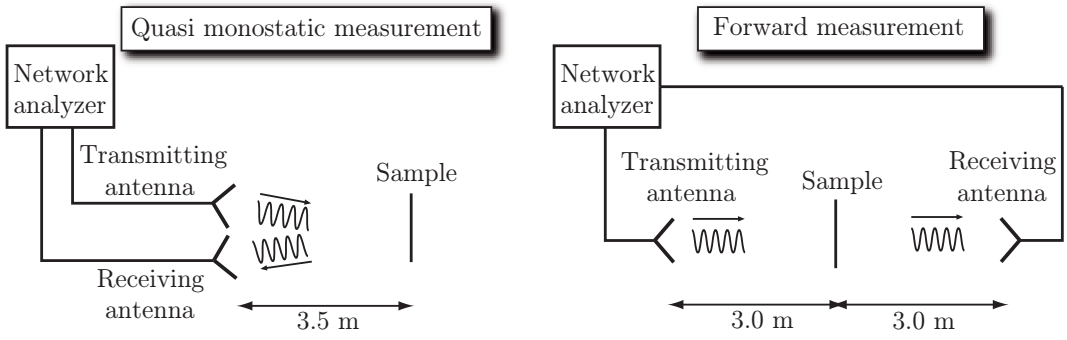

Figure 5: The experimental setups for quasi monostatic (left figure) and forward RCS (right figure) measurements.

5.2 Validation of the monostatic method and experimental verification of the sum rule

The left graph in Fig. 6 shows a comparison between measurements of the monostatic RCS and the forward RCS. The agreement is better than 0.5 dB except for the minimum at 10.7 GHz where the discrepancy is 2.5 dB. The measured differences are well within experimental error limits. It is therefore validated that the monostatic RCS and the forward RCS are equal within good accuracy for this thin and non-magnetic sample.

However, the phase of the RCS amplitude is also important since the extinction cross section is determined from the imaginary part of the RCS amplitude, *cf.*, the optical theorem (2.2). The right part[2] of Fig. 6 shows the extinction cross section determined from the optical theorem using both the monostatic and forward RCS amplitudes. The phase of the forward RCS amplitude is shifted according to the procedure described below in order to compare the two curves. The maximum discrepancy between the curves is 35 cm^2 at 15 GHz after an adjustment of the phase.

The real and imaginary parts of $A(f;\hat{\boldsymbol{k}},\hat{\boldsymbol{e}})/f^2$ are shown in Fig. 7. The phase of $A(f;\hat{\boldsymbol{k}},\hat{\boldsymbol{e}})/f^2$ obtained from the forward scattering experiment is adjusted using a time delay of 3.1 ps. We believe that the largest contribution to this phase shift is the time delay of the wave as it passes the 0.3 mm FR4 substrate and the 48 mm expanded polystyrene (EPS) sample support. Small alignment differences between the calibration plate and the sample in the monostatic case can also account for the observed phase difference. The difference between the two measurement methods is small which means that it is validated that conventional monostatic RCS measurements can be used to determine the extinction cross section for this class of thin and non-magnetic samples.

Different methods are used to experimentally verify (5.2). First the extinction

[2]For convenience, we use the frequency f instead of the wavenumber $k = 2\pi f/\mathrm{c}_0$ in the discussion of the experimental verification.

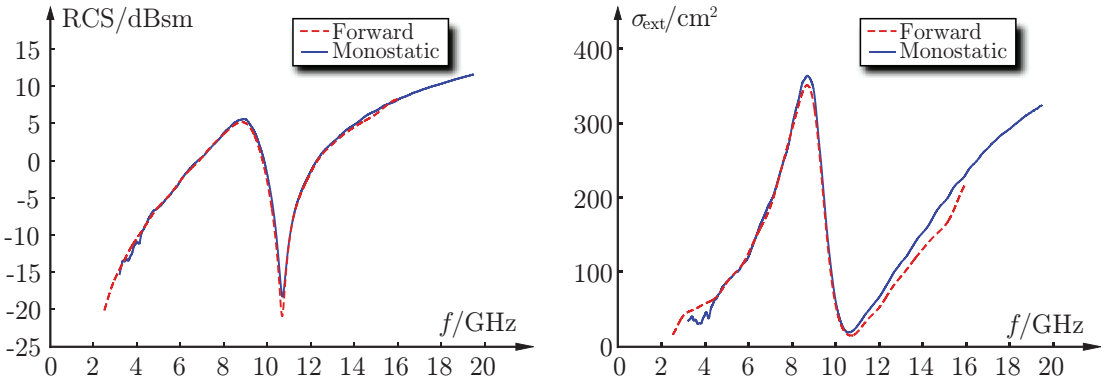

Figure 6: The forward and monostatic RCS (left figure) and the extinction cross section (right figure) determined from the RCS amplitude in the forward and backward directions.

cross section is integrated to obtain a lower bound of $\lim_{f\to 0} A(f;\hat{\boldsymbol{k}},\hat{\boldsymbol{e}})/f^2$. By integrating the measured data in the graph on the right-hand side of Fig. 6 a lower bound of 1.1 cm/GHz^2 is obtained using either the forward or the monostatic data.

A method to approximate $A(k;\hat{\boldsymbol{k}},\hat{\boldsymbol{e}})/k^2$ is to use a meromorphic function with roots and zeros in the lower half of the complex k-plane. Numerical tests using the algorithm in Ref. 6 indicate that it is sufficient to consider a rational function with a numerator and a denominator of second and fourth degree polynomials, respectively. This function can be represented by a sum of two Lorentz resonance models, *viz.*,

$$\frac{A^{(\mathrm{appr})}(k,\hat{\boldsymbol{k}},\hat{\boldsymbol{e}})}{k^2} = \sum_{n=1}^{2} a_n \frac{k_n^2 - \mathrm{i}k\nu_n}{k_n^2 - 2\mathrm{i}kk_n/Q_n - k^2} \tag{5.4}$$

The optical theorem, (2.2), can be used to determine an approximation to the extinction cross section, $\sigma_{\mathrm{ext}}^{(\mathrm{appr})}(k)$, from $A^{(\mathrm{appr})}(k,\hat{\boldsymbol{k}},\hat{\boldsymbol{e}})$,

$$\sigma_{\mathrm{ext}}^{(\mathrm{appr})}(k) = \frac{2\sqrt{\pi}}{k}\,\mathrm{Im}\,A^{(\mathrm{appr})}(k,\hat{\boldsymbol{k}},\hat{\boldsymbol{e}}) \tag{5.5}$$

The approximations (5.4) and (5.5) are depicted by the dotted lines in Fig. 7. It is concluded that the approximations are in good agreement with the experimental results.

A more accurate value for the quantity $\lim_{k\to 0} A(k;\hat{\boldsymbol{k}},\hat{\boldsymbol{e}})/k^2$ on the right-hand side of (5.2) is determined from (5.4). In fact, the lower bound 1.1 cm/GHz^2 should be compared with the corresponding value 1.5 cm/GHz^2 obtained by integrating $\sigma_{\mathrm{ext}}^{(\mathrm{appr})}(k)$ over the range $[0, 22]$ GHz. The lower bound 1.5 cm/GHz^2 is quite close to the static limit 1.8 cm/GHz^2, which is predicted by the parameters in the Lorentz resonance model (5.4).

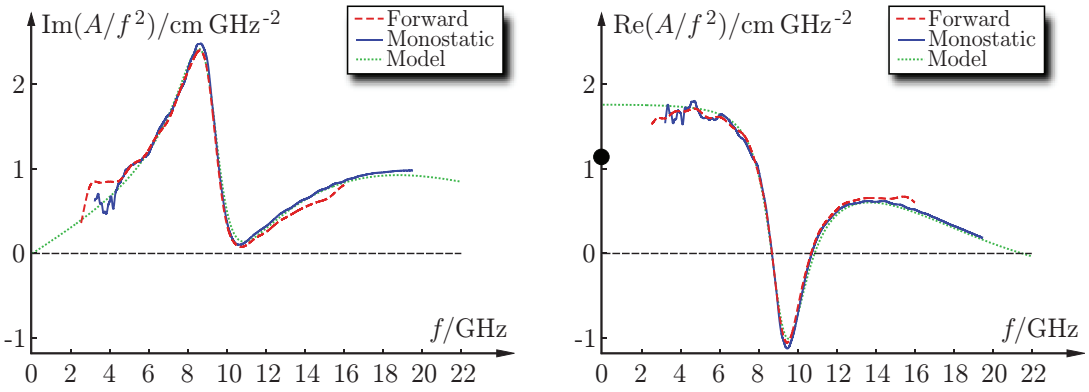

Figure 7: The imaginary part (left figure) and the real part (right figure) of A/f^2 determined from the RCS amplitude in the forward and backward directions. The dot for zero frequency indicates a lower bound of $\lim_{f\to 0} A(f;\hat{\boldsymbol{k}},\hat{\boldsymbol{e}})/f^2$ obtained by integrating the extinction cross section. The dotted lines are given by the approximation (5.4).

6 Conclusions

This paper exploits a sum rule for the extinction cross section to find bounds on scattering of electromagnetic waves by an object. The theory is both numerically and experimentally verified. The integrated extinction, which exclusively is determined by the static properties of the object, limits the total scattering properties of the object. Specifically, it is found that large scattering effects always have to be compensated by a loss of bandwidth. This loss of bandwidth can be quantified.

Moreover, we show that monostatic RCS amplitude measurements can be used to determine the extinction cross section for thin and non-magnetic samples by validating the experimental method with a forward RCS measurement. The experimental results show that the sum rule (5.2) is in good agreement with the measurements.

Acknowledgements

The financial support by the Swedish Research Council and the Swedish Foundation for Strategic Research is gratefully acknowledged. The authors also thank Saab Bofors Dynamics, Linköping, Sweden, and in particular Carl-Gustaf Svensson and Mats Andersson for generous hospitality and practical assistance in the measurement campaigns.

References

[1] C. F. Bohren and D. R. Huffman. *Absorption and Scattering of Light by Small Particles*. John Wiley & Sons, New York, 1983.

[2] M. Gustafsson, C. Sohl, and G. Kristensson. Physical limitations on antennas of arbitrary shape. *Proc. R. Soc. A*, **463**(2086), 2589–2607, 2007.

[3] R. E. Kleinman and T. B. A. Senior. Rayleigh scattering. In V. V. Varadan and V. K. Varadan, editors, *Low and High Frequency Asymptotics*, volume 2 of *Handbook on Acoustic, Electromagnetic and Elastic Wave Scattering*, chapter 1, pages 1–70. Elsevier Science Publishers, Amsterdam, 1986.

[4] E. F. Knott, J. F. Shaeffer, and M. T. Tuley. *Radar Cross Section*. SciTech Publishing Inc., 5601 N. Hawthorne Way, Raleigh, NC 27613, 2004.

[5] L. D. Landau and E. M. Lifshitz. *Statistical Physics, Part 1*. Butterworth-Heinemann, Linacre House, Jordan Hill, Oxford, third edition, 1980.

[6] E. C. Levi. Complex-curve fitting. *IRE Trans. on Automatic Control*, **AC-4**, 37–44, 1959.

[7] R. G. Newton. *Scattering Theory of Waves and Particles*. Dover Publications, New York, second edition, 2002.

[8] H. M. Nussenzveig. *Causality and Dispersion Relations*. Academic Press, London, 1972.

[9] W. K. H. Panofsky and M. Phillips. *Classical Electricity and Magnetism*. Addison-Wesley, Reading, second edition, 1962.

[10] B. Peterson and S. Ström. T-matrix for electromagnetic scattering from an arbitrary number of scatterers and representations of E(3). *Phys. Rev. D*, **8**, 3661–3678, 1973.

[11] E. M. Purcell. On the absorption and emission of light by interstellar grains. *J. Astrophys.*, **158**, 433–440, 1969.

[12] G. T. Ruck, D. E. Barrick, W. D. Stuart, and C. K. Krichbaum. *Radar Cross-Section Handbook*, volume 1 and 2. Plenum Press, New York, 1970.

[13] D. Schurig, J. J. Mock, and D. R. Smith. Electric-field-coupled resonators for negative permittivity metamaterials. *Appl. Phys. Lett.*, **88**, 041109, 2006.

[14] C. Sohl and M. Gustafsson. A priori estimates on the partial realized gain of ultra-wideband (UWB) antennas. *Quart. J. Mech. Appl. Math.*, **61**(3), 415–430, 2008.

[15] C. Sohl, M. Gustafsson, and G. Kristensson. Physical limitations on broadband scattering by heterogeneous obstacles. *J. Phys. A: Math. Theor.*, **40**(36), 11165–11182, 2007.

[16] C. Sohl, M. Gustafsson, and G. Kristensson. Physical limitations on metamaterials: Restrictions on scattering and absorption over a frequency interval. *J. Phys. D: Applied Phys.*, **40**(22), 7146–7151, 2007.

[17] C. Sohl, C. Larsson, M. Gustafsson, and G. Kristensson. A scattering and absorption identity for metamaterials: Experimental results and comparison with theory. *J. Appl. Phys.*, **103**(5), 054906, 2008.

[18] J. G. van Bladel. *Electromagnetic Fields*. IEEE Press, New York, 2007.

[19] H. Wallén and A. Sihvola. Polarizability of conducting sphere-doublets using series of images. *J. Appl Phys.*, **96**(4), 2330, 2004.

Some paradoxes associated with a recent summation rule in scattering theory

Christian Sohl, Mats Gustafsson, and Anders Bernland

Paper V

Based on: C. Sohl, M. Gustafsson, and A. Bernland. Some paradoxes associated with a recent summation rule in scattering theory. *Proceedings of the URSI General Assembly*, Chicago, U.S., August 7–16, 2008.

Abstract

This paper reports on some peculiarities associated with a recently published sum rule for scattering of electromagnetic waves. The sum rule states that the extinction cross section integrated over all frequencies is governed by the low-frequency response of the target. Although the sum rule is intriguing by itself, it becomes even more paradoxical when the conductivity model or the perfectly electric conducting boundary condition is introduced. The paradoxical character lies in the fact that the extinction cross section integrated over all frequencies is independent of the conductivity as long as it is non-zero. This puzzling result can be explained partially by rejecting the conductivity model at low frequencies as suggested by numerical simulations of a homogeneous and isotropic sphere. In addition, the low-frequency behavior of diamagnetic materials is investigated using Herglotz functions and arguments from the theory of special relativity.

1 Introduction

Under the assumption of linearity, passivity, and time-translational invariance, a sum rule for scattering of electromagnetic waves is derived in Refs. 7 and 8 from the holomorphic properties of the forward scattering dyadic. The result states that the extinction cross section, *i.e.*, the sum of the scattering and absorption cross sections, integrated over all frequencies is equal to the static polarizability dyadics. As a consequence, for a given target, there is only a limited amount of scattering and absorption available in any frequency interval. This far-reaching observation is applicable to a broad range of problems in theoretical physics involving wave interaction with matter on a macroscopic scale. In Ref. 3, the sum rule also holds with minor changes to a large class of causal and reciprocal antennas. Compared to the classical antenna bounds, the theoretical findings in Ref. 3 yield sharper inequalities, and, more importantly, a new fundamental understanding of antennas solely based on its low-frequency properties.

Consider a homogeneous and isotropic sphere of radius a, and let $\kappa = ka$, where k denotes the angular wave number in free space. Introduce the extinction efficiency $Q_{\text{ext}}(\kappa) = \sigma_{\text{ext}}(\kappa)/\pi a^2$ as the extinction cross section normalized with the geometrical cross section area πa^2. Let $\epsilon = \epsilon(\kappa)$ and $\mu = \mu(\kappa)$ measure the permittivity and permeability of the target relative to free space, and assume ϵ and μ are continuous at $\kappa = 0$. The sum rule in Ref. 7 then reduces to

$$\int_0^\infty \frac{Q_{\text{ext}}(\kappa)}{\kappa^2}\,\mathrm{d}\kappa = 2\pi\left(\frac{\epsilon(0)-1}{\epsilon(0)+2} + \frac{\mu(0)-1}{\mu(0)+2}\right). \tag{1.1}$$

Although the integral in (1.1) has a simple closed-form expression, this is generally not true for the integrand $Q_{\text{ext}}(\kappa)/\kappa^2$ for a fixed $\kappa \in [0,\infty)$. In particular, note that the right-hand side of (1.1) is independent of any temporal dispersion (although the integrand is not), depending only on the low-frequency response of the target. As expected, the right-hand side of (1.1) vanishes as $\epsilon(0) = \mu(0) = 1$ (*i.e.*, as the target reduces to free space), *cf.*, the Kramers-Kronig relations in Ref. 9. More generally,

if the equality in (1.1) is replaced by a less than or equal to sign, the new inequality holds also for any isotropic and homogeneous scatterer circumscribed by a sphere of radius a, see Ref. 7.

Under the assumption that ϵ and μ are continuous in the low-frequency limit, it follows from the Kramers-Kronig relations that $\epsilon(0)$ and $\mu(0)$ are bounded from below by the optical responses $\epsilon_\infty = \lim_{\kappa\to\infty}\epsilon(\kappa) \geqslant 1$ and $\mu_\infty = \lim_{\kappa\to\infty}\mu(\kappa) \geqslant 1$, respectively. Since ϵ_∞ and μ_∞ are non-unique from a modeling point of view, see Ref. 4, it is sufficient to set $\epsilon_\infty = \mu_\infty = 1$. Thus, $\epsilon(0)$ and $\mu(0)$ are bounded from below by unity, and it follows that the right-hand side of (1.1) is non-negative. This observation is consistent with the fact that the integrand in (1.1) by definition is non-negative, see Refs. 7 and 9.

However, the sum rule (1.1) is not valid if either ϵ or μ are discontinuous at $\kappa = 0$, which is the case for the conductivity model discussed on pp. 14–19 in Ref. 2. Numerical results in Ref. 8 with temporally dispersive material parameters in the form of a Drude model, *i.e.*, a difference between a conductivity term and a Debey model, suggest that (1.1) is independent of the conductivity as long as it is non-zero. Furthermore, diamagnetic materials with a low-frequency permeability less than unity seem to contradict (1.1) since the second term on the right-hand side then becomes negative. The purpose of this paper is to clarify the effects of the conductivity model (including the perfectly electric conducting limit) and diamagnetic material parameters in the context of (1.1) and the theoretical findings in Refs. 7 and 8.

2 The effects of conductivity at low frequencies

Introduce the dimensionless quantity $\varsigma = \sigma_{\mathrm{c}} a\eta_0 > 0$, where σ_{c} measures the conductivity, and η_0 is the wave impedance in free space. Let $\epsilon' = \epsilon'(\kappa)$ be an arbitrary complex-valued permittivity that is continuous at $\kappa = 0$. Consider the target in Sec. 1 with the following permittivity model which is singular at $\kappa = 0$:

$$\epsilon(\kappa) = \epsilon'(\kappa) + \mathrm{i}\frac{\varsigma}{\kappa}. \tag{2.1}$$

Without loss of generality, let the target be non-magnetic in the sense that $\mu(\kappa) = 1$ independent of $\kappa \in [0, \infty)$.[1] Then, it follows that the transition matrix in the null-field method is diagonal with electric 2^ℓ-pole (dipole, quadrupole, hexadecapole, ...) contributions given by, see Ref. 10,

$$t_{2\ell}(\kappa) = -\frac{\mathrm{j}_\ell(\kappa)(\kappa\sqrt{\epsilon(\kappa)}\mathrm{j}_\ell(\kappa\sqrt{\epsilon(\kappa)}))' - \epsilon(\kappa)(\kappa\mathrm{j}_\ell(\kappa))'\mathrm{j}_\ell(\kappa\sqrt{\epsilon(\kappa)})}{\mathrm{h}_\ell^{(1)}(\kappa)(\kappa\sqrt{\epsilon(\kappa)}\mathrm{j}_\ell(\kappa\sqrt{\epsilon(\kappa)}))' - \epsilon(\kappa)(\kappa\mathrm{h}_\ell^{(1)}(\kappa))'\mathrm{j}_\ell(\kappa\sqrt{\epsilon(\kappa)})}, \tag{2.2}$$

[1] This assumption is justified by the fact that electromagnetic fields decouple in the low-frequency limit, *cf.*, the right-hand side of (1.1).

where $\ell = 1, 2, 3, \ldots$, and a prime denotes differentiation with respect to either $\kappa\sqrt{\epsilon(\kappa)}$ or κ depending on the arguments of j_ℓ and $\mathrm{h}_\ell^{(1)}$.[2] Here, j_ℓ and $\mathrm{h}_\ell^{(1)}$ denote the spherical Bessel and Hankel functions of first kind, respectively, see Ref. 1. The extinction efficiency is related to the transition matrix via $Q_{\mathrm{ext}}(\kappa) = -2\,\mathrm{Re}\sum_\ell(2\ell+1)(t_{1\ell}(\kappa)+t_{2\ell}(\kappa))/\kappa^2$, *cf.*, the classical Mie series solution.

For the homogeneous and isotropic sphere, the right-hand side of (1.1) is equal to $\gamma_\infty/2$, where γ_∞ denotes the degenerate eigenvalue of the high-contrast polarizability dyadic in Refs. 7 and 8. This quantity is defined by the following limiting value for the lowest order ($\ell = 1$) transition matrix element:

$$\gamma_\infty = -6\pi\mathrm{i}\lim_{\kappa\to 0+}\frac{t_{21}(\kappa)}{\kappa^3}. \tag{2.4}$$

For a permittivity model which is continuous at $\kappa = 0$, it is straightforward to prove that the right-hand side of (1.1) is equal to $\gamma_\infty/2$. The corresponding limit for the permittivity model (2.1) is somewhat more complicated as the asymptotic expansion $\sqrt{\epsilon(\kappa)} = \mathrm{e}^{\mathrm{i}\pi/4}\sqrt{\varsigma/\kappa} + \mathcal{O}(\sqrt{\kappa})$ for $\kappa \to 0+$ must be inserted into (2.2). Together with the asymptotics $\mathrm{j}_\ell(\kappa) = 2^\ell\ell!\kappa^\ell/(2\ell+1)! + \mathcal{O}(\kappa^{\ell+2})$ and $\mathrm{h}_\ell^{(1)}(\kappa) = -\mathrm{i}(2\ell)!/2^\ell\ell!\kappa^{\ell+1} + \mathcal{O}(\kappa^{-\ell+1})$ as $\kappa \to 0+$, see p. 437 in Ref. 1, it is not hard to show that $\gamma_\infty = 4\pi$ for the permittivity model (2.1). Thus, it is concluded that

$$\int_0^\infty \frac{Q_{\mathrm{ext}}(\kappa)}{\kappa^2}\,\mathrm{d}\kappa = 2\pi \tag{2.5}$$

in the presence of a conductivity term. So, as long as an arbitrarily small conductivity is present in the materials of the target, the integral on the left-hand side of (1.1) is equal to 2π independent of the values of $\epsilon'(0)$ and ς. Here, the paradoxical character lies in the fact that the integral on the left-hand side of (1.1) is discontinuous in the limit as $\varsigma \to 0+$. This is a severe restriction in the sense that there is no longer a freedom to model an electrical insulator as a low-conductivity material or as a material with a conductivity which is identically zero.

The null-field method is also used to verify (2.5) by numerically computing the extinction efficiency. The result is depicted on the left-hand side of Fig. 1 (the right figure is a close-up at low frequencies) for $\epsilon'(\kappa) = 1$ and $\varsigma \in \{0.1, 1, 10, 10^4\}$ independent of $\kappa \in [0, \infty)$. A numerical integration shows that the integral in (2.5) indeed is equal to 2π (within relative errors less than 1% for the domain of definition $\kappa \in [0, 34]$) for the four curves in Fig. 1. The fifth curve labeled PEC is discussed in Sec. 3, and it can be shown that this curve has an integral equal to π rather than 2π when it is weighted with $1/\kappa^2$. At a first glance, one does not expect that the four curves in Fig. 1 have the same value of the integral. However, the left figure in Fig. 1 suggests that the curves with low conductivities are shifted towards lower

[2]The corresponding magnetic elements are given by, see Ref. 10,

$$t_{1\ell}(\kappa) = -\frac{\mathrm{j}_\ell(\kappa)(\kappa\sqrt{\epsilon(\kappa)}\mathrm{j}_\ell(\kappa\sqrt{\epsilon(\kappa)}))' - (\kappa\mathrm{j}_\ell(\kappa))'\mathrm{j}_\ell(\kappa\sqrt{\epsilon(\kappa)})}{\mathrm{h}_\ell^{(1)}(\kappa)(\kappa\sqrt{\epsilon(\kappa)}\mathrm{j}_\ell(\kappa\sqrt{\epsilon(\kappa)}))' - (\kappa\mathrm{h}_\ell^{(1)}(\kappa))'\mathrm{j}_\ell(\kappa\sqrt{\epsilon(\kappa)})}. \tag{2.3}$$

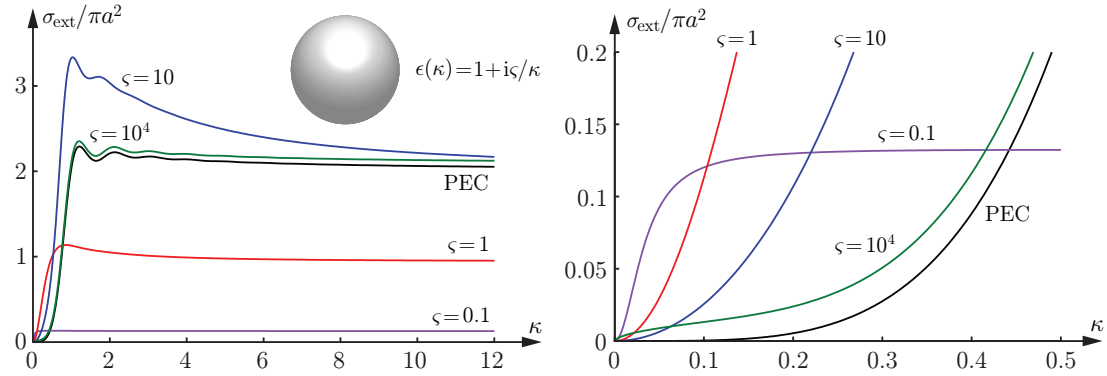

Figure 1: The extinction cross section in units of πa^2 for a homogeneous and isotropic sphere with $\epsilon' = 1$. The right figure is a close-up of the left figure for low frequencies, and as a consequence of (2.5), all curves (except for the one labeled PEC) have the same integrated value when they are weighted with $1/\kappa^2$.

frequencies in such a manner that the integrals are preserved. This behavior can further be understood by examining the zeros of the denominator in (2.2) in the vicinity of the negative imaginary axis in the complex κ-plane.

The puzzling identity (2.5) can partially be explained by rejecting the conductivity model at low frequencies. For example, this may be done by introducing a frequency dependent conductivity $\varsigma = \varsigma(\kappa)$ for sufficiently low frequencies, or, equivalently, through a regularization (*i.e.*, replacing $\mathrm{i}\varsigma/\kappa$ by $\mathrm{i}\varsigma/(\kappa+\mathrm{i}\varepsilon)$ for some $\varepsilon > 0$) of the conductivity model. This is analogous to the requirement of an infinitely large relaxation time in the Debey model. Alternatively, one may transform (2.5) into an inequality by removing a tiny portion of the integral in the neighborhood of $\kappa = 0$. In the latter case,

$$\int_{\varepsilon}^{\infty} \frac{Q_{\text{ext}}(\kappa)}{\kappa^2}\, \mathrm{d}\kappa \leqslant 2\pi, \tag{2.6}$$

for any $\varepsilon > 0$. The left-hand side of (2.6) now depends on both ε and ς, and in general it is no longer true that the integral is equal to 2π.

3 A comparison with the PEC material model

The transmission boundary conditions in (2.2) state that the tangential components of the electric and magnetic fields are continuous on the boundary surface of the target. This should be compared with the perfectly electric conducting (PEC) limit which requires that the tangential component of the electric field vanishes on the target. For a fixed $\kappa > 0$, (2.2) approaches the corresponding matrix elements for the perfectly electric conducting boundary condition as the magnitude of ϵ tends to infinity (*e.g.*, by letting $\varsigma \to \infty$ in the presence of a conductivity term). However, this is not true in the low-frequency limit as it is reasonable to expect that the index of refraction $n(\kappa) = \sqrt{\epsilon(\kappa)\mu(\kappa)}$ must be bounded as $\kappa \to 0+$. Instead, the perfectly electric conducting limit at low frequencies is obtained by simultaneously letting

$\epsilon(0) \to \infty$ and $\mu(0) \to 0+$ as suggested by the discussion in Ref. 7 and references therein.

4 Diamagnetism in the low-frequency limit

At a first glance, diamagnetic materials with $\mu(0)$ less than unity seem to contradict (1.1) since the second term on the right-hand side then becomes negative, *cf.*, p. 283 in Ref. 6. However, the negative value of $\mu(0)$ is compensated by a positive value of $\epsilon(0)$ as seen below. Use the fact that $\kappa\epsilon(\kappa)$ and $\kappa\mu(\kappa)$ are Herglotz functions, *i.e.*, holomorphic functions in the upper half part of the complex κ-plane, with the properties that $\operatorname{Im}\kappa\epsilon(\kappa) \geqslant 0$ and $\operatorname{Im}\kappa\mu(\kappa) \geqslant 0$, see Ref. 9. Then, $\kappa(n(\kappa)-n_\infty)$ defines a new Herglotz function, where $n_\infty = \lim_{\kappa\to\infty} n(\kappa)$ denotes the high-frequency index of refraction. Hence, $n(0)$ is bounded from below by n_∞, and from the inequality between the geometric and arithmetic mean values in Ref. 5, one has

$$\frac{\epsilon(0)+\mu(0)}{2} \geqslant \sqrt{\epsilon(0)\mu(0)} \geqslant n_\infty. \tag{4.1}$$

Equality on the left-hand side of (4.1) holds if and only if $\epsilon(0) = \mu(0)$. Now, since the causality postulate in the special theory of relativity states that no signal can propagate with a phase velocity greater than the phase velocity in free space, it is concluded that n_∞ is bounded from below by unity (alternatively, one may use the Kramers-Kronig relations), and (4.1) yields that $\epsilon(0) + \mu(0) \geqslant 2$. Under the assumption that $\epsilon(0)$ is positive (or more generally, not less than $\mu(0)$), the parenthesis on the right-hand side of (1.1) can be estimated from below by $(\epsilon(0) + \mu(0) - 2)/(\epsilon(0) + 2)$ which indeed is non-negative. It is thus concluded that the right-hand side of (1.1) remains positive in the presence of diamagnetic materials, and that there is no contradiction with the definition of the extinction efficiency.

5 Conclusions

It is concluded that the extinction cross section integrated over all frequencies is independent of the conductivity ς as long as it is non-zero. The perfectly electric conducting boundary condition is obtained in the low-frequency limit by letting not only the magnitude of $\epsilon(0)$ approach infinity, but simultaneously sending $\mu(0)$ to zero such that $n(0) = \sqrt{\epsilon(0)\mu(0)}$ remains bounded and well-defined. Furthermore, diamagnetic material parameters in the low-frequency limit cause no problems in (1.1) since a static permeability less than unity is compensated by a corresponding positive permittivity such that the right-hand side of (1.1) becomes non-negative.

Acknowledgments

The financial support by the Swedish Research Council is gratefully acknowledged. The authors are also grateful for fruitful discussions with Prof. Gerhard Kristens-

son at the Department of Electrical and Information Technology, Lund University, Sweden.

References

[1] M. Abramowitz and I. A. Stegun, editors. *Handbook of Mathematical Functions*. Applied Mathematics Series No. 55. National Bureau of Standards, Washington D.C., 1970.

[2] C. F. Bohren and D. R. Huffman. *Absorption and Scattering of Light by Small Particles*. John Wiley & Sons, New York, 1983.

[3] M. Gustafsson, C. Sohl, and G. Kristensson. Physical limitations on antennas of arbitrary shape. *Proc. R. Soc. A*, **463**(2086), 2589–2607, 2007.

[4] M. Gustafsson. On the non-uniqueness of the electromagnetic instantaneous response. *J. Phys. A: Math. Gen.*, **36**, 1743–1758, 2003.

[5] G. H. Hardy, J. E. Littlewood, and G. Pólya. *Inequalities*. Cambridge University Press, Cambridge, U.K., 1978.

[6] L. D. Landau, E. M. Lifshitz, and L. P. Pitaevskiĭ. *Electrodynamics of Continuous Media*. Pergamon Press, Oxford, second edition, 1984.

[7] C. Sohl, M. Gustafsson, and G. Kristensson. Physical limitations on broadband scattering by heterogeneous obstacles. *J. Phys. A: Math. Theor.*, **40**(36), 11165–11182, 2007.

[8] C. Sohl, M. Gustafsson, and G. Kristensson. Physical limitations on metamaterials: Restrictions on scattering and absorption over a frequency interval. *J. Phys. D: Applied Phys.*, **40**(22), 7146–7151, 2007.

[9] C. Sohl. *Dispersion Relations for Extinction of Acoustic and Electromagnetic Waves*. Licentiate thesis, Lund University, Department of Electrical and Information Technology, P.O. Box 118, S-221 00 Lund, Sweden, 2007.

[10] P. C. Waterman. Matrix methods in potential theory and electromagnetic scattering. *J. Appl. Phys.*, **50**(7), 4550–4566, 1979.

A general approach for deriving bounds in electromagnetic theory

Christian Sohl, Mats Gustafsson, Gerhard Kristensson, and Sven Nordebo

Paper VI

Based on: C. Sohl, M. Gustafsson, G. Kristensson, and S. Nordebo. A general approach for deriving bounds in electromagnetic theory. *Proceedings of the URSI General Assembly*, Chicago, U.S., August 7–16, 2008.

Abstract

This paper reports on a systematic procedure for deriving bounds in electromagnetic theory. The approach is based on the holomorphic properties of certain Herglotz functions and their asymptotic expansions in the low- and high-frequency regimes. A family of integral identities or sum rules is obtained with values governed by the coefficients in the low- and high-frequency expansions. In particular, sum rules for plane-wave scattering by a homogeneous and isotropic sphere are derived and numerically verified by computing the extinction cross section and the bistatic radar cross section in the forward direction. It is concluded that the obtained sum rules show great potential for deriving new physical bounds in, *e.g.*, scattering and antenna problems.

1 Introduction

Sum rules, or more generally, dispersion relations, are promising techniques in theoretical physics for analyzing particle collisions and scattering of acoustic, electromagnetic, and elastic waves, see Ref. 6. There are at least three main advantages of sum rules in the modeling of macroscopic wave interaction with matter: (i) they provide consistency checks of calculated quantities when the underlying mathematical model a priori is known to be causal, (ii) they may be used to verify whether a given mathematical model or an experimental outcome behaves causally or not, and (iii) they yield bounds and estimates on quantities with experimental significance. In addition, sum rules are valuable as benchmark results for comparing different numerical methods. Techniques based on sum rules have successfully been applied in Refs. 1, 4, and 5 to a large class of scattering and antenna problems to establish bounds on the amount of electromagnetic interaction available in a given frequency interval. This paper, however, takes a more general approach and presents a systematic way of deriving new sum rules in electromagnetic theory.

2 Sum rules for Herglotz functions

Consider an arbitrary Herglotz function $h = h(\kappa)$ defined as a mapping from the upper half part of the complex κ-plane into itself, *i.e.*, let $h(\kappa)$ be a holomorphic function with the property that $\operatorname{Im} h(\kappa) > 0$ for $\operatorname{Im} \kappa > 0$, see Ref. 3. Assume that $h(\kappa)$ has the following low-frequency expansion in the vicinity of the origin:

$$h(\kappa) = a_{-1}\kappa^{-1} + a_1\kappa + \ldots + a_{2N-1}\kappa^{2N-1} + \mathcal{O}(\kappa^{2N}) \quad \text{as } \kappa \to 0, \tag{2.1}$$

where $a_{-n} = 0$ for $n = 2, 3, \ldots$. The corresponding asymptotic series at infinity with $b_m = 0$ for $m = 2, 3, \ldots$ reads

$$h(\kappa) = b_1\kappa + b_{-1}\kappa^{-1} + \ldots + b_{1-2M}\kappa^{1-2M} + \mathcal{O}(\kappa^{-2M}) \quad \text{as } \kappa \to \infty, \tag{2.2}$$

where it has been used that $h(\kappa)/\kappa$ and $\kappa h(\kappa)$ are bounded as $\kappa \to \infty$ and $\kappa \to 0$, respectively. The latter statement follows from the previous by observing that

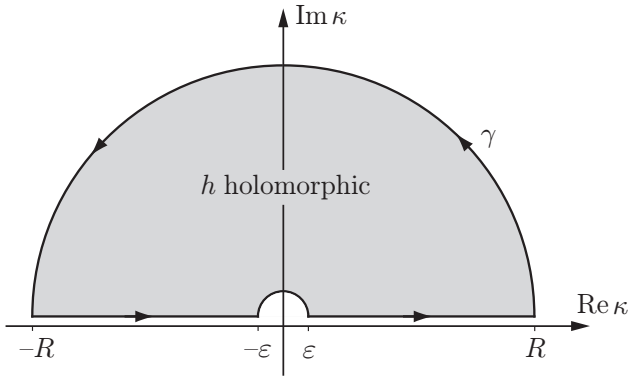

Figure 1: Trajectory γ in the complex κ-plane for the contour integral (2.3).

$-1/h(\kappa)$ defines a new Herglotz function whenever $h(\kappa)$ is a Herglotz function. The non-negative integers N and M are chosen such that they correspond to the first even monomials in (2.1) and (2.2), respectively.

Assume $h(\kappa)$ satisfies the cross symmetry $h(\kappa) = -h^*(-\kappa^*)$ for complex-valued κ, implying that a_{2n-1} and b_{1-2m} are real-valued for $n, m = 0, 1, \ldots$ (in addition, it is known that $-a_{-1}$ and b_1 are non-negative), and consider the integral of $h(\kappa)/\kappa^\ell$ with respect to the contour in Fig. 1. Then, for any integer ℓ and $0 < \varepsilon < R$ one has

$$\int_{\varepsilon<|\kappa|<R} \frac{h(\kappa)}{\kappa^\ell}\,\mathrm{d}\kappa = \mathrm{i}\varepsilon^{1-\ell}\int_0^\pi h(\varepsilon \mathrm{e}^{\mathrm{i}\phi})\mathrm{e}^{\mathrm{i}(1-\ell)\phi}\,\mathrm{d}\phi - \mathrm{i}R^{1-\ell}\int_0^\pi h(R\mathrm{e}^{\mathrm{i}\phi})\mathrm{e}^{\mathrm{i}(1-\ell)\phi}\,\mathrm{d}\phi, \quad (2.3)$$

where κ is real-valued in the first integral on the left-hand side of (2.3). Here, the small and large semicircles in Fig. 1 are parameterized by $\kappa(\phi) = \varepsilon \mathrm{e}^{\mathrm{i}(\pi-\phi)}$ and $\kappa(\phi) = R\mathrm{e}^{\mathrm{i}\phi}$, respectively, where $\phi \in [0, \pi]$. In order to evaluate the right-hand side of (2.3), introduce the auxiliary integral

$$I_\ell = \int_0^\pi \mathrm{e}^{\mathrm{i}\ell\phi}\,\mathrm{d}\phi = \mathrm{i}\frac{1-\mathrm{e}^{\mathrm{i}\pi\ell}}{\ell} = \mathrm{i}\frac{2\alpha_\ell}{\ell}, \qquad \ell \neq 0, \quad (2.4)$$

with $I_0 = \pi$. Here, $\alpha_\ell = (1-(-1)^\ell)/2$, so $\alpha_\ell = 1$ for odd ℓ-values, and $\alpha_\ell = 0$ for even ℓ-values. When (2.1) is inserted into (2.3) for a fixed $\varepsilon > 0$, the first integral on the right-hand side of (2.3) becomes

$$\begin{aligned}\mathrm{i}\varepsilon^{1-\ell}\int_0^\pi h(\varepsilon\mathrm{e}^{\mathrm{i}\phi})\mathrm{e}^{\mathrm{i}(1-\ell)\phi}\,\mathrm{d}\phi &= \mathrm{i}\left(a_{-1}\varepsilon^{-\ell}I_{-\ell} + \ldots + a_{2N-1}\varepsilon^{2N-\ell}I_{2N-\ell} + \mathcal{O}(\varepsilon^{2N+1-\ell})\right)\\ &= f(\varepsilon) + \mathcal{O}(\varepsilon^{2N+1-\ell}) + \mathrm{i}\pi\alpha_{\ell-1}a_{\ell-1}, \quad (2.5)\end{aligned}$$

where f is a real-valued function not necessarily continuous at $\varepsilon = 0$. Analogous to (2.5), for a fixed $R > 0$, the second integral on the right-hand side of (2.3) yields

$$\begin{aligned}-\mathrm{i}R^{1-\ell}\int_0^\pi h(R\mathrm{e}^{\mathrm{i}\phi})\mathrm{e}^{\mathrm{i}(1-\ell)\phi}\,\mathrm{d}\phi &= -\mathrm{i}\left(b_1R^{2-\ell}I_{2-\ell} + \ldots + b_{1-2M}R^{2-2M-\ell}I_{2-2M-\ell}\right.\\ &\left.+\mathcal{O}(R^{1-2M-\ell})\right) = f'(R) + \mathcal{O}(R^{1-2M-\ell}) - \mathrm{i}\pi\alpha_{\ell-1}b_{\ell-1}, \quad (2.6)\end{aligned}$$

where f' is a new real-valued function not necessarily continuous at infinity. Note that the rest terms $\mathcal{O}(\varepsilon^{2N+1-\ell})$ and $\mathcal{O}(R^{1-2M-\ell})$ in general are complex-valued.

Now, from the cross symmetry $h(\kappa) = -h^*(-\kappa^*)$, it follows that $\operatorname{Re} h(\kappa) = -\operatorname{Re} h(-\kappa)$ and $\operatorname{Im} h(\kappa) = \operatorname{Im} h(-\kappa)$ for real-valued κ, and sending $\varepsilon \to 0$ and $R \to \infty$ in (2.3) therefore yields

$$\lim_{\varepsilon\to 0}\lim_{R\to\infty}\int_{\varepsilon<|\kappa|<R}\frac{h(\kappa)}{\kappa^\ell}\,\mathrm{d}\kappa = 2\alpha_\ell\int_0^\infty\frac{\operatorname{Re} h(\kappa)}{\kappa^\ell}\,\mathrm{d}\kappa + 2\mathrm{i}\alpha_{\ell-1}\int_0^\infty\frac{\operatorname{Im} h(\kappa)}{\kappa^\ell}\,\mathrm{d}\kappa. \quad (2.7)$$

When $\varepsilon \to 0$ and $R \to \infty$, the rest terms in (2.5) and (2.6) vanish for $\ell = \ldots, 2N-1, 2N$ and $\ell = 2-2M, 3-2M, \ldots$, respectively. Thus, the left-hand side of (2.3) is well-defined if and only if $\ell = 2-2M, 3-2M, \ldots, 2N$. Thus, taking the imaginary part of (2.3) finally yields the following family of sum rules ($p = \ell/2$):

$$\int_0^\infty\frac{\operatorname{Im} h(\kappa)}{\kappa^{2p}}\,\mathrm{d}\kappa = \frac{\pi}{2}(a_{2p-1} - b_{2p-1}), \qquad p = 1-M, 2-M, \ldots, N, \quad (2.8)$$

where it has been used that odd ℓ-values vanish due to (2.7). Since $\operatorname{Im} h(\kappa)$ is non-negative, (2.8) can further be estimated from below by integrating over any finite interval $K \subset [0,\infty)$ with center frequency $\kappa = \kappa_0$, *i.e.*,

$$B\kappa_0^{1-2p}\min_{\kappa\in K}\operatorname{Im} h(\kappa) + \mathcal{O}(B^3) \leqslant \int_K\frac{\operatorname{Im} h(\kappa)}{\kappa^{2p}}\,\mathrm{d}\kappa \leqslant \frac{\pi}{2}(a_{2p-1} - b_{2p-1}), \quad (2.9)$$

where $p = 1-M, 2-M, \ldots, N$, and $B = \int_K \mathrm{d}\kappa/\kappa_0$ denotes the relative bandwidth of K. Note that the left-hand side of (2.9) is evaluated in the narrow bandwidth approximation as $B \ll 1$, and that a more complicated expression holds when B is close to unity.

3 Plane-wave scattering by a sphere

In order to exemplify the theoretical results in Sec. 2, consider the direct scattering problem of a plane wave $\hat{\boldsymbol{e}}\mathrm{e}^{\mathrm{i}\kappa\hat{\boldsymbol{k}}\cdot\boldsymbol{x}}$ of unit amplitude impinging in the $\hat{\boldsymbol{k}}$-direction on a homogeneous and isotropic sphere of radius a. Here, $\boldsymbol{x}$ measures the position vector in units of a, and $\kappa = ka$, where k denotes the wave number in free space. The target is assumed to be non-magnetic with lossless material parameters modeled by the permittivity $\epsilon = \epsilon(\kappa)$ relative to free space. The scattered electric field in the far-field region then reads, see Ref. 2,

$$\boldsymbol{E}_{\mathrm{s}}(\kappa;\boldsymbol{x}) = \frac{\mathrm{e}^{\mathrm{i}\kappa x}}{x}\mathbf{S}(\kappa;\hat{\boldsymbol{x}})\cdot\hat{\boldsymbol{e}} + \mathcal{O}(x^{-2}) \quad \text{as } x\to\infty, \quad (3.1)$$

where $x = |\boldsymbol{x}|$, and the scattering dyadic $\mathbf{S}$ represents the mapping from an incoming plane wave (evaluated at the origin) into the amplitude of an outgoing spherical wave in the $\hat{\boldsymbol{x}}$-direction. This scattering problem is causal in the forward direction $\hat{\boldsymbol{x}} = \hat{\boldsymbol{k}}$ since the forward scattered field cannot precede the incident field. As a consequence, the arguments in Refs. 4 and 5 suggest that $h(\kappa) = 4\hat{\boldsymbol{e}}^*\cdot\mathbf{S}(\kappa;\hat{\boldsymbol{k}})\cdot\hat{\boldsymbol{e}}/\kappa$ can be extended

to a Herglotz function for a fixed electric polarization $\hat{\boldsymbol{e}}$. This Herglotz function has the property that $h(\kappa) = -h^*(-\kappa^*)$ for $\operatorname{Im}\kappa > 0$, see Ref. 2.

Now, introduce the extinction efficiency $Q_{\text{ext}}(\kappa) = \operatorname{Im} h(\kappa)$ as the extinction cross section (*i.e.*, the sum of the scattering and absorption cross sections) in units of the geometrical cross section area πa^2, *cf.*, the optical theorem in Ref. 2. From the null-field method in Ref. 7, the low-frequency expansion of $h(\kappa)$ is calculated to be

$$h(\kappa) = 4\frac{\epsilon_{\text{s}} - 1}{\epsilon_{\text{s}} + 2}\kappa + \frac{4}{15}\frac{\epsilon_{\text{s}}^4 + 25\epsilon_{\text{s}}^3 - 15\epsilon_{\text{s}}^2 - 49\epsilon_{\text{s}} + 38}{(\epsilon_{\text{s}} + 2)^2(2\epsilon_{\text{s}} + 3)}\kappa^3 + \mathcal{O}(\kappa^4) \quad \text{as } \kappa \to 0, \tag{3.2}$$

where $\epsilon_{\text{s}} = \epsilon(0)$ denotes the static response of the target. The corresponding high-frequency expansion is assumed to satisfy $h(\kappa) = \mathcal{O}(1)$ as $\kappa \to \infty$, *cf.*, the extinction paradox in Ref. 4. Thus, inserting $N = 2$ and $M = 0$ into (2.8), it is concluded that the following two sum rules hold for the lossless dielectric sphere:[1]

$$\int_0^\infty \frac{Q_{\text{ext}}(\kappa)}{\kappa^2}\,\mathrm{d}\kappa = 2\pi\frac{\epsilon_{\text{s}} - 1}{\epsilon_{\text{s}} + 2}, \quad \int_0^\infty \frac{Q_{\text{ext}}(\kappa)}{\kappa^4}\,\mathrm{d}\kappa = \frac{2\pi}{15}\frac{\epsilon_{\text{s}}^4 + 25\epsilon_{\text{s}}^3 - 15\epsilon_{\text{s}}^2 - 49\epsilon_{\text{s}} + 38}{(\epsilon_{\text{s}} + 2)^2(2\epsilon_{\text{s}} + 3)}. \tag{3.3}$$

Here, the first integral is proportional to the diagonal elements of the electric polarizability dyadic. As expected, both integrals vanish in the limit as $\epsilon_{\text{s}} \to 1$. Also, note that the second integral is unbounded whereas the first integral approaches 2π in the high-contrast limit as $\epsilon_{\text{s}} \to \infty$. Furthermore, since $-1/h(\kappa)$ defines a new Herglotz function, one has

$$-\frac{1}{h(\kappa)} = -\frac{1}{4}\frac{\epsilon_{\text{s}} + 2}{\epsilon_{\text{s}} - 1}\kappa^{-1} + \frac{1}{60}\frac{\epsilon_{\text{s}}^2 + 27\epsilon_{\text{s}} + 38}{2\epsilon_{\text{s}} + 3}\kappa + \mathcal{O}(\kappa^2) \quad \text{as } \kappa \to 0. \tag{3.4}$$

A straightforward calculation using the fact that $\operatorname{Im}(-1/h(\kappa)) = \operatorname{Im} h(\kappa)/|h(\kappa)|^2$ and $|h(\kappa)|^2 = 4\sigma_{\text{rcs}}(\kappa)/\kappa^2$ yields the following sum rule for $N = 1$ and $M = 0$:

$$\int_0^\infty \frac{Q_{\text{ext}}(\kappa)}{\sigma_{\text{rcs}}(\kappa)}\,\mathrm{d}\kappa = \frac{\pi}{30}\frac{\epsilon_{\text{s}}^2 + 27\epsilon_{\text{s}} + 38}{2\epsilon_{\text{s}} + 3}, \tag{3.5}$$

where $\sigma_{\text{rcs}}(\kappa)$ measures the bistatic radar cross in the forward direction in units of πa^2. Note that the right-hand side of (3.5) is unbounded as $\epsilon_{\text{s}} \to \infty$. Furthermore, the limiting value of (3.5) as $\epsilon_{\text{s}} \to 1$ is $11\pi/25$, which is intriguing since one expects the integrand to vanish when the material parameters in the scatterer become identical to free space. The extinction efficiency and the bistatic radar cross section in the forward direction are depicted in Fig. 2 for the lossless and non-dispersive permittivities $\epsilon = 2$ and $\epsilon = 4$. A numerical integration of the two curves in Fig. 2 (except for the curve labeled PEC) verifies that (3.3) and (3.5) hold within a relative error that can be made arbitrary small.

The corresponding low-frequency expansions of $h(\kappa)$ and $-1/h(\kappa)$ in the perfectly electric conducting (PEC) limit read

$$h(\kappa) = 2\kappa + \frac{113}{45}\kappa^3 + \mathcal{O}(\kappa^4), \qquad -\frac{1}{h(\kappa)} = -\frac{1}{2}\kappa^{-1} + \frac{113}{180}\kappa + \mathcal{O}(\kappa^2) \tag{3.6}$$

[1]The first integral in (3.3) with weighting factor $1/\kappa^2$ also holds in the lossy case as discussed in Refs. 4 and 5.

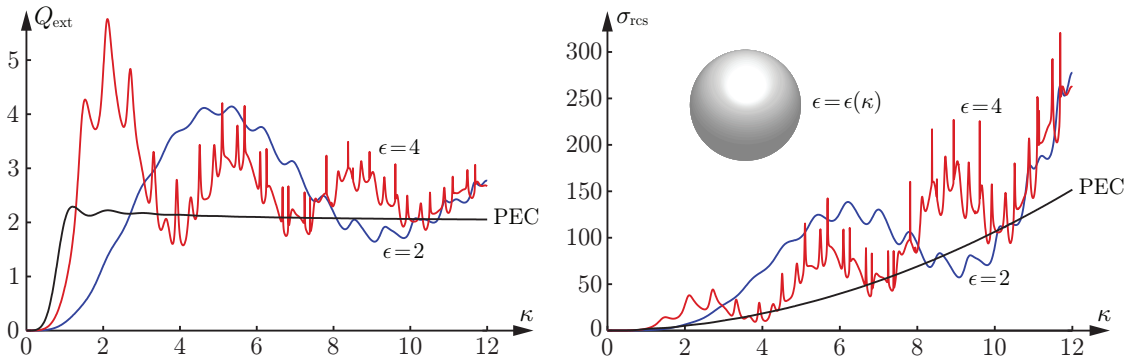

Figure 2: The extinction efficiency (left) and the forward bistatic radar cross section (right) for a homogeneous and isotropic sphere of radius a. Note that both $Q_{\text{ext}}(\kappa)$ and $\sigma_{\text{rcs}}(\kappa)$ are dimensionless quantities measured in units of the geometrical cross section area πa^2.

as $\kappa \to 0$. Thus, the three sum rules corresponding to (3.3) and (3.5) for the perfectly electric conducting sphere read

$$\int_0^\infty \frac{Q_{\text{ext}}(\kappa)}{\kappa^2}\,\mathrm{d}\kappa = \pi, \qquad \int_0^\infty \frac{Q_{\text{ext}}(\kappa)}{\kappa^4}\,\mathrm{d}\kappa = \frac{113\pi}{90}, \qquad \int_0^\infty \frac{Q_{\text{ext}}(\kappa)}{\sigma_{\text{rcs}}(\kappa)}\,\mathrm{d}\kappa = \frac{113\pi}{90}. \tag{3.7}$$

The extinction efficiency and the bistatic radar cross section in the forward direction for the perfectly electric conducting sphere are also depicted in Fig. 2. A numerical integration of the two curves labeled PEC shows that the sum rules in (3.7) hold to arbitrary precision. Due to the non-negative character of the integrands in (3.3) to (3.7), these sum rules can also be formulated as physical bounds with respect to any finite κ-interval as suggested by (2.9).

4 Conclusions

It is concluded that (2.8) and (2.9) show great potential for deriving new physical bounds in electromagnetic theory. The results in this paper can also be generalized to include functions which are bounded in magnitude by unity, *e.g.*, transmission and reflection coefficients, by mapping the unit disk into the upper half part of the κ-plane using a linear fractional transformation. A variety of new sum rules can also be established by observing that the composition of two Herglotz functions defines a new Herglotz function.

Acknowledgments

The financial support by the Swedish Research Council is gratefully acknowledged.

References

[1] M. Gustafsson, C. Sohl, and G. Kristensson. Physical limitations on antennas of arbitrary shape. *Proc. R. Soc. A*, **463**(2086), 2589–2607, 2007.

[2] R. G. Newton. *Scattering Theory of Waves and Particles*. Dover Publications, New York, second edition, 2002.

[3] H. M. Nussenzveig. *Causality and Dispersion Relations*. Academic Press, London, 1972.

[4] C. Sohl, M. Gustafsson, and G. Kristensson. Physical limitations on broadband scattering by heterogeneous obstacles. *J. Phys. A: Math. Theor.*, **40**(36), 11165–11182, 2007.

[5] C. Sohl, M. Gustafsson, and G. Kristensson. Physical limitations on metamaterials: Restrictions on scattering and absorption over a frequency interval. *J. Phys. D: Applied Phys.*, **40**(22), 7146–7151, 2007.

[6] C. Sohl. *Dispersion Relations for Extinction of Acoustic and Electromagnetic Waves*. Licentiate thesis, Lund University, Department of Electrical and Information Technology, P.O. Box 118, S-221 00 Lund, Sweden, 2007.

[7] V. V. Varadan, Y. Ma, V. K. Varadan, and A. Lakhtakia. Scattering of waves by spheres and cylinders. In V. V. Varadan, A. Lakhtakia, and V. K. Varadan, editors, *Field Representations and Introduction to Scattering*, volume 1 of *Handbook on Acoustic, Electromagnetic and Elastic Wave Scattering*, chapter 4, pages 211–324. Elsevier Science Publishers, Amsterdam, 1991.

A time-domain approach to the extinction paradox for scattering of electromagnetic waves

Mats Gustafsson, Christian Sohl, Anders Karlsson, and Gerhard Kristensson

Paper VII

Based on: M. Gustafsson, C. Sohl, A. Karlsson, and G. Kristensson. A time-domain approach to the extinction paradox for scattering of electromagnetic waves. *Proceedings of the URSI General Assembly*, Chicago, U.S., August 7–16, 2008.

Abstract

The extinction paradox states that a perfectly electric conducting target that is large compared to the wavelength removes from the incident radiation exactly twice the amount of power it can intercept by its geometrical cross section area. In this paper, the extinction paradox is generalized to include temporally dispersive material parameters with finite values of the permittivity and the permeability. Using a time-domain approach, it is shown that the high-frequency limit of the extinction cross section depends on the material parameters of the target and that a limiting value not necessarily exists. The theoretical findings are exemplified by numerical illustrations with different values of the extinction cross section in the high-frequency limit.

1 Introduction

The extinction paradox states that, in the high-frequency regime, a perfectly electric conducting (PEC) target removes exactly twice the amount of energy it can intercept by its geometrical cross section area [1, 4, 6]. Here, the paradoxical character lies in the fact that the effective cross section area becomes twice as large as one would expect from the geometrical optics approximation. For a PEC sphere of radius a, this means that the extinction cross section (*i.e.*, the sum of the scattering and absorption cross sections) approaches $2\pi a^2$ as the wavelength of the incident radiation becomes much smaller than a, *cf.*, the limiting value of the Mie series in Ref. 4. A common explanation for the high-frequency contribution to the extinction cross section, besides the geometrical cross section area due to a direct removal of energy from the incident radiation, is that the additional effect originates from diffraction phenomena or small-angle scattering. This explanation is presented in Refs. 6 and 2 as a result of Babinet's principle and scalar diffraction theory. However, the use of Babinet's principle is unsatisfactory in many ways, *e.g.*, numerical illustrations in this paper indicate that the high-frequency limit of the extinction cross section may very well be oscillatory and thus not well-defined. Another common approach to the extinction paradox of convex targets is based on the physical optics approximation which correctly reproduces twice the geometrical cross section area in the high-frequency limit.

The analysis of the extinction paradox in Refs. 6 and 1 is also restrictive since it does not apply to penetrable targets with finite values of the permittivity and the permeability. In contrast to the many frequency domain approaches found in the literature, this paper investigates the extinction paradox using time-domain ideas discussed in Ref. 3. In particular, this paper shows that for a large class of targets with temporally dispersive material parameters, the extinction cross section does not approach twice the geometrical cross section area in the high-frequency limit. Instead, the results suggest that the extinction paradox depends on the high-frequency behavior of the chosen material models. The study of the extinction paradox is motivated by a new theory for broadband scattering of electromagnetic waves set forth in Ref. 5. Numerical results also support the conclusion by L. Brillouin in Ref. 2

that the extinction paradox "*... is of such general character that it must certainly apply to a variety of similar problems in acoustics and wave mechanics*".

2 Energy conservation

Consider a bounded target in an otherwise empty space with vacuum. An incident plane pulse propagating in the $\hat{\boldsymbol{k}}$-direction is given by $\boldsymbol{E}_{\mathrm{i}}(\boldsymbol{x},t) = \sqrt{\epsilon_0}\hat{\boldsymbol{e}} f(t-\hat{\boldsymbol{k}}\cdot\boldsymbol{x}/\mathrm{c}_0)$, where $f(\tau') = 0$ for $\tau' < 0$, and $\tau' > \tau$ and η_0 and c_0 denote the wave impedance and phase velocity of free space, respectively. Let a circular cylinder of finite length with the $\hat{\boldsymbol{k}}$-axis as symmetry axis and surface ∂V with outward-directed normal unit vector $\hat{\boldsymbol{n}}$ circumscribe the target such that the object does not touch the cylinder. The projection of the target on the bottom surface of the cylinder is denoted by $\mathcal{A}$ and has the area A, see Fig. 1. Decomposed the total electric field into an incident and a scattered field according to $\boldsymbol{E}(\boldsymbol{x},t) = \boldsymbol{E}_{\mathrm{i}}(\boldsymbol{x},t) + \boldsymbol{E}_{\mathrm{s}}(\boldsymbol{x},t)$.

The extinguished energy is the sum of the absorbed and scattered energies at a sufficiently large time ($t = \infty$)

$$-\int_{\mathbb{R}}\int_{\partial V}\big(\boldsymbol{E}(\boldsymbol{x},t)\times\boldsymbol{H}(\boldsymbol{x},t) - \boldsymbol{E}_{\mathrm{s}}(\boldsymbol{x},t)\times\boldsymbol{H}_{\mathrm{s}}(\boldsymbol{x},t)\big)\cdot\hat{\boldsymbol{n}}(\boldsymbol{x})\,\mathrm{d}S\,\mathrm{d}t$$
$$= -\int_{\mathbb{R}}\int_{\partial V}\big(\boldsymbol{E}_{\mathrm{i}}(\boldsymbol{x},t)\times\boldsymbol{H}_{\mathrm{s}}(\boldsymbol{x},t) + \boldsymbol{E}_{\mathrm{s}}(\boldsymbol{x},t)\times\boldsymbol{H}_{\mathrm{i}}(\boldsymbol{x},t)\big)\cdot\hat{\boldsymbol{n}}(\boldsymbol{x})\,\mathrm{d}S\,\mathrm{d}t \quad (2.1)$$

Causality ensures that when the pulse width goes to zero, $\tau \to 0$, the support of the incident and scattered fields can only overlap at the planar surface $\mathcal{A}$ with outward-directed unit normal vector $\hat{\boldsymbol{n}} = \hat{\boldsymbol{k}}$. This simplifies (2.1) to

$$W_{\mathrm{ext}} = -\mathrm{c}_0 \lim_{\tau\to 0}\int_{\mathbb{R}}\int_{\mathcal{A}} \mu_0\boldsymbol{H}_{\mathrm{i}}(\boldsymbol{x},t)\cdot\boldsymbol{H}_{\mathrm{s}}(\boldsymbol{x},t) + \epsilon_0\boldsymbol{E}_{\mathrm{s}}(\boldsymbol{x},t)\cdot\boldsymbol{E}_{\mathrm{i}}(\boldsymbol{x},t)\,\mathrm{d}S\,\mathrm{d}t. \quad (2.2)$$

Define the short pulse extinction cross section as the quotient between the extinguished energy and the incident energy flux, *i.e.*,

$$\Sigma_{\mathrm{ext}} = \frac{W_{\mathrm{ext}}}{\mathrm{c}_0\int_{\mathbb{R}}|f(\tau')|^2\,\mathrm{d}\tau'} = 2A -$$
$$\lim_{\tau\to 0}\frac{\int_{\mathbb{R}}\int_{\mathcal{A}}\epsilon_0\boldsymbol{E}(\boldsymbol{x},t)\cdot\boldsymbol{E}_{\mathrm{i}}(\boldsymbol{x},t) + \mu_0\boldsymbol{H}_{\mathrm{i}}(\boldsymbol{x},t)\cdot\boldsymbol{H}(\boldsymbol{x},t)\,\mathrm{d}S\,\mathrm{d}t}{\int_{\mathbb{R}}|f(\tau')|^2\,\mathrm{d}\tau'}. \quad (2.3)$$

The short pulse extinction cross section depends on the geometry of the target and its material parameters. Here, an isotropic non-magnetic material is considered with a the time-domain constitutive relation given by $\boldsymbol{D} = \epsilon_0(\epsilon_\infty\boldsymbol{E} + \chi * \boldsymbol{E})$, where $\chi(t)$ denotes the susceptibility kernel and $*$ denotes temporal convolution. The corresponding frequency domain relations are quantified by the permittivity $\epsilon(\omega)$, where ω denotes the angular frequency. The following four important special cases as illustrated in Fig 1:

1. The target is perfectly electric conducting (PEC). In this case $\boldsymbol{E}\cdot\boldsymbol{E}_{\mathrm{i}} = 0$ and $\boldsymbol{H}\cdot\boldsymbol{H}_{\mathrm{i}} = 0$ when $\boldsymbol{x}\in\mathcal{A}$ and hence $\Sigma_{\mathrm{ext}} = 2A$.

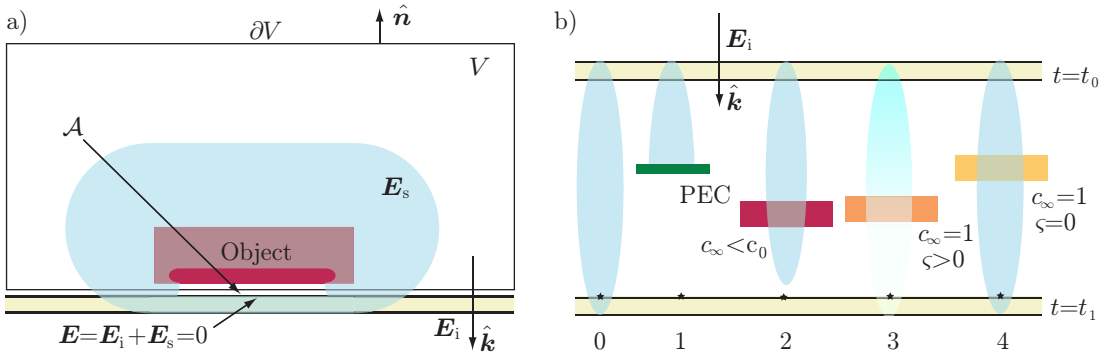

Figure 1: a) The temporal and spatial support of the scattered and incident fields for an object with a phase velocity $c_\infty < \mathrm{c}_0$. b) Illustrations of the shadow regions for various scattering targets.

2. The target is a dielectric material with an optical response $\epsilon_\infty > 1$. The wave front travels with the phase velocity $c_\infty = \mathrm{c}_0/\sqrt{\epsilon_\infty}$ in the target implying that $\boldsymbol{E}\cdot\boldsymbol{E}_\mathrm{i} = 0$ and $\boldsymbol{H}\cdot\boldsymbol{H}_\mathrm{i} = 0$ when $\boldsymbol{x}\in\mathcal{A}$. Hence $\Sigma_\mathrm{ext} = 2A$.

3. The object is a dispersive medium with phase velocity $c_\infty = \mathrm{c}_0$ and $\chi(0) > 0$, or equivalently $\epsilon(\omega) = 1 - \mathrm{i}\varsigma/\omega + \mathcal{O}(\omega^{-2})$ as $\omega\to\infty$, where $\varsigma = 1/\chi(0)$, *cf.*, the Debye and conductivity models. The wave front travels with the speed c_0 but is attenuated. One can show that the shape of the wave front is unaffected by the object but that attenuated by a factor of $\exp(-\chi(0)\Delta\ell/2\mathrm{c}_0)$ when it travels a distance $\Delta\ell$ in the medium. Thus $0 < \boldsymbol{E}_\mathrm{i}\cdot\boldsymbol{E} < |\boldsymbol{E}_\mathrm{i}|^2$ when $\boldsymbol{x}\in\mathcal{A}$ and hence $0 < \Sigma_\mathrm{ext} < 2A$.

4. The object is a dispersive medium with phase velocity $c_\infty = \mathrm{c}_0$ and $\chi(0) = 0$, or equivalently $\epsilon(\omega) = 1 + \mathcal{O}(\omega^{-2})$ as $\omega\to\infty$, *cf.*, the Lorentz model. In this case the wave front is not affected by the medium and hence $\Sigma_\mathrm{ext} = 0$.

The first two cases are the time domain (or short pulse) analogy of the extinction paradox, *i.e.*, the energy an object absorbs and scatters is twice the amount that it intercepts by its geometrical cross section area. It is illustrative to relate the time-domain extinction paradox to the corresponding high-frequency version. Fourier synthesis of the short pulse extinction cross section is

$$\Sigma_\mathrm{ext}(\hat{\boldsymbol{k}},\hat{\boldsymbol{e}}) = \lim_{\tau\to 0}\frac{\int_0^\infty \sigma_\mathrm{ext}(\omega;\hat{\boldsymbol{k}},\hat{\boldsymbol{e}})|g(\omega)|^2\,\mathrm{d}\omega}{\int_0^\infty |g(\omega)|^2\,\mathrm{d}\omega}, \tag{2.4}$$

where σ_ext denotes the extinction cross section and $g(\omega)$ is the Fourier transform of $f(t)$. Although, the derivation is based on a finite pulse width, it can be generalized, giving

$$\Sigma_\mathrm{ext}(\hat{\boldsymbol{k}},\hat{\boldsymbol{e}}) = \lim_{\omega\to\infty}\frac{1}{\omega}\int_0^\omega \sigma_\mathrm{ext}(\omega';\hat{\boldsymbol{k}},\hat{\boldsymbol{e}})\,\mathrm{d}\omega', \tag{2.5}$$

where it is seen that the running average of the extinction cross section approaches Σ_ext in the high frequency limit. The extinction paradox then reads: *in the high*

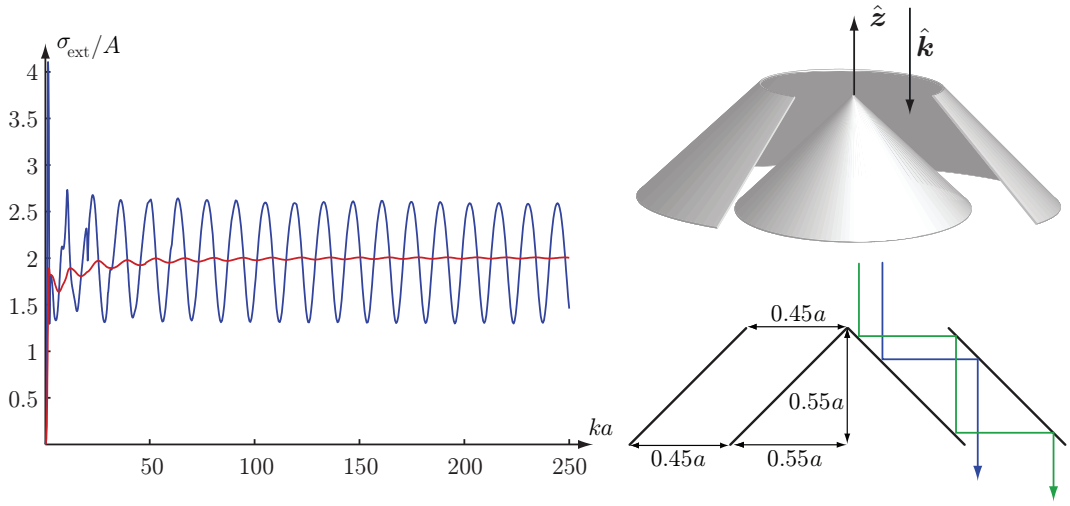

Figure 2: The extinction cross section and running averages extinction cross section in units of the geometrical cross section area $A = \pi a^2$ for the PEC geometry depicted on the right hand side.

frequency limit, on average the absorbed and scattered power of an object is less then or equal to twice the power that it can intercept by its geometrical cross section area, where equality holds for objects with phase velocity $c_\infty < \mathrm{c}_0$.

3 Numerical examples

Numerical results for a truncated cone with a displaced top, dielectric sphere, and temporal dispersive layered sphere are used to illustrate the high-frequency limit of the extinction cross section, running average extinction cross section, and the short pulse extinction cross section.

The truncated cone with a displaced top is illuminated by a plane wave incident along the symmetry axis, as depicted in Fig. 2. The object is PEC and has a geometrical cross section area $A = \pi a^2$ for $\hat{\boldsymbol{k}} = -\hat{\boldsymbol{z}}$. The extinction cross section is determined with a MoM code for $1 \leqslant ka \leqslant 250$. A simple geometrical optics analysis suggests that it is only the rays that are reflected between the conical surfaces that can contribute to the forward scattering. These rays are phase shifted causing a constructive and destructive interference pattern in the forward scattering, and, hence, an oscillatory extinction cross section. Note that the oscillation frequency $ka \approx 14 \approx 2\pi/0.45$ is consistent with the geometrical optics approximation. It is observed that high frequency limit of the extinction cross section does not exist. Moreover, σ_{ext} does not simple oscillate symmetrically around $2A$. However, the running average (2.5) of the extinction cross section approaches $2A$.

The extinction cross section of a dielectric sphere with a constant permittivity $\epsilon = 2$ is depicted to the left in Fig. 3. It is observed that σ_{ext} oscillates around $2A$ and that the amplitude of the oscillations decreases with ka. The corresponding running averages extinction cross section (2.5) is given by the smooth curve that slowly

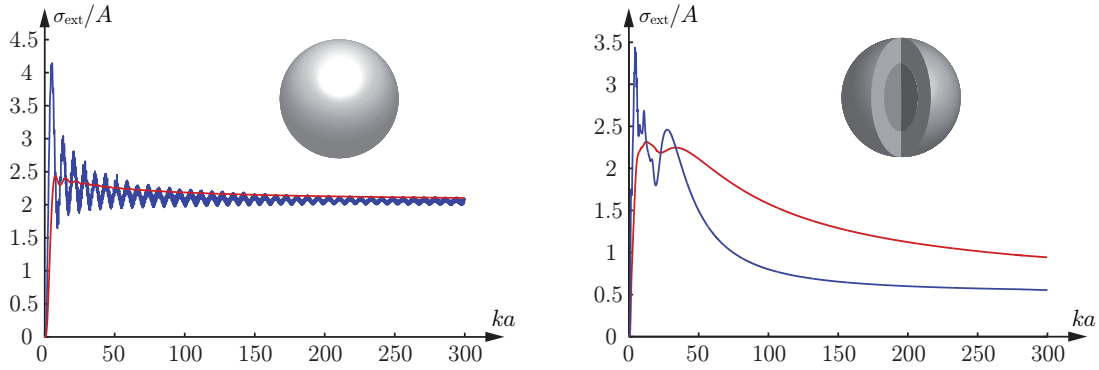

Figure 3: The extinction cross section in units of the geometrical cross section area $A = \pi a^2$ for a sphere of radius a. The left figure represents a homogeneous sphere with a constant permittivity $\epsilon = 2$ while the right figure is for a stratified sphere with a Lorentz dispersive media in the outermost layer. The corresponding running average extinction cross sections are illustrated by the smoothly varying curves.

approaches $2A$. A stratified sphere with a PEC core (with radius $a/2$) surrounded by a Lorentz dispersive media is illustrating the effect of temporal dispersion on the short pulse extinction cross section. The Lorentz model is given by $\epsilon(\kappa) = 1 - \kappa_{\text{p}}^2/(\kappa^2 - \kappa_0^2 + \text{i}\kappa\nu)$, where $\kappa = ka$, $\kappa_0 = \kappa_{\text{p}} = 10$, and $\nu = 0.1\kappa_0$. It is observed that σ_{ext} approaches $A/2$ as $ka \to \infty$ in the right hand side of Fig. 3. This agrees with the general result as the wave front is unaffected by the Lorentz medium giving a shadow region defined by the projection of the PEC core. The convergence of the running average extinction cross section is seen to converge slower.

4 Conclusions

The time domain approach offers new insights into the underlying physics of the extinction paradox. In contrast to the classical frequency domain explanations, the new approach is solely based on energy conservation and causality and does not utilize either scattering theory nor high-frequency approximations. A short pulse extinction cross section is defined and shown to be bounded by twice the geometrical cross section area of the object. Moreover, it is shown that the running average of the high-frequency extinction cross section approaches the short pulse extinction cross section in the high frequency limit.

References

[1] C. F. Bohren and D. R. Huffman. *Absorption and Scattering of Light by Small Particles*. John Wiley & Sons, New York, 1983.

[2] L. Brillouin. The scattering cross section of spheres for electromagnetic waves.

Appl. Phys., **20**, 1110–1125, 1949.

[3] A. Karlsson. On the time domain version of the optical theorem. *Am. J. Phys*, **68**(4), 344–349, 2000.

[4] R. G. Newton. *Scattering Theory of Waves and Particles*. Dover Publications, New York, second edition, 2002.

[5] C. Sohl, M. Gustafsson, and G. Kristensson. Physical limitations on broadband scattering by heterogeneous obstacles. *J. Phys. A: Math. Theor.*, **40**(36), 11165–11182, 2007.

[6] H. van de Hulst. *Light Scattering by Small Particles*. John Wiley & Sons, Inc., New York, 1957.

The integrated extinction for broadband scattering of acoustic waves

Christian Sohl, Mats Gustafsson, and Gerhard Kristensson

Paper VIII

Based on: C. Sohl, M. Gustafsson, and G. Kristensson. The integrated extinction for broadband scattering of acoustic waves. *Journal of the Acoustical Society of America*, vol. 122, no. 6, pp. 3206–3210, December 2007.

Abstract

In this paper, physical bounds on scattering of acoustic waves over a frequency interval are discussed based on the holomorphic properties of the scattering amplitude in the forward direction. The result is a dispersion relation for the extinction cross section which yields an upper bound on the product of the extinction cross section and the associated bandwidth of any frequency interval. The upper bound is shown to depend only on the geometry and the material properties of the scatterer in the static or low-frequency limit. The results are exemplified by permeable and impermeable scatterers with homogeneous and isotropic material parameters.

1 Introduction

Linear acoustics with propagation and scattering of waves in air and water has been a subject of considerable interest for more than a century. Major contributions to the scattering theory of both acoustic and electromagnetic waves from bounded obstacles was provided by Lord Rayleigh in a sequence of papers. From a theoretical point of view, scattering of acoustic waves shares many features with electromagnetic and elastodynamic wave interaction. For a comprehensive introduction to linear acoustics, see, *e.g.*, Refs. 5 and 13.

The objective of this paper is to derive physical bounds on broadband scattering of acoustic waves. In more detail, the scattering problem discussed here involves how a scatterer of arbitrary shape perturbs a known incident field over a frequency interval. The analysis is based on a forward dispersion relation for the extinction cross section applied to a set of linear and passive constitutive relations. This forward dispersion relation, known as the integrated extinction, is a direct consequence of causality and power conservation via the holomorphic properties of the scattering amplitude in the forward direction. As far as the authors know, the integrated extinction was first introduced in Ref. 7 concerning absorption and emission of electromagnetic waves by interstellar dust. The analysis in Ref. 7, however, is restricted to homogeneous and isotropic spheroids. This narrow class of scatterers was generalized in Ref. 8 to include bi-anisotropic and heterogeneous obstacles of arbitrary shape.

The present paper is a direct application to linear acoustics of the physical bounds for scattering of electromagnetic waves introduced in Refs. 8 and 9. The broad usefulness of the integrated extinction is illustrated by its diversity of applications, see, *e.g.*, Ref. 9 for upper bounds on the bandwidth of the interaction of electromagnetic waves with metamaterials. The integrated extinction has also fruitfully been applied to antennas of arbitrary shape in Ref. 2 to establish bounds on the directivity and the bandwidth of any antenna. The theory for broadband scattering of acoustic waves is motivated by the sum rules in Ref. 10 and the analogy with causality in the scattering theory for particles in Ref. 6.

In Sec. 2, the integrated extinction is derived based on the holomorphic properties of the scattering amplitude in the forward direction. The derivation utilizes only the properties of the fields in the exterior region, and the results are hence independent

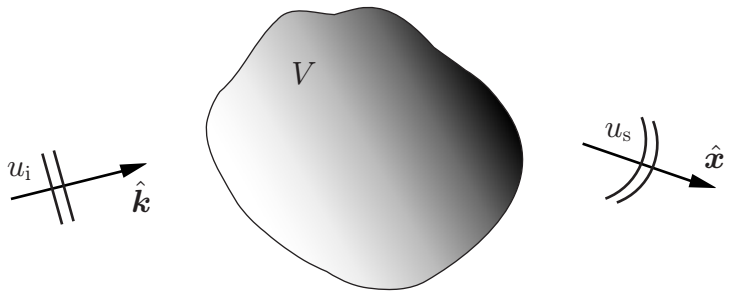

Figure 1: Illustration of the direct scattering problem: the scatterer V is subject to a plane wave $u_\mathrm{i} = \mathrm{e}^{\mathrm{i}k\hat{\boldsymbol{k}}\cdot\boldsymbol{x}}$ impinging in the $\hat{\boldsymbol{k}}$-direction. The incident field is perturbed by V and a scattered field u_s is detected in the $\hat{\boldsymbol{x}}$-direction.

of the boundary conditions imposed on the scatterer as long as the material is linear and passive. The effects of various boundary conditions are examined in Sec. 3, and there applied to the results in Sec. 2. In the final section, Sec. 4, the main results of the paper are summarized and possible applications of the integrated extinction are discussed.

2 The integrated extinction

Consider a time-harmonic plane wave $u_\mathrm{i} = \mathrm{e}^{\mathrm{i}k\hat{\boldsymbol{k}}\cdot\boldsymbol{x}}$ (complex excess pressure field) with time dependence $\mathrm{e}^{-\mathrm{i}\omega t}$ incident on a bounded, but not necessary simply connected, scatterer with support $V \subset \mathbb{R}^3$ of arbitrary shape, see Fig. 1. The plane wave is impinging in the $\hat{\boldsymbol{k}}$-direction, and $\boldsymbol{x}$ denotes the position vector with respect to some origin. The scatterer V is assumed to be linear and time-translational invariant with passive material properties modeled by general anisotropic and heterogeneous constitutive relations. The analysis includes the impermeable case as well as transmission problems with or without losses. The scatterer V is embedded in the exterior region $\mathbb{R}^3 \setminus \overline{V}$, which is assumed to be a compressible homogeneous and isotropic fluid characterized by the wave number $k = \omega/c$. The material in $\mathbb{R}^3 \setminus \overline{V}$ is assumed to be lossless and independent of time.

Let $u = u_\mathrm{i} + u_\mathrm{s}$ denote the total field in $\mathbb{R}^3 \setminus \overline{V}$, where the time-dependent physical excess pressure p is related to u as $p = \mathrm{Re}\{u\mathrm{e}^{-\mathrm{i}\omega t}\}$. The scattered field u_s represents the disturbance of the incoming field in the presence of V. It satisfies the Helmholtz wave equation in the exterior of V, see Ref. 13, *i.e.*,

$$\nabla^2 u_\mathrm{s} + k^2 u_\mathrm{s} = 0, \qquad \boldsymbol{x} \in \mathbb{R}^3 \setminus \overline{V}. \tag{2.1}$$

The boundary condition imposed on u_s at large distances $x = |\boldsymbol{x}|$ is the Sommerfeld radiation condition

$$\lim_{x\to\infty} x\left(\frac{\partial u_\mathrm{s}}{\partial x} - \mathrm{i}k u_\mathrm{s}\right) = 0, \tag{2.2}$$

which is assumed to hold uniformly in all directions $\hat{\boldsymbol{x}} = \boldsymbol{x}/x$. The condition (2.2) establishes the outgoing character of u_s, and provides a condition for a well-posed

exterior boundary-value problem. For a discussion of various boundary conditions imposed on V, see Sec. 3.

From the integral representations in Ref. 11, it is clear that every solution to (2.1) satisfying (2.2) has an asymptotic behavior of an outgoing spherical wave, *i.e.*,

$$u_{\mathrm{s}} = \frac{\mathrm{e}^{\mathrm{i}kx}}{x} S(k, \hat{\boldsymbol{x}}) + \mathcal{O}(x^{-2}) \quad \text{as } x \to \infty. \tag{2.3}$$

The scattering amplitude S is independent of x, and it describes the interaction of V with the incident field. From a time-domain description of the problem, it follows that S is the Fourier transform of some temporal scattering amplitude S_{t}. Assume that S_{t} is causal in the forward direction in the sense that $S_{\mathrm{t}}(\tau, \hat{\boldsymbol{k}}, \hat{\boldsymbol{k}}) = 0$ for $\tau < 0$, where $\tau = ct - \hat{\boldsymbol{k}} \cdot \boldsymbol{x}$. Based on this condition, the Fourier transform of S_{t} reduces to a one-sided integral over $\tau > 0$, *i.e.*,

$$S(k; \hat{\boldsymbol{k}}) = \int_0^\infty S_{\mathrm{t}}(\tau, \hat{\boldsymbol{k}}, \hat{\boldsymbol{k}}) \mathrm{e}^{\mathrm{i}k\tau} \, \mathrm{d}\tau. \tag{2.4}$$

The convergence of (2.4) is improved by extending its domain of definition to complex-valued k with $\operatorname{Im} k > 0$. Such an extension defines a holomorphic function S in the upper half plane $\operatorname{Im} k > 0$, see Ref. 6. Note that S in general is not a holomorphic function at infinity for $\operatorname{Im} k > 0$ in the absence of the causality condition.

The description of broadband scattering is simplified by introducing a weighted function ϱ of the forward scattering amplitude. For this purpose, let ϱ denote

$$\varrho(k; \hat{\boldsymbol{k}}) = S(k; \hat{\boldsymbol{k}})/k^2, \qquad \operatorname{Im} k > 0. \tag{2.5}$$

Since S_{t} is real-valued, it follows from (2.4) that ϱ is real-valued on the imaginary axis, and that it satisfies the cross symmetry $\varrho(-k^*; \hat{\boldsymbol{k}}) = \varrho^*(k; \hat{\boldsymbol{k}})$ (a star denotes the complex conjugate) for complex-valued k with $\operatorname{Im} k \geqslant 0$. Assume that ϱ vanishes uniformly as $|k| \to \infty$ for $\operatorname{Im} k \geqslant 0$.

An important measure of the total power that V extracts from the incident field in the form of radiation and absorption is given by the extinction cross section σ_{ext}. The extinction cross section is related to ϱ via the optical theorem, see Ref. 6,

$$\sigma_{\mathrm{ext}} = 4\pi k \operatorname{Im} \varrho, \tag{2.6}$$

where $k \in [0, \infty)$. The optical theorem is a direct consequence of power conservation (or conservation of probability in the theory of the Schrödinger equation) and states that the total power removed from the incident field is solely determined by $\operatorname{Im} \varrho$. The extinction cross section is commonly decomposed into the scattering cross section σ_{s} and the absorption cross section σ_{a}, *i.e.*,

$$\sigma_{\mathrm{ext}} = \sigma_{\mathrm{s}} + \sigma_{\mathrm{a}}. \tag{2.7}$$

Here, σ_{s} and σ_{a} are defined as the scattered and absorbed power divided by the incident power flux. The scattering and absorption cross sections are related to u_{s} and u on the boundary ∂V via, see Ref. 1,

$$\sigma_{\mathrm{s}} = \frac{4\pi}{k} \operatorname{Im} \int_{\partial V} u_{\mathrm{s}}^* \frac{\partial u_{\mathrm{s}}}{\partial n} \, \mathrm{d}S, \qquad \sigma_{\mathrm{a}} = \frac{4\pi}{k} \operatorname{Im} \int_{\partial V} u \frac{\partial u^*}{\partial n} \, \mathrm{d}S, \tag{2.8}$$

where the normal derivative $\partial/\partial n$ is evaluated with respect to the outward-directed unit normal vector. In the case of lossy material parameters, the absorption cross section represents the total power absorbed by V. For a lossless scatterer, $\sigma_{\mathrm{a}} = 0$.

Assume that ϱ vanishes uniformly as $|k| \to \infty$ for $\operatorname{Im} k \geqslant 0$. This assumption is justified by the argument that the high-frequency response of a material is non-unique from a modeling point of view. The assumption is also supported by the extinction paradox, which states that σ_{ext} approaches at most twice the geometrical cross section area in the high-frequency regime, *i.e.*, $\operatorname{Im} \varrho(k; \hat{\boldsymbol{k}}) = \mathcal{O}(k^{-1})$ as $k \to \infty$ for real-valued k. For a discussion of the extinction paradox for electromagnetic waves, see Ref. 12. Under this assumption, it follows from the analysis in Refs. 6 and 10 that ϱ satisfies the Hilbert transform or the Plemelj formula

$$\operatorname{Re} \varrho(k'; \hat{\boldsymbol{k}}) = \frac{1}{\pi} \mathcal{P} \int_{-\infty}^{\infty} \frac{\operatorname{Im} \varrho(k; \hat{\boldsymbol{k}})}{k - k'} \, \mathrm{d}k, \tag{2.9}$$

where k' is real-valued and $\mathcal{P}$ denotes Cauchy's principal value. It is particularly interesting to evaluate (2.9) in the static limit as $k' \to 0$. For this purpose, assume that $\operatorname{Re} \varrho(k'; \hat{\boldsymbol{k}}) = \mathcal{O}(1)$ and $\operatorname{Im} \varrho(k'; \hat{\boldsymbol{k}}) = \mathcal{O}(k')$ as $k' \to 0$, and that ϱ is sufficiently regular to interchange the principal value and the static limit. Based on these assumptions, (2.6) yields

$$\lim_{k \to 0} \operatorname{Re} \varrho(k; \hat{\boldsymbol{k}}) = \frac{2}{\pi} \int_0^{\infty} \frac{\operatorname{Im} \varrho(k; \hat{\boldsymbol{k}})}{k} \, \mathrm{d}k, \tag{2.10}$$

where it has been used that $\operatorname{Im} \varrho(k; \hat{\boldsymbol{k}}) = -\operatorname{Im} \varrho(-k; \hat{\boldsymbol{k}})$ for real-valued k. The optical theorem (2.6) inserted into (2.10) finally yields

$$\int_0^{\infty} \frac{\sigma_{\mathrm{ext}}(k; \hat{\boldsymbol{k}})}{k^2} \, \mathrm{d}k = 2\pi^2 \lim_{k \to 0} \operatorname{Re} \varrho(k; \hat{\boldsymbol{k}}). \tag{2.11}$$

The left-hand side of (2.11) is referred to as the integrated extinction. The identity provides a forward dispersion relation for the extinction cross section as a direct consequence of causality and power conservation. Due to the lack of any length scale in the static or low-frequency limit, the right-hand side of (2.11) is proportional to the volume of V since ϱ has the dimension of volume, *cf.*, the discussion in Ref. 8. Furthermore, the right-hand side of (2.11) depends only on the static material properties of V, and it is presented in Sec. 3 for a large class of homogeneous and isotropic scatterers.

The weak assumptions imposed on ϱ in the derivation above are summarized as follows: $\varrho(k; \hat{\boldsymbol{k}}) \to 0$ uniformly as $|k| \to \infty$ for $\operatorname{Im} k \geqslant 0$, and $\operatorname{Re} \varrho(k; \hat{\boldsymbol{k}}) = \mathcal{O}(1)$ and $\operatorname{Im} \varrho(k; \hat{\boldsymbol{k}}) = \mathcal{O}(k)$ as $k \to 0$ for real-valued k. In general, (2.11) is not valid if any of these assumptions are violated as illustrated in Sec. 3.3. In fact, the above-noted requirements can be relaxed by the introduction of the Plemelj formula for generalized functions. The integrated extinction can also be derived using Cauchy's integral theorem, see Ref. 8.

The integrated extinction (2.11) may be used to establish physical bounds on broadband scattering of acoustic waves. Since σ_{ext} is defined as the sum of the

scattered and absorbed power divided by the incident power flux, it is by definition non-negative. Hence, the left-hand side of (2.11) is estimated from below by

$$|K| \min_{k\in K} \frac{\sigma(k)}{k^2} \leqslant \int_K \frac{\sigma(k)}{k^2}\, \mathrm{d}k \leqslant \int_0^\infty \frac{\sigma_{\mathrm{ext}}(k;\hat{\boldsymbol{k}})}{k^2}\, \mathrm{d}k, \tag{2.12}$$

where $|K|$ denotes the absolute bandwidth of any frequency interval $K \subset [0,\infty)$, and σ represents either σ_{ext}, σ_{s}, or σ_{a}. By combining the left-hand side of (2.12) with the right-hand side of (2.11), one obtains the fundamental inequality

$$|K| \min_{k\in K} \frac{\sigma(k)}{k^2} \leqslant 2\pi^2 \lim_{k\to 0} \operatorname{Re} \varrho(k;\hat{\boldsymbol{k}}). \tag{2.13}$$

The interpretation of (2.13) is that it yields an upper bound on the absolute bandwidth $|K|$ for a given scattering and/or absorption cross section $\min_{k\in K} \sigma(k)/k^2$. From (2.13), it is seen that the static limit of $\operatorname{Re}\varrho$ bounds the total amount of power extracted by V within the frequency interval K. The electromagnetic analogy to (2.13) is, *i.a.*, central for establishing upper bounds on the performance of antennas of arbitrary shape, see Ref. 2.

3 The effect of various boundary conditions

In the following, the static limit of $\operatorname{Re}\varrho$ is examined for various boundary conditions and applied to the integrated extinction (2.11). For this purpose, V is assumed to be homogeneous and isotropic with sufficiently smooth boundary ∂V to guarantee the existence of boundary values in the classical sense.

3.1 The acoustically hard problem

The Neumann problem or acoustically hard problem corresponds to an impermeable scatterer with boundary condition $\partial u/\partial n = 0$ for $\boldsymbol{x} \in \partial V$. The physical interpretation of the Neumann boundary condition is that the velocity field on ∂V is zero since no local displacements are admitted. From the fact that u_{s} only exists in $\mathbb{R}^3 \setminus \overline{V}$, it follows that the corresponding scattered field in the time-domain cannot precede the incident field in the forward direction, *i.e.*, the causality condition imposed on S_{t} in Sec. 2 is valid for the homogeneous Neumann problem. The static limit of S is derived in Refs. 1 and 3 from a power series expansion of u_{i} and u_{s}. The result in terms of $\operatorname{Re}\varrho$ reads

$$\lim_{k\to 0} \operatorname{Re} \varrho(k;\hat{\boldsymbol{k}}) = \frac{1}{4\pi}(\hat{\boldsymbol{k}} \cdot \boldsymbol{\gamma}_{\mathrm{m}} \cdot \hat{\boldsymbol{k}} - |V|), \tag{3.1}$$

where $|V|$ denotes the volume of V. Here, $\boldsymbol{\gamma}_{\mathrm{m}}$ models the scattering of acoustic waves in the low-frequency limit. In analogy with the corresponding theory for electromagnetic waves in Ref. 8, $\boldsymbol{\gamma}_{\mathrm{m}}$ is termed the magnetic polarizability dyadic. The magnetic polarizability dyadic is proportional to $|V|$, and closed-form expressions of $\boldsymbol{\gamma}_{\mathrm{m}}$ exist for the homogeneous and isotropic ellipsoids.

An expression of the integrated extinction for the Neumann problem is obtained by inserting (3.1) into (2.11), *viz.*,

$$\int_0^\infty \frac{\sigma_{\text{ext}}(k;\hat{\boldsymbol{k}})}{k^2}\,\mathrm{d}k = \frac{\pi}{2}(\hat{\boldsymbol{k}}\cdot\boldsymbol{\gamma}_{\text{m}}\cdot\hat{\boldsymbol{k}} - |V|). \tag{3.2}$$

Note that (3.2) is independent of $\hat{\boldsymbol{k}}$ when $\boldsymbol{\gamma}_{\text{m}}$ is isotropic, *i.e.*, $\boldsymbol{\gamma}_{\text{m}} = \gamma_{\text{m}}\mathbf{I}_3$, where $\mathbf{I}_3$ denotes the unit dyadic in $\mathbb{R}^3$, corresponding to a scatterer which is invariant under certain point groups, see Ref. 8 and references therein. The product $\hat{\boldsymbol{k}}\cdot\boldsymbol{\gamma}_{\text{m}}\cdot\hat{\boldsymbol{k}}$ on the right-hand side of (3.2) can be estimated from above by the largest eigenvalue of $\boldsymbol{\gamma}_{\text{m}}$, and associated upper bounds on these eigenvalues are extensively discussed in Ref. 8. The static limit of $\operatorname{Re}\varrho$ in (3.1) can also be inserted into the right-hand side of (2.13) to yield an upper bound on the scattering and absorption properties of V within any finite interval K.

The integrated extinction (3.2) takes a particularly simple form for the sphere. In this case, $\boldsymbol{\gamma}_{\text{m}}$ is isotropic with $\gamma_{\text{m}} = 3|V|/2$, see Refs. 3 and 8, and the right-hand side of (3.2) is reduced to $\pi|V|/4$. This result has numerically been verified using the classical Mie-series expansion in Ref. 5.

3.2 The acoustically permeable problem

In addition to the exterior boundary-value problem (2.1), the transmission problem or acoustically permeable problem is defined by the interior requirement that $\nabla^2 u_{\text{s}} + k_\star^2 u_{\text{s}} = 0$ for $\boldsymbol{x} \in V$, with the induced boundary conditions $u^+ = u^-$ and $\rho_\delta \partial u^+/\partial n = \partial u^-/\partial n$. Here, $k_\star = \omega/c_\star$ denotes the wave number in V, and u^+ and u^- represent the limits of u from $\mathbb{R}^3 \setminus \overline{V}$ and V, respectively. The quantity ρ_δ is related to the relative mass density $\rho_{\text{rel}} = \rho_\star/\rho$ via $\rho_\delta = \rho_{\text{rel}}/(1 - \mathrm{i}\omega\delta_\star\kappa_\star)$, where $\kappa_\star$ and $\rho_\star$ denote the compressibility (the relative volume reduction per unit increase in surface pressure) and the mass density of V, respectively. The conversion of mechanical energy into thermal energy due to losses in V are modeled by the compressional viscosity $\delta_\star > 0$, which represents the rate of change of mass per unit length. In the lossless case, *i.e.*, $\delta_\star = 0$, the phase velocity is $c_\star = 1/\sqrt{\kappa_\star\rho_\star}$ and $\rho_\delta = \rho_{\text{rel}}$.

The causality condition introduced in Sec. 2 is valid for the transmission problem provided $\operatorname{Re} c_\star \leqslant c$, *i.e.*, when the incident field precedes the scattered field in the forward direction. If V does not fulfill this requirement, ϱ is not holomorphic for $\operatorname{Im} k > 0$, and the analysis in Sec. 2 does not hold. Hence, the integrated extinction (2.11) is not valid if $\operatorname{Re} c_\star > c$. This defect can partially be justified by replacing the definition of ϱ by $\varrho = \mathrm{e}^{2\mathrm{i}ka} S(k;\hat{\boldsymbol{k}})/k^2$, where $a > 0$ is sufficiently large to guarantee the existence of causality in the forward direction. The compensating factor $\mathrm{e}^{2\mathrm{i}ka}$ corresponds to a time-delay in the scattered field, and for homogeneous and isotropic scatterers, a sufficient condition for a is that $2a > \operatorname{diam} V$, where $\operatorname{diam} V$ denotes the diameter of V. A drawback of the introduction of the factor $\mathrm{e}^{2\mathrm{i}ka}$ in the definition of ϱ is that the optical theorem no longer can be identity in the derivation. Instead, the integrated extinction reduces to an integral identities for ϱ. Unfortunately, in this case the integrand does not have a definite sign and therefore the estimate (2.13) is not valid.

The static limit of the scattering amplitude S for the transmission problem is derived in Refs. 1 and 3. The result in terms of $\operatorname{Re} \varrho$ reads

$$\lim_{k \to 0} \operatorname{Re} \varrho(k; \hat{\boldsymbol{k}}) = \frac{1}{4\pi}((\kappa_{\mathrm{rel}} - 1)|V| - \hat{\boldsymbol{k}} \cdot \boldsymbol{\gamma}(\rho_{\mathrm{rel}}^{-1}) \cdot \hat{\boldsymbol{k}}), \tag{3.3}$$

where $\kappa_{\mathrm{rel}} = \kappa_\star / \kappa$ denotes the relative compressibility of V, and $\boldsymbol{\gamma}$ represents the general polarizability dyadic. In the derivation of (3.3), it has been used that possible losses $\delta_\star > 0$ in V do not contribute in the static limit of $\operatorname{Re} \varrho$, which supports that the argument in $\boldsymbol{\gamma}$ is ρ_{rel} rather than ρ_δ. Analogous to $\boldsymbol{\gamma}_{\mathrm{m}}$, the general polarizability dyadic is proportional to $|V|$, and closed-form expressions for $\boldsymbol{\gamma}$ exist for the ellipsoids, see Refs. 1, 3, and 8. From the properties of $\boldsymbol{\gamma}$ and $\boldsymbol{\gamma}_{\mathrm{m}}$ in Refs. 1, 3, and 8, it follows that $\boldsymbol{\gamma}(\rho_{\mathrm{rel}}^{-1}) \to -\boldsymbol{\gamma}_{\mathrm{m}}$ as $\rho_{\mathrm{rel}} \to \infty$, and hence the static limit of $\operatorname{Re} \varrho$ reduces to (3.1) for the Neumann problem as $\kappa_{\mathrm{rel}} \to 0+$ and $\rho_{\mathrm{rel}} \to \infty$. Another interesting limit corresponding to vanishing mass density in V is given by $\boldsymbol{\gamma}(\rho_{\mathrm{rel}}^{-1}) \to \boldsymbol{\gamma}_{\mathrm{e}}$ as $\rho_{\mathrm{rel}} \to 0+$, where $\boldsymbol{\gamma}_{\mathrm{e}}$ is termed the electric polarizability dyadic in analogy with the low-frequency scattering of electromagnetic waves, see Refs. 1, 3, and 8.

The integrated extinction for the transmission problem is given by (3.3) inserted into (2.11). The result is

$$\int_0^\infty \frac{\sigma_{\mathrm{ext}}(k; \hat{\boldsymbol{k}})}{k^2} \, \mathrm{d}k = \frac{\pi}{2}((\kappa_{\mathrm{rel}} - 1)|V| - \hat{\boldsymbol{k}} \cdot \boldsymbol{\gamma}(\rho_{\mathrm{rel}}^{-1}) \cdot \hat{\boldsymbol{k}}). \tag{3.4}$$

Note that (3.4) is independent of any losses $\delta_\star > 0$, and that the directional character of the integrated extinction only depends on the relative mass density ρ_{rel}. For $\rho_{\mathrm{rel}} \to 1$, *i.e.*, identical mass densities in V and $\mathbb{R}^3 \setminus \overline{V}$, the integrated extinction is independent of the incident direction $\hat{\boldsymbol{k}}$, depending only on the relative compressibility κ_{rel}. Furthermore, the integrated extinction (3.2) vanishes in the limit as $\kappa_{\mathrm{rel}} \to 1$ and $\rho_{\mathrm{rel}} \to 1$, corresponding to identical material properties in V and $\mathbb{R}^3 \setminus \overline{V}$. Due to the non-negative character of the extinction cross section, this limit implies that $\sigma_{\mathrm{ext}} = 0$ independent of the frequency, as expected. Analogous to the Neumann problem, (3.4) is also independent of the incident direction $\hat{\boldsymbol{k}}$ for scatterers with $\boldsymbol{\gamma} = \gamma \mathbf{I}_3$ for some real-valued γ. The product $\hat{\boldsymbol{k}} \cdot \boldsymbol{\gamma} \cdot \hat{\boldsymbol{k}}$ on the right-hand side of (3.4) is bounded from above by the largest eigenvalue of $\boldsymbol{\gamma}$, and associated upper bounds on these eigenvalues are discussed in Ref. 8. The static limit of $\operatorname{Re} \varrho$ in (3.1) can also be inserted into the right-hand side of (2.13) to yield an upper bound on the scattering and absorption properties of V over any finite frequency interval K.

For the simple case of an isotropic and homogeneous sphere, $\gamma = 3|V|(1 - \rho_{\mathrm{rel}})/(2\rho_{\mathrm{rel}} + 1)$, and the right-hand side of (3.3) is independent of the incident direction as required by symmetry. Also this result for the sphere has been verified numerically to arbitrary precision using the classical Mie-series expansion.

3.3 Boundary conditions with contradictions

The integrated extinction (2.11) and the analysis in Sec. 2 are not applicable to the Dirichlet or acoustically soft problem with $u = 0$ for $\boldsymbol{x} \in \partial V$. The physical

interpretation of the Dirichlet boundary condition is that the scatterer offers no resistance to pressure. The Dirichlet problem defines an impermeable scatterer for which u_s only exist in $\mathbb{R}^3 \setminus \overline{V}$. Hence, the causality condition introduced in Sec. 2 is valid. However, the assumption that $\operatorname{Re} \varrho(k; \hat{\boldsymbol{k}}) = \mathcal{O}(1)$ as $k \to 0$ for real-valued k is not valid in this case. Instead, Refs. 1 and 3 suggest that

$$\operatorname{Re} \varrho(k; \hat{\boldsymbol{k}}) = \mathcal{O}(k^{-2}) \quad \text{as } k \to 0 \tag{3.5}$$

for real-valued k. The conclusion is therefore that the integrated extinction (2.11) is not valid for the Dirichlet problem.

The same conclusion also holds for the Robin problem with impedance boundary condition $\partial u/\partial n + \mathrm{i}k\nu u = 0$. The Robin problem models an intermediate behavior between the Dirichlet and Neumann problems, see Ref. 1. The real-valued parameter ν is related to the exterior acoustic impedance η (defined by the ratio of the excess pressure and the normal velocity on the boundary) via $\eta\nu = \sqrt{\rho/\kappa}$, where κ and ρ denote the compressibility and mass density of $\mathbb{R}^3 \setminus \overline{V}$, respectively. In the limits $\nu \to 0+$ and $\nu \to \infty$, the Robin problem reduces to the Neumann and Dirichlet problems, respectively. For the Robin problem, the static limit of $\operatorname{Re} \varrho$ for $\nu \neq 0$ reads, see Refs. 1 and 3,

$$\operatorname{Re} \varrho(k; \hat{\boldsymbol{k}}) = \mathcal{O}(k^{-1}) \quad \text{as } k \to 0 \tag{3.6}$$

for real-valued k. Hence, the assumption in Sec. 2 that $\operatorname{Re} \varrho(k; \hat{\boldsymbol{k}}) = \mathcal{O}(1)$ as $k \to 0$ is not valid for the Robin problem either. The question whether a similar identity to the integrated extinction exists for the Dirichlet and Robin problems with other weight functions than $1/k^2$ is addressed in a forthcoming paper.

4 Conclusions

The static limits of $\operatorname{Re} \varrho$ in Sec. 3 can be used in (2.13) to establish physical bounds on the amount of power a scatterer can extract from a known incident field in any frequency interval $K \subset [0, \infty)$. Both absorbed and radiated power are taken into account. From the analysis of homogeneous and isotropic scatterers in Sec. 3, it is clear that the integrated extinction holds for both Neumann and transmission problems. However, the present formulation of the integrated extinction fails for the Dirichlet and Robin problems since the assumption in Sec. 2 that $\operatorname{Re} \varrho(k; \hat{\boldsymbol{k}}) = \mathcal{O}(1)$ as $k \to 0$ for real-valued k is violated for these boundary conditions.

The eigenvalues of the polarizability dyadics $\boldsymbol{\gamma}$, $\boldsymbol{\gamma}_\mathrm{e}$, and $\boldsymbol{\gamma}_\mathrm{m}$ are easily calculated using either the finite element method or the boundary element method. Some numerical results of these eigenvalues are presented in Refs. 8 and 9 together with comprehensive illustrations of the integrated extinction for scattering and absorption of electromagnetic waves.

The integrated extinction (2.11) can also be used to establish additional information on the inverse scattering problem of linear acoustics. One advantage of the integrated extinction is that it only requires measurements of the scattering amplitude in the forward direction. The theoretical findings may also be used to obtain

additional insights into the possibilities and limitations of engineered composite materials such as acoustic metamaterials in Ref. 4. However, the main importance of the integrated extinction (2.11) is that it provides a fundamental knowledge of the physical processes involved in wave interaction with matter in any frequency interval. It is also crucial for the understanding of the physical effects imposed on a system by the first principles of causality and power conservation.

Acknowledgments

The financial support by the Swedish Research Council is gratefully acknowledged. The authors are also grateful for fruitful discussions with Prof. Anders Karlsson at the Department of Electrical and Information Technology, Lund University, Sweden.

References

[1] G. Dassios and R. Kleinman. *Low Frequency Scattering*. Oxford University Press, Oxford, 2000.

[2] M. Gustafsson, C. Sohl, and G. Kristensson. Physical limitations on antennas of arbitrary shape. *Proc. R. Soc. A*, **463**(2086), 2589–2607, 2007.

[3] R. E. Kleinman and T. B. A. Senior. Rayleigh scattering. In V. V. Varadan and V. K. Varadan, editors, *Low and High Frequency Asymptotics*, volume 2 of *Handbook on Acoustic, Electromagnetic and Elastic Wave Scattering*, chapter 1, pages 1–70. Elsevier Science Publishers, Amsterdam, 1986.

[4] J. Li and C. T. Chan. Double-negative acoustic metamaterial. *Phys. Rev. E*, **70**(5), 055602, 2004.

[5] P. M. Morse and K. U. Ingard. *Theoretical Acoustics*. McGraw-Hill, New York, 1968.

[6] H. M. Nussenzveig. *Causality and Dispersion Relations*. Academic Press, London, 1972.

[7] E. M. Purcell. On the absorption and emission of light by interstellar grains. *J. Astrophys.*, **158**, 433–440, 1969.

[8] C. Sohl, M. Gustafsson, and G. Kristensson. Physical limitations on broadband scattering by heterogeneous obstacles. *J. Phys. A: Math. Theor.*, **40**(36), 11165–11182, 2007.

[9] C. Sohl, M. Gustafsson, and G. Kristensson. Physical limitations on metamaterials: Restrictions on scattering and absorption over a frequency interval. *J. Phys. D: Applied Phys.*, **40**(22), 7146–7151, 2007.

[10] C. Sohl. *Dispersion Relations for Extinction of Acoustic and Electromagnetic Waves*. Licentiate thesis, Lund University, Department of Electrical and Information Technology, P.O. Box 118, S-221 00 Lund, Sweden, 2007.

[11] S. Ström. Introduction to integral representations and integral equations for time-harmonic acoustic, electromagnetic and elastodynamic wave fields. In V. V. Varadan, A. Lakhtakia, and V. K. Varadan, editors, *Field Representations and Introduction to Scattering*, volume 1 of *Handbook on Acoustic, Electromagnetic and Elastic Wave Scattering*, chapter 2, pages 37–141. Elsevier Science Publishers, Amsterdam, 1991.

[12] H. van de Hulst. *Light Scattering by Small Particles*. John Wiley & Sons, Inc., New York, 1957.

[13] V. V. Varadan and V. K. Varadan. Acoustic, electromagnetic and elastodynamics fields. In V. V. Varadan, A. Lakhtakia, and V. K. Varadan, editors, *Field Representations and Introduction to Scattering*, Acoustic, Electromagnetic and Elastic Wave Scattering, chapter 1, pages 1–35. Elsevier Science Publishers, Amsterdam, 1991.

Physical limitations on antennas of arbitrary shape

Mats Gustafsson, Christian Sohl, and Gerhard Kristensson

Paper IX

Based on: M. Gustafsson, C. Sohl, and G. Kristensson. Physical limitations on antennas of arbitrary shape. *Proceedings of the Royal Society A: Mathematical, Physical & Engineering Sciences*, vol. 463, no. 2086, pp. 2589–2607, October 2007.

Abstract

In this paper, physical bounds on bandwidth, realized gain, Q-value, and directivity are derived for antennas of arbitrary shape. The product of bandwidth and realizable gain is shown to be bounded from above by the eigenvalues of the long-wavelength polarizability dyadics in the high-contrast limit. These dyadics are proportional to the antenna volume and are easily determined for an arbitrary geometry. Ellipsoidal antenna volumes are analyzed in detail, and numerical results for some generic geometries are presented. The theoretical approach is verified against the classical bounds for spherical geometries and shown to yield sharper bounds for the ratio of the directivity and the Q-value for non-spherical geometries.

1 Introduction

The concept of physical bounds for electrically small antennas was first introduced more than half a century ago in Refs. 4 and 24, respectively. Since then, much attention has been drawn to the subject and numerous papers have been published, see Ref. 13 and references therein. Unfortunately, almost all these papers are restricted to the sphere via the spherical vector wave expansions, deviating only slightly from the pioneering ideas introduced in Ref. 4.

The objective of this paper is to derive physical bounds on bandwidth, realized gain, Q-value, and directivity for antennas of arbitrary shape. The bounds presented here generalize in many aspects the classical results by Chu. The most important advantage of the new bounds is that they no longer are restricted to the sphere but instead hold for arbitrary antenna volumes. In fact, the smallest circumscribing sphere is far from optimal for many antennas, *cf.*, the dipole and loop antennas in Sec. 8. Furthermore, the new bounds successfully separate the electric and magnetic material properties of the antennas and quantify them in terms of their polarizability dyadics.

The new bounds introduced here are also important from a radio system point of view. Specifically, they are based on the bandwidth and realizable gain as well as the Q-value and the directivity. The interpretation of the Q-value in terms of the bandwidth is still subject to some research, see Ref. 25. Moreover, the new bounds permit the study of polarization effects and their influence on the antenna performance. An example of such an effect is polarization diversity for applications in MIMO communication systems.

The present paper is a direct application of the physical bounds for broadband scattering introduced in Refs. 19 and 20, where the integrated extinction is related to the long wavelength polarizability dyadics. The underlying mathematical description is strongly influenced by the consequences of causality and the summation rules and dispersion relations in the scattering theory for the Schrödinger equation, see Refs. 16, 17 and 22.

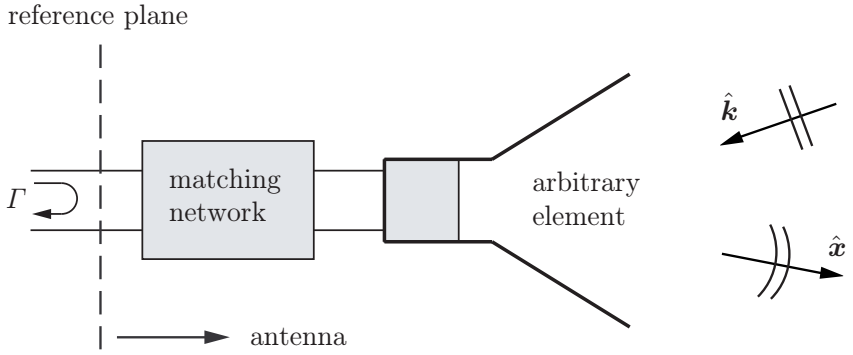

Figure 1: Illustration of a hypothetic antenna subject to an incident plane-wave in the $\hat{\boldsymbol{k}}$-direction.

2 Scattering and absorption of antennas

The present theory is inspired by the general scattering formalism of particles and waves in Refs. 16 and 22. In fact, based on the assumptions of linearity, time-translational invariance and causality there is no fundamental difference between antennas and properly modeled scatterers. This kind of fruitful equivalence between antenna and scattering theory has already been encountered in the literature, *cf.*, the bounds on the absorption efficiency in Ref. 2 and its relation to minimum scattering antennas. Without loss of generality, the integrated extinction and the theory introduced in Ref. 19 can therefore be argued to also hold for antennas of arbitrary shape. In contrast to Ref. 19, the present paper focuses on the absorption cross section rather than scattering properties.

For this purpose, consider an antenna of arbitrary shape surrounded by free space and subject to a plane-wave excitation impinging in the $\hat{\boldsymbol{k}}$-direction, see Fig. 1. The antenna is assumed to be lossless with respect to ohmic losses and satisfy the fundamental principles of linearity, time-translational invariance and causality. The dynamics of the antenna is modeled by the Maxwell equations with general reciprocal anisotropic constitutive relations. The constitutive relations are expressed in terms of the electric and magnetic susceptibility dyadics, $\boldsymbol{\chi}_{\mathrm{e}}$ and $\boldsymbol{\chi}_{\mathrm{m}}$, respectively, which are functions of the material properties of the antenna.

The assumption of a lossless antenna is not severe since the analysis can be modified to include ohmic losses, see the discussion in Sec. 9. In fact, ohmic losses are important for small antennas, and taking such effects into account, suggest that the lossless antenna is more advantageous than the corresponding antenna with ohmic losses. Recall that $\boldsymbol{\chi}_{\mathrm{e}}$ and $\boldsymbol{\chi}_{\mathrm{m}}$ also depend on the angular frequency ω of the incident plane-wave in the presence of losses.

The bounding volume V of the antenna is of arbitrary shape with the restriction that the complete absorption of the incident wave is contained within V. The bounding volume is naturally delimited by a reference plane or a port at which a unique voltage and current relation can be defined, see Fig. 1. The present definition of the antenna structure includes the matching network and is of the same kind as

the descriptions in Refs. 4 and 25. The reflection coefficient Γ at the port is due to the unavoidable impedance mismatch of the antenna over a given wavelength interval, see Ref. 6. The present analysis is restricted to single port antennas with a scalar (single) reflection coefficient. The extension to multiple ports is commented briefly in Sec. 9.

For any antenna, the scattered electric field $\boldsymbol{E}_\mathrm{s}$ in the forward direction $\hat{\boldsymbol{k}}$ can be expressed in terms of the forward scattering dyadic $\mathbf{S}$ as, see App. A,

$$\boldsymbol{E}_\mathrm{s}(k, x\hat{\boldsymbol{k}}) = \frac{\mathrm{e}^{\mathrm{i}kx}}{x}\mathbf{S}(k, \hat{\boldsymbol{k}}) \cdot \boldsymbol{E}_0 + \mathcal{O}(x^{-2}) \quad \text{as } x \to \infty. \tag{2.1}$$

Here, $\boldsymbol{E}_0$ denotes the Fourier amplitude of the incident field $\boldsymbol{E}_\mathrm{i}(\mathrm{c}_0 t - \hat{\boldsymbol{k}} \cdot \boldsymbol{x})$, and k is a complex variable with $\operatorname{Re} k = \omega/\mathrm{c}_0$ and $\operatorname{Im} k \geqslant 0$. For a large class of antennas, the elements of $\mathbf{S}$ are holomorphic in k and Cauchy's integral theorem can be applied to

$$\varrho(k) = \frac{1}{k^2}\hat{\boldsymbol{p}}_\mathrm{e}^* \cdot \mathbf{S}(k, \hat{\boldsymbol{k}}) \cdot \hat{\boldsymbol{p}}_\mathrm{e}, \quad k \in \mathbb{C}. \tag{2.2}$$

Here, $\hat{\boldsymbol{p}}_\mathrm{e} = \boldsymbol{E}_0/|\boldsymbol{E}_0|$ denotes the electric polarization, which is assumed to be independent of k.[1] The complex-valued function (2.2) is referred to as the extinction volume and it provides a holomorphic extension of the extinction cross section to $\operatorname{Im} k \geqslant 0$, see App. A.

A dispersion relation or summation rule for the extinction cross section can be derived in terms of the electric and magnetic polarizability dyadics $\boldsymbol{\gamma}_\mathrm{e}$ and $\boldsymbol{\gamma}_\mathrm{m}$, respectively. The derivation is based on energy conservation via the optical theorem in Refs. 16 and 22. The optical theorem $\sigma_\mathrm{ext} = 4\pi k \operatorname{Im} \varrho$ and the asymptotic behavior of the extinction volume ϱ in the long wavelength limit, $|k| \to 0$, are the key building blocks in the derivation. The result is the integrated extinction

$$\int_0^\infty \sigma_\mathrm{ext}(\lambda)\ \mathrm{d}\lambda = \pi^2(\hat{\boldsymbol{p}}_\mathrm{e}^* \cdot \boldsymbol{\gamma}_\mathrm{e} \cdot \hat{\boldsymbol{p}}_\mathrm{e} + \hat{\boldsymbol{p}}_\mathrm{m}^* \cdot \boldsymbol{\gamma}_\mathrm{m} \cdot \hat{\boldsymbol{p}}_\mathrm{m}), \tag{2.3}$$

where the magnetic (or cross) polarization $\hat{\boldsymbol{p}}_\mathrm{m} = \hat{\boldsymbol{k}} \times \hat{\boldsymbol{p}}_\mathrm{e}$ has been introduced. The functional dependence on $\hat{\boldsymbol{k}}$ and $\hat{\boldsymbol{p}}_\mathrm{e}$ is for simplicity suppressed from the argument on the left hand side of (2.3). Note that (2.3) also can be formulated in $k = 2\pi/\lambda$ via the transformation $\sigma_\mathrm{ext}(\lambda) \to 2\pi\sigma_\mathrm{ext}(2\pi/k)/k^2$. For details on the derivation of (2.3) and definition of the extinction cross section σ_ext and the polarizability dyadics $\boldsymbol{\gamma}_\mathrm{e}$ and $\boldsymbol{\gamma}_\mathrm{m}$, see App. A and B. The integrated extinction applied to scattering problems is exploited in Ref. 19.

It is already at this point important to notice that the right hand side of (2.3) only depends on the long wavelength limit or static response of the antenna, while the left hand side is a dynamic quantity which includes the absorption and scattering properties of the antenna. Furthermore, electric and magnetic properties are seen to be treated on equal footing in (2.3), both in terms of material properties and polarization description.

[1] Observe that the assumption that $\hat{\boldsymbol{p}}_\mathrm{e}$ is independent of k does not imply that the polarization of the antenna in Fig. 1 is frequency independent.

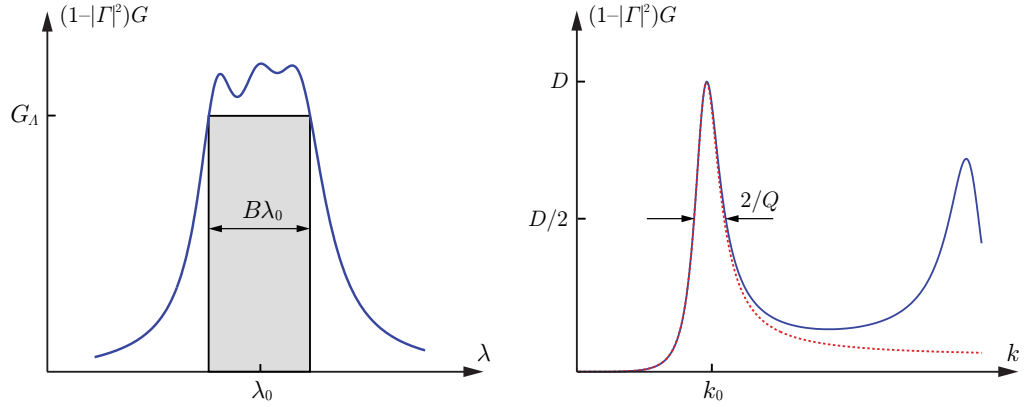

Figure 2: Illustration of the two types of physical bounds considered in this paper: $G_\Lambda B$ represented by the shaded box (left figure) and D/Q related to the dotted resonance model (right figure).

The antenna parameters of importance in this paper are the partial gain G and the partial directivity D, see App. E and Ref. 3. In general, both G and D depend on the incident direction $\hat{\boldsymbol{k}}$ and the electric polarization $\hat{\boldsymbol{p}}_\mathrm{e}$ as well as the wave number k. In addition, the partial realized gain, $(1-|\Gamma|^2)G$, depends on the reflection coefficient Γ. In the forthcoming analysis, the relative bandwidth B, the Q-value, and the associated center wavelength λ_0 are naturally introduced as intrinsic parameters in the sense that neither of them depend on $\hat{\boldsymbol{k}}$ or $\hat{\boldsymbol{p}}_\mathrm{e}$ for a given single port antenna.

Two different types of bounds on the first resonance of an antenna are addressed in this paper, see Fig. 2. The bounds relate the integral (2.3) of two generic integrands to the polarizability dyadics. The bound on the partial realized gain, $(1-|\Gamma|^2)G$, in the left figure takes the form of a box, *i.e.*, it estimates the integral with the bandwidth times the partial realized gain. The bound in the right figure utilizes the classical resonance shape of the integrand giving a bound expressed in terms of the partial directivity and the associated Q-value.

3 Bounds on bandwidth and gain

From the definition of the extinction cross section σ_ext it is clear that it is non-negative and bounded from below by the absorption cross section σ_a. For an unmatched antenna, σ_a is reduced by the reflection loss $1-|\Gamma|^2$ according to $\sigma_\mathrm{a} = (1-|\Gamma|^2)\sigma_{\mathrm{a}0}$, where $\sigma_{\mathrm{a}0}$ denotes the absorption cross section or partial effective area for the corresponding perfectly matched antenna, see Refs. 18 and 3. The absorption cross section $\sigma_{\mathrm{a}0}$ is by reciprocity related to the partial antenna directivity D as $D = 4\pi\sigma_{\mathrm{a}0}/\lambda^2$, see Ref. 18. Thus, for any wavelength $\lambda \in [0,\infty)$,

$$\sigma_\mathrm{ext} \geqslant \sigma_\mathrm{a} = (1-|\Gamma|^2)\sigma_{\mathrm{a}0} = \frac{1}{4\pi}(1-|\Gamma|^2)\lambda^2 D. \tag{3.1}$$

Recall that D depends on the electric polarization $\hat{\boldsymbol{p}}_{\mathrm{e}}$ as well as the incident direction $\hat{\boldsymbol{k}}$. In the present case of no ohmic losses, the partial gain G coincides with the partial directivity D.

Introduce the wavelength interval $\mathit{\Lambda} = [\lambda_1, \lambda_2]$ with center wavelength $\lambda_0 = (\lambda_2 + \lambda_1)/2$ and associated relative bandwidth

$$B = 2\frac{\lambda_2 - \lambda_1}{\lambda_2 + \lambda_1} = 2\frac{k_1 - k_2}{k_2 + k_1}, \tag{3.2}$$

where $0 < B \leqslant 2$ and $k = 2\pi/\lambda \in K$ denotes the angular wave number in $K = [k_2, k_1]$. Thus, for any wavelength interval $\mathit{\Lambda}$, the estimate $\sigma_{\mathrm{ext}} \geqslant \sigma_{\mathrm{a}}$ in (3.1) yields

$$\int_0^\infty \sigma_{\mathrm{ext}}(\lambda)\ \mathrm{d}\lambda \geqslant \int_{\mathit{\Lambda}} \sigma_{\mathrm{a}}(\lambda)\ \mathrm{d}\lambda = \frac{1}{4\pi}\int_{\mathit{\Lambda}} (1 - |\mathit{\Gamma}|^2)\lambda^2 G(\lambda)\ \mathrm{d}\lambda, \tag{3.3}$$

where $D = G$ is used.[2]

In order to simplify the notation, introduce $G_{\mathit{\Lambda}} = \inf_{\lambda\in\mathit{\Lambda}}(1 - |\mathit{\Gamma}|^2)G$ as the minimum partial realized gain over the wavelength interval $\mathit{\Lambda}$. Following this notation, the integral on the right hand side of (3.3) can be estimated from below as

$$\int_{\mathit{\Lambda}} (1 - |\mathit{\Gamma}|^2)\lambda^2 G(\lambda)\ \mathrm{d}\lambda \geqslant G_{\mathit{\Lambda}} \int_{\mathit{\Lambda}} \lambda^2\ \mathrm{d}\lambda = \lambda_0^3 G_{\mathit{\Lambda}} B\left(1 + \frac{B^2}{12}\right). \tag{3.4}$$

Without loss of generality, the factor $1 + B^2/12$ can be estimated from below by unity. This estimate is also supported by the fact that $B \ll 2$ in many applications. Based upon this observation, (2.3), (3.3) and (3.4) can be summarized to yield the following bound on the product $G_{\mathit{\Lambda}}B$ valid for any antenna satisfying the general assumptions stated in Sec. 2:

$$G_{\mathit{\Lambda}} B \leqslant \frac{4\pi^3}{\lambda_0^3}(\hat{\boldsymbol{p}}_{\mathrm{e}}^* \cdot \boldsymbol{\gamma}_{\mathrm{e}} \cdot \hat{\boldsymbol{p}}_{\mathrm{e}} + \hat{\boldsymbol{p}}_{\mathrm{m}}^* \cdot \boldsymbol{\gamma}_{\mathrm{m}} \cdot \hat{\boldsymbol{p}}_{\mathrm{m}}). \tag{3.5}$$

Relation (3.5) is one of the main results of this paper. Note that the factor $4\pi^3/\lambda_0^3$ neatly can be expressed as $k_0^3/2$ in terms of the angular wave number $k_0 = 2\pi/\lambda_0$.

The estimate $1 + B^2/12 \geqslant 1$ in (3.4) is motivated by the simple form of (3.5). In broadband applications, B is in general not small compared to unity, and the higher order term in B should be included on the left hand side of (3.5).

The right hand side of (3.5) depends on both $\hat{\boldsymbol{p}}_{\mathrm{e}}$ and $\hat{\boldsymbol{k}} = \hat{\boldsymbol{p}}_{\mathrm{e}} \times \hat{\boldsymbol{p}}_{\mathrm{m}}$, as well as the long wavelength limit (static limit with respect to $k = 2\pi/\lambda$) material properties and shape of the antenna. It is indeed surprising that it is just the long wavelength limit properties of the antenna that bound the product $G_{\mathit{\Lambda}}B$ in (3.5). Since $\boldsymbol{\gamma}_{\mathrm{e}}$ and $\boldsymbol{\gamma}_{\mathrm{m}}$ are proportional to the volume V of the antenna, see Ref. 19, it follows from (3.5) that the upper bound on the product $G_{\mathit{\Lambda}}B$ is directly proportional to V/λ_0^3 or $k_0^3 a^3$, where a denotes the radius of the volume-equivalent sphere.

[2]The equality sign on the left hand side in (3.3) is motivated by the broadband absorption efficiency introduced in (3.8).

In many antenna applications it is desirable to bound the product $G_\Lambda B$ independently of the material properties. For this purpose, introduce the high-contrast polarizability dyadic $\boldsymbol{\gamma}_\infty$ as the limit of either $\boldsymbol{\gamma}_\mathrm{e}$ or $\boldsymbol{\gamma}_\mathrm{m}$ when the elements of $\boldsymbol{\chi}_\mathrm{e}$ or $\boldsymbol{\chi}_\mathrm{m}$ in the long wavelength limit simultaneously approach infinity.[3] Note that this definition implies that $\boldsymbol{\gamma}_\infty$ is independent of any material properties, depending only on the geometry of the antenna. From the variational properties of $\boldsymbol{\gamma}_\mathrm{e}$ and $\boldsymbol{\gamma}_\mathrm{m}$ discussed in Ref. 19 and references therein, it follows that both $\boldsymbol{\gamma}_\mathrm{e}$ and $\boldsymbol{\gamma}_\mathrm{m}$ are bounded from above by $\boldsymbol{\gamma}_\infty$. Hence, (3.5) yields

$$G_\Lambda B \leqslant \frac{4\pi^3}{\lambda_0^3}(\hat{\boldsymbol{p}}_\mathrm{e}^* \cdot \boldsymbol{\gamma}_\infty \cdot \hat{\boldsymbol{p}}_\mathrm{e} + \hat{\boldsymbol{p}}_\mathrm{m}^* \cdot \boldsymbol{\gamma}_\infty \cdot \hat{\boldsymbol{p}}_\mathrm{m}). \tag{3.6}$$

The introduction of the high-contrast polarizability dyadic $\boldsymbol{\gamma}_\infty$ in (3.6) is the starting point of the analysis below.

The high-contrast polarizability dyadic $\boldsymbol{\gamma}_\infty$ is real-valued and symmetric, and consequently diagonalizable with real-valued eigenvalues. Let $\gamma_1 \geqslant \gamma_2 \geqslant \gamma_3$ denote the three eigenvalues. Based on the constraint $\hat{\boldsymbol{p}}_\mathrm{e} \cdot \hat{\boldsymbol{p}}_\mathrm{m} = 0$, which is a consequence of the free space plane-wave excitation, the right hand side of (3.6) can be estimated from above as

$$\sup_{\hat{\boldsymbol{p}}_\mathrm{e} \cdot \hat{\boldsymbol{p}}_\mathrm{m} = 0} G_\Lambda B \leqslant \frac{4\pi^3}{\lambda_0^3}(\gamma_1 + \gamma_2). \tag{3.7}$$

The interpretation of the operator $\sup_{\hat{\boldsymbol{p}}_\mathrm{e} \cdot \hat{\boldsymbol{p}}_\mathrm{m} = 0}$ is polarization matching, *i.e.*, the polarization of the antenna coincides with the polarization of the incident wave. In the case of non-magnetic antennas, $\boldsymbol{\gamma}_\mathrm{m} = \mathbf{0}$, the second eigenvalue γ_2 in (3.7) vanishes. Hence, the right hand side of (3.7) can be improved by at most a factor of two by utilizing magnetic materials. Note that the upper bounds in (3.6) and (3.7) coincide when $\boldsymbol{\gamma}_\infty$ is isotropic.

Since γ_1 and γ_2 only depend on the long wavelength properties of the antenna, they can easily be calculated for arbitrary geometries using either the finite element method (FEM) or the method of moments (MoM). Numerical results of γ_1 and γ_2 for the Platonic solids, the rectangular parallelepiped and some classical antennas are presented in Secs. 7 and 8. Important variational properties of γ_j are discussed in Ref. 19 and references therein. The influence of supporting ground planes and the validity of the method of images for high-contrast polarizability calculations are presented in App. C.

The estimate in (3.3) can be improved based on a priori knowledge of the scattering properties of the antenna. In fact, $\sigma_\mathrm{ext} \geqslant \sigma_\mathrm{a}$ in (3.1) may be replaced by $\sigma_\mathrm{ext} = \sigma_\mathrm{a}/\eta$, where $0 < \eta \leqslant 1$ denotes the absorption efficiency of the antenna, see Ref. 2. For most antennas at the resonance frequency, $\eta \leqslant 1/2$, but exceptions from this rule of thumb exist. In particular, minimum scattering antennas (MSA) defined by $\eta = 1/2$ yield an additional factor of two on the right hand side of (3.1). The inequality in (3.3) can be replaced by the equality

$$\int_\Lambda \sigma_\mathrm{ext}(\lambda)\ \mathrm{d}\lambda = \widetilde{\eta}^{-1} \int_\Lambda \sigma_\mathrm{a}(\lambda)\ \mathrm{d}\lambda. \tag{3.8}$$

[3]Recall that $\boldsymbol{\chi}_\mathrm{e}$ and $\boldsymbol{\chi}_\mathrm{m}$ are real-valued in the long wavelength limit. In the case of finite or infinite conductivity, see App. B.

The constant $\widetilde{\eta}$ is bounded from above by the absorption efficiency via $\widetilde{\eta} \leqslant \sup_{\lambda\in\Lambda} \eta$, and provides a broadband generalization of the absorption efficiency. If $\widetilde{\eta}$ is invoked in (3.3), the right hand side of the inequalities (3.5), (3.6), and (3.7) are sharpened by the multiplicative factor $\widetilde{\eta}$.

4 Bounds on Q-value and directivity

Under the assumption of N non-interfering resonances characterized by the real-valued angular wave numbers k_n, a multiple resonance model for the absorption cross section is

$$\sigma_{\mathrm{a}}(k) = 2\pi \sum_{n=1}^{N} \varrho_n \frac{Q_n k_n}{1 + Q_n^2 (k/k_n - k_n/k)^2/4}, \tag{4.1}$$

where k is assumed real-valued and ϱ_n are positive weight functions satisfying $\sum_n \varrho_n = \varrho(0)$. Here, the Q-value of the resonance at k_n is denoted by Q_n, and for $Q_n \gg 1$, the associated relative half-power bandwidth is $B_n \sim 2/Q_n$, see Fig. 3. Recall that $Q_n \geqslant 1$ is consistent with $0 < B_n \leqslant 2$. For the resonance model (4.1), one can argue that Q_n in fact coincides with the corresponding antenna Q-value in App. F when the relative bandwidth $2/Q_n$ is based on the half-power threshold, see also Refs. 7 and 25. In the case of strongly interfering resonances, the model (4.1) either has to be modified or the estimates in Sec. 3 have to be used.

The absorption cross section is the imaginary part, $\sigma_{\mathrm{a}} = 4\pi k \operatorname{Im} \varrho_{\mathrm{a}}$, of the function

$$\varrho_{\mathrm{a}}(k) = \sum_{n=1}^{N} \varrho_n \frac{\mathrm{i} Q_n k_n/(2k)}{1 - \mathrm{i} Q_n \left(k/k_n - k_n/k\right)/2}, \tag{4.2}$$

for real-valued k. The function $\varrho_{\mathrm{a}}(k)$ is holomorphic for $\operatorname{Im} k > 0$ and has a symmetrically distributed pair of poles for $\operatorname{Im} k < 0$, see Fig. 3. The integrated absorption cross section is

$$\frac{1}{4\pi^2} \int_{-\infty}^{\infty} \frac{\sigma_{\mathrm{a}}(k)}{k^2} \, \mathrm{d}k = \varrho_{\mathrm{a}}(0) = \widetilde{\eta}\varrho(0) \leqslant \varrho(0), \tag{4.3}$$

where $\varrho(0)$ is given by the long wavelength limit (A.6).

For antennas with a dominant first resonance at $k = k_1$, it follows from (3.1) and (4.1) that the partial realized gain G satisfies

$$(1 - |\Gamma|^2) G = \frac{k^2 \sigma_{\mathrm{a}}}{\pi} \leqslant \varrho(0) \frac{2k^2 Q k_1}{1 + Q^2 (k/k_1 - k_1/k)^2/4}, \tag{4.4}$$

where $\varrho_1 \leqslant \varrho(0)$ has been used. The right hand side of (4.4) reaches its maximum value $\varrho(0) 2k_1^3 Q/(1 - Q^{-2})$ at $k_0 = k_1(1 - 2Q^{-2})^{-1/2}$ or $k_0 = k_1 + \mathcal{O}(Q^{-2})$ as $Q \to \infty$. Hence, k_0 is a good approximation to k_1 if $Q \gg 1$. For a lossless antenna which is perfectly matched at $k = k_0$, the partial realized gain $(1 - |\Gamma|^2)G$ coincides with the partial directivity D. Under this assumption, (4.4) yields $D/Q \leqslant \varrho(0) 2k_1^3/(1 - Q^{-2})$ which further can be estimated from above as

$$\frac{D}{Q} \leqslant \frac{k_0^3}{2\pi} \left(\hat{\boldsymbol{p}}_{\mathrm{e}}^* \cdot \boldsymbol{\gamma}_{\mathrm{e}} \cdot \hat{\boldsymbol{p}}_{\mathrm{e}} + \hat{\boldsymbol{p}}_{\mathrm{m}}^* \cdot \boldsymbol{\gamma}_{\mathrm{m}} \cdot \hat{\boldsymbol{p}}_{\mathrm{m}} \right), \tag{4.5}$$

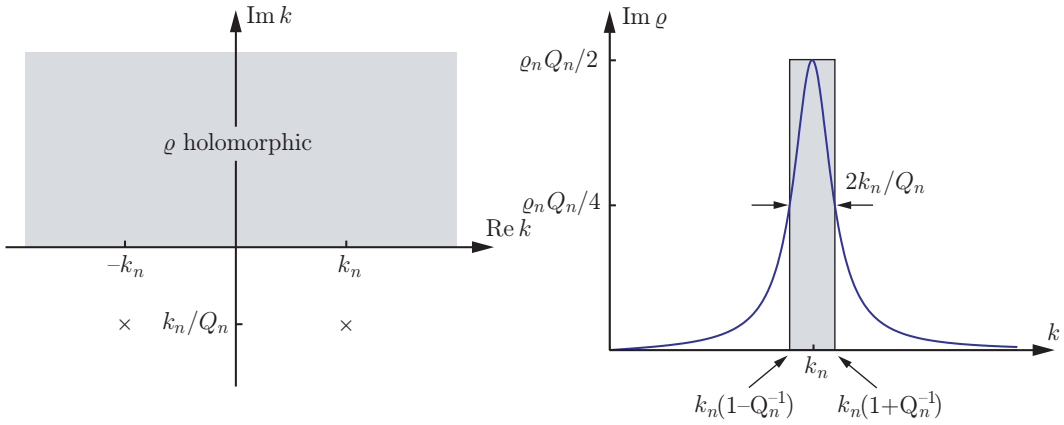

Figure 3: The symmetrically distributed pair of poles (×) of the extinction volume ϱ in the complex k-plane (left figure) and the corresponding single resonance model of $\operatorname{Im}\varrho$ when $Q_n \gg 1$ (right figure).

where (A.6) have been used. Relation (4.5) together with (3.6) constitute the main results of this paper.

Analogous to (3.6) and (3.7), it is clear that (4.5) can be estimated from above by the high-contrast polarizability dyadic $\boldsymbol{\gamma}_\infty$ and the associated eigenvalues γ_1 and γ_2, *viz.*,

$$\sup_{\hat{\boldsymbol{p}}_\mathrm{e}\cdot\hat{\boldsymbol{p}}_\mathrm{m}=0} \frac{D}{Q} \leqslant \frac{k_0^3}{2\pi}(\gamma_1+\gamma_2). \tag{4.6}$$

Here, (4.6) is subject to polarization matching and therefore independent of the electric and magnetic polarizations, $\hat{\boldsymbol{p}}_\mathrm{e}$ and $\hat{\boldsymbol{p}}_\mathrm{m}$, respectively. Note that the upper bounds in (4.5) and (4.6) only differ from the corresponding results in (3.6) and (3.7) by a factor of π, *i.e.*, $G_\Lambda B \leqslant \pi C$ and $D/Q \leqslant C$. Hence, it is sufficient to consider either the $G_\Lambda B$ bound or the D/Q bound for a specific antenna. The estimates (4.5) and (4.6) can be improved by the multiplicative factor $\widetilde{\eta}$ if a priori knowledge of the scattering properties of the antenna (3.8) is invoked in (4.4).

The resonance model for the absorption cross section in (4.1) is also directly applicable to the theory of broadband scattering in Ref. 19. In that reference, (4.1) can be used to model absorption and scattering properties and yield new bounds on broadband scattering.

5 Comparison with Chu and Chu-Fano

In this section, the bounds on $G_\Lambda B$ and D/Q subject to matched polarizations, *i.e.*, inequalities (3.7) and (4.6), are compared with the corresponding results by Chu and Fano in Refs. 4 and 6, respectively.

5.1 Bounds on Q-value and directivity

The classical bounds derived by Chu in Ref. 4 relate the Q-value and the directivity D to the quantity $k_0 a$ of the smallest circumscribing sphere. Using the notation of Secs. 3 and 4, the classical result by Chu for an omni-directional antenna (for example in the azimuth plane) reads

$$\sup_{\hat{\boldsymbol{p}}_{\mathrm{e}}\cdot\hat{\boldsymbol{p}}_{\mathrm{m}}=0} \frac{D}{Q} \leqslant \frac{3}{2}\frac{k_0^3 a^3}{k_0^2 a^2 + 1} = \frac{3}{2} k_0^3 a^3 + \mathcal{O}(k_0^5 a^5) \quad \text{as } k_0 a \to 0. \tag{5.1}$$

In the general case of both TE- and TM-modes, (5.1) must be modified, see Ref. 13, *viz.*,

$$\sup_{\hat{\boldsymbol{p}}_{\mathrm{e}}\cdot\hat{\boldsymbol{p}}_{\mathrm{m}}=0} \frac{D}{Q} \leqslant \frac{6 k_0^3 a^3}{2 k_0^2 a^2 + 1} = 6 k_0^3 a^3 + \mathcal{O}(k_0^5 a^5) \quad \text{as } k_0 a \to 0. \tag{5.2}$$

Note that (5.2) differs from (5.1) by approximately a factor of four when $k_0 a \ll 1$.

The bounds in (5.1) and (5.2) should be compared with the corresponding result in Sec. 4 for the sphere. For a sphere of radius a, the eigenvalues γ_1 and γ_2 are degenerated and equal to $4\pi a^3$, see Sec. 6. Insertion of $\gamma_1 = \gamma_2 = 4\pi a^3$ into (4.6) yields $\sup_{\hat{\boldsymbol{p}}_{\mathrm{e}}\cdot\hat{\boldsymbol{p}}_{\mathrm{m}}=0} D/Q \leqslant C$, where the constant C is given by

$$C = 4 k_0^3 a^3, \qquad C = 2 k_0^3 a^3, \qquad C = k_0^3 a^3. \tag{5.3}$$

The three different cases in (5.3) correspond to both electric and magnetic material properties ($C = 4k_0^3 a^3$), pure electric material properties ($C = 2k_0^3 a^3$), and pure electric material properties with a priori knowledge of minimum scattering characteristics ($C = k_0^3 a^3$ with $\widetilde{\eta} = 1/2$), respectively. Note that the third case in (5.3) more generally can be expressed as $C = 2k_0^3 a^3 \widetilde{\eta}$ for any broadband absorption efficiency $0 < \widetilde{\eta} \leqslant 1$. The bounds in (5.2) and (5.3) are comparable although the new bounds (5.3) are sharper. In the omni-directional case, (5.1) provides a sharper bound than (5.3), except for the pure electric case with absorption efficiency $\widetilde{\eta} < 3/4$.

5.2 Bounds on bandwidth and gain

The bound (3.7) should also be compared with the result of Chu when the Fano theory of broadband matching is used. The Fano theory includes the impedance variation over the frequency interval to yield bounds on the bandwidth, see Ref. 6. For a resonance circuit model, the Fano theory yields that the relation between B and Q is, see Ref. 7,

$$B \leqslant \frac{\pi}{Q \ln 1/|\Gamma|}. \tag{5.4}$$

The reflection coefficient Γ is due to mismatch of the antenna. It is related to the standing wave ratio SWR as $|\Gamma| = (\mathrm{SWR} - 1)/(1 + \mathrm{SWR})$.

Introduce Q_{s} as the Q-value of the smallest circumscribing sphere with $1/Q_{\mathrm{s}} = k_0^3 a^3 + \mathcal{O}(k_0^5 a^5)$ as $k_0 a \to 0$ for omni-directional antennas. Under this assumption, it

follows from (5.1) that $\sup_{\hat{\boldsymbol{p}}_\mathrm{e}\cdot\hat{\boldsymbol{p}}_\mathrm{m}=0} D \leqslant 3Q/2Q_\mathrm{s}$. Insertion of this inequality into (5.4) then yields

$$\sup_{\hat{\boldsymbol{p}}_\mathrm{e}\cdot\hat{\boldsymbol{p}}_\mathrm{m}=0} G_\Lambda B \leqslant \frac{3\pi}{2}\frac{1-|\Gamma|^2}{\ln 1/|\Gamma|}k_0^3a^3. \tag{5.5}$$

For a given k_0a, the right hand side of (5.5) is monotone in $|\Gamma|$ and bounded from above by $3\pi k_0^3a^3$. However, note that the Chu-Fano bound (5.5) is restricted to omni-directional antennas with $k_0a \ll 1$.

Inequality (5.5) should be compared with the corresponding result in Sec. 3 for the smallest circumscribing sphere. Since the upper bounds (3.7) and (4.6) only differ by a factor of π, *i.e.*, $\sup_{\hat{\boldsymbol{p}}_\mathrm{e}\cdot\hat{\boldsymbol{p}}_\mathrm{m}=0} G_\Lambda B \leqslant C'$ and $\sup_{\hat{\boldsymbol{p}}_\mathrm{e}\cdot\hat{\boldsymbol{p}}_\mathrm{m}=0} D/Q \leqslant C$ where $C' = \pi C$, it follows from (5.3) that

$$C' = 4\pi k_0^3a^3, \qquad C' = 2\pi k_0^3a^3, \qquad C' = \pi k_0^3a^3. \tag{5.6}$$

The three cases in (5.3) correspond to both electric and magnetic material properties ($C' = 4\pi k_0^3a^3$), pure electric material properties ($C' = 2\pi k_0^3a^3$), and pure electric material properties with a priori knowledge of minimum scattering characteristics ($C' = \pi k_0^3a^3$), respectively.

The bounds on $G_\Lambda B$ based on (5.6) are comparable with (5.5) for most reflections coefficients $|\Gamma|$. For $|\Gamma| < 0.65$ the Chu-Fano bound (5.5) provides a slightly sharper bound on $G_\Lambda B$ than (5.6) for pure electric materials. However, recall that the spherical geometry gives an unfavorable comparison with the present theory, since for many antennas the eigenvalues γ_1 and γ_2 are reduced considerably compared with the smallest circumscribing sphere, *cf.*, the dipole in Sec. 8.1 and the loop antenna in Sec. 8.2.

6 Ellipsoidal geometries

Closed-form expressions of $\boldsymbol{\gamma}_\mathrm{e}$ and $\boldsymbol{\gamma}_\mathrm{m}$ exist for the ellipsoidal geometries, see Ref. 19, *viz.*,

$$\boldsymbol{\gamma}_\mathrm{e} = V\boldsymbol{\chi}_\mathrm{e}\cdot(\mathbf{I}+\mathbf{L}\cdot\boldsymbol{\chi}_\mathrm{e})^{-1}, \qquad \boldsymbol{\gamma}_\mathrm{m} = V\boldsymbol{\chi}_\mathrm{m}\cdot(\mathbf{I}+\mathbf{L}\cdot\boldsymbol{\chi}_\mathrm{m})^{-1}. \tag{6.1}$$

Here, $\mathbf{I}$ denotes the unit dyadic and $V = 4\pi a_1a_2a_3/3$ is the volume of ellipsoid in terms of the semi-axes a_j. The depolarizability dyadic $\mathbf{L}$ is real-valued and symmetric, and hence diagonalizable with real-valued eigenvalues. The eigenvalues of $\mathbf{L}$ are the depolarizing factors L_j, given by

$$L_j = \frac{a_1a_2a_3}{2}\int_0^\infty \frac{\mathrm{d}s}{(s+a_j^2)\sqrt{(s+a_1^2)(s+a_2^2)(s+a_3^2)}}, \quad j = 1,2,3. \tag{6.2}$$

The depolarizing factors L_j satisfy $0 \leqslant L_j \leqslant 1$ and $\sum_j L_j = 1$. The semi-axes a_j are assumed to be ordered such that $L_1 \leqslant L_2 \leqslant L_3$. Closed-form expressions of (6.2) in terms of the semi-axis ratio $\xi = (\min_j a_j)/(\max_j a_j)$ exist for the ellipsoids of revolution, *i.e.*, the prolate spheroids ($L_2 = L_3$) and the oblate spheroids ($L_1 = L_2$), see App. G.

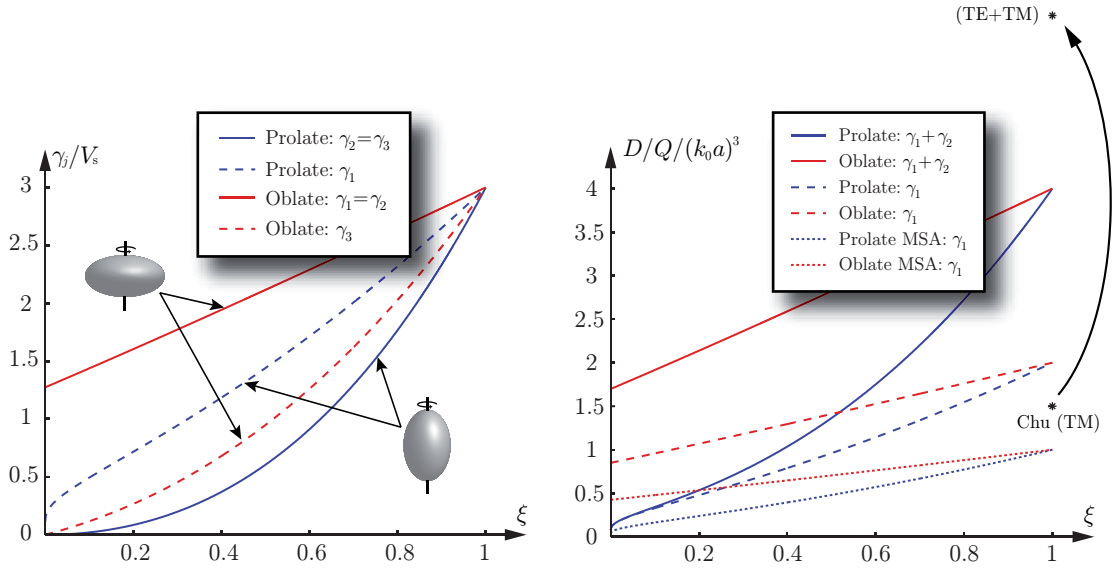

Figure 4: The eigenvalues $\gamma_1 \geqslant \gamma_2 \geqslant \gamma_3$ (left figure) and the quotient D/Q (right figure) for the prolate and oblate spheroids as function of the semi-axis ratio ξ. Note the normalization with the volume $V_s = 4\pi a^3/3$ of the smallest circumscribing sphere.

The high-contrast polarizability dyadic $\boldsymbol{\gamma}_\infty$ is given by (6.1) as the elements of $\boldsymbol{\chi}_e$ or $\boldsymbol{\chi}_m$ simultaneously approach infinity. From (6.1) it is clear that the eigenvalues of $\boldsymbol{\gamma}_\infty$ are given by $\gamma_j = V/L_j$. For the prolate and oblate spheroids, V is neatly expressed in terms of the volume $V_s = 4\pi a^3/3$ of the smallest circumscribing sphere. The results are $V = \xi^2 V_s$ and $V = \xi V_s$ for the prolate and oblate spheroids, respectively. The eigenvalues γ_1 and γ_2 for the prolate and oblate spheroids are depicted in the left figure in Fig. 4. Note that the curves for the oblate spheroid approach $4/\pi$ in the limit as $\xi \to 0$, see App. G. The corresponding limiting value for the curves as $\xi \to 1$ is 3.

The general bound on $G_\Lambda B$ for arbitrary ellipsoidal geometries is obtained by inserting (6.1) into (3.5), *i.e.*,

$$G_\Lambda B \leqslant \frac{4\pi^3 V}{\lambda_0^3} \left(\hat{\boldsymbol{p}}_e^* \cdot \boldsymbol{\chi}_e \cdot (\mathbf{I} + \mathbf{L} \cdot \boldsymbol{\chi}_e)^{-1} \cdot \hat{\boldsymbol{p}}_e + \hat{\boldsymbol{p}}_m^* \cdot \boldsymbol{\chi}_m \cdot (\mathbf{I} + \mathbf{L} \cdot \boldsymbol{\chi}_m)^{-1} \cdot \hat{\boldsymbol{p}}_m \right). \quad (6.3)$$

Independent of both material properties and polarization effects, the right hand side of (6.3) can be estimated from above in analogy with (3.7). The result is

$$\sup_{\hat{\boldsymbol{p}}_e \cdot \hat{\boldsymbol{p}}_m = 0} G_\Lambda B \leqslant \frac{4\pi^3 V}{\lambda_0^3} \left(\frac{1}{L_1} + \frac{1}{L_2} \right). \quad (6.4)$$

In the non-magnetic case, the second term on the right hand side of (6.3) and (6.4) vanishes. For the prolate and oblate spheroids, the closed-form expressions of L_j in App. G can be introduced to yield explicit upper bounds on $G_\Lambda B$.

The corresponding results for the quotient D/Q are obtained from the observation that $G_\Lambda B \leqslant \pi C$ is equivalent to $D/Q \leqslant C$, see Sec. 4. For the general case

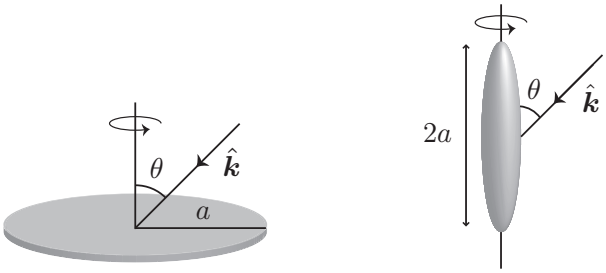

circular disk circular needle

Figure 5: Geometry of the circular disk and needle.

including polarization and material properties, (6.3) yields

$$\frac{D}{Q} \leqslant \frac{k_0^3 V}{2\pi} \left(\hat{\boldsymbol{p}}_{\mathrm{e}}^* \cdot \boldsymbol{\chi}_{\mathrm{e}} \cdot (\mathbf{I} + \mathbf{L} \cdot \boldsymbol{\chi}_{\mathrm{e}})^{-1} \cdot \hat{\boldsymbol{p}}_{\mathrm{e}} + \hat{\boldsymbol{p}}_{\mathrm{m}}^* \cdot \boldsymbol{\chi}_{\mathrm{m}} \cdot (\mathbf{I} + \mathbf{L} \cdot \boldsymbol{\chi}_{\mathrm{m}})^{-1} \cdot \hat{\boldsymbol{p}}_{\mathrm{m}} \right). \tag{6.5}$$

Analogous to (6.4), the restriction to matched polarizations for the quotient D/Q reads

$$\sup_{\hat{\boldsymbol{p}}_{\mathrm{e}} \cdot \hat{\boldsymbol{p}}_{\mathrm{m}} = 0} \frac{D}{Q} \leqslant \frac{k_0^3 V}{2\pi} \left(\frac{1}{L_1} + \frac{1}{L_2} \right). \tag{6.6}$$

The upper bound in (6.6) is depicted in the right figure in Fig. 4 for the prolate and oblate spheroids. The solid curves correspond to combined electric and magnetic material properties, while the dashed curves represent the pure electric case. The non-magnetic minimum scattering case ($\widetilde{\eta} = 1/2$) is given by the dotted curves. Note that the three curves in the right figure vanish for the prolate spheroid as $\xi \to 0$. The corresponding limiting values for the oblate spheroid are $16/3\pi$, $8/3\pi$ and $4/3\pi$, see App. G.

The curves depicted in the right figure in Fig. 4 should be compared with the classical results for the sphere in (5.1) and (5.2). The omni-directional bound (5.1) and its generalization (5.2) are marked in Fig. 4 by Chu (TE) and (TE+TM), respectively. From the figure, it is clear that (6.6) provides a sharper bound than (5.2). For omni-directional antennas, (5.1) is slightly sharper than (6.6) for the sphere, but when a priori knowledge of minimum scattering characteristics ($\widetilde{\eta} = 1/2$) is used, the reversed conclusion holds. Recall that the classical results in Sec. 5.1 are restricted to the sphere, in contrast to the theory introduced in this paper.

Based on the results in App. G, it is interesting to evaluate (6.4) in the limit as $\xi \to 0$. This limit corresponds to the axially symmetric needle and circular disk in Fig. 5. For a needle of length $2a$ with semi-axis $\xi \ll 1$, (G.3) inserted into (6.4) yields

$$G_\Lambda B \leqslant \frac{16\pi^4 a^3}{3\lambda_0^3} \frac{f(\theta)}{\ln 2/\xi - 1} + \mathcal{O}(\xi^2) \quad \text{as } \xi \to 0. \tag{6.7}$$

Here, $f(\theta) = \sin^2\theta$ for the TE- and TM-polarizations in the case of both electric and magnetic material properties. In the non-magnetic case, $f(\theta) = 0$ for the TE- and $f(\theta) = \sin^2\theta$ for the TM-polarization. Note that the $\sin^2\theta$ term in (6.7) and

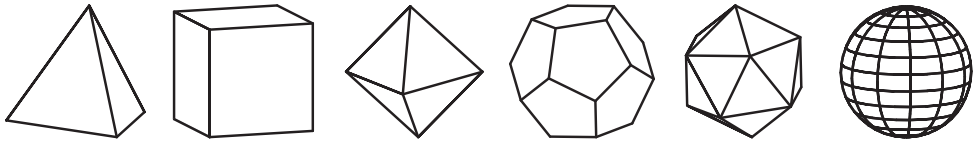

$5.029V$	$3.644V$	$3.551V$	$3.178V$	$3.130V$	$3V$
(0.205)	(0.445)	(0.377)	(0.704)	(0.632)	(1)

Figure 6: The eigenvalues γ (upper row) for the five Platonic solids and the sphere. The number in parenthesis are γ in units of $4\pi a^3$, where a denotes the radius of the smallest circumscribing sphere.

the logarithmic singularity in the denominator agree with the radiation pattern and the impedance of the dipole antenna in Sec. 8.1, see Ref. 5.

The corresponding result for the circular disk of radius a is non-vanishing in the limit as $\xi \to 0$, *viz.*,

$$G_\Lambda B \leqslant \frac{64\pi^3 a^3}{3\lambda_0^3} f(\theta). \tag{6.8}$$

Here, $f(\theta) = 1 + \cos^2\theta$ for the TE- and TM-polarizations in the case of both electric and magnetic material properties. In the non-magnetic case, $f(\theta) = 1$ for the TE- and and $f(\theta) = \cos^2\theta$ for the TM-polarization. Note the direct application of (6.8) for planar spiral antennas.

7 The high-contrast polarizability dyadic

In this section, some numerical results of $\boldsymbol{\gamma}_\infty$ are presented and analyzed in terms of the physical bounds discussed in Sec. 3.

7.1 The Platonic solids

Since the Platonic solids are invariant under appropriate point groups, see Ref. 12, their corresponding high-contrast polarizability dyadics $\boldsymbol{\gamma}_\infty$ are isotropic, *i.e.*, $\boldsymbol{\gamma}_\infty = \gamma_\infty \mathbf{I}$, where $\mathbf{I}$ denotes the unit dyadic in $\mathbb{R}^3$. Let $\gamma = \gamma_j$ represent the eigenvalues of $\boldsymbol{\gamma}_\infty$ for $j = 1, 2, 3$. The Platonic solids are depicted in Fig. 6 together with the eigenvalues γ in terms of the volume V of the solids. The five Platonic solids are from left to right the tetrahedron, hexahedron, octahedron, dodecahedron and icosahedron, with 4, 6, 8, 12 and 20 facets, respectively. Included in the figure are also γ in units of $4\pi a^3$, where a denotes the radius of the smallest circumscribing sphere. This comparison with the smallest circumscribing sphere is based on straightforward calculations which is further discussed in Sec. 7.2. The numerical values of γ in Fig. 6 are based on Method of Moments (MoM) calculations, see Ref. 19 and references therein.

Since the upper bound in (3.7) is linear in γ, it follows that among the Platonic solids, the tetrahedron provides the largest upper bound on $G_\Lambda B$ for a given volume

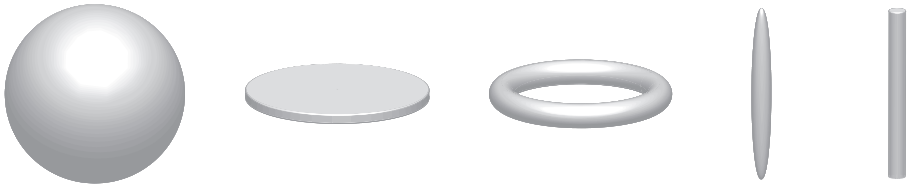

(1) (0.42) (0.24) (0.050) (0.056)

Figure 7: The eigenvalue γ_1 in units of $4\pi a^3$, where a denotes the radius of the smallest circumscribing sphere. The prolate spheroid, the circular ring and the circular cylinder correspond to the generalized semi-axis ratio $\xi = 10^{-3}$.

V. The eigenvalues γ in Fig. 6 are seen to approach $3V$ as the number of facets increases. This observation is confirmed by the variational principle discussed in Ref. 19, which states that for a given volume the sphere minimizes the trace of $\boldsymbol{\gamma}_\infty$ among all isotropic high-contrast polarizability dyadics. Hence, a lower bound on γ is given by the sphere for which $\gamma = 3V$.

For matched polarizations, the eigenvalues in Fig. 6 can directly be applied to (3.7) to yield an upper bound on the performance of any antenna circumscribed by a given Platonic solid. For example, the non-magnetic tetrahedron yields $G_\Lambda B \leqslant 624V/\lambda_0^3$ or $G_\Lambda B \leqslant 0.19$ for $V = 1\,\mathrm{cm}^3$ and center frequency $\mathrm{c}_0/\lambda_0 = 2\,\mathrm{GHz}$. The corresponding bound on the quotient D/Q differ only by a factor of π, *i.e.*, $D/Q \leqslant 0.059$.

It is interesting to note that the pertinent point group symmetries of the Platonic solids are preserved if their geometries are altered appropriately. Such symmetric changes yield a large class of geometries for which $\boldsymbol{\gamma}_\infty$ is isotropic and the upper bound on $G_\Lambda B$ is independent of the polarization. This observation together with the fact that the variational principle discussed above also can be applied to arbitrary isotropic high-contrast polarizability dyadics, are particularly interesting from a MIMO-perspective, see Ref. 10 and references therein.

7.2 Comparison with the sphere

From the discussion of the polarizability dyadics in Ref. 19, it is clear that both γ_1 and γ_2 are directly proportional to the volume of the antenna with a purely geometry dependent proportionality factor. For the circular disk, it follows from App. G that even though the volume of the disk vanishes, the eigenvalues γ_1 and γ_2 are non-zero. This result is due to the fact that the geometry dependent proportionality factors $1/L_1$ and $1/L_2$ approach infinity in the limit as the semi-axis ratio approaches zero. In other words, it is not sufficient to only consider the volume part of γ_1 and γ_2 to draw conclusions of the potential in antenna performance for a given volume. In addition, also the shape dependent proportionality factor must be taken into account.

Motivated by the discussion above, it is interesting to compare γ_1 and γ_2 for the different geometries discussed in Secs. 7 and 8, and in Ref. 8. The comparison refers

to the smallest circumscribing sphere with radius a, for which γ_1 and γ_2 are equal to $4\pi a^3$, see Ref. 8. For this purpose, introduce $\gamma_1/4\pi a^3$, which, in the case of pure electric material properties, yields a direct measure of the antenna performance in terms of (3.7) and (4.6). The main question addressed in this section is therefore: how much antenna performance can be gained for a given geometry by instead utilizing the full volume of the smallest circumscribing sphere?

In Fig. 7, the goodness number $\gamma_1/4\pi a^3$ are presented for the sphere, circular disk, toroidal ring, and prolate and cylindrical needles, respectively. The generalized semi-axis ratio[4] for the toroidal ring and the prolate and cylindrical needles are $\xi = 10^{-3}$. The values for the prolate needle and the toroidal ring are given by (G.3) and (H.9), respectively, while the cylindrical needle is based on FEM simulation for the dipole antenna in Sec. 8.1. The value for the circular disk is $4/3\pi \approx 0.42$ given by (G.4).

The results in Fig. 7 should be compared with the corresponding values in Fig. 6 for the Platonic solids. For example, it is seen that the potential of utilizing the tetrahedron is about 20.5% compared to the smallest circumscribing sphere. Since the high-contrast polarizability dyadics $\boldsymbol{\gamma}_\infty$ are isotropic for the Platonic solids and the sphere, it follows that the results in Fig. 6 also hold for the second and third eigenvalues, γ_2 and γ_3, respectively. This is however not the case for the geometries depicted in Fig. 7 since the circular disk, toroidal ring, and the prolate and cylindrical needles have no isotropic high-contrast polarizability dyadics. For the circular disk and the toroidal ring, γ_1 and γ_2 are equal, and therefore yield the same results as in Fig. 7 for combined electric and magnetic material properties.

In Fig. 7, it is seen that the physical bounds on $G_\Lambda B$ and D/Q for any two-dimensional antenna confined to the circular disk corresponds to about 42% of the potential to utilize the full sphere. This result is rather surprising since, in contrast to the sphere, the circular disk has zero volume. In other words, there is only a factor of $1/0.42 \approx 2.4$ to gain in antenna performance by utilizing three-dimensions compared to two for a given maximum dimension a of the antenna. Since the prolate and cylindrical needles vanish in the limit as the semi-axis ratio approaches zero, the performance of any one-dimensional antenna restricted to the line is negligible as compared to the performance of an antenna in the sphere.

Since γ_1 and γ_2 in the right hand side of (3.7) and (4.6) are determined from separate electric and magnetic problems in the long wavelength limit, see App. B, it is clear that electric and magnetic material properties, and hence also γ_1 and γ_2, can be combined separately. For example, any antenna with magnetic properties confined to the circular disk and electric properties confined to the toroidal ring has a potential which is $100(0.42 + 0.24) = 66\%$ of the sphere with no magnetic material properties present.

[4]The generalized semi-axis ratio for the cylindrical needle and the toroidal ring are defined by $\xi = b/a$, where a and b are given in Figs. 9 and 11, respectively.

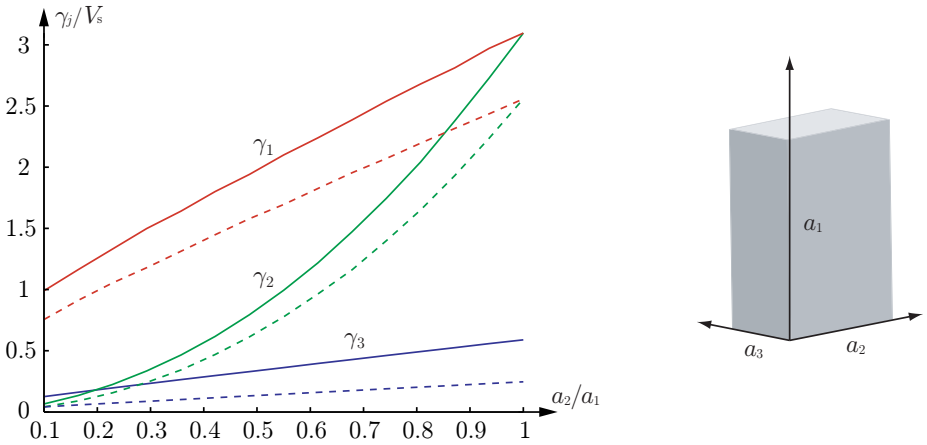

Figure 8: The eigenvalues γ_1, γ_2 and γ_3 as function of the ratio a_2/a_1 for a rectangular parallelepiped of edge lengths a_1, a_2 and a_3. The solid curves are for $a_1/a_3 = 5$ and the dotted curve is for $a_1/a_3 = 10$. Note the normalization with the volume $V_s = \pi a_1^3/6$ of the sphere of radius $a_1/2$.

7.3 The rectangular parallelepiped

The rectangular parallelepiped is a generic geometry that can be used to model, *e.g.*, mobile phones, laptops, and PDAs. The eigenvalues γ_1, γ_2 and γ_3 for a rectangular parallelepiped with edge lengths a_1, a_2 and a_3 are shown in Fig. 8 as a function of the ratio a_2/a_1. The solid and dotted curves correspond to $a_1/a_3 = 5$ and $a_1/a_3 = 10$, respectively. The eigenvalues are ordered $\gamma_1 \geqslant \gamma_2 \geqslant \gamma_3$ and the principal axes of the eigenvalues γ_i correspond to the directions parallel to a_i if $a_1 \geqslant a_2 \geqslant a_3$. The eigenvalues degenerate if the lengths of the corresponding edges coincide.

The performance of any non-magnetic antenna inscribed in the parallelepiped is limited as shown by (3.6) with $\boldsymbol{\gamma}_m = \mathbf{0}$. Specifically, the bounds on antennas polarized in the a_i direction are given by the eigenvalue, γ_i. Obviously, it is advantageous to utilize the longest dimension of the parallelepiped for the polarization of single port antennas. The bound (3.6) also quantifies the degradation in using the other directions for the polarization. This is useful for the understanding of fundamental bounds and synthesis of MIMO antennas.

For example, a typical mobile phone is approximately 10 cm high, 5 cm wide, and 1 cm to 2 cm thick. The corresponding eigenvalues γ_1, γ_2 and γ_3 for $a_1 = 10$ cm are seen in Fig. 8 for $a_3 = 2$ cm (solid lines) and $a_3 = 1$ cm (broken lines). The distribution of the eigenvalues γ_1, γ_2 and γ_3 quantifies the trade off between pattern and polarization diversity for multiple antennas systems in the mobile phone. Pattern diversity utilizes the largest eigenvalue but requires an increased directivity at the cost of bandwidth (3.6). Similarly, polarization diversity utilizes at least two eigenvalues. It is observed that it is advantageous to use polarization and pattern diversity for $a_2 \approx a_1$ and $a_2 \ll a_1$, respectively. For a mobile phone where $a_2 \approx a_1/2$, either pattern diversity or a combined pattern and polarization diversity as linear combinations of the a_1 and a_2 directions can be used. Moreover, note that magnetic

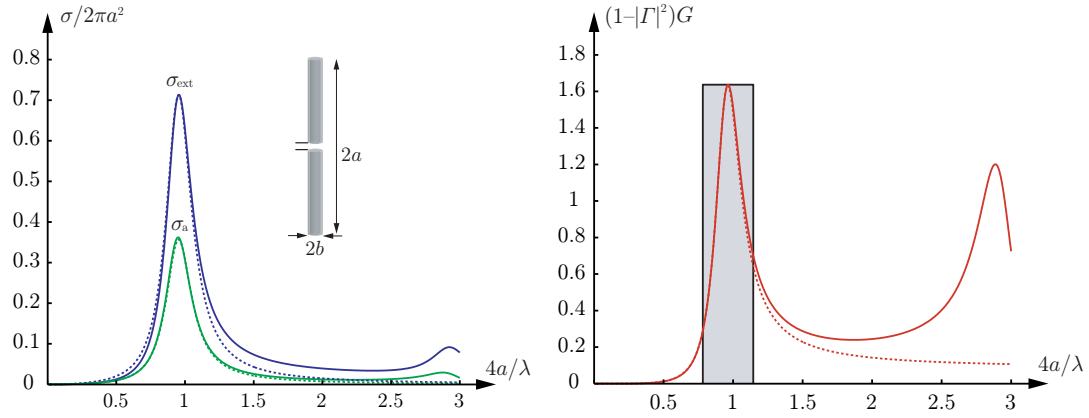

Figure 9: The extinction and absorption cross sections (left figure) and the realized gain (right figure) for a cylindrical dipole antenna with axial ratio $b/a = 10^{-3}$. The different curves correspond to Hallén's integral equation (solid curves), directivity and Q-value bound (4.6) (dashed curves), and gain and bandwidth bound (3.7) (shaded box).

materials, increase the bound (3.6) and offer additional possibilities.

8 Analysis of some classical antennas

In this section, numerical simulations of some classical antennas are presented and analyzed in terms of the physical bounds discussed in Sec. 3.

8.1 The dipole antenna

The cylindrical dipole antenna is one of the simplest and most well known antennas. Here, the MoM solution of the Hallén's integral equation in Ref. 11 together with a gap feed model is used to determine the cross sections and impedance for a cylindrical dipole antenna with axial ratio $b/a = 10^{-3}$. The extinction and absorption cross sections and the realized gain are depicted in Fig. 9. The antenna is resonant at $2a \approx 0.48\lambda$ with directivity $D = 1.64$ and radiation resistance $73\,\Omega$. The half-power bandwidth is $B = 25\%$ and the corresponding Q-value is estimated to $Q = 8.3$ by numerical differentiation of the impedance, see Ref. 25. The absorption efficiency η is depicted in Fig. 10. It is observed that $\eta \approx 0.5$ at the resonance frequency and $\widetilde{\eta} = 0.52$ for $0 \leqslant 4a/\lambda \leqslant 3$.

The MoM solution is also used to determine the forward scattering properties of the antenna. The forward scattering is represented by the extinction volume ϱ in Fig. 10. Recall that $\varrho(0)$ and $\operatorname{Im}\varrho$ directly are related to the polarizability dyadics and the extinction cross section, see Sec. 3.

Moreover, since $\operatorname{Re}\varrho \approx 0$ at the resonance frequency, it follows that the real-valued part of the forward scattering is negligible at this frequency. This observation is important in the understanding of the absorption efficiency of antennas, see Ref. 2.

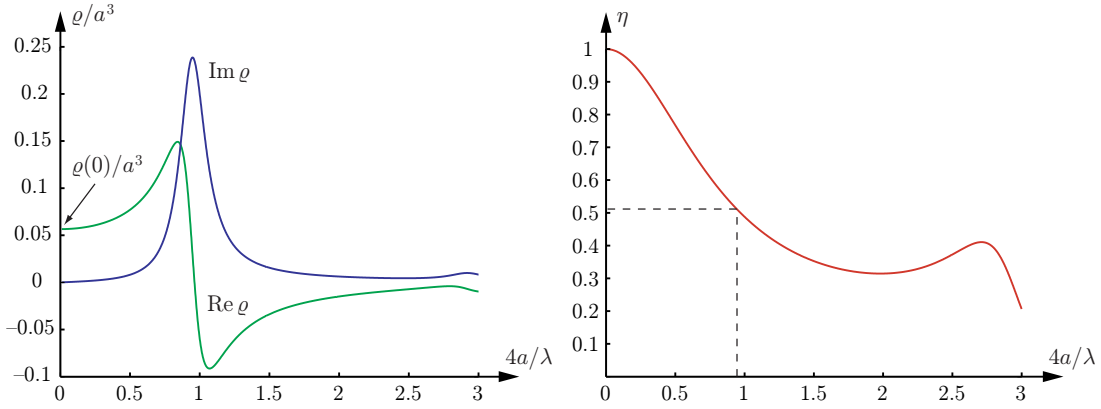

Figure 10: The extinction volume ϱ (left figure) and the absorption efficiency η (right figure) as function of $4a/\lambda$ for the dipole antenna.

FEM simulations are used to determine the polarizability dyadic and the eigenvalues of the cylindrical region in Fig. 9. The eigenvalue γ_1, corresponding to a polarization along the dipole, is $\gamma_1 = 0.71a^3$ and the other eigenvalues $\gamma_2 = \gamma_3$ are negligible. The result agrees with the integrated extinction (2.3) of the MoM solution within 2% for $0 \leqslant 4a/\lambda \leqslant 3$.

The eigenvalues $\gamma_1 = 0.71a^3$ and $\gamma_2 = 0$ inserted into (4.6) give physical bounds on the quotient D/Q of any resonant antenna confined to the cylindrical region, *i.e.*,

$$\sup_{\hat{\boldsymbol{p}}_{\mathrm{e}}\cdot\hat{\boldsymbol{p}}_{\mathrm{m}}=0} \frac{D}{Q} \leqslant \widetilde{\eta}\frac{k_0^3\gamma_1}{2\pi} \approx 0.39\widetilde{\eta}. \tag{8.1}$$

The corresponding bound on the Q-value is $Q \geqslant 8.1$, if $D = 1.64$ and $\widetilde{\eta} = 0.52$ are used. In Fig. 9, it is observed that the single resonance model (dashed curves) with $Q = 8.5$ is a good approximation of the cross sections and realized gain. The corresponding half-power bandwidth is 24%. The eigenvalue γ_1 also gives a bound on the product $G_\Lambda B$ in (3.7) as illustrated with the rectangular region in the right figure for an arbitrary minimum scattering antenna ($\widetilde{\eta} = 0.5$). The realized gain $G_\Lambda = 1.64$ gives the relative bandwidth $B = 38\%$.

It is also illustrative to compare the physical bounds with the MoM simulation for a short dipole. The resonance frequency of the dipole is reduced to $2a \approx 0.2\lambda$ with an inductive loading of 5 μH connected in series with the dipole. The MoM impedance computations of the short dipole give the half-power bandwidth $B = 1.4\%$ and the radiation resistance 8 Ω. The D/Q bound (4.6) gives $Q \geqslant 110$ for the directivity $D = 1.52$ and an absorption efficiency $\widetilde{\eta} = 1/2$ corresponding to the half-power bandwidth $B \leqslant 1.8\%$.

Obviously, the simple structure of the dipole and the absence of broadband matching networks make the resonance model favorable. The bound (4.6) is in excellent agreement with the performance of the dipole antenna for the absorption efficiency $\widetilde{\eta} = 0.52$, *i.e.*, $Q \geqslant 8.1$ from (4.6) compared to $Q = 8.3$ from the MoM solution. The $G_\Lambda B$ bound overestimates the bandwidth, but a broadband matching network can be used to enhance the bandwidth of the dipole, see Ref. 6.

Observe that the dipole antenna has a circumscribing sphere with $ka \approx 1.5$ and is not considered electrically small according to the Chu bounds in Ref. 4. The corresponding limit for the $2a \approx 0.2\lambda_0$ dipole ($ka \approx 0.63$ and $D = 1.52$) is $Q \geqslant 5.6$ and the half-power bandwidth of $36\% \gg 1.4\%$. In conclusion, the dipole utilizes the cylindrical region very efficiently but obviously not the spherical region.

8.2 The loop antenna

The magnetic counterpart to the dipole antenna in Sec. 8.1 is the loop antenna. The geometry of the loop antenna is conveniently described in toroidal coordinates, see Sec. H. Laplace's equation separates in the toroidal coordinate system and hence permits an explicit calculation of the high-contrast polarizability dyadic $\boldsymbol{\gamma}_\infty$. In this section the attention is restricted to the loop antenna of vanishing thickness and non-magnetic material properties. Under the assumptions of vanishing thickness, the analysis in Sec. H yields closed-form expressions of the eigenvalues γ_1, γ_2 and γ_3. Recall that the loop antenna coincides with the magnetic dipole in the long wavelength limit $a/\lambda \ll 1$.

In order to quantify the vanishing thickness limit, introduce the semi-axis ratio $\xi = b/a$, where a and b denote the axial and cross section radii, respectively, see Fig. 11. The three eigenvalues $\gamma_1 = \gamma_2$ and γ_3 are seen to vanish in the limit $\xi \to 0$. However, γ_1 and γ_2 vanish slower than γ_3, see Sec. H. The eigenvalues in the limit $\xi \to 0$ inserted into (4.5) yields

$$\frac{D}{Q} \leqslant \pi k_0^3 a^3 \frac{f(\theta)}{\ln 2/\xi - 1} + \mathcal{O}(\xi^2) \quad \text{as } \xi \to 0, \tag{8.2}$$

where $f(\theta) = 1$ for the TE- and $f(\theta) = \cos^2\theta$ for the TM-polarization. Here, $\theta \in [0, \pi]$ is the polar angle measured from the z-axis of symmetry in Fig. 11. Note that the logarithmic singularity in (8.2) is the same as for the dipole antenna, see Sec. H. Since the axial radius a is the only length scale that is present in the loop antenna in the limit $\xi \to 0$, it is natural that γ_1, γ_2, and γ_3 are proportional to a^3, see App. B.

By comparing the discussion above with the results in Ref. 8 and Sec. 8.1, it is concluded that there is a strong equivalence between the electric and magnetic dipoles. For the most advantageous polarization the upper bound on $G_\Lambda B$ is a factor of $3\pi/2$ larger for the loop antenna compared to the electric dipole.

The results are exemplified for a self-resonant loop with $k_0 a = 1.1$ and a capacitively loaded loop, $C = 10\,\text{pF}$, with $k_0 a = 0.33$, both with $\xi = 0.01$. The corresponding bounds (4.6) are $D/Q \leqslant 0.95\bar{\eta}$ and $D/Q \leqslant 0.025\bar{\eta}$, respectively. The MoM is used to determine the impedance and realized gain of the loop antenna with a gap feed at $\phi = 0$, see Fig. 11. The Q-value of the self-resonant antenna is estimated to $Q = 5$ from numerical differentiation of the impedance, see Ref. 25. The corresponding main beam is in the $\hat{\boldsymbol{z}}$-direction with a directivity $D = 2.36$ giving $D/Q = 0.47$. Similarly, the tuned loop has $Q \approx 164$ and $D = 1.43$ in $\theta = 90^\circ$ and $\phi = 90^\circ$ giving $D/Q \approx 0.0086$.

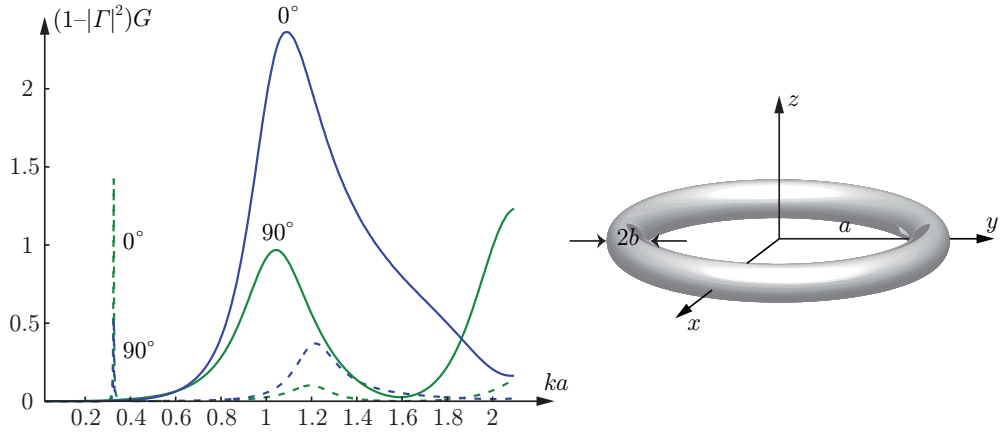

Figure 11: The realized partial gain of two loop antennas for $\theta = 0°, 90°$. One self resonant ($ka \approx 1$) and one capacitively tuned to $ka \approx 1/3$.

It is observed that the physical bounds (4.6) of the loops agree well with the MoM results. This difference can be reduced by introducing the appropriate absorption efficiency in the physical bound. The corresponding results for the Chu bound are $D/Q \leqslant 2.3$ for $k_0a = 1.1$ and $D/Q \leqslant 0.18$ for $k_0a = 0.33$, where the combined TE- and TM-case have been used as the loops are not omnidirectional, see Refs. 4 and 13.

8.3 Conical antennas

The bandwidth of a dipole antenna increases with the thickness of the antenna. The bandwidth can also be increased with conical dipoles, *i.e.*, the biconical antenna. The corresponding conical monopole and discone antennas are obtained by replacing one of the cones with a ground plane, see Ref. 21.

In Fig. 12, the eigenvalues $\gamma_x = \gamma_y$ and γ_z, corresponding to horizontal and vertical polarizations, respectively, are shown as a function of the ground plane radius, b, for the conical monopoles with angles $\theta = 10°$ and $30°$. The eigenvalues are normalized with a^3, where a is the height of the cone. It is observed that the eigenvalues increase with the radius, b, of the ground plane and the cone angle θ. This is a general result as the polarizability dyadic is non-decreasing with increasing susceptibilities, see Ref. 19.

The horizontal eigenvalues $\gamma_x = \gamma_y$ are dominated by the ground plane and increase approximately as b^3 according to the polarizability of the circular disk, see App. C. The vertical eigenvalue γ_z approaches $\gamma_{bz}/2$ as $b \to \infty$, where γ_{bz} denotes the vertical eigenvalue of the corresponding biconical antenna.

It is interesting to compare the D/Q estimate (4.6) for the biconical antenna and conical monopole antenna with a large but finite ground plane. The vertical eigenvalue γ_z of the conical monopole antenna is approximately half of the corresponding eigenvalue of the biconiocal antenna and the Q-values of the two antennas are similar. The physical bound on the directivity in the $\theta = 90°$ direction of the conical

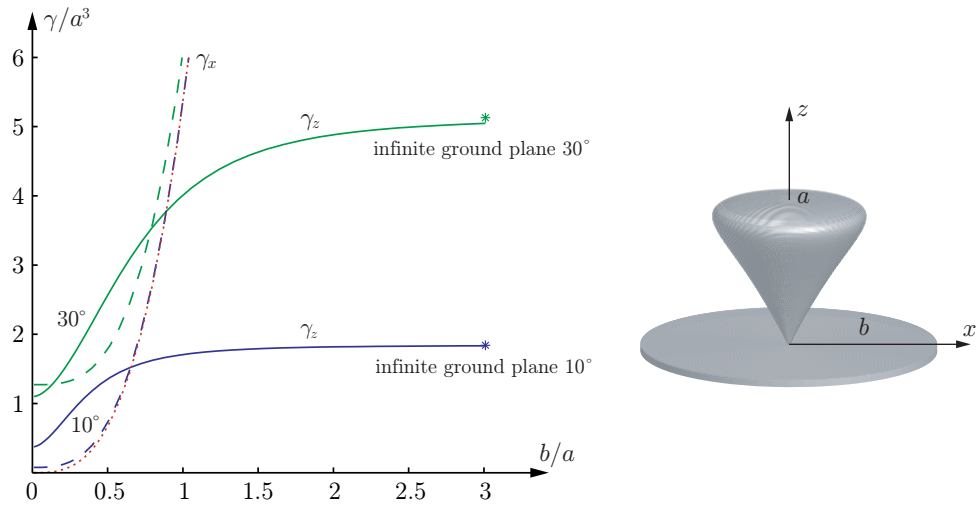

Figure 12: The vertical and horizontal eigenvalues γ_z and γ_x as function of the radius b for a biconical antenna of half vertex angle 10° and 30°, respectively.

monopole is hence half of the directivity of the corresponding biconical antenna. This might appear contradictory as it is well known that the maximal directivity of a monopole is approximately twice the directivity of the corresponding dipole. However, the $\theta = 90°$ direction is on the border between the illuminated and the shadow regions. The integral representation of the far field shows that the induced ground-plane currents do not contribute to the far field in this direction, implying that the directivity is reduced a factor of four as suggested by the physical bounds, see App. D.

The rapid increase in $\gamma_x = \gamma_y$ with the radius of the ground plane suggests that it is advantageous to utilize the polarization in the theses directions. This is done by the discone antenna that has an omnidirectional pattern with a maximal directivity above $\theta = 90°$.

9 Conclusion and future work

In this paper, physical bounds on reciprocal antennas of arbitrary shape are derived based on the holomorphic properties of the forward scattering dyadic. The results are very general in the sense that the underlying analysis solely depends on energy conservation and the fundamental principles of linearity, time-translational invariance, and causality. Several deficiencies and drawbacks of the classical bounds of Chu and Wheeler in Refs. 4 and 24 are overcomed with this new formulation. The main advantages of the new bounds are at least fivefold: 1) they hold for arbitrary antenna geometries; 2) they are formulated in the gain and bandwidth as well as the directivity and the Q-value; 3) they permit study of polarization effects such as diversity in applications for MIMO communication systems; 4) they successfully separate electric and magnetic antenna properties in terms of the intrinsic material parameters; 5) they are isoperimetric from a practical point of view in the sense

that for some geometries, physical antennas can be realized which yield equality in the bounds.

The main results of the present theory are the bounds on the partial realized gain and partial directivity in (3.5) and (4.5), respectively. Since the upper bounds in (3.5) and (4.5) are proportional to $k_0^3 a^3$, where a denotes the radius of, say, the volume equivalent sphere, it is clear that no broadband electrically small antennas exist unless gain or directivity is sacrificed for bandwidth or Q-value. This is also the main conclusion in Ref. 13, but there presented on more vague grounds. Furthermore, the present theory suggests that, in addition to electric material properties, also magnetic materials could be invoked in the antenna design to increase the performance, *cf.*, the ferrite loaded loop antenna in Ref. 5.

In contrast to the classical results by Chu and Wheeler in Refs. 4 and 24, these new bounds are believed to be isoperimetric in the sense that the bounds hold for some physical antenna. A striking example of the intrinsic accuracy of the theory is illustrated by the dipole antenna in Sec. 8.1. In fact, many wire antennas are believed to be close to the upper bounds since these antennas make effective use of their volumes.

It is important to remember that a priori knowledge of the absorption efficiency $\eta = \sigma_{\mathrm{a}}/\sigma_{\mathrm{ext}}$ can sharpen the bounds in (3.5) and (4.5), *cf.*, the half-wave dipole antenna in Sec. 8.1 for which $\widetilde{\eta} \approx 1/2$ is used. Similarly, a priori knowledge of the radiation efficiency, η_{r}, can be used to improve the estimate in (3.3) using $G = \eta_{\mathrm{r}} D$.

The performance of an arbitrary antenna can be compared with the upper bounds in Secs. 3 and 4 using either the method of moments (MoM) or the finite difference time domain method (FDTD). For such a comparison, it is beneficial to determine the integrated extinction and compare the result using (2.3) rather than (3.5) and (4.5). The reason for this is that the full absorption and scattering properties are contained within (2.3) in contrast to (3.5) and (4.5). In fact, (2.3) is the fundamental physical relation and should be the starting point of much analysis.

In addition to the broadband absorption efficiency $\widetilde{\eta}$, several implications of the present theory remains to investigate. Future work include the effect of non-simple connected geometries (array antennas) and its relation to capacitive coupling, and additional analysis of classical antennas. From a wireless communication point of view it is also interesting to investigate the connection between the present theory and the concept of correlation and capacity in MIMO communication systems. Some of the problems mentioned here will be addressed in forthcoming papers.

Acknowledgment

The financial support by the Swedish Research Council and the SSF Center for High Speed Wireless Communication are gratefully acknowledged. The authors are also grateful for fruitful discussions with Anders Karlsson and Anders Derneryd at Dept. of Electrical and Information Technology, Lund University, Sweden.

Appendix A Details on the derivation of (2.3)

Consider a plane-wave excitation $\boldsymbol{E}_{\mathrm{i}}(\mathrm{c}_0 t - \hat{\boldsymbol{k}} \cdot \boldsymbol{x})$ incident in the $\hat{\boldsymbol{k}}$-direction, see Fig. 1. In the far field region, the scattered electric field $\boldsymbol{E}_{\mathrm{s}}$ is described by the far field amplitude $\boldsymbol{F}$ as

$$\boldsymbol{E}_{\mathrm{s}}(t, \boldsymbol{x}) = \frac{\boldsymbol{F}(\mathrm{c}_0 t - x, \hat{\boldsymbol{x}})}{x} + \mathcal{O}(x^{-2}) \quad \text{as } x \to \infty, \tag{A.1}$$

where c_0 denotes the speed of light in vacuum, and $\hat{\boldsymbol{x}} = \boldsymbol{x}/x$ with $x = |\boldsymbol{x}|$. The far field amplitude $\boldsymbol{F}$ in the forward direction $\hat{\boldsymbol{k}}$ is assumed to be causal and related to the incident field $\boldsymbol{E}_{\mathrm{i}}$ via the linear and time-translational invariant convolution

$$\boldsymbol{F}(\tau, \hat{\boldsymbol{k}}) = \int_{-\infty}^{\tau} \mathbf{S}_{\mathrm{t}}(\tau - \tau', \hat{\boldsymbol{k}}, \hat{\boldsymbol{k}}) \cdot \boldsymbol{E}_{\mathrm{i}}(\tau') \, \mathrm{d}\tau'. \tag{A.2}$$

Here, $\tau = \mathrm{c}_0 t - x$ and $\mathbf{S}_{\mathrm{t}}$ is the appropriate dimensionless temporal dyadic.

Introduce the forward scattering dyadic $\mathbf{S}$ as the Fourier transform of $\mathbf{S}_{\mathrm{t}}$ evaluated in the forward direction, *i.e.*,

$$\mathbf{S}(k, \hat{\boldsymbol{k}}) = \int_{0^-}^{\infty} \mathbf{S}_{\mathrm{t}}(\tau, \hat{\boldsymbol{k}}, \hat{\boldsymbol{k}}) \mathrm{e}^{\mathrm{i}k\tau} \, \mathrm{d}\tau, \tag{A.3}$$

where k is complex-valued with $\operatorname{Re} k = \omega/\mathrm{c}_0$. Recall that $\mathbf{S}(\mathrm{i}k, \hat{\boldsymbol{k}})$ is real-valued for real-valued k and that the crossing symmetry $\mathbf{S}(k, \hat{\boldsymbol{k}}) = \mathbf{S}^*(-k^*, \hat{\boldsymbol{k}})$ holds for complex-valued k. For a large class of temporal dyadics $\mathbf{S}_{\mathrm{t}}$, the elements of $\mathbf{S}$ are holomorphic in the upper half plane $\operatorname{Im} k > 0$.

From the analysis above, it follows that the Fourier transform of (A.1) in the forward direction reads

$$\boldsymbol{E}_{\mathrm{s}}(k, x\hat{\boldsymbol{k}}) = \frac{\mathrm{e}^{\mathrm{i}kx}}{x} \mathbf{S}(k, \hat{\boldsymbol{k}}) \cdot \boldsymbol{E}_0 + \mathcal{O}(x^{-2}) \quad \text{as } x \to \infty, \tag{A.4}$$

where $\boldsymbol{E}_0$ is the Fourier amplitude of the incident field. Introduce the extinction volume $\varrho(k) = \hat{\boldsymbol{p}}_{\mathrm{e}}^* \cdot \mathbf{S}(k, \hat{\boldsymbol{k}}) \cdot \hat{\boldsymbol{p}}_{\mathrm{e}}/k^2$, where $\hat{\boldsymbol{p}}_{\mathrm{e}} = \boldsymbol{E}_0/|\boldsymbol{E}_0|$ and $\hat{\boldsymbol{p}}_{\mathrm{m}} = \hat{\boldsymbol{k}} \times \hat{\boldsymbol{p}}_{\mathrm{e}}$ denote the electric and magnetic polarizations, respectively. Since the elements of $\mathbf{S}$ are holomorphic in k for $\operatorname{Im} k > 0$, it follows that also the extinction volume ϱ is a holomorphic function in the upper half plane. The Cauchy integral theorem with respect to the contour in Fig. 13 then yields

$$\varrho(\mathrm{i}\varepsilon) = \int_0^{\pi} \frac{\varrho(\mathrm{i}\varepsilon - \varepsilon \mathrm{e}^{\mathrm{i}\phi})}{2\pi} \, \mathrm{d}\phi + \int_0^{\pi} \frac{\varrho(\mathrm{i}\varepsilon + R\mathrm{e}^{\mathrm{i}\phi})}{2\pi} \, \mathrm{d}\phi + \int_{\varepsilon<|k|<R} \frac{\varrho(k + \mathrm{i}\varepsilon)}{2\pi \mathrm{i}k} \, \mathrm{d}k. \tag{A.5}$$

Here, it is assumed that the extinction volume ϱ is sufficiently regular to extend the contour to the real-axis in the last integral on the right hand side of (A.5). Relation (A.5) is subject to the limits as $\varepsilon \to 0$ and $R \to \infty$.

The left hand side of (A.5) and the integrand in the first integral on the right hand side are well-defined in the limit as $\varepsilon \to 0$. For a sufficiently regular ϱ in the vicinity of the origin, the analysis in Ref. 14 yield

$$\varrho(\mathrm{i}\varepsilon) = \frac{1}{4\pi} (\hat{\boldsymbol{p}}_{\mathrm{e}}^* \cdot \boldsymbol{\gamma}_{\mathrm{e}} \cdot \hat{\boldsymbol{p}}_{\mathrm{e}} + \hat{\boldsymbol{p}}_{\mathrm{m}}^* \cdot \boldsymbol{\gamma}_{\mathrm{m}} \cdot \hat{\boldsymbol{p}}_{\mathrm{m}}) + \mathcal{O}(\varepsilon) \quad \text{as } \varepsilon \to 0. \tag{A.6}$$

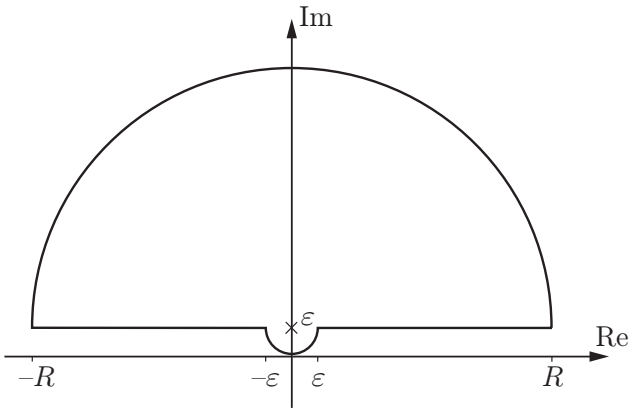

Figure 13: Integration contour in the complex k-plane used in (A.5).

Here, $\boldsymbol{\gamma}_{\mathrm{e}}$ and $\boldsymbol{\gamma}_{\mathrm{m}}$ denote the electric and magnetic polarizability dyadics in App. B. Since the short wavelength response of a material is non-unique from a modeling point of view, see Ref. 9, the second term on the right hand side of (A.5) is assumed to approach zero in the limit $R \to \infty$. In fact, for a large class of temporal dyadics $\mathbf{S}_{\mathrm{t}}$, the integrand $\varrho(\mathrm{i}\varepsilon + R\mathrm{e}^{\mathrm{i}\phi})/2\pi$ is proportional to the projected area A in the forward direction, *viz.*,

$$\varrho(k) = -\frac{A(\hat{\boldsymbol{k}})}{2\pi \mathrm{i}k} + \mathcal{O}(|k|^{-2}) \quad \text{as } |k| \to \infty, \qquad \operatorname{Im} k \geqslant 0. \tag{A.7}$$

The asymptotic behavior (A.7) is known as the extinction paradox, see Ref. 23. The constant A is real-valued since $\mathbf{S}(\mathrm{i}k, \hat{\boldsymbol{k}})$ is real-valued for real-valued k.

In order to proceed, the scattering, absorption and extinction cross sections are introduced. The scattering cross section σ_{s} and absorption cross section σ_{a} are defined as the ratio of the scattered and absorbed power, respectively, to the incident power flow density in the forward direction. The sum of the scattering and absorption cross sections is the extinction cross section $\sigma_{\mathrm{ext}} = \sigma_{\mathrm{s}} + \sigma_{\mathrm{a}}$. The three cross sections σ_{s}, σ_{a} and σ_{ext} are by definition real-valued and non-negative. The principle of energy conservation takes the form as a relation between the extinction volume ϱ and the extinction cross section. The relation is known as the optical theorem, see Refs. 16 and 22,

$$\sigma_{\mathrm{ext}}(k) = 4\pi k \operatorname{Im} \varrho(k), \tag{A.8}$$

where k is real-valued.

In summary, the real part of (A.5) subject to the limits $\varepsilon \to 0$ and $R \to \infty$ yields

$$\varrho(0) = \frac{1}{\pi} \int_{-\infty}^{\infty} \frac{\operatorname{Im} \varrho(k)}{k} \, \mathrm{d}k. \tag{A.9}$$

The optical theorem (A.8) applied to (A.9) then implies

$$\varrho(0) = \frac{1}{4\pi^2} \int_{-\infty}^{\infty} \frac{\sigma_{\mathrm{ext}}(k)}{k^2} \, \mathrm{d}k = \frac{1}{4\pi^3} \int_{0}^{\infty} \sigma_{\mathrm{ext}}(\lambda) \, \mathrm{d}\lambda, \tag{A.10}$$

where the wavelength $\lambda = 2\pi/k$ has been introduced. Hence, invoking (A.6) finally yields the integrated extinction

$$\int_0^\infty \sigma_{\mathrm{ext}}(\lambda)\ \mathrm{d}\lambda = \pi^2\,(\hat{\boldsymbol{p}}_{\mathrm{e}}^* \cdot \boldsymbol{\gamma}_{\mathrm{e}} \cdot \hat{\boldsymbol{p}}_{\mathrm{e}} + \hat{\boldsymbol{p}}_{\mathrm{m}}^* \cdot \boldsymbol{\gamma}_{\mathrm{m}} \cdot \hat{\boldsymbol{p}}_{\mathrm{m}})\,. \tag{A.11}$$

In fact, the already weak assumptions on the extinction volume ϱ in the analysis above can be relaxed via the introduction of certain classes of distributions, see Ref. 17.

Appendix B The polarizability dyadics

Let $\boldsymbol{\tau}$ denote a finite material dyadic ($\boldsymbol{\chi}_{\mathrm{e}}$ without a conductivity term, or $\boldsymbol{\chi}_{\mathrm{m}}$) with compact support. The entries of the polarizability dyadic $\boldsymbol{\gamma}$ ($\boldsymbol{\gamma}_{\mathrm{e}}$ or $\boldsymbol{\gamma}_{\mathrm{m}}$ depending on whether the problem is electric or magnetic) are defined as the volume integral

$$\hat{\boldsymbol{e}}_i \cdot \boldsymbol{\gamma} \cdot \hat{\boldsymbol{e}}_j = \frac{1}{E_0}\hat{\boldsymbol{e}}_i \cdot \int_{\mathbb{R}^3} \boldsymbol{\tau}(\boldsymbol{x}) \cdot \boldsymbol{E}_j(\boldsymbol{x})\ \mathrm{d}v, \qquad i,j = 1,2,3. \tag{B.1}$$

Here, the total field $\boldsymbol{E}$ has been decomposed as $\boldsymbol{E}_j = E_0\hat{\boldsymbol{e}}_j + \boldsymbol{E}_{\mathrm{s}j}$ with respect to the mutually orthonormal vectors $\hat{\boldsymbol{e}}_j$. In the electric and magnetic cases, $\boldsymbol{E}$ represents the electric and magnetic field, respectively.

In the high-contrast limit, when the entries of $\boldsymbol{\tau}$ simultaneously approach infinity uniformly in $\boldsymbol{x}$, the pertinent definition of the high-contrast polarizability dyadic $\boldsymbol{\gamma}_\infty$ is, see Ref. 14,

$$\hat{\boldsymbol{e}}_i \cdot \boldsymbol{\gamma}_\infty \cdot \hat{\boldsymbol{e}}_j = \frac{1}{E_0}\hat{\boldsymbol{e}}_i \cdot \sum_{n=1}^{N} \int_{\mathrm{S}_n} (\hat{\boldsymbol{\nu}}(\boldsymbol{x})\Phi_j(\boldsymbol{x}) - \boldsymbol{x}\hat{\boldsymbol{\nu}}(\boldsymbol{x}) \cdot \nabla\Phi_j(\boldsymbol{x}))\ \mathrm{d}S. \tag{B.2}$$

The surface integral representation (B.2) holds for N disjunct bounding surfaces S_n with outward-directed unit normal vectors $\hat{\boldsymbol{\nu}}$. The potential $\Psi_j(\boldsymbol{x}) = \Phi_j(\boldsymbol{x}) - E_0 x_j$ is for each $n = 1, 2, \ldots, N$ the solution to the boundary value problem

$$\begin{cases} \nabla^2\Psi_j(\boldsymbol{x}) = 0, \quad \boldsymbol{x} \text{ outside } \mathrm{S}_n \\ \displaystyle\int_{\mathrm{S}_n} \hat{\boldsymbol{\nu}}(\boldsymbol{x}) \cdot \nabla\Psi_j(\boldsymbol{x})\ |_+\ \mathrm{d}S = 0 \\ \Psi_j(\boldsymbol{x}) \to -E_0 x_j + \mathcal{O}(|\boldsymbol{x}|^{-2}) \quad \text{as } |\boldsymbol{x}| \to \infty \end{cases} \tag{B.3}$$

The presence of a finite or infinite conductivity term in $\boldsymbol{\chi}_{\mathrm{e}}$ is discussed in Ref. 14. The conclusion is that the electric polarizability dyadic $\boldsymbol{\gamma}_{\mathrm{e}}$ should be replaced by $\boldsymbol{\gamma}_\infty$ independently of the real-part of $\boldsymbol{\chi}_{\mathrm{e}}$ when a conductivity term is present. This may at first seem contradictory, since there is no continuity in the limit as the conductivity vanishes.

In Ref. 19, the polarizability dyadic $\boldsymbol{\gamma}$ is proved to be symmetric provided $\boldsymbol{\tau}$ is symmetric at all points $\boldsymbol{x}$. The dyadic $\boldsymbol{\gamma}$ is real-valued, and hence diagonalizable with real-valued eigenvalues. The corresponding set of orthogonal eigenvectors are

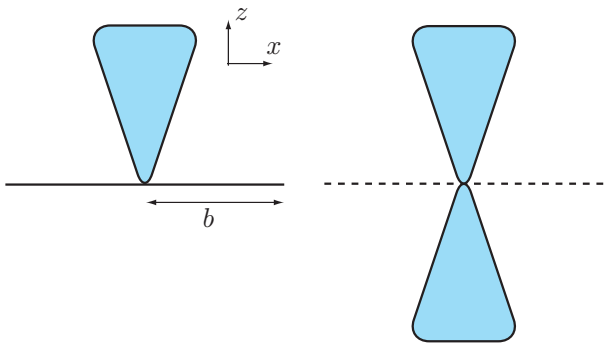

Figure 14: Illustration of an arbitrary antenna volume supported by a ground plane (left figure) and its corresponding mirror object (right figure).

the principal axes of the obstacle under consideration. The principal axes are particularly easy to determine for obstacles with continuous or discrete symmetries, *e.g.*, the ellipsoids and the Platonic solids in Sec. 7.1.

An important property of $\boldsymbol{\gamma}$ which is proved in Ref. 19, is that it is proportional to the volume of the support of $\boldsymbol{\tau}$. This is a direct consequence of the absence of any length scales in the long wavelength limit.

Appendix C Supporting ground planes

Supporting ground planes are central structures in many antenna applications. Consider an arbitrary volume, modeling the antenna, situated above a supporting ground plane of finite or infinite extent, see Fig. 14. To simplify the terminology, use monopole to denote object with a ground plane and dipole to denote the object together with its mirror object. The ground plane is assumed to be a circular disk of radius b with vanishing thickness. Since $\boldsymbol{\gamma}_\infty$ is independent of any coordinate representation, let the ground plane be given by $z = 0$.

For a polarization parallel with the ground plane, *i.e.*, spanned by $\hat{\boldsymbol{e}}_x$ and $\hat{\boldsymbol{e}}_y$, it is clear from the results in App. B of the circular disk that the contribution to $\boldsymbol{\gamma}_\infty$ from the ground plane is large. Indeed, a circular ground plane of radius b yields $\gamma_{\mathrm{x}} = \gamma_{\mathrm{y}} = 16b^3/3$, where γ_{x} and γ_{y} denote the eigenvalues of $\boldsymbol{\gamma}_\infty$ corresponding to the $\hat{\boldsymbol{e}}_x$ and $\hat{\boldsymbol{e}}_y$ directions, respectively (G.4).

The polarizability of the monopole for an electric polarization parallel with the $\hat{\boldsymbol{e}}_z$-direction has one contribution from the charge distribution on the object $z > 0$ and one part from the charge distribution on the ground plane $z = 0$. The contribution from the ground plane vanishes in (B.2) since $z = 0$. For a ground plane of infinite extent the method of images is applicable to determine the charge distribution for $z > 0$. In this method, the ground plane is replaced with a copy of the object placed in the mirror position of the object, *i.e.*, the dipole. The charge distribution is odd in z and the charge distribution for $z > 0$ is identical in the monopole and dipole cases. The polarizability of the dipole is hence exactly twice the polarizability of the corresponding monopole.

The difference between the finite and infinite ground planes is negligible as long as the charge distribution on the monopole can be approximated by the charge distribution in the corresponding dipole case.

Appendix D Directivity along ground planes

The integral representation of the far-field can be used to analyze the directivity of antennas in directions along the supporting ground plane. The pertinent integral representation reads

$$\boldsymbol{F}(\hat{\boldsymbol{r}}) = \frac{\mathrm{i}kZ_0}{4\pi}\int_S \hat{\boldsymbol{r}} \times (\boldsymbol{J}(\boldsymbol{x}) \times \hat{\boldsymbol{r}})\mathrm{e}^{-\mathrm{i}k\hat{\boldsymbol{r}}\cdot\boldsymbol{x}}\,\mathrm{d}S, \tag{D.1}$$

where $\boldsymbol{J}$ and Z_0 denote the induced current and the free space impedance, respectively.

Consider a monopole, *i.e.*, an object on a large but finite ground plane, at $z = 0$ with $\hat{\boldsymbol{e}}_z$ as a symmetry axis, see Fig. 14. The far-field of the monopole (D.1) can be written as a sum of one integral over the ground plane and one integral over the object. Let S_+ and S_0 denote the corresponding surfaces of the object and the ground plane, respectively. Assume that the ground plane is sufficiently large such that the currents on the monopole can be approximated with the currents on the corresponding dipole case for $z > 0$. Moreover, assume that the current is rotationally symmetric and that the current in the ϕ-direction is negligible giving an omni-directional radiation pattern. Hence, it is sufficient to consider the far-field pattern in the $\hat{\boldsymbol{r}} = \hat{\boldsymbol{e}}_x$-direction.

The induced currents on the ground plane are in the radial direction giving the term $\hat{\boldsymbol{e}}_x \times (\boldsymbol{J}(\boldsymbol{x}) \times \hat{\boldsymbol{e}}_x) = \hat{\boldsymbol{e}}_y J_\rho(\rho)\sin\phi$ in (D.1). It is seen that the currents on the ground plane does not contribute to the far field as

$$\boldsymbol{F}(\hat{\boldsymbol{e}}_x) = \hat{\boldsymbol{e}}_y\frac{\mathrm{i}k\eta}{4\pi}\int_{S_0} \mathrm{e}^{-\mathrm{i}k\rho\cos\phi}J_\rho(\rho)\sin\phi\rho\,\mathrm{d}\phi\,\mathrm{d}\rho = \boldsymbol{0}. \tag{D.2}$$

The contribution from the currents on the object can be analyzed with the method of images. From (D.2), it is seen the it is only the currents in the $\hat{\boldsymbol{e}}_z$-direction that contributes to the far field, *i.e.*,

$$\boldsymbol{F}(\hat{\boldsymbol{e}}_x) = \hat{\boldsymbol{e}}_z\frac{\mathrm{i}k\eta}{4\pi}\int_{S_+} \mathrm{e}^{-\mathrm{i}k\rho\cos\phi}J_z(\rho, z)\,\mathrm{d}S, \tag{D.3}$$

where $J_z\hat{\boldsymbol{e}}_z = \hat{\boldsymbol{e}}_x \times (\boldsymbol{J} \times \hat{\boldsymbol{e}}_x)$. The method of images shows that J_z is even in z so the z-directed currents above and below the ground plane give equal contributions to the far field. The directivity of the monopole antenna is hence a quarter of the directivity of the corresponding dipole antenna in the $\hat{\boldsymbol{e}}_x$-direction.

Appendix E Definition of some antenna terms

The following definitions of antenna terms are based on the IEEE standard 145-1993 in Ref. 3. The definitions refer to the electric polarization $\hat{\boldsymbol{p}}_\mathrm{e}$ (co-polarization) rather

than the magnetic polarization $\hat{\boldsymbol{p}}_{\mathrm{m}} = \hat{\boldsymbol{k}} \times \hat{\boldsymbol{p}}_{\mathrm{e}}$ (cross-polarization). The antennas are assumed to reciprocal, *i.e.*, they have similar properties as transmitting and receiving devices.

Absolute gain $G(\hat{\boldsymbol{k}})$. The absolute gain is the ratio of the radiation intensity in a given direction to the intensity that would be obtained if the power accepted by the antenna was radiated isotropically.

Partial gain $G(\hat{\boldsymbol{k}}, \hat{\boldsymbol{p}}_{\mathrm{e}})$. The partial gain in a given direction is the ratio of the part of the radiation intensity corresponding to a given polarization to the radiation intensity that would be obtained if the power accepted by the antenna was radiated isotropically. The absolute gain is equal to the sum of the partial gains for two orthogonal polarizations, *i.e.*, $G(\hat{\boldsymbol{k}}) = G(\hat{\boldsymbol{k}}, \hat{\boldsymbol{p}}_{\mathrm{e}}) + G(\hat{\boldsymbol{k}}, \hat{\boldsymbol{p}}_{\mathrm{m}})$.

Realized gain $G(\hat{\boldsymbol{k}}, \Gamma)$. The realized gain is the absolute gain of an antenna reduced by the losses due to impedance mismatch of the antenna, *i.e.*, $G(\hat{\boldsymbol{k}}, \Gamma) = (1 - |\Gamma|^2) G(\hat{\boldsymbol{k}})$.

Partial realized gain $G(\hat{\boldsymbol{k}}, \hat{\boldsymbol{p}}_{\mathrm{e}}, \Gamma)$. The partial realized gain is the partial gain for a given polarization reduced by the losses due to impedance mismatch of the antenna, *i.e.*, $G(\hat{\boldsymbol{k}}, \hat{\boldsymbol{p}}_{\mathrm{e}}, \Gamma) = (1 - |\Gamma|^2) G(\hat{\boldsymbol{k}}, \hat{\boldsymbol{p}}_{\mathrm{e}})$.

Absolute directivity $D(\hat{\boldsymbol{k}})$. The absolute directivity is the ratio of the radiation intensity in a given direction to the radiation intensity averaged over all directions. The averaged radiation intensity is equal to the total power radiated divided by 4π.

Partial directivity $D(\hat{\boldsymbol{k}}, \hat{\boldsymbol{p}}_{\mathrm{e}})$. The partial directivity in a given direction is the ratio of that part of the radiation intensity corresponding to a given polarization to the radiation intensity averaged over all directions. The averaged radiation intensity is equal to the total power radiated divided by 4π.

Absorption cross section $\sigma_{\mathrm{a}}(\hat{\boldsymbol{k}}, \hat{\boldsymbol{p}}_{\mathrm{e}}, \Gamma)$. The absorption cross section for a given polarization and incident direction is the ratio of the absorbed power in the antenna to the incident power flow density when subject to a plane-wave excitation. For a perfectly matched antenna, the absorption cross section coincides with the partial effective area.

Scattering cross section $\sigma_{\mathrm{s}}(\hat{\boldsymbol{k}}, \hat{\boldsymbol{p}}_{\mathrm{e}}, \Gamma)$. The scattering cross section for a given polarization and incident direction is the ratio of the scattered power by the antenna to the incident power flow density when subject to a plane-wave excitation.

Extinction cross section $\sigma_{\mathrm{ext}}(\hat{\boldsymbol{k}}, \hat{\boldsymbol{p}}_{\mathrm{e}}, \Gamma)$. The extinction cross section for a given polarization and incident direction is the sum of the absorbed and scattered power of the antenna to the incident power flow density when subject to a plane-wave excitation, *i.e.*, $\sigma_{\mathrm{ext}}(\hat{\boldsymbol{k}}, \hat{\boldsymbol{p}}_{\mathrm{e}}, \Gamma) = \sigma_{\mathrm{a}}(\hat{\boldsymbol{k}}, \hat{\boldsymbol{p}}_{\mathrm{e}}, \Gamma) + \sigma_{\mathrm{s}}(\hat{\boldsymbol{k}}, \hat{\boldsymbol{p}}_{\mathrm{e}}, \Gamma)$.

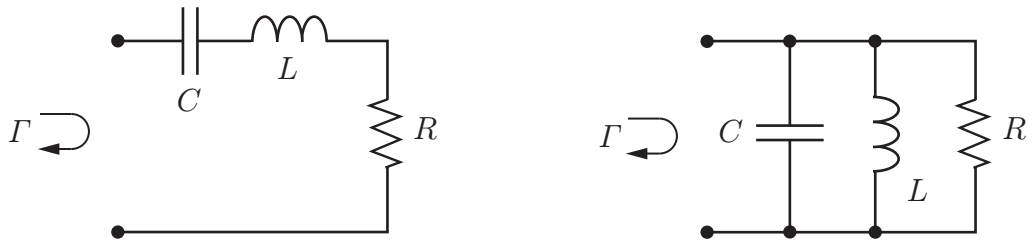

Figure 15: The RCL circuits corresponding to the plus (left figure) and minus (right figure) signs in (F.1).

Absorption efficiency[5] $\eta(\hat{\boldsymbol{k}}, \hat{\boldsymbol{p}}, \Gamma)$**.** The absorption efficiency of an antenna for a given polarization and incident direction is the ratio of the absorbed power to the total absorbed and scattered power when subject to a plane-wave excitation, *i.e.*, $\eta(\hat{\boldsymbol{k}}, \hat{\boldsymbol{p}}_\mathrm{e}, \Gamma) = \sigma_\mathrm{a}(\hat{\boldsymbol{k}}, \hat{\boldsymbol{p}}_\mathrm{e}, \Gamma)/\sigma_\mathrm{ext}(\hat{\boldsymbol{k}}, \hat{\boldsymbol{p}}_\mathrm{e}, \Gamma)$.

Quality value Q**.** The quality factor of a resonant antenna is the ratio of 2π times the energy stored in the fields excited by the antenna to the energy radiated and dissipated per cycle. For electrically small antennas, it is equal to one-half the magnitude of the ratio of the incremental change in impedance to the corresponding incremental change in frequency at resonance, divided by the ratio of the antenna resistance to the resonant frequency.

Appendix F Q-value and bandwidth

The quality factor, or Q-factor, is often used to estimate the bandwidth of an antenna. It is defined as the ratio of the energy stored in the reactive field to the radiated energy, *i.e.*, $Q = 2\omega \max(W_\mathrm{m}, W_\mathrm{e})/P$, see App. E and Refs. 7 and 25. Here, W_e and W_m denote the stored electric and magnetic energies, respectively, P is the dissipated power, and $\omega = kc_0$ the angular frequency. At the resonance, $k = k_0$, there are equal amounts of stored electric and magnetic energy, *i.e.*, $W_\mathrm{e} = W_\mathrm{m}$.

For many applications it is sufficient to model the antenna as a simple RCL resonance circuit around the resonance frequency. The reflection coefficient Γ of the antenna is then given by

$$\Gamma = \frac{Z(k) - R}{Z(k) + R} = \pm \frac{1 - (k/k_0)^2}{1 - (k/k_0)^2 - 2\mathrm{i}k/(k_0 Q)} \tag{F.1}$$

where Z denotes the frequency dependent part of the impedance, and the plus and minus signs in (F.1) correspond to the series and parallel circuits in Fig. 15, respectively. The reflection coefficient Γ is holomorphic in the upper half plane $\mathrm{Im}\,\omega > 0$ and characterized by the poles

$$k = \pm k_0 \sqrt{1 - Q^{-2}} - \mathrm{i}k_0/Q, \tag{F.2}$$

[5]This term is not defined in Ref. 3; the present definition is instead based on Ref. 2.

which are symmetrically distributed with respect to the imaginary axis.

The bandwidth of the resonances in (F.2) depends on the threshold level of the reflection coefficient. The relative bandwidths of half-power, $|\Gamma|^2 \leqslant 0.5$, is given by $B \approx 2/Q$. The corresponding losses due to the antenna mismatch are calculated from

$$1 - |\Gamma|^2 = \frac{1}{1 + Q^2(k/k_0 - k_0/k)^2/4}. \tag{F.3}$$

The definition of the Q-factor in terms of the quotient between stored and radiated energies is however not adequate for the present analysis. This is because the decomposition of the total energy into the stored and dissipated parts is a fundamentally difficult task. As noted in Refs. 7 and 25, the Q-factor at the resonance frequency $k = k_0$ can instead be determined by differentiating the reflection coefficient or impedance, *i.e.*,

$$\left|\frac{\partial \Gamma}{\partial k}\right| = \frac{1}{2R}\left|\frac{\partial Z}{\partial k}\right| = \frac{Q}{k_0}, \tag{F.4}$$

where the derivatives in (F.4) are evaluated at $k = k_0$. Relation (F.4) is exact for the single resonance circuit and is also a good approximation for multiple resonance models if Q is sufficiently large. In Sec. 4, a multiple resonance model is considered for the extinction volume ϱ introduced in App. A. The multiple resonance model is obtained by superposition of single resonance terms with poles of the type (F.2).

Appendix G The depolarizing factors

For the ellipsoids of revolution, *i.e.*, the prolate and oblate spheroids, closed-form expressions of (6.2) exist in terms of the semi-axis ratio $\xi \in [0, 1]$. The result for the prolate spheroid is ($a_2 = a_3$)

$$\begin{cases} L_1(\xi) = \dfrac{\xi^2}{2(1-\xi^2)^{3/2}}\left(\ln\dfrac{1+\sqrt{1-\xi^2}}{1-\sqrt{1-\xi^2}} - 2\sqrt{1-\xi^2}\right) \\ L_2(\xi) = L_3(\xi) = \dfrac{1}{4(1-\xi^2)^{3/2}}\left(2\sqrt{1-\xi^2} - \xi^2 \ln\dfrac{1+\sqrt{1-\xi^2}}{1-\sqrt{1-\xi^2}}\right) \end{cases} \tag{G.1}$$

while for the oblate spheroid ($a_1 = a_2$)

$$\begin{cases} L_1(\xi) = L_2(\xi) = \dfrac{\xi^2}{2(1-\xi^2)}\left(-1 + \dfrac{\arcsin\sqrt{1-\xi^2}}{\xi\sqrt{1-\xi^2}}\right) \\ L_3(\xi) = \dfrac{1}{1-\xi^2}\left(1 - \dfrac{\xi \arcsin\sqrt{1-\xi^2}}{\sqrt{1-\xi^2}}\right) \end{cases} \tag{G.2}$$

The depolarizing factors (G.1) and (G.2) are depicted in Fig. 16. Note that (G.1) and (G.2) differ in indices from the depolarizing factors in Ref. 19 due to the order relation $L_1 \leqslant L_2 \leqslant L_3$ assumed in Sec. 6 in this paper.

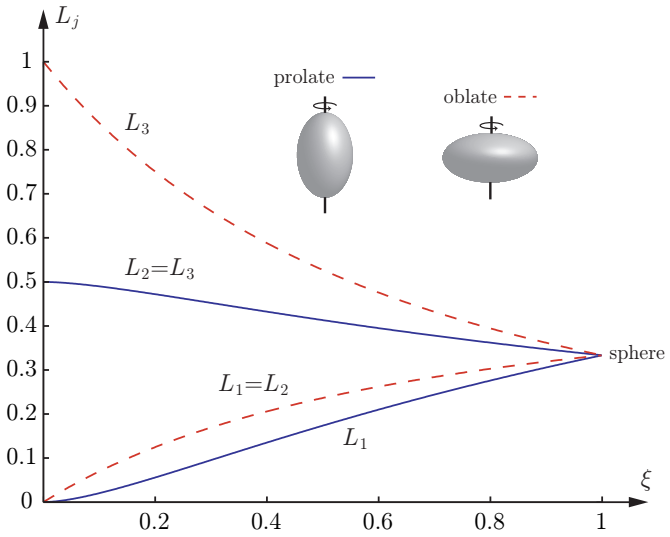

Figure 16: The depolarizing factors for the prolate (solid) and oblate (dashed) spheroids as function of the semi-axis ratio ξ. Note the degeneracy for the sphere.

Introduce the eigenvalues $\gamma_j(\xi) = V(\xi)/L_j(\xi)$ of the high-contrast polarizability dyadic. In terms of the radius a of the smallest circumscribing sphere, the spheroidal volume $V(\xi)$ is given by $\xi^2 4\pi a^3/3$ and $\xi 4\pi a^3/3$ for the prolate and oblate spheroids, respectively. For the analysis in Sec. 6, the limit of $\gamma_j(\xi)$ as $\xi \to 0$ is particular interesting, corresponding to the circular needle for the prolate spheroid and the circular disk for the oblate spheroid. The result for the circular needle reads

$$\begin{cases} \gamma_1(\xi) = \dfrac{4\pi a^3}{3} \dfrac{1}{\ln 2/\xi - 1} + \mathcal{O}(\xi^2) \\ \gamma_2(\xi) = \gamma_3(\xi) = \mathcal{O}(\xi^2) \end{cases} \qquad \text{as } \xi \to 0 \tag{G.3}$$

while for the circular disk,

$$\begin{cases} \gamma_1(\xi) = \gamma_2(\xi) = \dfrac{16a^3}{3} + \mathcal{O}(\xi) \\ \gamma_3(\xi) = \mathcal{O}(\xi) \end{cases} \qquad \text{as } \xi \to 0 \tag{G.4}$$

Closed-form expressions of (6.2) can also be evaluated for the elliptic needle and disk in terms of the complete elliptic integrals of the first and second kind, see Ref. 19.

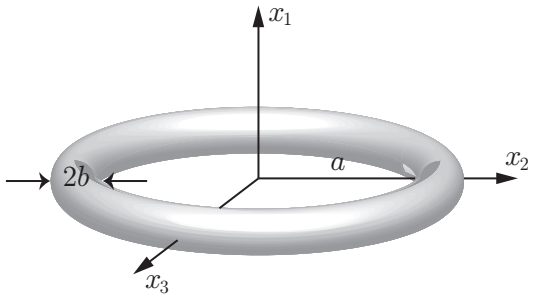

Figure 17: The toroidal ring and the Cartesian coordinate system (x_1, x_2, x_3).

Appendix H The toroidal ring

The general solution to Laplace's equation for the electrostatic potential ψ in toroidal coordinates[6] is, see Ref. 15,

$$\psi(u,v,\phi) = \sqrt{\cosh v - \cos u} \sum_{n,m=0}^{\infty} (a_m \cos m\phi + b_m \sin m\phi) \cdot (c_m \cos nu + d_m \sin nu) \left(A_{mn} \mathrm{P}^m_{n-\frac{1}{2}}(\cosh v) + B_{mn} \mathrm{Q}^m_{n-\frac{1}{2}}(\cosh v) \right), \tag{H.2}$$

where $\mathrm{P}^m_{n-1/2}$ and $\mathrm{Q}^m_{n-1/2}$ are the ring functions of the first and second kinds, respectively, see Ref. 1. The toroidal ring of axial radius a and cross section radius b is given by the surface $v = v_0$, see Fig. 17. Introduce the semi-axis ratio $\xi \in [0,1]$ as the quotient $\xi = b/a = 1 \cosh v_0$.

In this appendix, the eigenvalues of the high-contrast polarizability dyadic are derived for the loop antenna in Sec. 8.2 of vanishing thickness. Due to rotational symmetry in the x_1x_2-plane, the analysis is reduced to two exterior boundary value problems defined by the region $v \in [0, v_0]$ and $u, \phi \in [0, 2\pi)$. Due to the singular behavior of $\mathrm{Q}^m_{n-1/2}(\cosh v)$ as $v \to 0$ it is required that $B_{mn} = 0$. In addition, the electrostatic potential must vanish at infinity, *i.e.*, $\psi(u,v,\phi) \to 0$ when $u, v \to 0$ simultaneously. On the surface of the toroidal ring the two different boundary conditions of interest are, $\psi(u, v_0, \phi) = x_1$ and $\psi(u, v_0, \phi) = x_3$, see App. B. The following representations of the Cartesian coordinates in terms of $\mathrm{Q}^m_{n-1/2}$ are proved

[6]The toroidal coordinate system (u,v,ϕ) is defined in terms of the Cartesian coordinates (x_1, x_2, x_3) as

$$x_1 = \frac{\zeta \sinh v \cos\phi}{\cosh v - \cos u}, \qquad x_2 = \frac{\zeta \sinh v \sin\phi}{\cosh v - \cos u}, \qquad x_2 = \frac{\zeta \sin u}{\cosh v - \cos u}, \tag{H.1}$$

where $u, \phi \in [0, 2\pi)$ and $v \in [0, \infty)$. The toroidal ring of axial radius a and cross section radius b is described by the surface $v = v_0$, where $a = \zeta \coth v_0$ and $b = \zeta / \sinh v_0$. Note that the present notation (u,v,ϕ) differs from (η, μ, ϕ) in Ref. 15.

to be useful:

$$\begin{cases} x_1 = -\dfrac{\zeta\sqrt{8}\cos\phi}{\pi}\sqrt{\cosh v_0 - \cos u}\displaystyle\sum_{n=0}^{\infty}\varepsilon_n \mathrm{Q}^1_{n-\frac{1}{2}}(\cosh v_0)\cos nu \\ x_3 = \dfrac{\zeta\sqrt{8}}{\pi}\sqrt{\cosh v_0 - \cos u}\displaystyle\sum_{n=1}^{\infty} n\mathrm{Q}_{n-\frac{1}{2}}(\cosh v_0)\sin nu \end{cases} \tag{H.3}$$

Two different boundary value problems are associated with the loop antenna in Sec. 8.2 depending on whether the magnetic polarization $\hat{\boldsymbol{p}}_{\mathrm{m}}$ is parallel or orthogonal to the x_3-axis. The solution of these boundary value problems are then closely related to the components of the electric polarizability dyadic. Only the case when the thickness of the toroidal ring vanishes, *i.e.*, when $\xi \to 0$ or equivalently $v_0 \to \infty$, is treated here.

H.1 Magnetic polarization perpendicular to the x_3-axis

A magnetic polarization $\hat{\boldsymbol{p}}_{\mathrm{m}}$ perpendicular to the x_3-axis is via the plane-wave condition $\hat{\boldsymbol{k}} = \hat{\boldsymbol{p}}_{\mathrm{e}} \times \hat{\boldsymbol{p}}_{\mathrm{m}}$ equivalent to the electric polarization $\hat{\boldsymbol{p}}_{\mathrm{e}}$ parallel with the x_3-axis. A straightforward calculation to this problem can be proved to yield

$$\psi(u,v,\phi) = \frac{\zeta\sqrt{8}}{\pi}\sqrt{\cosh v - \cos u}\sum_{n=1}^{\infty} n\frac{\mathrm{Q}_{n-\frac{1}{2}}(\cosh v_0)}{\mathrm{P}_{n-\frac{1}{2}}(\cosh v_0)}\mathrm{P}_{n-\frac{1}{2}}(\cosh v)\sin nu. \tag{H.4}$$

In terms of the normal derivative $\partial\psi/\partial\nu$ evaluated at $v = v_0$, the third eigenvalue of $\boldsymbol{\gamma}_\infty$ is given by

$$\gamma_3 = 2\pi\int_0^{2\pi} x_3\frac{\partial\psi(u,v_0,\phi)}{\partial\nu}\frac{\zeta^2\sinh v_0}{(\cosh v_0 - \cos u)^2}\,\mathrm{d}u \tag{H.5}$$

By insertion of (H.3) into (H.5), the asymptotic behavior of γ_3 in the limit $\xi \to 0$, or equivalently $v_0 \to \infty$, can be proved to be ($\zeta \to a$ as $v_0 \to \infty$)

$$\gamma_3 = \mathcal{O}(\xi^2) \quad \text{as } \xi \to 0. \tag{H.6}$$

Hence, the third eigenvalue γ_3 of the high-contrast polarizability dyadic vanishes as the thickness of the toroidal ring approaches zero.

H.2 Magnetic polarization parallel with the x_3-axis

The solution to the boundary value problem with the magnetic polarization $\hat{\boldsymbol{p}}_{\mathrm{m}}$ parallel with the x_3-axis, *i.e.*, $\hat{\boldsymbol{p}}_{\mathrm{e}}$ perpendicular to the x_1-axis, is

$$\psi(u,v,\phi) = -\frac{\zeta\sqrt{8}\cos\phi}{\pi}\sqrt{\cosh v - \cos u}\sum_{n=0}^{\infty}\varepsilon_n\frac{\mathrm{Q}^1_{n-\frac{1}{2}}(\cosh v_0)}{\mathrm{P}^1_{n-\frac{1}{2}}(\cosh v_0)}\mathrm{P}^1_{n-\frac{1}{2}}(\cosh v)\cos nu, \tag{H.7}$$

where $\varepsilon_n = 2 - \delta_{n0}$ is the Neumann factor. In terms of the normal derivative $\partial\psi/\partial\nu$ evaluated at $v = v_0$, the first and second eigenvalues of $\boldsymbol{\gamma}_\infty$ are

$$\gamma_1 = \gamma_2 = \int_0^{2\pi} \int_0^{2\pi} x_1 \frac{\partial\psi(u, v_0, \phi)}{\partial\nu} \frac{\zeta^2 \sinh v_0}{(\cosh v_0 - \cos u)^2} \, \mathrm{d}\phi \, \mathrm{d}u, \tag{H.8}$$

where x_1 as function of u and ϕ is given by (H.3). The asymptotic behavior of (H.8) as $\xi \to 0$, or equivalently $v_0 \to \infty$, can be proved to be ($\zeta \to a$ as $v_0 \to \infty$)

$$\gamma_1 = \gamma_2 = \frac{2\pi^2 a^3}{\ln 2/\xi - 1} + \mathcal{O}(\xi^2) \quad \text{as } \xi \to 0. \tag{H.9}$$

Note that (H.9) vanishes slower than (H.6) as $\xi \to 0$ due to the logarithmic singularity.

References

[1] M. Abramowitz and I. A. Stegun, editors. *Handbook of Mathematical Functions*. Applied Mathematics Series No. 55. National Bureau of Standards, Washington D.C., 1970.

[2] J. B. Andersen and A. Frandsen. Absorption efficiency of receiving antennas. *IEEE Trans. Antennas Propagat.*, **53**(9), 2843–2849, 2005.

[3] Antenna Standards Committee of the IEEE Antennas and Propagation Society. IEEE Standard Definitions of Terms for Antennas, 1993. IEEE Std 145-1993.

[4] L. J. Chu. Physical limitations of omni-directional antennas. *Appl. Phys.*, **19**, 1163–1175, 1948.

[5] R. S. Elliott. *Antenna Theory and Design*. IEEE Press, New York, 2003. Revised edition.

[6] R. M. Fano. Theoretical limitations on the broadband matching of arbitrary impedances. *Journal of the Franklin Institute*, **249**(1,2), 57–83 and 139–154, 1950.

[7] M. Gustafsson and S. Nordebo. Bandwidth, Q-factor, and resonance models of antennas. *Progress in Electromagnetics Research*, **62**, 1–20, 2006.

[8] M. Gustafsson, C. Sohl, and G. Kristensson. Physical limitations on antennas of arbitrary shape. *Proc. R. Soc. A*, **463**(2086), 2589–2607, 2007.

[9] M. Gustafsson. On the non-uniqueness of the electromagnetic instantaneous response. *J. Phys. A: Math. Gen.*, **36**, 1743–1758, 2003.

[10] M. Gustafsson and S. Nordebo. Characterization of MIMO antennas using spherical vector waves. *IEEE Trans. Antennas Propagat.*, **54**(9), 2679–2682, 2006.

[11] E. Hallén. *Theoretical Investigations into the Transmitting and Receiving Qualities of Antennae*, volume 11, No. 4 of *Nova acta Regiae Societatis Scientarium Upsaliensis IV*. Almqvist & Wiksell, Stockholm, 1938.

[12] M. Hamermesh. *Group Theory and its Application to Physical Problems*. Dover Publications, New York, 1989.

[13] R. C. Hansen. *Electrically Small, Superdirective, and Superconductive Antennas*. John Wiley & Sons, New Jersey, 2006.

[14] R. E. Kleinman and T. B. A. Senior. Rayleigh scattering. In V. V. Varadan and V. K. Varadan, editors, *Low and High Frequency Asymptotics*, volume 2 of *Handbook on Acoustic, Electromagnetic and Elastic Wave Scattering*, chapter 1, pages 1–70. Elsevier Science Publishers, Amsterdam, 1986.

[15] P. M. Morse and H. Feshbach. *Methods of Theoretical Physics*, volume 2. McGraw-Hill, New York, 1953.

[16] R. G. Newton. *Scattering Theory of Waves and Particles*. Springer-Verlag, New York, 1982.

[17] H. M. Nussenzveig. *Causality and Dispersion Relations*. Academic Press, London, 1972.

[18] S. Silver. *Microwave Antenna Theory and Design*, volume 12 of *Radiation Laboratory Series*. McGraw-Hill, New York, 1949.

[19] C. Sohl, M. Gustafsson, and G. Kristensson. Physical limitations on broadband scattering by heterogeneous obstacles. *J. Phys. A: Math. Theor.*, **40**(36), 11165–11182, 2007.

[20] C. Sohl, M. Gustafsson, and G. Kristensson. Physical limitations on metamaterials: Restrictions on scattering and absorption over a frequency interval. Technical Report LUTEDX/(TEAT-7154)/1–11/(2007), Lund University, Department of Electrical and Information Technology, P.O. Box 118, S-221 00 Lund, Sweden, 2007. http://www.eit.lth.se.

[21] W. L. Stutzman and G. A. Thiele. *Antenna Theory and Design*. John Wiley & Sons, New York, second edition, 1998.

[22] J. R. Taylor. *Scattering Theory: The Quantum Theory of Nonrelativistic Collisions*. Robert E. Krieger Publishing Company, Malabar, 1983.

[23] H. van de Hulst. *Light Scattering by Small Particles*. John Wiley & Sons, Inc., New York, 1957.

[24] H. A. Wheeler. Fundamental limitations of small antennas. *Proc. IRE*, **35**(12), 1479–1484, 1947.

[25] A. D. Yaghjian and S. R. Best. Impedance, bandwidth, and Q of antennas. *IEEE Trans. Antennas Propagat.*, **53**(4), 1298–1324, 2005.

A priori estimates on the partial realized gain of ultra-wideband (UWB) antennas

Christian Sohl and Mats Gustafsson

Paper X

Based on: C. Sohl and M. Gustafsson. A priori estimates on the partial realized gain of ultra-wideband (UWB) antennas. *Quarterly Journal of Mechanics & Applied Mathematics*, vol. 61, no. 3, pp. 415–430, August 2008.

Abstract

A sum rule valid for a large class of linear and reciprocal antennas is presented in terms of the electric and magnetic polarizability dyadics. The identity is based on the holomorphic properties of the forward scattering dyadic and includes arbitrarily shaped antennas modeled by linear and time-translational invariant constitutive relations. In particular, a priori estimates on the partial realized gain are introduced, and lower bounds on the onset frequency are derived for two important archetypes of UWB antennas: those with a constant partial realized gain and those with a constant effective antenna aperture. The theoretical findings are illustrated by an equiangular spiral antenna, and comparison with numerical simulations show great potential for future applications in antenna design.

1 Introduction

Since the pioneering ideas introduced by Chu [3] and Wheeler [23] more than half a century ago, a priori bounds on the directivity and the Q-factor of electrically small antennas have attracted great attention in the scientific community. Unfortunately, the results by Chu and Wheeler, and many of the subsequent papers discussed in [9], not only overestimate the true antenna performance but also show severe restrictions with respect to its material parameters and polarization dependence. To overcome these imperfections, a new set of isoperimetric bounds that apply to a large class of linear and reciprocal antennas was introduced in [6, 8]. These new bounds are based on the first principles of causality and power conservation rather than the traditional approach of using the spherical vector waves. Another drawback of the classical formulation is due to the difficulty of extending the spherical vector waves to accurately model the electromagnetic field inside the smallest circumscribing sphere.

The above-mentioned classical bounds also show severe restrictions with respect to the electrical size of the investigated antenna. In fact, the classical bounds are only meaningful for electrically small and resonant antennas due to their underlying assumption of a dominant lowest order spherical vector mode. As far as the authors know, no similar bounds to Chu and Wheeler exist in the literature for non-resonant antennas with a broadband partial realized gain. An exception is given by [10] and [22] which address limitations on the bandwidth using Fano's theory of broadband matching. Since non-resonant antennas show great potential in future communication technologies such as ultra-wideband (UWB), it is of scientific interest to develop physical bounds on such antennas.

The underlying idea of UWB systems is the spreading of the transmitted data over an absolute bandwidth exceeding the lesser of 500 MHz or 20% of the center frequency [15].[1] UWB systems use a low-power spectral density for short-range communication, implying that frequency bands already assigned to other services can be reused in a cooperative manner without introducing significant interference.

[1] For example, in North America, $[3.1, 10.6]$ GHz is authorized by the Federal Communications Commission as the appropriate frequency band for UWB communication.

Among other things, UWB antennas show great potential for applications in stealth technology, radar imaging and precision positioning. In these applications, an undesired feature of many UWB antennas is temporal dispersion, *i.e.*, the stretching of a time-domain signal into a more distorted waveform in the sense that the phase center or effective origin of the radiated field varies with frequency. This variation is due to the fact that small-scale portions of the antenna radiate or receive high-frequency components, while large-scale portions radiate or receive low-frequency components. The present paper does not further address the problem of temporal dispersion and its effect on the UWB system performance. Neither does it discuss how to minimize dispersion effects associated with a radiation pattern that varies with frequency.

The physical bounds presented in this paper follow [7] by regarding the antenna from a scattering point of view using the theory in [2, 14]. Specifically, the holomorphic properties of the forward scattering dyadic are employed in [17–19] to derive a sum rule for the extinction cross section. This identity is extended in [6] from the scattering scenario to a large class of antennas via reciprocity and the effective antenna aperture. Here, the variational results in [11, 12] play an essential role for the far-reaching conclusions that are obtained from this new approach. However, the main importance of the theoretical findings is that they can be invoked directly in antenna design to establish upper bounds on the partial realized gain and the bandwidth of any antenna circumscribed by an arbitrarily shaped geometry. The results are also crucial for the understanding of the fundamental antenna restrictions imposed by the first principles of causality and power conservation.

2 The integrated partial realized gain

Consider a linear, lossless and reciprocal antenna in free space as depicted in Fig. 1. The assumption of a reciprocal material in the antenna means that either the transmission case or the reception case may be examined. From a scattering point of view, the antenna is assumed to be causal, *i.e.*, the scattered field in the forward direction cannot precede the incident field when the antenna is subject to a plane-wave excitation. Let $\hat{\boldsymbol{k}}$ denote a fixed direction in $\mathbb{R}^3$ and consider a radiated field with an electric polarization $\hat{\boldsymbol{e}}$ satisfying $\hat{\boldsymbol{k}} \cdot \hat{\boldsymbol{e}} = 0$ in the far-field region. Introduce the partial realized gain g as a measure of the antenna's ability to direct power. This quantity is defined as the partial gain G in the $\hat{\boldsymbol{k}}$-direction with respect to the $\hat{\boldsymbol{e}}$-polarization, weighted with the reflection loss $1 - |\Gamma|^2$ due to the antenna mismatch (Γ denotes the reflection coefficient at the feeding port), *i.e.*,

$$g(k; \hat{\boldsymbol{k}}, \hat{\boldsymbol{e}}) = (1 - |\Gamma(k)|^2) G(k; \hat{\boldsymbol{k}}, \hat{\boldsymbol{e}}), \tag{2.1}$$

where $k \in [0, \infty)$ denotes the angular wave number in free space.[2] This definition includes both the transverse electric (TE) polarization and the transverse magnetic

[2] According to the Institute of Electrical and Electronic Engineers (IEEE) standard [1], the partial gain G in a given direction is defined as "that part of the radiation intensity corresponding to a given polarization divided by the radiation intensity that would be obtained if the power accepted by the antenna were radiated isotropically". Thus, the partial realized gain contains more

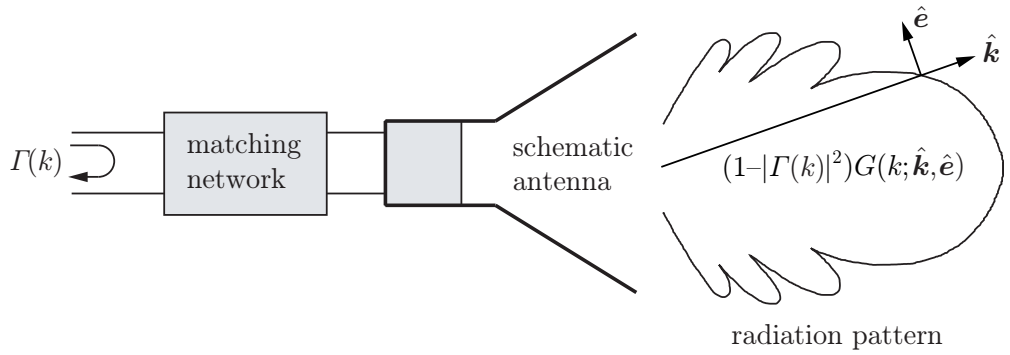

Figure 1: The radiation pattern of a schematic antenna and its partial realized gain in the $\hat{\boldsymbol{k}}$-direction with respect to the $\hat{\boldsymbol{e}}$-polarization.

(TM) polarizations or any combination thereof.

Based on the above-stated assumptions, a sum rule known as the integrated partial realized gain is derived in [6] in terms of the electric and magnetic polarizability dyadics, $\boldsymbol{\gamma}_{\mathrm{e}}$ and $\boldsymbol{\gamma}_{\mathrm{m}}$, respectively. The result is

$$\int_0^\infty \frac{g(k;\hat{\boldsymbol{k}},\hat{\boldsymbol{e}})}{k^4}\,\mathrm{d}k = \frac{\eta(-\hat{\boldsymbol{k}},\hat{\boldsymbol{e}}^*)}{2}\left(\hat{\boldsymbol{e}}^*\cdot\boldsymbol{\gamma}_{\mathrm{e}}\cdot\hat{\boldsymbol{e}} + (\hat{\boldsymbol{k}}\times\hat{\boldsymbol{e}}^*)\cdot\boldsymbol{\gamma}_{\mathrm{m}}\cdot(\hat{\boldsymbol{k}}\times\hat{\boldsymbol{e}})\right), \tag{2.2}$$

where an asterisk denotes the complex conjugate and the generalized absorption efficiency $\eta \in [0,1)$ is defined in Sec. 3. Relation (2.2) also holds for non-reciprocal antennas if g is restricted to the partial realized gain in receiving mode.

The identity (2.2) is valid for perfectly electric conducting material parameters as often employed in numerical simulations of antennas. However, (2.2) is also valid for the larger class of bi-anisotropic and lossless heterogeneous materials. Lossy material parameters (temporal dispersion with or without a conductivity term) is also covered by the identity if the equality sign in (2.2) is changed to a less than or equal to sign. The material parameters of the antenna are quantified by the real-valued and symmetric dyadics $\boldsymbol{\gamma}_{\mathrm{e}}$ and $\boldsymbol{\gamma}_{\mathrm{m}}$, defined in Sec. 4 by certain electrostatic and magnetostatic boundary-value problems. These dyadics depend on the antenna geometry and its static material parameters, but they are independent of any matching network. On the other hand, the generalized absorption efficiency η depends on the dynamical properties of the antenna (including the matching network) through the ratio of the integrated absorption to the integrated extinction. The generalized absorption efficiency is a real-valued number in the unit interval quantifying the overall scattering and absorption properties of the antenna.

information than, *e.g.*, the maximum gain $G_{\max}(k) = \max_{\hat{\boldsymbol{k}}\cdot\hat{\boldsymbol{e}}=0} G(k;\hat{\boldsymbol{k}},\hat{\boldsymbol{e}})$ which is maximized with respect to both the $\hat{\boldsymbol{k}}$- and $\hat{\boldsymbol{e}}$-directions.

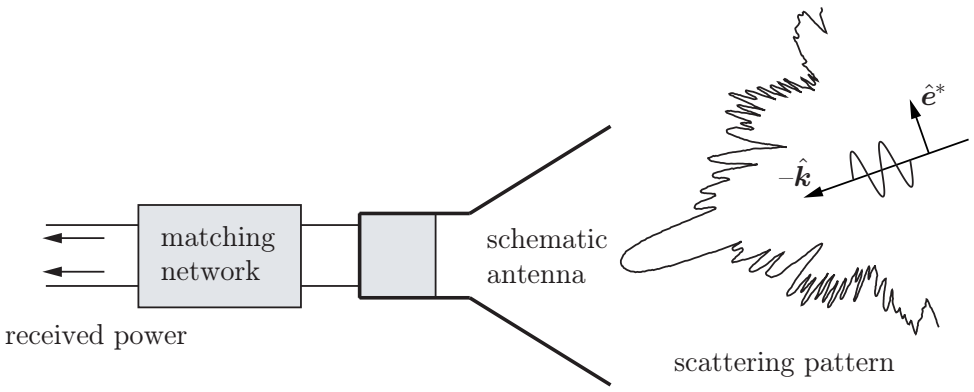

Figure 2: The resulting scattering pattern when the antenna in Fig. 1 is illuminated by the plane wave $\mathrm{e}^{-\mathrm{i}k\hat{\boldsymbol{k}}\cdot\boldsymbol{x}}\hat{\boldsymbol{e}}^*$ of unit amplitude.

3 Scattering and absorption of antennas

Now, consider the schematic antenna in Fig. 2 subject to the plane wave $\mathrm{e}^{-\mathrm{i}k\hat{\boldsymbol{k}}\cdot\boldsymbol{x}}\hat{\boldsymbol{e}}^*$ (time dependence $\mathrm{e}^{-\mathrm{i}kt/\mathrm{c}_0}$ where c_0 denotes the speed of light in free space) of unit amplitude. A common measure of an antenna's scattering properties is the scattering cross section σ_s, defined as the scattered power divided by the incident power flux in the forward direction [13]. A corresponding measure for the absorbed power in the antenna is the effective antenna aperture or absorption cross section σ_a. The latter is determined by integrating the scattering dyadic $\mathbf{S}$ over the unit sphere Ω with respect to $\hat{\boldsymbol{x}} = \boldsymbol{x}/x$:

$$\sigma_\mathrm{s}(k; -\hat{\boldsymbol{k}}, \hat{\boldsymbol{e}}^*) = \int_\Omega |\mathbf{S}(k; -\hat{\boldsymbol{k}} \curvearrowright \hat{\boldsymbol{x}}) \cdot \hat{\boldsymbol{e}}^*|^2 \, \mathrm{d}S, \tag{3.1}$$

where the notation $-\hat{\boldsymbol{k}} \curvearrowright \hat{\boldsymbol{x}}$ refers to the mapping of an incoming plane wave in the negative $\hat{\boldsymbol{k}}$-direction into the amplitude of an outgoing spherical wave in the $\hat{\boldsymbol{x}}$-direction. The scattering dyadic $\mathbf{S}$ is related to the scattered electric field $\boldsymbol{E}_\mathrm{s}$ in the far-field region via

$$\mathbf{S}(k; -\hat{\boldsymbol{k}} \curvearrowright \hat{\boldsymbol{x}}) \cdot \hat{\boldsymbol{e}}^* = \lim_{x\to\infty} x\mathrm{e}^{-\mathrm{i}kx} \boldsymbol{E}_\mathrm{s}(k, \boldsymbol{x}; -\hat{\boldsymbol{k}}, \hat{\boldsymbol{e}}^*), \tag{3.2}$$

where $x = |\boldsymbol{x}|$ denotes the magnitude of the position vector. It is assumed that the antenna is causal in the forward direction, $\hat{\boldsymbol{x}} = -\hat{\boldsymbol{k}}$, in the sense that the inverse Fourier transform of $\hat{\boldsymbol{e}} \cdot \mathbf{S}(k; -\hat{\boldsymbol{k}} \curvearrowright -\hat{\boldsymbol{k}}) \cdot \hat{\boldsymbol{e}}^*$ vanishes almost everywhere on the negative real axis [17].

The effective antenna aperture measures an antenna's ability to intercept an incident wave. In terms of the optical theorem, the effective antenna aperture is given by [14]

$$\sigma_\mathrm{a}(k; -\hat{\boldsymbol{k}}, \hat{\boldsymbol{e}}^*) = \frac{4\pi}{k} \operatorname{Im}\left\{\hat{\boldsymbol{e}} \cdot \mathbf{S}(k, -\hat{\boldsymbol{k}} \curvearrowright -\hat{\boldsymbol{k}}) \cdot \hat{\boldsymbol{e}}^*\right\} - \sigma_\mathrm{s}(k; -\hat{\boldsymbol{k}}, \hat{\boldsymbol{e}}^*). \tag{3.3}$$

Reciprocity implies that the effective antenna aperture is related to the partial realized gain g through [16]

$$\sigma_{\mathrm{a}}(k; -\hat{\boldsymbol{k}}, \hat{\boldsymbol{e}}^*) = \frac{\pi g(k; \hat{\boldsymbol{k}}, \hat{\boldsymbol{e}})}{k^2}. \tag{3.4}$$

The interpretation of (3.3) and (3.4) is that the power accepted by the antenna when it is subject to the plane-wave excitation $\mathrm{e}^{-\mathrm{i}k\hat{\boldsymbol{k}}\cdot\boldsymbol{x}}\hat{\boldsymbol{e}}^*$ simply is the product of the effective antenna aperture and the incident power flux $1/2\eta_0$ ($\eta_0 = \sqrt{\mu_0/\epsilon_0}$ denotes the wave impedance in free space).

The generalized absorption efficiency η is defined as the ratio of the integrated absorption to the integrated extinction, *i.e.*,

$$\eta(-\hat{\boldsymbol{k}}, \hat{\boldsymbol{e}}^*) = \int_0^\infty \frac{\sigma_{\mathrm{a}}(k; -\hat{\boldsymbol{k}}, \hat{\boldsymbol{e}}^*)}{k^2}\,\mathrm{d}k \Bigg/ \int_0^\infty \frac{\sigma_{\mathrm{ext}}(k; -\hat{\boldsymbol{k}}, \hat{\boldsymbol{e}}^*)}{k^2}\,\mathrm{d}k, \tag{3.5}$$

where $\sigma_{\mathrm{ext}} = \sigma_{\mathrm{a}} + \sigma_{\mathrm{s}}$ denotes the extinction cross section. For a large class of matched antennas, η is close to $1/2$ if $\hat{\boldsymbol{k}}$ and $\hat{\boldsymbol{e}}$ coincide with the antenna's main beam and dominant electric polarization, respectively. The integrated absorption depends on the presence of any matching network, and it is determined by loading the feeding port with the appropriate radiation resistance and calculating the absorbed power when the antenna is subject to the plane-wave excitation $\mathrm{e}^{-\mathrm{i}k\hat{\boldsymbol{k}}\cdot\boldsymbol{x}}\hat{\boldsymbol{e}}^*$.

The denominator in (3.5) is further related to the electric and magnetic polarizability dyadics, $\boldsymbol{\gamma}_{\mathrm{e}}$ and $\boldsymbol{\gamma}_{\mathrm{m}}$, respectively, via the integrated extinction [17]

$$\int_0^\infty \frac{\sigma_{\mathrm{ext}}(k; -\hat{\boldsymbol{k}}, \hat{\boldsymbol{e}}^*)}{k^2}\,\mathrm{d}k = \frac{\pi}{2}\left(\hat{\boldsymbol{e}}^* \cdot \boldsymbol{\gamma}_{\mathrm{e}} \cdot \hat{\boldsymbol{e}} + (\hat{\boldsymbol{k}} \times \hat{\boldsymbol{e}}^*) \cdot \boldsymbol{\gamma}_{\mathrm{m}} \cdot (\hat{\boldsymbol{k}} \times \hat{\boldsymbol{e}})\right). \tag{3.6}$$

The identity (3.6) is based on the causal properties of the forward scattering dyadic $\mathbf{S}(k; -\hat{\boldsymbol{k}} \curvearrowright -\hat{\boldsymbol{k}})$ when considered as a holomorphic function in the upper half part of the complex k-plane. In particular, since the polarizability dyadics are real valued and symmetric, it is observed that the right-hand side of (3.6) is invariant when $\hat{\boldsymbol{e}}$ is replaced with $\hat{\boldsymbol{e}}^*$, implying that the integrated extinction is independent whether the chirality of the $\hat{\boldsymbol{e}}$-polarization is left or right handed.

Following the ideas set forth in [6, 17], it is convenient to introduce the extinction volume ϱ as a complex-valued extension of the extinction cross section:

$$\varrho(k; -\hat{\boldsymbol{k}}, \hat{\boldsymbol{e}}^*) = \frac{\hat{\boldsymbol{e}} \cdot \mathbf{S}(k; -\hat{\boldsymbol{k}} \curvearrowright -\hat{\boldsymbol{k}}) \cdot \hat{\boldsymbol{e}}^*}{k^2}. \tag{3.7}$$

This quantity defines a holomorphic function for $\operatorname{Im} k > 0$, and it satisfies

$$\varrho(k; -\hat{\boldsymbol{k}}, \hat{\boldsymbol{e}}^*) = \varrho(k; -\hat{\boldsymbol{k}}, \hat{\boldsymbol{e}}) \tag{3.8}$$

so that also ϱ is invariant when the electric polarization is complex conjugated. For real-valued k, the extinction cross section is related to the imaginary part of the extinction volume via the optical theorem [17]

$$\sigma_{\mathrm{ext}}(k; -\hat{\boldsymbol{k}}, \hat{\boldsymbol{e}}^*) = 4\pi k \operatorname{Im} \varrho(k; -\hat{\boldsymbol{k}}, \hat{\boldsymbol{e}}^*). \tag{3.9}$$

Analogous to the Kramers-Kronig relations in material modeling, the real and imaginary parts of ϱ are connected by the Hilbert transform [20]. In particular, it follows that ϱ is real-valued in the static limit and there satisfies the integral identity

$$\varrho(0; -\hat{\boldsymbol{k}}, \hat{\boldsymbol{e}}^*) = \frac{2}{\pi} \int_0^\infty \frac{\operatorname{Im} \varrho(k; -\hat{\boldsymbol{k}}, \hat{\boldsymbol{e}}^*)}{k} \, \mathrm{d}k. \tag{3.10}$$

Relation (3.10) is useful as a consistency check when ϱ is either measured or numerically determined by a simulation.

4 The three polarizability dyadics $\boldsymbol{\gamma}_{\mathrm{e}}$, $\boldsymbol{\gamma}_{\mathrm{m}}$ and $\boldsymbol{\gamma}_\infty$

Depending on the nature of the problem, let $\boldsymbol{\chi}_\ell$ denote either the electric ($\ell = \mathrm{e}$) or the magnetic ($\ell = \mathrm{m}$) susceptibility dyadic in the static limit.[3] Assume that $\boldsymbol{\chi}_\ell$ is compactly supported and symmetric for all $\boldsymbol{x} \in \mathbb{R}^3$. In the absence of a conductivity term, the electric and magnetic polarizability dyadics are defined by [17]

$$\boldsymbol{\gamma}_\ell = \sum_{i,j=1}^{3} \left(\hat{\boldsymbol{a}}_i \cdot \int_{\mathbb{R}^3} \boldsymbol{\chi}_\ell(\boldsymbol{x}) \cdot (\hat{\boldsymbol{a}}_j - \nabla \psi_j(\boldsymbol{x})) \, \mathrm{d}v \right) \hat{\boldsymbol{a}}_i \hat{\boldsymbol{a}}_j, \tag{4.1}$$

where $\hat{\boldsymbol{a}}_1$, $\hat{\boldsymbol{a}}_2$ and $\hat{\boldsymbol{a}}_3$ form an arbitrary set of linearly independent unit vectors. Here, the scalar potential ψ_j is the unique solution to the static boundary-value problem

$$\begin{cases} \nabla \cdot ((\boldsymbol{\chi}_\ell(\boldsymbol{x}) + \mathbf{I}_3) \cdot \nabla \psi_j(\boldsymbol{x})) = \nabla \cdot (\boldsymbol{\chi}_\ell(\boldsymbol{x}) \cdot \hat{\boldsymbol{a}}_j) \\ \psi_j(\boldsymbol{x}) = \mathcal{O}(x^{-2}) \text{ as } x \to \infty \end{cases} \qquad \boldsymbol{x} \in \mathbb{R}^3, \tag{4.2}$$

where $\mathbf{I}_3$ denotes the unit dyadic in $\mathbb{R}^3$. From (4.1) and (4.2), it is observed that $\boldsymbol{\gamma}_\ell$ merely is defined as the induced dipole moment when the antenna is subject to a static excitation of unit amplitude. As a consequence, $\boldsymbol{\gamma}_\ell$ is independent of the $\hat{\boldsymbol{k}}$-direction and the electric and magnetic polarizations, $\hat{\boldsymbol{e}}$ and $\hat{\boldsymbol{k}} \times \hat{\boldsymbol{e}}$, respectively. Furthermore, from (4.1) and (4.2) it follows that $\boldsymbol{\gamma}_\ell$ is real-valued and symmetric since $\boldsymbol{\chi}_\ell$ is assumed to be symmetric for all $\boldsymbol{x} \in \mathbb{R}^3$. Due to the absence of any length scale in the static limit, $\boldsymbol{\gamma}_\ell$ scales with the volume V of the antenna support [17]

$$\Lambda = \{\boldsymbol{x} \in \mathbb{R}^3 \, : \, \boldsymbol{\chi}_{\mathrm{e}}(\boldsymbol{x}) \neq \mathbf{0} \text{ or } \boldsymbol{\chi}_{\mathrm{m}}(\boldsymbol{x}) \neq \mathbf{0}\}. \tag{4.3}$$

Closed-form expressions of $\boldsymbol{\gamma}_\ell$ for various homogeneous and isotropic geometries are presented in [4, 13] and references therein. Further discussions on the physical nature of $\boldsymbol{\gamma}_\ell$ are found in [2, 21].

From a modeling point of view, it is also interesting to include a static conductivity in the susceptibility dyadic. For this purpose, assume that $\boldsymbol{\chi}_\ell$ is isotropic, *i.e.*, $\boldsymbol{\chi}_\ell = \chi_\ell \mathbf{I}_3$, and introduce the conductivity $\varsigma > 0$ and free space wave impedance $\eta_0 = \sqrt{\mu_0/\epsilon_0}$. In the presence of an isotropic conductivity term $\mathrm{i}\eta_0\varsigma/k$ in χ_ℓ, the

[3] Here, $\boldsymbol{\chi}_{\mathrm{e}} = \boldsymbol{\epsilon} - \mathbf{I}_3$ and $\boldsymbol{\chi}_{\mathrm{m}} = \boldsymbol{\mu} - \mathbf{I}_3$, where $\boldsymbol{\epsilon}$ and $\boldsymbol{\mu}$ denote the static permittivity and permeability dyadics relative to free space, respectively.

pertinent definition of $\boldsymbol{\gamma}_\ell$ must be altered due to the singularity of $i\eta_0\varsigma/k$ in the static limit. Under this assumption, it follows from [4, 13] that $\boldsymbol{\gamma}_\ell$ should be evaluated in the high-contrast limit as χ_ℓ approaches infinity. For this purpose, introduce the high-contrast polarizability dyadic $\boldsymbol{\gamma}_\infty$ via the limiting process ($i, j = 1, 2, 3$)

$$\hat{\boldsymbol{a}}_i \cdot \boldsymbol{\gamma}_\infty \cdot \hat{\boldsymbol{a}}_j = \lim_{\chi_\ell(\boldsymbol{x})\to\infty} \hat{\boldsymbol{a}}_i \cdot \boldsymbol{\gamma}_\ell \cdot \hat{\boldsymbol{a}}_j \tag{4.4}$$

for all $\boldsymbol{x} \in \Lambda$, where the dependence on χ_ℓ has been omitted on the right-hand side of (4.4). Equivalently, the high-contrast polarizability dyadic is defined by [17]

$$\boldsymbol{\gamma}_\infty = \sum_{i,j=1}^{3} \left(V + \hat{\boldsymbol{a}}_i \cdot \int_{\partial\Lambda} \psi_j(\boldsymbol{x}) \hat{\boldsymbol{\nu}}(\boldsymbol{x}) - \boldsymbol{x}\hat{\boldsymbol{\nu}}(\boldsymbol{x}) \cdot (\hat{\boldsymbol{a}}_j + \nabla\psi_j(\boldsymbol{x})) \, \mathrm{d}S \right) \hat{\boldsymbol{a}}_i \hat{\boldsymbol{a}}_j, \tag{4.5}$$

where the surface integral is evaluated over the antenna boundary $\partial\Lambda$ with outward-directed unit normal vector $\hat{\boldsymbol{\nu}}$. Here, ψ_j is the unique solution to the exterior problem

$$\begin{cases} \nabla^2\psi_j(\boldsymbol{x}) = 0 \\ \psi_j(\boldsymbol{x}) = -\hat{\boldsymbol{a}}_j \cdot \boldsymbol{x} + \mathcal{O}(x^{-2}) \text{ as } x \to \infty \end{cases} \qquad \boldsymbol{x} \in \mathbb{R}^3 \setminus \Lambda, \tag{4.6}$$

with the boundary condition that ψ_j is constant on $\partial\Lambda$. The constant value of ψ_j is specified by the requirement that the total charge $Q_j = \int \hat{\boldsymbol{\nu}}(\boldsymbol{x}) \cdot \nabla\psi_j(\boldsymbol{x}) \, \mathrm{d}S$ should vanish on each non-simply connected subset of $\partial\Lambda$.

5 Bounds on the integrated partial realized gain

A drawback of (2.2) is the presence of η on the right-hand side of the identity. In contrast to the polarizability dyadics in Sec. 4, the generalized absorption efficiency is not the solution of a pure electrostatic or magnetostatic problem. It is therefore important to realize that the following estimate can be invoked directly in the subsequent analysis:

$$0 \leqslant \eta(-\hat{\boldsymbol{k}}, \hat{\boldsymbol{e}}^*) < 1. \tag{5.1}$$

By introducing (5.1), the equality sign in (2.2) is turned into an inequality with an upper bound which only depends on the solution of a purely static boundary-value problem.

In many cases, it is desirable to bound the left-hand side of (2.2) from above independently of the materials in the antenna. This is achieved by introducing the variational results in [11, 12] which are valid for general isotropic and heterogeneous material parameters. The results in [11, 12] state that the eigenvalues of $\boldsymbol{\gamma}_\ell$ increase monotonically as χ_ℓ increases for any $\boldsymbol{x} \in \mathbb{R}^3$. Hence, it follows from (4.4) that both $\boldsymbol{\gamma}_\mathrm{e}$ and $\boldsymbol{\gamma}_\mathrm{m}$ are bounded from above by $\boldsymbol{\gamma}_\infty$, *viz.*,

$$\int_0^\infty \frac{g(k; \hat{\boldsymbol{k}}, \hat{\boldsymbol{e}})}{k^4} \, \mathrm{d}k \leqslant \frac{\eta(-\hat{\boldsymbol{k}}, \hat{\boldsymbol{e}}^*)}{2} \left(\hat{\boldsymbol{e}}^* \cdot \boldsymbol{\gamma}_\infty \cdot \hat{\boldsymbol{e}} + (\hat{\boldsymbol{k}} \times \hat{\boldsymbol{e}}^*) \cdot \boldsymbol{\gamma}_\infty \cdot (\hat{\boldsymbol{k}} \times \hat{\boldsymbol{e}}) \right). \tag{5.2}$$

As a consequence, the large pair of parenthesis on the right-hand side of (5.2) also hold for any extended support Λ_+ in the sense that $\boldsymbol{\gamma}_\infty$ can be estimated from above

by the corresponding solution of (4.5) and (4.6) when Λ is replaced by Λ_+. This procedure becomes particularly useful for estimating the integrated partial realized gain of an antenna with a complicated geometry. In this case, the large pair of parenthesis on the right-hand side of (5.2) is bounded from above by, for example, solving (4.5) and (4.6) for the smallest circumscribing cylinder with isotropic and homogeneous material parameters in the high-contrast limit.

The large pair of parenthesis on the right-hand side of (5.2) is recognized as the Rayleigh quotients of $\boldsymbol{\gamma}_\infty$, implying that the integrated partial realized gain further is bounded from above by the eigenvalues of $\boldsymbol{\gamma}_\infty$ (recall that $\boldsymbol{\gamma}_\infty$ is real-valued and symmetric and hence diagonalizable). When subject to the constraint $\hat{\boldsymbol{k}} \cdot \hat{\boldsymbol{e}} = 0$ of transverse wave propagation in the far-field region, (5.2) yields

$$\int_0^\infty \frac{g(k; \hat{\boldsymbol{k}}, \hat{\boldsymbol{e}})}{k^4} \, \mathrm{d}k \leqslant \frac{\eta(-\hat{\boldsymbol{k}}, \hat{\boldsymbol{e}}^*)}{2} (\gamma_1 + \gamma_2), \tag{5.3}$$

where γ_1 and γ_2 denote the largest and second largest eigenvalues of $\boldsymbol{\gamma}_\infty$, respectively. However, note that $(\hat{\boldsymbol{k}} \times \hat{\boldsymbol{e}}^*) \cdot \boldsymbol{\gamma}_\infty \cdot (\hat{\boldsymbol{k}} \times \hat{\boldsymbol{e}})$ and γ_2 vanish from the right-hand side of (5.2) and (5.3) for non-magnetic materials. For a discussion on the isoperimetric nature of (5.2) and (5.3), see [6, 17].

6 A priori estimates on UWB antennas

In this section, a priori estimates are presented for two archetypes of UWB antennas, *viz.*, antennas characterized by a constant partial realized gain and antennas characterized by a constant effective antenna aperture. A generalization of these models to include a more complex frequency characteristic is also discussed.

6.1 Constant partial realized gain $g_\mathrm{p}(\hat{\boldsymbol{k}}, \hat{\boldsymbol{e}})$

Due to the non-negative character of the partial realized gain, the left-hand side of (2.2) can be estimated from below by integrating over $K = [k_\mathrm{p}, \infty)$ rather than the entire positive real axis. Thus, a straightforward calculation using the threshold $g_\mathrm{p}(\hat{\boldsymbol{k}}, \hat{\boldsymbol{e}}) = \min_{k \in K} g(k; \hat{\boldsymbol{k}}, \hat{\boldsymbol{e}})$ yields

$$\int_0^\infty \frac{g(k; \hat{\boldsymbol{k}}, \hat{\boldsymbol{e}})}{k^4} \, \mathrm{d}k \geqslant g_\mathrm{p}(\hat{\boldsymbol{k}}, \hat{\boldsymbol{e}}) \int_K \frac{\mathrm{d}k}{k^4} = \frac{g_\mathrm{p}(\hat{\boldsymbol{k}}, \hat{\boldsymbol{e}})}{3k_\mathrm{p}^3}. \tag{6.1}$$

Combining this estimate with (2.2) implies that

$$\frac{g_\mathrm{p}(\hat{\boldsymbol{k}}, \hat{\boldsymbol{e}})}{3k_\mathrm{p}^3} \leqslant \frac{\eta(-\hat{\boldsymbol{k}}, \hat{\boldsymbol{e}}^*)}{2} \left(\hat{\boldsymbol{e}}^* \cdot \boldsymbol{\gamma}_\mathrm{e} \cdot \hat{\boldsymbol{e}} + (\hat{\boldsymbol{k}} \times \hat{\boldsymbol{e}}^*) \cdot \boldsymbol{\gamma}_\mathrm{m} \cdot (\hat{\boldsymbol{k}} \times \hat{\boldsymbol{e}}) \right), \tag{6.2}$$

with equality if and only if $g(k; \hat{\boldsymbol{k}}, \hat{\boldsymbol{e}}) = g_\mathrm{p}(\hat{\boldsymbol{k}}, \hat{\boldsymbol{e}})$, for $k \in [k_\mathrm{p}, \infty)$, and zero elsewhere. The interpretation of (6.2) is that it yields a lower bound on the antenna onset frequency k_p (the first frequency for which the antenna is sufficiently well matched),

or, equivalently, an upper bound on the threshold $g_{\mathrm{p}}(\hat{\boldsymbol{k}}, \hat{\boldsymbol{e}})$, in terms of the antenna geometry and its static material parameters. An antenna with a constant partial realized gain is characterized by receiving less power as frequency increases since the effective antenna aperture then varies inversely with the square of the frequency. Nearly self-complementary structures such as the planar and conical equiangular spiral antennas are often modeled by a constant partial realized gain.

6.2 Constant effective antenna aperture $\pi g_{\mathrm{a}}(\hat{\boldsymbol{k}}, \hat{\boldsymbol{e}})/k_{\mathrm{a}}^2$

A constant effective antenna aperture implies that the partial realized gain varies with the square of the frequency. For this purpose, introduce the constant effective antenna aperture $\pi g_{\mathrm{a}}(\hat{\boldsymbol{k}}, \hat{\boldsymbol{e}})/k_{\mathrm{a}}^2$ corresponding to the threshold $g_{\mathrm{a}}(\hat{\boldsymbol{k}}, \hat{\boldsymbol{e}}) = k_{\mathrm{a}}^2 \min_{k \in K} g(k; \hat{\boldsymbol{k}}, \hat{\boldsymbol{e}})/k^2$, where $K = [k_{\mathrm{a}}, \infty)$. Then,

$$\int_0^\infty \frac{g(k; \hat{\boldsymbol{k}}, \hat{\boldsymbol{e}})}{k^4} \, \mathrm{d}k \geqslant \frac{g_{\mathrm{a}}(\hat{\boldsymbol{k}}, \hat{\boldsymbol{e}})}{k_{\mathrm{a}}^2} \int_K \frac{\mathrm{d}k}{k^2} = \frac{g_{\mathrm{a}}(\hat{\boldsymbol{k}}, \hat{\boldsymbol{e}})}{k_{\mathrm{a}}^3}. \tag{6.3}$$

Analogous to (6.2), it is concluded that

$$\frac{g_{\mathrm{a}}(\hat{\boldsymbol{k}}, \hat{\boldsymbol{e}})}{k_{\mathrm{a}}^3} \leqslant \frac{\eta(-\hat{\boldsymbol{k}}, \hat{\boldsymbol{e}}^*)}{2} \left(\hat{\boldsymbol{e}}^* \cdot \boldsymbol{\gamma}_{\mathrm{e}} \cdot \hat{\boldsymbol{e}} + (\hat{\boldsymbol{k}} \times \hat{\boldsymbol{e}}^*) \cdot \boldsymbol{\gamma}_{\mathrm{m}} \cdot (\hat{\boldsymbol{k}} \times \hat{\boldsymbol{e}}) \right), \tag{6.4}$$

with equality if and only if $g(k; \hat{\boldsymbol{k}}, \hat{\boldsymbol{e}}) = g_{\mathrm{a}}(\hat{\boldsymbol{k}}, \hat{\boldsymbol{e}}) k^2/k_{\mathrm{a}}^2$, for $k \in [k_{\mathrm{a}}, \infty)$, and zero elsewhere. Various waveguide horns and reflectors such as Hertz's classical cylindrical antenna are examples of antennas with an approximately constant effective antenna aperture.

For a given right-hand side of (2.2), a comparison between (6.2) and (6.4) shows that the antenna onset frequencies k_{p} and k_{a} satisfy

$$\frac{k_{\mathrm{p}}}{k_{\mathrm{a}}} = \left(\frac{g_{\mathrm{p}}(\hat{\boldsymbol{k}}, \hat{\boldsymbol{e}})}{3 g_{\mathrm{a}}(\hat{\boldsymbol{k}}, \hat{\boldsymbol{e}})} \right)^{1/3}, \tag{6.5}$$

implying that $k_{\mathrm{p}} > k_{\mathrm{a}}$, for $g_{\mathrm{p}}(\hat{\boldsymbol{k}}, \hat{\boldsymbol{e}}) > 3 g_{\mathrm{a}}(\hat{\boldsymbol{k}}, \hat{\boldsymbol{e}})$, and $k_{\mathrm{p}} < k_{\mathrm{a}}$, for $g_{\mathrm{p}}(\hat{\boldsymbol{k}}, \hat{\boldsymbol{e}}) < 3 g_{\mathrm{a}}(\hat{\boldsymbol{k}}, \hat{\boldsymbol{e}})$. This comparison is illustrated in Fig. 3 using the following models with identical values of the integrated partial realized gain: $g(k; \hat{\boldsymbol{k}}, \hat{\boldsymbol{e}}) = g_{\mathrm{p}}(\hat{\boldsymbol{k}}, \hat{\boldsymbol{e}})$, for $k \in [k_{\mathrm{p}}, \infty)$, and $g(k; \hat{\boldsymbol{k}}, \hat{\boldsymbol{e}}) = g_{\mathrm{a}}(\hat{\boldsymbol{k}}, \hat{\boldsymbol{e}}) k^2/k_{\mathrm{a}}^2$, for $k \in [k_{\mathrm{a}}, \infty)$, and zero elsewhere. In particular, the two cases $g_{\mathrm{p}}(\hat{\boldsymbol{k}}, \hat{\boldsymbol{e}}) < 3 g_{\mathrm{a}}(\hat{\boldsymbol{k}}, \hat{\boldsymbol{e}})$ and $g_{\mathrm{p}}(\hat{\boldsymbol{k}}, \hat{\boldsymbol{e}}) > 3 g_{\mathrm{a}}(\hat{\boldsymbol{k}}, \hat{\boldsymbol{e}})$ examined in Fig. 3 refer to the antenna onset frequencies $k_{\mathrm{p}} < k_{\mathrm{a}}$ and $k_{\mathrm{p}} > k_{\mathrm{a}}$, respectively. Of course, it is unphysical to include an infinitely high frequency in the above-mentioned models. However, it is not a severe restriction since the damping factor $1/k^4$ in (2.2) implies that the integrated partial realized gain mainly is dominated by the antenna's low- and intermediate-frequency behavior.

6.3 More general models of UWB antennas

Although many UWB antennas may be characterized as having a constant partial realized gain or a constant effective antenna aperture, there are also antennas that

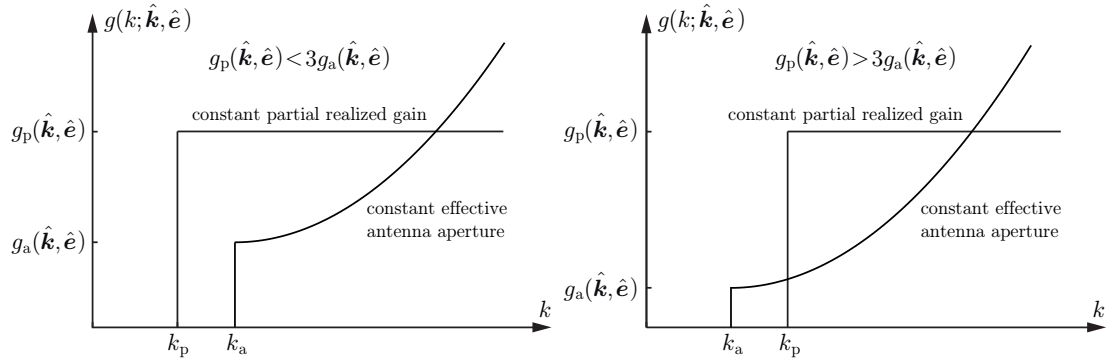

Figure 3: A comparison between a priori estimates for a constant partial realized gain $g_{\rm p}(\hat{\boldsymbol{k}},\hat{\boldsymbol{e}})$ and a constant effective antenna aperture $\pi g_{\rm a}(\hat{\boldsymbol{k}},\hat{\boldsymbol{e}})/k_{\rm a}^2$.

do not fall into this classification. In fact, the UWB antenna is only one part of a broadband communication system designed to meet an overall specification. It is therefore motivated to briefly discuss more general models of UWB antennas based on the lossy transmission problem in [4, 13]. From the analysis in [4, 13], it is clear that the low-frequency behavior of the effective antenna aperture is governed by $\sigma_{\rm a}(k;\hat{\boldsymbol{k}},\hat{\boldsymbol{e}}) = \mathcal{O}(k^2)$ as $k \to 0$, or equivalently,

$$g(k;\hat{\boldsymbol{k}},\hat{\boldsymbol{e}}) = \mathcal{O}(k^4) \text{ as } k \to 0, \tag{6.6}$$

where (3.4) has been used. Relation (6.6) is a natural asymptotic behavior to guarantee the existence of (2.2) in the classical sense. Instead of choosing a constant partial realized gain or a constant effective antenna aperture which obviously lacks any continuity properties at $k = k_{\rm p}$ and $k = k_{\rm a}$, each antenna engineer may create his or her own model to fulfill the overall system requirements. Then, based on this model, the antenna onset frequency is determined by numerically solving the static boundary-value problems discussed in Sec. 4.

6.4 A numerical example for the circular disk

As an example of how the estimates in Secs. 5 and 6 can be utilized in modern antenna design, consider a planar perfectly electric conducting antenna Λ circumscribed by a circular disk Λ_+ of radius a. Let $\hat{\boldsymbol{\nu}}$ denote an arbitrary outward-directed unit normal vector of the disk and let $\hat{\boldsymbol{k}} = \hat{\boldsymbol{\nu}}$ and $\hat{\boldsymbol{e}} = \hat{\boldsymbol{\rho}}$, where $\hat{\boldsymbol{\rho}}$ is a radial unit vector in polar coordinates. This choice of $\hat{\boldsymbol{k}}$ and $\hat{\boldsymbol{e}}$ corresponds to a direction of observation and an electric polarization which are perpendicular and parallel to the disk, respectively. Introduce the UWB frequency band $[3.1, 10.6]\,\text{GHz}$, or equivalently $[0.65, 2.22]\,\text{cm}^{-1}$, as briefly discussed in Sec. 1. Assume that Λ is specified to have a partial realized gain

$$g(k;\hat{\boldsymbol{\nu}},\hat{\boldsymbol{\rho}}) \geqslant \begin{cases} g_{\rm level}(\hat{\boldsymbol{\nu}},\hat{\boldsymbol{\rho}})k^4/k_1^4 & k \in [0, k_1] \\ g_{\rm level}(\hat{\boldsymbol{\nu}},\hat{\boldsymbol{\rho}}) & k \in [k_1, k_2] \\ 0 & \text{otherwise} \end{cases} \tag{6.7}$$

where $k_1 = 0.65\,\mathrm{cm}^{-1}$ and $k_2 = 2.22\,\mathrm{cm}^{-1}$. Then, for a given threshold $g_{\mathrm{level}}(\hat{\boldsymbol{\nu}}, \hat{\boldsymbol{\rho}})$, it is desirable to determine the smallest radius a such that it is feasible for Λ to have a partial realized gain which satisfies (6.7).

Based on the requirement in (6.7), the left-hand side of (2.2) is estimated from below by

$$\int_0^\infty \frac{g(k;\hat{\boldsymbol{\nu}},\hat{\boldsymbol{\rho}})}{k^4}\,\mathrm{d}k \geqslant g_{\mathrm{level}}(\hat{\boldsymbol{\nu}},\hat{\boldsymbol{\rho}})\left(\frac{1}{k_1^3}+\int_{k_1}^{k_2}\frac{\mathrm{d}k}{k^4}\right) = \frac{g_{\mathrm{level}}(\hat{\boldsymbol{\nu}},\hat{\boldsymbol{\rho}})}{3}\frac{4k_2^3-k_1^3}{k_1^3k_2^3}. \tag{6.8}$$

From the analysis of the elliptical disk in [17], it follows that the electric and magnetic polarizability dyadics of the circular disk in the perfectly electric conducting limit are $\boldsymbol{\gamma}_{\mathrm{e}} = 16a^3\mathbf{I}_\perp/3$ and $\boldsymbol{\gamma}_{\mathrm{m}} = \mathbf{0}$, where $\mathbf{I}_\perp = \mathbf{I}_3 - \hat{\boldsymbol{\nu}}\hat{\boldsymbol{\nu}}$ denotes the projection dyadic in $\mathbb{R}^3$. Hence, by inserting (6.8) into (2.2), one obtains

$$\frac{g_{\mathrm{level}}(\hat{\boldsymbol{\nu}},\hat{\boldsymbol{\rho}})}{a^3} \leqslant 0.55\eta(-\hat{\boldsymbol{\nu}},\hat{\boldsymbol{\rho}}), \tag{6.9}$$

where a now measures the radius of the disk in units of centimeters. For example, by invoking (5.1), it is concluded that the minimum radius of the disk is 1.8 cm for $g_{\mathrm{level}}(\hat{\boldsymbol{\nu}},\hat{\boldsymbol{\rho}}) = 3$ and 1.9 cm for $g_{\mathrm{level}}(\hat{\boldsymbol{\nu}},\hat{\boldsymbol{\rho}}) = 4$. For a well-matched antenna, η is close to $1/2$ and a more realistic bound on a is therefore 2.2 cm and 2.4 cm for $g_{\mathrm{level}}(\hat{\boldsymbol{\nu}},\hat{\boldsymbol{\rho}}) = 3$ and $g_{\mathrm{level}}(\hat{\boldsymbol{\nu}},\hat{\boldsymbol{\rho}}) = 4$, respectively. Finally, note that (6.9) is of such general character that it can be compared to any planar antenna to establish how effectively the antenna makes use of its surface area.

7 Dyson's equiangular spiral antenna

In this section, numerical results for Dyson's equiangular spiral antenna are presented and compared with the estimates introduced in Secs. 5 and 6.

7.1 General properties

Dyson's equiangular planar spiral antenna in Fig. 4 is an example of a nearly self-complementary antenna often modeled by a constant partial realized gain [5]. It is parameterized by the azimuthal angle ϕ; in terms of $\vartheta = 5/4$ and the radius a of the smallest circumscribing disk, the parametrization of the two spiral arms reads $r_1(\phi) = a\vartheta^{\phi-4\pi}$ and $r_2(\phi) = a\vartheta^{\phi-9\pi/2}$, for $\phi \in [0, 4\pi]$, and $r_3(\phi) = a\vartheta^{\phi-5\pi}$ and $r_4(\phi) = a\vartheta^{\phi-11\pi/2}$, for $\phi \in [\pi, 5\pi]$. Introduce the coordinate system $(\hat{\boldsymbol{u}}, \hat{\boldsymbol{v}}, \hat{\boldsymbol{z}})$ with the $\hat{\boldsymbol{z}}$-axis being outward directed from the plane of the antenna, see Fig. 4. Then, according to the IEEE standard [1], the transmitted waves from the antenna result in right-circularly polarized (RCP or $\hat{\boldsymbol{e}}_{\mathrm{R}}$-polarized) radiation in the positive $\hat{\boldsymbol{z}}$-direction and thus left-circularly polarized (LCP or $\hat{\boldsymbol{e}}_{\mathrm{L}}$-polarized) radiation in the negative $\hat{\boldsymbol{z}}$-direction. Here, the electric polarizations $\hat{\boldsymbol{e}}_{\mathrm{R}}$ and $\hat{\boldsymbol{e}}_{\mathrm{L}}$ are defined by

$$\begin{cases} \hat{\boldsymbol{e}}_{\mathrm{R}} = \frac{1}{\sqrt{2}}(\hat{\boldsymbol{u}} + \mathrm{i}\hat{\boldsymbol{v}}) & (\mathrm{RCP}) \\ \hat{\boldsymbol{e}}_{\mathrm{L}} = \frac{1}{\sqrt{2}}(\hat{\boldsymbol{u}} - \mathrm{i}\hat{\boldsymbol{v}}) & (\mathrm{LCP}) \end{cases}, \qquad \begin{cases} \hat{\boldsymbol{e}}_{\mathrm{R}} = \frac{1}{\sqrt{2}}(\hat{\boldsymbol{u}} - \mathrm{i}\hat{\boldsymbol{v}}) & (\mathrm{RCP}) \\ \hat{\boldsymbol{e}}_{\mathrm{L}} = \frac{1}{\sqrt{2}}(\hat{\boldsymbol{u}} + \mathrm{i}\hat{\boldsymbol{v}}) & (\mathrm{LCP}) \end{cases}, \tag{7.1}$$

for radiation in the positive and negative $\hat{\boldsymbol{z}}$-directions, respectively.

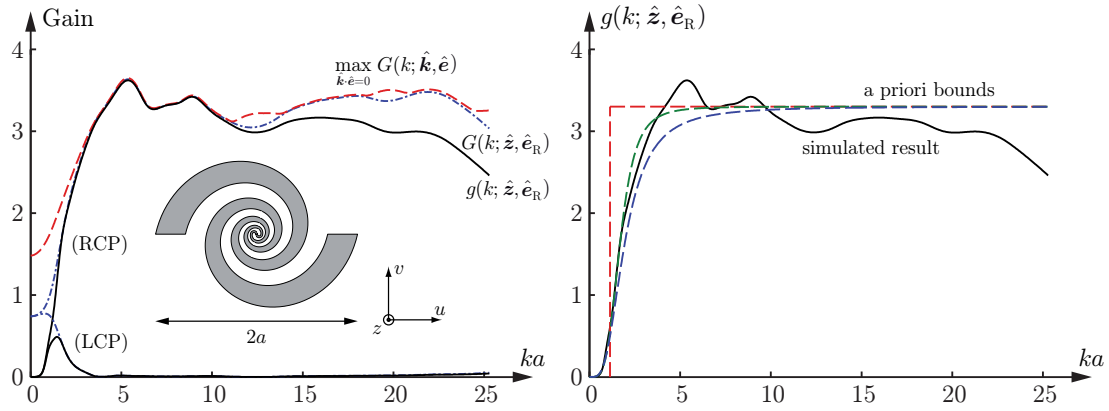

Figure 4: Left: maximum gain $\max_{\hat{\boldsymbol{k}}\cdot\hat{\boldsymbol{e}}=0} G(k;\hat{\boldsymbol{k}},\hat{\boldsymbol{e}})$ (red dashed line), partial gain $G(k;\hat{\boldsymbol{z}},\cdot)$ (blue dashed-dotted line) and partial realized gain $g(k;\hat{\boldsymbol{z}},\cdot)$ (black solid line), for both the $\hat{\boldsymbol{e}}_{\mathrm{R}}$- and $\hat{\boldsymbol{e}}_{\mathrm{L}}$-polarizations. Right: a priori estimates on the partial realized gain $g(k;\hat{\boldsymbol{z}},\hat{\boldsymbol{e}}_{\mathrm{R}})$ derived from the antenna's electrostatic properties using $\eta(-\hat{\boldsymbol{z}},\hat{\boldsymbol{e}}_{\mathrm{R}}^{*}) = 0.62$.

7.2 Numerical results

A numerical solution of the Maxwell equations using the EFIELD commercial method of moments solver is employed to illustrate the estimates in Secs. 5 and 6. For this purpose, the antenna is modeled by perfectly electric conducting material parameters and matched to the input impedance $250\,\Omega$. It is simulated using a delta-gap feed model and the resulting reflection coefficient Γ is depicted in Fig. 5. Based on the threshold of a voltage standing wave ratio less than two, or equivalently $|\Gamma| \leqslant 1/3$, the bandwidth is calculated to be 171% relative to the center frequency $k_0 a = 10.5$. The maximum gain $G_{\max}(k) = \max_{\hat{\boldsymbol{k}}\cdot\hat{\boldsymbol{e}}=0} G(k;\hat{\boldsymbol{k}},\hat{\boldsymbol{e}})$, the partial gain $G(k;\hat{\boldsymbol{z}},\cdot)$ in the positive $\hat{\boldsymbol{z}}$-direction and the partial realized gain $g(k;\hat{\boldsymbol{z}},\cdot)$ in the positive $\hat{\boldsymbol{z}}$-direction are depicted on the left-hand side of Fig. 4. It is observed that $g(k;\hat{\boldsymbol{z}},\hat{\boldsymbol{e}}_{\mathrm{R}})$ is approximately constant over a large frequency interval with a main beam in the $\hat{\boldsymbol{z}}$-direction. For comparison, the corresponding results for the LCP radiation are included in Fig. 4 with an overall partial realized gain $g(k;\hat{\boldsymbol{z}},\hat{\boldsymbol{e}}_{\mathrm{L}})$ less than unity.

The antenna is also simulated in plane-wave scattering when it is loaded with $250\,\Omega$ in series with the feeding port. The resulting extinction cross section, scattering cross section and effective antenna aperture are depicted on the right-hand side of Fig. 5.[4] It is observed that the scattering effects are dominant when the incident field is $\mathrm{e}^{-\mathrm{i}k\hat{\boldsymbol{z}}\cdot\boldsymbol{x}}\hat{\boldsymbol{e}}_{\mathrm{R}}$, while the absorption properties are more noticeable for the $\mathrm{e}^{-\mathrm{i}k\hat{\boldsymbol{z}}\cdot\boldsymbol{x}}\hat{\boldsymbol{e}}_{\mathrm{L}}$ excitation. The high-frequency limit $A(-\hat{\boldsymbol{z}}) = 0.36$ of the extinction cross section is marked by a star in Fig. 5, *cf.*, the "extinction paradox" which states that A is twice the projected area in the $\hat{\boldsymbol{z}}$-direction in units of $2\pi a^2$ [17, 20]. The corresponding curves for the pointwise absorption efficiency $\sigma_{\mathrm{a}}/\sigma_{\mathrm{ext}}$ and the extinc-

[4]The notations (RCP) and (LCP) in Figs. 5 and 6 refer to the polarization of the antenna rather than the polarization of the incident wave, *i.e.*, the labels (RCP) and (LCP) should be interpreted as the incident plane wave being LCP and RCP, respectively.

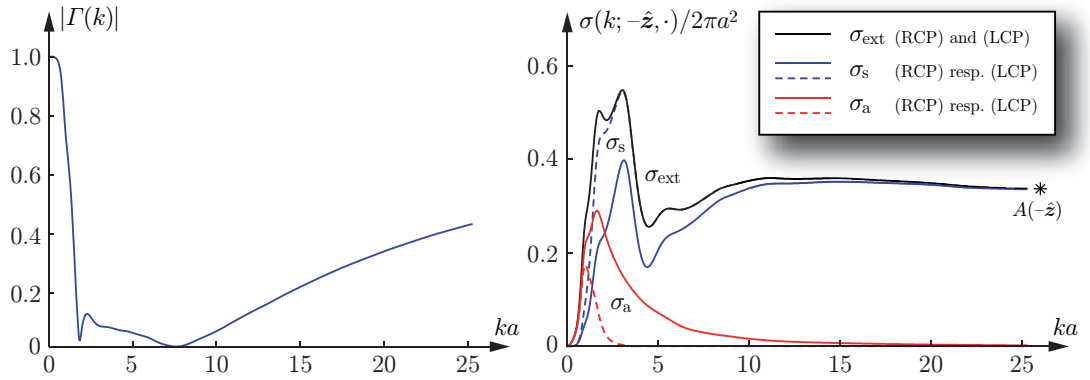

Figure 5: Left: the magnitude of the reflection coefficient Γ when the antenna is matched to the input impedance $250\,\Omega$. Right: the extinction cross section, scattering cross section and effective antenna aperture, σ_{ext}, σ_{s}, and σ_{a}, respectively, in units of $2\pi a^2$.

tion volume ϱ are illustrated in Fig. 6 (recall that ϱ is identical for both the $\hat{\boldsymbol{e}}_{\text{R}}$- and $\hat{\boldsymbol{e}}_{\text{L}}$-polarizations). The star on the right-hand side of Fig. 6 indicates the value of the right-hand side of (3.10), and it is concluded that (3.10) holds for Dyson's equiangular spiral antenna.

The generalized absorption efficiency is calculated from the ratio of the integrated absorption to the integrated extinction. The result is $\eta_{\text{R}} = 0.62$ and $\eta_{\text{L}} = 0.40$, where $\eta_{\text{R}} = \eta(-\hat{\boldsymbol{z}}, \hat{\boldsymbol{e}}_{\text{R}}^*)$ and $\eta_{\text{L}} = \eta(-\hat{\boldsymbol{z}}, \hat{\boldsymbol{e}}_{\text{L}}^*)$. This result implies that the quotients $\eta_{\text{R}}/(\eta_{\text{R}}+\eta_{\text{L}}) = 0.61$ and $\eta_{\text{L}}/(\eta_{\text{R}}+\eta_{\text{L}}) = 0.39$ may be interpreted as efficiency factors for the antenna's overall ability to intercept any of the $\hat{\boldsymbol{e}}_{\text{L}}$- and $\hat{\boldsymbol{e}}_{\text{R}}$-polarizations.

7.3 Analysis of the associated polarizability dyadics

The electric polarizability dyadic is determined by numerically solving (4.2) in the perfectly electric conducting limit. In terms of the $(\hat{\boldsymbol{u}}, \hat{\boldsymbol{v}}, \hat{\boldsymbol{z}})$ basis, the result is the following symmetric matrix:

$$[\boldsymbol{\gamma}_{\text{e}}] = \begin{pmatrix} 2.82 & -0.63 & 0 \\ -0.63 & 1.98 & 0 \\ 0 & 0 & 0 \end{pmatrix} a^3. \tag{7.2}$$

The corresponding magnetic counterpart vanishes since no magnetic dipole moment is supported by the antenna geometry. In particular, note that the elements in (7.2) in the third row and third column are identically zero, reflecting the vanishing thickness of the antenna. The largest eigenvalue to (7.2) is $\gamma_1 = 3.16a^3$ which should be compared with the corresponding number $16a^3/3$ for the smallest circumscribing disk in the high-contrast limit. Based on the variational results in Sec. 5, the number $16a^3/3$, or approximately $5.33a^3$, is a priori known to be an upper bound on γ_1. Although the equiangular spiral antenna only occupies 36% of the smallest circumscribing disk (recall that $A(-\hat{\boldsymbol{z}}) = 0.36$), it is concluded that the antenna in fact

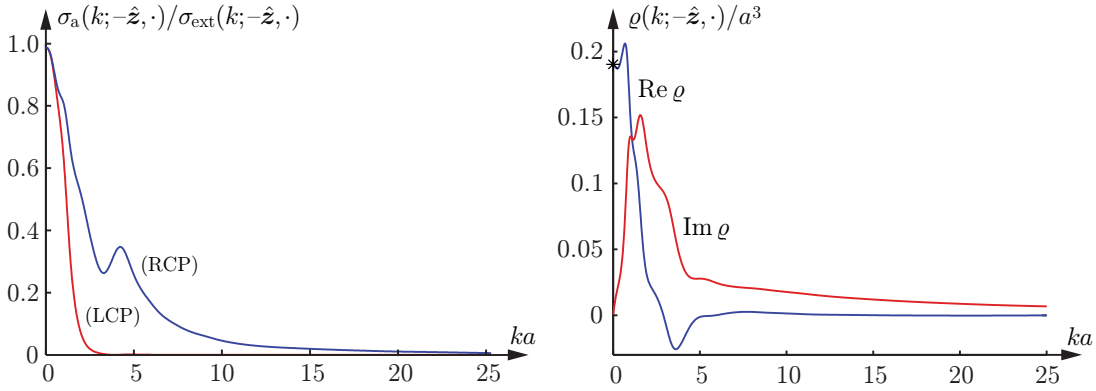

Figure 6: The pointwise absorption efficiency σ_a/σ_{ext} (left) and the real and imaginary parts of the extinction volume ϱ in units of a^3 (right). The star on the right-hand side of the figure represents the integral in (3.10).

makes effectively use of its surface area since $\gamma_1/(\pi a^2 A(-\hat{\boldsymbol{z}})) = 2.79a$ is larger than the corresponding number $1.70a$ if the entire disk is utilized as an antenna.

The first Rayleigh quotient on the right-hand side of (2.2) is obtained from (7.2) by a straightforward matrix multiplication:

$$\hat{\boldsymbol{e}}^* \cdot [\boldsymbol{\gamma}_e] \cdot \hat{\boldsymbol{e}} = \frac{1}{2} \begin{pmatrix} 1 \\ \pm \mathrm{i} \\ 0 \end{pmatrix}^\dagger \begin{pmatrix} 2.82 & -0.63 & 0 \\ -0.63 & 1.98 & 0 \\ 0 & 0 & 0 \end{pmatrix} \begin{pmatrix} 1 \\ \pm \mathrm{i} \\ 0 \end{pmatrix} a^3 = 2.40a^3, \tag{7.3}$$

where a dagger denotes the complex conjugate transpose and the upper and lower signs in (7.3) refer to the electric polarizations $\hat{\boldsymbol{e}} = \hat{\boldsymbol{e}}_R$ and $\hat{\boldsymbol{e}} = \hat{\boldsymbol{e}}_L$, respectively. The result in (7.3) should also be compared with the corresponding number $5.33a^3$ for the smallest circumscribing disk. Both $3.16a^3$ and $5.33a^3$ yield upper bounds on the integrated partial realized gain when inserted into the right-hand side of (5.3). However, recall that γ_2 vanishes from the right-hand side of (5.3) since no magnetic dipole moment is supported by the antenna geometry.

7.4 A priori estimates on the partial realized gain

Without loss of generality, throughout this section consider only RCP radiation in the positive $\hat{\boldsymbol{z}}$-direction, *i.e.*, let $\hat{\boldsymbol{e}} = \hat{\boldsymbol{e}}_R$, $\hat{\boldsymbol{k}} = \hat{\boldsymbol{z}}$ and $\eta = \eta_R$. Furthermore, introduce the scaled partial realized gain $f(\kappa) = g(k; \hat{\boldsymbol{z}}, \hat{\boldsymbol{e}}_R)$, where $\kappa = ka$. A simple change of variables in (2.2) then yields

$$\int_0^\infty \frac{g(k;\hat{\boldsymbol{z}},\hat{\boldsymbol{e}}_R)}{k^4}\,\mathrm{d}k = a^3 \int_0^\infty \frac{f(\kappa)}{\kappa^4}\,\mathrm{d}\kappa = \frac{\eta_R}{2}\Big(\hat{\boldsymbol{e}}_R^* \cdot \boldsymbol{\gamma}_e \cdot \hat{\boldsymbol{e}}_R + (\hat{\boldsymbol{z}} \times \hat{\boldsymbol{e}}_R^*) \cdot \boldsymbol{\gamma}_m \cdot (\hat{\boldsymbol{z}} \times \hat{\boldsymbol{e}}_R)\Big). \tag{7.4}$$

Equivalently, by invoking (7.3) and $\eta_R = 0.62$, one obtains the following identity which is independent of the radius a of the smallest circumscribing disk:

$$\int_0^\infty \frac{f(\kappa)}{\kappa^4}\,\mathrm{d}\kappa = 0.74. \tag{7.5}$$

As a consequence, any non-negative function f satisfying (7.5) with the correct low-frequency behavior $f(\kappa) = \mathcal{O}(\kappa^4)$ as $\kappa \to 0$ is a possible candidate for the partial realized gain of the antenna in Fig. 4. Additional knowledge or specification of the frequency characteristic of the antenna must now be invoked to further establish estimates on the partial realized gain. For example, let $f(\kappa) = 3.3$, for $\kappa \in [\kappa_\mathrm{p}, \infty)$, and zero elsewhere. This model is illustrated by the uppermost dashed line on the right-hand side of Fig. 4. The associated onset frequency $\kappa_\mathrm{p} = k_\mathrm{p} a$ is given by (6.2), *viz.*,

$$\kappa_\mathrm{p} \geqslant \left(\frac{3.3}{3 \cdot 0.74} \right)^{1/3} = 1.14. \tag{7.6}$$

However, a more realistic model of the partial realized gain is $f(\kappa) = 3.3\kappa^4/(\alpha+\kappa^4)$, where the constant α satisfies

$$\int_0^\infty \frac{f(\kappa)}{\kappa^4} \, \mathrm{d}\kappa = g_\mathrm{level} \int_0^\infty \frac{\mathrm{d}\kappa}{\alpha + \kappa^4} = \frac{2.40 \cdot 0.62}{2} = 0.74. \tag{7.7}$$

A numerical solution of (7.7) yields $\alpha = 8.40$, implying that $f(\kappa) = 3.3\kappa^4/(8.40+\kappa^4)$ is a potential candidate for the partial realized gain. This estimate is illustrated by the intervening dashed line in Fig. 4. Finally, a slightly different bound is obtained using $f(\kappa) = 3.3\kappa^4/(\beta + \kappa^{8/3})^{3/2}$, where the constant $\beta = 3.58$ is the solution of

$$\int_0^\infty \frac{f(\kappa)}{\kappa^4} \, \mathrm{d}\kappa = 3.3 \int_0^\infty \frac{\mathrm{d}\kappa}{(\beta + \kappa^{8/3})^{3/2}} = \frac{2.40 \cdot 0.62}{2} = 0.74. \tag{7.8}$$

This estimate is illustrated by the lowermost dashed line. From Fig. 4, it is concluded that the three models discussed above estimate the overall partial realized gain of the antenna remarkably well.

8 Conclusions

This paper investigates a sum rule valid for a large class of linear and reciprocal antennas. A priori estimates on the partial realized gain and onset frequency are derived for two important archetypes of UWB antennas: those with a constant partial realized gain and those with a constant effective antenna aperture. These estimates are numerically exemplified in Secs. 6 and 7 by the smallest circumscribing disk and Dyson's equiangular spiral antenna, respectively.

Although the electric and magnetic polarizability dyadics are restricted to the static limit, the above-mentioned examples suggest that the polarizability dyadics in fact are crucial for the understanding of an antenna's ability to direct power over a frequency interval. For example, from (4.5) and (4.6) it is clear that the high-contrast polarizability dyadic merely is defined as the first moment of the induced charge density. As a consequence, the further the accumulated charges are separated, the larger are the corresponding elements of the polarizability dyadics. Another striking consequence of (4.5) and (4.6) is that the interior of an antenna has less influence on the elements of the polarizability dyadics compared with its boundary

surface. Removing interior parts of the antenna will only slightly reduce the left-hand side of (2.2), but mainly redistribute the integrand along the frequency axis. It is thus concluded that the high-contrast polarizability dyadic reproduces and quantifies the well-known rule of thumb that the boundary is the critical parameter in antenna design, far more so than the surface area or interior geometry of the antenna. However, from a practical point of view, the detailed structure of an antenna's feeding port and matching network is also of considerable importance for the overall antenna performance.

The estimates introduced in this paper are also valuable for comparing existing antennas with various circumscribing geometries. Such a comparison suggests that it is beneficial to classify an antenna in terms of its surface or volume efficiency, *cf.*, the discussion in Sec. 6.4. Of course, the polarizability dyadics cannot completely quantify the performance of an antenna. For example, these dyadics are ignorant of whether it is advantageous to model a given structure as a resonant antenna or as an antenna having a broadband frequency characteristic.

Acknowledgments

The financial support by the Swedish Research Council and the SSF Center for High Speed Wireless Communication is gratefully acknowledged. The authors are also grateful for fruitful discussions with Prof. Gerhard Kristensson and Prof. Anders Karlsson at the Department of Electrical and Information Technology, Lund University, Sweden.

References

[1] Antenna Standards Committee of the IEEE Antennas and Propagation Society. IEEE Standard Definitions of Terms for Antennas, 1993. IEEE Std 145-1993.

[2] S. Chandrasekhar. *Radiative Transfer*. Dover Publications, New York, 1960.

[3] L. J. Chu. Physical limitations of omni-directional antennas. *Appl. Phys.*, **19**, 1163–1175, 1948.

[4] G. Dassios and R. Kleinman. *Low Frequency Scattering*. Oxford University Press, Oxford, 2000.

[5] J. Dyson. The equiangular spiral antenna. *IEEE Trans. Antennas Propagat.*, **7**(2), 181–187, 1959.

[6] M. Gustafsson, C. Sohl, and G. Kristensson. Physical limitations on antennas of arbitrary shape. *Proc. R. Soc. A*, **463**(2086), 2589–2607, 2007.

[7] M. Gustafsson, C. Sohl, and G. Kristensson. Physical limitations on scattering and absorption of antennas. In *Proceedings of the Second European Conference*

on Antennas and Propagation. The Institution of Engineering and Technology, 2007.

[8] M. Gustafsson, C. Sohl, and G. Kristensson. Physical limitations on antennas of arbitrary shape. Technical Report LUTEDX/(TEAT-7153)/1–37/(2007), Lund University, Department of Electrical and Information Technology, P.O. Box 118, S-221 00 Lund, Sweden, 2007. http://www.eit.lth.se.

[9] R. C. Hansen. *Electrically Small, Superdirective, and Superconductive Antennas*. John Wiley & Sons, New Jersey, 2006.

[10] A. Hujanen, J. Holmberg, and J. C.-E. Sten. Bandwidth limitations of impedance matched ideal dipoles. *IEEE Trans. Antennas Propagat.*, **53**(10), 3236–3239, 2005.

[11] D. S. Jones. Low frequency electromagnetic radiation. *J. Inst. Maths. Applics.*, **23**(4), 421–447, 1979.

[12] D. S. Jones. Scattering by inhomogeneous dielectric particles. *Quart. J. Mech. Appl. Math.*, **38**, 135–155, 1985.

[13] R. E. Kleinman and T. B. A. Senior. Rayleigh scattering. In V. V. Varadan and V. K. Varadan, editors, *Low and High Frequency Asymptotics*, volume 2 of *Handbook on Acoustic, Electromagnetic and Elastic Wave Scattering*, chapter 1, pages 1–70. Elsevier Science Publishers, Amsterdam, 1986.

[14] R. G. Newton. *Scattering Theory of Waves and Particles*. Dover Publications, New York, second edition, 2002.

[15] H. Schantz. *The Art and Science of Ultra-wideband Antennas*. Artech House, Boston, London, 2005.

[16] S. Silver. *Microwave Antenna Theory and Design*, volume 12 of *Radiation Laboratory Series*. McGraw-Hill, New York, 1949.

[17] C. Sohl, M. Gustafsson, and G. Kristensson. Physical limitations on broadband scattering by heterogeneous obstacles. *J. Phys. A: Math. Theor.*, **40**(36), 11165–11182, 2007.

[18] C. Sohl, M. Gustafsson, and G. Kristensson. Physical limitations on metamaterials: Restrictions on scattering and absorption over a frequency interval. *J. Phys. D: Applied Phys.*, **40**(22), 7146–7151, 2007.

[19] C. Sohl, C. Larsson, M. Gustafsson, and G. Kristensson. A scattering and absorption identity for metamaterials: Experimental results and comparison with theory. *J. Appl. Phys.*, **103**(5), 054906, 2008.

[20] C. Sohl. *Dispersion Relations for Extinction of Acoustic and Electromagnetic Waves*. Licentiate thesis, Lund University, Department of Electrical and Information Technology, P.O. Box 118, S-221 00 Lund, Sweden, 2007.

[21] H. van de Hulst. *Light Scattering by Small Particles*. John Wiley & Sons, Inc., New York, 1957.

[22] M. C. Villalobos, H. D. Foltz, J. S. McLean, and I. Sen Gupta. Broadband tuning limits on UWB antennas based on Fano's formulation. In C. E. Baum, A. P. Stone, and J. S. Tyo, editors, *Ultra-Wideband, Short-Pulse Electromagnetics 8*, pages 83–87. Springer-Verlag, New York, 2007.

[23] H. A. Wheeler. Fundamental limitations of small antennas. *Proc. IRE*, **35**(12), 1479–1484, 1947.

Summation rules for the antenna input impedance

Mats Gustafsson and Christian Sohl

Paper XI

Based on: M. Gustafsson and C. Sohl. Summation rules for the antenna input impedance. *Proceedings of the IEEE International Symposium on Antennas and Propagation*, San Diego, U.S., July 5–12, 2008.

Abstract

This paper deals with sum rules for the input impedance, admittance, and reflection coefficient of a large class of linear and reciprocal antennas. The derivation is based on certain Herglotz functions and their appropriate Cauchy integrals. The derived sum rules are shown to be governed by the capacitance and the inductance properties of the antenna in the low- and high-frequency regimes. In particular, the results are applied to a first dominant resonance and it is shown to yield a useful estimate of the Q-value in terms of the radiation resistance of the antenna and its capacitance and inductance at low frequencies. The theoretical findings are compared with numerical simulations of different dipole antennas.

1 Introduction

The Kramers-Kronig relations are probably the most well known dispersion relations, see Ref. 6. These dispersion relations relate the real and imaginary parts of the constitutive relations. Sum rules are closely related to dispersion relations, and they are important for consistency checks as well as deriving various bounds and estimates in theoretical physics. In Refs. 4, 8, 9, and 10, a sum rule that relates the absorption and scattering cross sections to the polarizability dyadics is analyzed, and, *e.g.*, used to derive physical bounds on antennas of arbitrary shape. Similar relations are of great importance in quantum mechanics, circuit theory with early contributions by Fano in Ref. 2, and planar radar absorbers in Ref. 7.

Herglotz (or positive real) functions are considered as the mathematical background to dispersion relations and sum rules. They are defined as holomorphic mappings from the upper (or right) complex half-plane into itself, *cf.*, Hardy spaces and bounded analytical functions in Ref. 6. One can argue that causality implies analyticity, and passivity (or stability) implies the definite sign of the imaginary (or real) part that characterizes these functions. The choice of the upper or right half-plane depends on the time convention used in the Fourier (or Laplace) transform, and it is recognized that the upper and right half-planes are most commonly used in theoretical physics and circuit theory, respectively.

2 Antenna impedance as a Herglotz function

A general lossless, single-port antenna including a matching network and a transmission line is considered, see Ref. 4. The reflection coefficient Γ is defined in a reference plane in the transmission line. Causality, *i.e.*, the fact that the reflected wave and the incident wave are time-ordered, implies that Γ can be extended to a holomorphic function in a complex half-plane. Moreover, passivity implies $|\Gamma| \leqslant 1$. The antenna input impedance Z is then given by a Cayley transform of the reflection coefficient, and is hence a Herglotz function, see Ref. 6.

It is assumed that Z is well defined for all finite frequencies, and that it can be expanded in an asymptotic series at $\omega = 0$ and $\omega = \infty$, where ω denotes the angular

frequency. Specifically, the low-frequency expansion is assumed to have the form

$$Z(\omega) = \frac{1}{\mathrm{i}\omega C} + \mathrm{i}\omega L + \mathcal{O}(\omega^2) \quad \text{as } \omega \to 0, \tag{2.1}$$

where $C > 0$ and $L > 0$, and the high-frequency asymptote is assumed to be $Z(\omega) = \mathrm{i}\omega L_\infty + \mathcal{O}(1)$ as $\omega \to \infty$, where $L_\infty \leqslant L$. Note that the low-frequency expansion is consistent with the ladder network representations in Ref. 1 for the impedance of the spherical vector waves. The antenna is termed electric if $1/C > 0$. The corresponding magnetic antenna with $1/C = 0$ is analyzed with an analogous low-frequency expansion for the admittance $Y = 1/Z$.

Now, integrate $Z(\omega)/\omega^2$ over a half circle in the appropriate half-plane to get the following sum rule for the radiation resistance $R = \operatorname{Re} Z$:

$$\int_0^\infty \frac{R(\omega)}{\omega^2}\, \mathrm{d}\omega = \frac{\pi}{2}(L - L_\infty). \tag{2.2}$$

There are two additional sum rules for the corresponding admittance. The admittance $Y = 1/Z = G + \mathrm{i}B$ has the asymptotic expansions $Y(\omega) = \mathrm{i}\omega C + \mathrm{i}\omega^3 LC^2 + \mathcal{O}(\omega^4)$ as $\omega \to 0$ and $Y(\omega) = \omega B_\infty + \mathcal{O}(1)$ as $\omega \to \infty$. Note that $B_\infty = 0$ if $L_\infty > 0$. Integrate $Y(\omega)/\omega^2$ and $Y(\omega)/\omega^4$ over a half circle to obtain the identities

$$\int_0^\infty \frac{G(\omega)}{\omega^2}\, \mathrm{d}\omega = \frac{\pi}{2}(C - B_\infty), \qquad \int_0^\infty \frac{G(\omega)}{\omega^4}\, \mathrm{d}\omega = \frac{\pi}{2}LC^2. \tag{2.3}$$

Although, these identities are interesting by themselves, it is easier to interpret the related sum rules for the reflection coefficient. The reflection coefficient is bounded in magnitude by unity, and thus $\ln \Gamma$ is holomorphic in an appropriate half-plane. However, as Γ in general has zeros in the considered half-plane it is necessary to remove these by extracting the associated Blaschke product, see Ref. 6. The logarithm of Γ has the low-frequency expansion

$$-\ln \Gamma(\omega) = -\ln \frac{Z(\omega) - R_0}{Z(\omega) + R_0} = 2CR_0\mathrm{i}\omega - 2CR_0(C^2R_0^2/3 - CL)\mathrm{i}\omega^3 + \mathcal{O}(\omega^4) \tag{2.4}$$

as $\omega \to 0$, where R_0 denotes the characteristic impedance of the transmission line. The Herglotz function identities then give the following sum rules:

$$\int_0^\infty \frac{1}{\omega^2} \ln \frac{1}{|\Gamma(\omega)|}\, \mathrm{d}\omega = \pi CR_0 + \pi \sum_n \operatorname{Im} \frac{1}{\omega_n} \tag{2.5}$$

and

$$\int_0^\infty \frac{1}{\omega^4} \ln \frac{1}{|\Gamma(\omega)|}\, \mathrm{d}\omega = \pi CR_0(CL - C^2R_0^2/3) + \frac{\pi}{3} \sum_n \operatorname{Im} \frac{1}{\omega_n^3}, \tag{2.6}$$

where $\ln |\Gamma(\omega)|^{-1} \geqslant 0$ and ω_n denote the complex valued zeros of Γ.

The integral identities (2.5) and (2.6) can be used to derive various bounds on the reflection coefficient and the bandwidth, *cf.*, the Fano theory in Refs. 2 and 3. The narrow-band result for $\omega \in [\omega_1, \omega_2]$ is

$$B \leqslant \frac{\pi C^2 LR_0}{\ln \Gamma_0^{-1}} \omega_0^3, \tag{2.7}$$

where $\Gamma_0 = \max_{\omega_1 \leqslant \omega \leqslant \omega_2} |\Gamma|$, $\omega_0 = (\omega_1 + \omega_2)/2$, and $B = (\omega_2 - \omega_1)/\omega_0$.

3 Resonance models and Q-values

Many antennas have a multi-resonance characteristic where it is common to utilize the first dominant resonance. It is also observed that the weighting functions ω^2 and ω^4 in (2.2) to (2.3) and (2.5) to (2.6) emphasize the behavior of the antenna around the first resonance. For these types of antennas, it is interesting to compare the results with a single resonance model. Consider an antenna that is resonant at ω_0 and perfectly matched to the characteristic impedance R_0 with the input impedance having the low-frequency asymptotic (2.1). The simple resonance model

$$Z(\omega) = \frac{1}{\mathrm{i}\omega C} + \frac{\mathrm{i}\omega L}{1 + \nu \mathrm{i}\omega/\omega_1 - \omega^2/\omega_1^2}, \tag{3.1}$$

cf., the Lorentz model for temporally dispersive media, can be used to model this impedance up to ω_0. Note that the integral identities derived above are valid for this model as it satisfies all mathematical requirements. The parameters ω_1 and ν are given by $\omega_1 = \omega_0/\sqrt{1-\beta}$ and $\nu = \omega_1 C R_0 \beta$, respectively, where $\beta = \omega_0^2 LC/(1 + \omega_0^2 C^2 R_0^2)$. The Q-value at $\omega = \omega_0$ is easily estimated as

$$Q \approx \frac{\omega_0 |Z'(\omega_0)|}{2R_0} \approx \frac{1}{C^2 L R_0 \omega_0^3}, \tag{3.2}$$

where the similarities with (2.7) is observed, *i.e.*, $BQ \leqslant \pi/\ln \Gamma_0^{-1}$ as for the case with an RCL resonance circuit [3].

4 A comparison with partial waves

The partial (or spherical vector) wave expansion is often used to derive physical bounds on antennas [1, 3, 5]. The lowest order TM (or electrical dipole) modes have the input impedance [1] $Z(\omega) = 1/\mathrm{i}\omega C + \mathrm{i}\omega L/(1 + \mathrm{i}\omega L/R)$, where $CR = a/\mathrm{c}_0$, $L/R = a/\mathrm{c}_0$, and a denotes the radius of the circumscribing sphere and c_0 is the phase velocity of light in free space. Apply the bounds (2.7) and (3.2) to get

$$Q \approx \frac{\mathrm{c}_0^3}{\omega_0^3 a^3} + \mathcal{O}(\omega_0^{-1}) \quad \text{and } B \leqslant \frac{\pi \omega_0^3 a^3}{\mathrm{c}_0^3 \ln \Gamma_0^{-1}}. \tag{4.1}$$

These bounds are consistent with the Chu and Chu-Fano theory [1, 3, 5].

5 Numerical bounds for dipole antennas

The dipole is probably the simplest electrical antenna. Here, cylindrical dipoles with semi-axis ratios $\ell/d = \{1000, 500, 100\}$ and capacitively loaded dipoles with a length to top diameter ratio $\ell/d = \{10, 1\}$ are considered, see Tab. 1. The antennas are center fed with a simple gap model in the MoM simulations and the input impedances are determined from low frequencies up to the first resonance. The low frequency result is used to estimate C and L in (2.1), see the table, where the radius

$a = \sqrt{\ell^2 + d^2}/2$ and the free space permittivity, permeability, and impedance ϵ_0, μ_0, η_0, respectively, are used. The MoM results are also used to estimate the resonance frequency, $\omega_0 = k_0 \mathrm{c}_0$, and the corresponding radiation resistance from which the Q-value is calculated by numerical differentiation (3.2). To compare the results with the single resonance model, L, C, R_0, and $k_0 a$ are used to estimate the Q-value, where Q_r denote the Q-value in (3.2).

#	ℓ/d	$C/(\epsilon_0 a)$	$L/(\mu_0 a)$	R_0/η_0	$k_0 a$	Q	Q/Q_r
1	1000	0.54	0.64	0.19	1.51	8.2	0.98
2	500	0.62	0.56	0.19	1.51	7.3	0.97
3	100	0.92	0.37	0.19	1.48	5.3	0.95
4	10	1.36	0.40	0.17	1.17	5.1	0.95
5	1	3.06	0.72	0.04	0.63	14	0.99

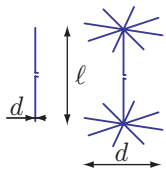

Table 1: Numerical results of various dipole antennas.

Acknowledgments

The financial support by the Swedish Research Council and the SSF Center for High Speed Wireless Communication is gratefully acknowledged.

References

[1] L. J. Chu. Physical limitations of omni-directional antennas. *Appl. Phys.*, **19**, 1163–1175, 1948.

[2] R. M. Fano. Theoretical limitations on the broadband matching of arbitrary impedances. *Journal of the Franklin Institute*, **249**(1,2), 57–83 and 139–154, 1950.

[3] M. Gustafsson and S. Nordebo. Bandwidth, Q-factor, and resonance models of antennas. *Progress in Electromagnetics Research*, **62**, 1–20, 2006.

[4] M. Gustafsson, C. Sohl, and G. Kristensson. Physical limitations on antennas of arbitrary shape. *Proc. R. Soc. A*, **463**(2086), 2589–2607, 2007.

[5] R. C. Hansen. *Electrically Small, Superdirective, and Superconductive Antennas.* John Wiley & Sons, New Jersey, 2006.

[6] H. M. Nussenzveig. *Causality and Dispersion Relations.* Academic Press, London, 1972.

[7] K. N. Rozanov. Ultimate thickness to bandwidth ratio of radar absorbers. *IEEE Trans. Antennas Propagat.*, **48**(8), 1230–1234, August 2000.

[8] C. Sohl and M. Gustafsson. A priori estimates on the partial realized gain of ultra-wideband (UWB) antennas. *Quart. J. Mech. Appl. Math.*, **61**(3), 415–430, 2008.

[9] C. Sohl, M. Gustafsson, and G. Kristensson. Physical limitations on broadband scattering by heterogeneous obstacles. *J. Phys. A: Math. Theor.*, **40**(36), 11165–11182, 2007.

[10] C. Sohl, M. Gustafsson, and G. Kristensson. Physical limitations on metamaterials: Restrictions on scattering and absorption over a frequency interval. *J. Phys. D: Applied Phys.*, **40**(22), 7146–7151, 2007.